

STRUCTURAL RESPONSE AND DESIGN OF ALUMINIUM ALLOY MEMBERS

EVANGELIA GEORGANTZIA

A thesis submitted in partial fulfilment of the requirements of Liverpool
John Moores University for the degree of Doctor of Philosophy

June 2022

To my parents, **Vaios** and **Areti**, and my sister, **Despoina**.

For their ongoing love, unconditional support, and for pushing me to be the best version
of myself in all of my endeavours.

List of Publications

The present thesis is based on the work published in the following papers. The publication list includes the peer reviewed journal papers along with the conference papers.

Peer Reviewed Journal papers

- (1) **Georgantzia E**, Bin Ali S, Gkantou M, Kamaris GS, Kansara K, Atherton W. Flexural buckling performance of concrete-filled aluminium alloy tubular columns. *Eng. Struct.* 2021; 242:112546.
- (2) **Georgantzia E**, Gkantou M, Kamaris GS. Aluminium alloys as structural material: A review of research. *Eng. Struct.* 2021; 227(1):13-37.
- (3) **Georgantzia E**, Gkantou M, Kamaris GS. Numerical modelling and design of aluminium alloy angles under uniform compression. *CivilEng.* 2021;2:632-651.
- (4) **Georgantzia E**, Gkantou M, Kamaris GS, Kansara KD. Design of aluminium alloy channel sections under minor axis bending. *Thin-Walled Struct.* 2022;174:109098.
- (5) **Georgantzia E**, Gkantou M, Kamaris GS, Kansara KD. Ultimate response and plastic design of aluminium alloy continuous beams. *Structures.* 2022;39:175-193.
- (6) **Georgantzia E**, Gkantou M, Kamaris GS. Aluminium alloy channel columns under axial compression: Testing, numerical modelling and design. *Thin-Walled Struct.* 2023;174:110242.

Peer Reviewed Conference papers

- (1) **Georgantzia E.** Structural response and design of aluminium alloy members. 2022. Presented in the 24th Young Researchers Conference, The Institution of Structural Engineers, United Kingdom. 15 March 2022 (selected for poster presentation).
- (2) **Georgantzia E.** Aluminium alloys as structural material: Towards a sustainable construction future. 2021. Presented in the 1st International Congress of Civil Engineering and Architecture (ICCEA2021), Venezuela. 24 October 2021 (invited speaker).
- (3) **Georgantzia E.** Structural response and design of aluminium alloy members. 2021. Presented in the British Federation of Women Graduates North West - Academic Presentation Day, Port Sunlight Village, United Kingdom. 9 October 2021 (invited speaker).
- (4) **Georgantzia E**, Bin Ali S, Gkantou M, Kamaris GS, Kansara KD, Atherton W. Structural response of aluminium alloy concrete filled tubular columns. *ce/papers*, 2021;4:614-620. Presented in the 9th European Conference on Steel and Composite Structures (EUROSTEEL 2021), Sheffield, United Kingdom. 01-03 September 2021.
- (5) **Georgantzia E.** Structural response and design of aluminium alloy members. 2021. Presented in the Three Minute Thesis (3MT) Competition, Liverpool John Moores University. Liverpool, United Kingdom. 24 June 2021.
- (6) **Georgantzia E**, Bin Ali S, Gkantou M, Kamaris GS, Kot P, Hashim K. Numerical modelling of concrete-filled aluminium alloy 6082-T6 columns under axial compression. *IOP Conference Series: Materials Science and Engineering*. 2021;1058:012010. Presented in the 15th Global Congress on Manufacturing and Management (GCMM 2021), Liverpool, United Kingdom. 07-09 June 2021.
- (7) Bin Ali S, **Georgantzia E**, Gkantou M, Kamaris GS, Kot P. Experimental study of square and rectangular hollow section aluminium alloy columns. *IOP Conference Series: Materials Science and Engineering*. 2021;1058:012010. Presented in the 15th Global Congress on Manufacturing and Management (GCMM 2021), Liverpool, United Kingdom. 07-09 June 2021.

- (8) **Georgantzia E.** Structural response and design of aluminium alloy members. 2021. Presented in the FET Postgraduate Research Day, Liverpool John Moores University. Liverpool, United Kingdom. 19 May 2021 (selected for pitch presentation).
- (9) **Georgantzia E,** Gkantou M, Kamaris GS, Kansara KD, Hashim K. Aluminium alloy cross-sections under uniaxial bending and compression: A numerical study IOP Conference Series: Materials Science and Engineering. 2021;1058: 012011. Presented in the 1st Conference on Science and Technology for early career researchers and postgraduate students (STEPS 2020), Erbil, Iraq. 20-22 December 2020.
- (10) **Georgantzia E,** Gkantou M. Flexural buckling of circular concrete-filled hollow sections: Numerical modelling and design Advances in Geotechnics and Structural Engineering. Lecture Notes in Civil Engineering. 2021;143:697-707. Presented in the 3rd International Conference on Trends and Recent Advances in Civil Engineering (TRACE 2020), Amity University Uttar Pradesh, Noida, India. 20-21 August 2020.

Abstract

6xxx series aluminium alloys, widely known as structural alloys, are characterised by a wide variety of advantages, such as high strength-to-weight ratio, ease of fabrication, high degree of workability, great durability, excellent electrical and thermal conductivity, high corrosion resistance and recyclability and attractive appearance at their natural finish. The aforementioned advantageous features have contributed to increased usage of aluminium alloys in structural applications, where their application can allow for a reduction of the total structural weight.

Despite the benefits of structural aluminium alloys, a comprehensive literature review conducted herein, revealed that there are still limitations in their design which forces the designers to favour more conventional materials. This is related to the fact that the current design specifications are based on limited amount of experimental and numerical results, whilst sometimes adopt similar principles to their steel structure counterparts, without sufficient consideration of the differences between the two materials. This practice leads to inaccurate strength predictions, which are opposed to an economical and efficient design philosophy. However, additional research work can lead to modifications of the existing design codes and potentially increase structural engineers' confidence towards a more frequent employment of aluminium alloys as primary structural material.

The literature review has identified a gap in knowledge on the structural performance of bare tubular, concrete-filled tubular and channel sections. To this end, a series of experimental tests combined with finite element (FE) modelling studies is conducted to investigate the compressive and flexural performance of bare tubular, concrete-filled tubular and channel sections. Material testing including tensile tests on coupons and compressive tests on concrete cubes is carried out to determine the mechanical properties of the examined aluminium alloy and concrete, respectively. Upon material testing, 22 fix-ended stub column tests are executed to study the cross-sectional response of bare tubular, concrete-filled tubular and channel cross-sections. The same types of cross-sections are also employed to perform 24 pin-ended column tests to investigate their minor-axis buckling behaviour. Moreover, 9 bare tubular and 4 concrete-filled tubular cross-sections are tested under three-point bending, whilst 5 bare tubular and 14 channel

cross-sections are tested under four-point bending to quantify their moment resistance and rotational capacity. Finally, 5 two-span continuous beam tests employing bare tubular cross-sections are also executed to estimate the rotational capacity and the potential for moment redistribution of aluminium alloy indeterminate beams.

Subsequent parametric studies are carried out to supplement the experimentally obtained data sets providing a deeper understanding about the structural response of the considered cross-sections. Particularly, an extensive numerical modelling study consisting of 47 FE models is performed to investigate further the cross-sectional response of channel cross-sections. 133 in total parametric studies are also undertaken to generate additional structural performance data for the buckling behaviour of bare tubular, concrete-filled tubular and channel cross-sections. Moreover, the flexural behaviour of channel cross-sections under four-point bending configuration is better clarified through 140 additional numerical analyses. Finally, the experimental results for the bare tubular cross-sections obtained from the three- and four-point bending tests as well as the two-span continuous beam tests are utilised to generate 108 results aimed to extend the pool of performance data for aluminium alloy indeterminate structures.

Following, the results obtained from the testing programme in conjunction with those generated from the parametric studies are used to examine the influence of various parameters on the behaviour of aluminium alloy structural elements. Moreover, the experimental and numerical ultimate strengths are utilised to assess the applicability and accuracy of the existing design specifications with particular emphasis on current European Standards, i.e., Eurocode 9 (EC9) and Eurocode 4 (EC4). The applicability of the Continuous Strength Method (CSM) and Direct Strength Method (DSM) to aluminium alloy structural elements are also evaluated herein. Particularly, revised buckling curves are proposed for Class A aluminium alloy bare tubular and channel pin-ended columns improving the strength predictions by 12% and 5%, respectively. A strength increase in the range of 23% to 93.1% of the concrete-filled tubular members is captured compared to their bare counterparts. Moreover, in absence of codified criteria for composite aluminium-concrete cross-sections and members, the present study proposes adopting the European design formulae for composite steel-concrete cross-sections and members, i.e., EC4, replacing the material properties of steel by those of

aluminium alloy. In addition, the DSM is suggested for the design of aluminium alloy channel sections and members subjected to concentric compression providing improved strength predictions by 13% and 7%, respectively. This study also suggests revised EC9 Class 2 and Class 3 slenderness limits for outstand elements under stress gradient. A modified plastic effective width method is also recommended for the design of slender aluminium alloy channel sections subjected to minor axis bending offering 52% more accurate strength predictions than those of EC9. Finally, this study concludes that employing the plastic design concept and particularly the plastic hinge method and the CSM in case of 6082-T6, 6063-T5 and 6061-T6 aluminium alloy indeterminate structures, 20% more accurate strength predictions could be achieved than those resulting from global elastic analysis.

The design recommendations suggested in the present study are in line with the observed structural response and thus providing quite accurate and consistent strength predictions towards a more safe and economically efficient design process.

Acknowledgements

It would not have been possible to write the present doctoral thesis without the help and support of the kind people around me, to only some of whom it is possible to give particular mention here.

This thesis would not have been possible without the help, support and patience of my lead supervisor, Dr. Michaela Gkantou, not to mention her advice and unsurpassed knowledge of metallic structures. The good advice, support and friendship of my second supervisor, Dr. George S. Kamaris, have been invaluable on both an academic and a personal level, for which I am extremely grateful. I would certainly be remiss to not mention and sincerely thank my third supervisor, Dr. Kunal D. Kansara, for his technical advice and encouragement throughout this research.

I would like also to acknowledge the financial, academic and technical support of Liverpool John Moores University, and its staff, particularly in the award of a Postgraduate Research Studentship that provided the necessary financial support for this research. The laboratory and library facilities of the University have been indispensable. I thank profusely the technicians of both School of Civil Engineering and Built Environment, and School of Engineering, for their kind help and co-operation throughout my research.

A heartfelt thanks to my friends, laboratory and office mates for their deepest comprehension, tolerance and moral support as well as for all stimulating discussions we have had during these years.

I would like also to thank my parents, Vaios and Areti, and my sister, Despoina, who have given me their unequivocal support throughout, as always, for which my mere expression of thanks likewise does not suffice.

Last but not least, I would like to express my utmost gratitude to Prof. Mohammad Mehdi Kashani who supported me sharing his wisdom and denoting great insight during writing up this thesis. It was a great privilege to meet you while completing my research pursuit, for which I am eternally grateful.

Table of Contents

List of Publications	iii
Abstract	vi
Acknowledgements	ix
Table of contents	x
List of Figures	xiv
List of Tables.....	xxiii
Nomenclature	xxviii
CHAPTER 1: Introduction	1
1.1. Background	1
1.2. Aim.....	4
1.3. Objectives.....	4
1.4. Outline of thesis	4
CHAPTER 2: Literature review.....	6
2.1. Introduction.....	6
2.2. Material properties	6
2.2.1. Material properties under monotonic loading.....	8
2.2.2. Material properties under cyclic loading.....	11
2.2.3. Material properties of Heat-Affected Zone.....	12
2.2.4. Material properties at elevated temperatures	12
2.3. Columns	14
2.3.1. Local buckling.....	14
2.3.2. Flexural buckling	20
2.3.3. Welded columns.....	22
2.3.4. Columns at elevated temperatures.....	22
2.4. Beams.....	24
2.4.1. Flexural resistance.....	24
2.4.2. Welded beams	28
2.4.3. Beams at elevated temperatures.....	28
2.5. Beam-columns.....	30
2.6. Residual stresses.....	30

2.7. Web crippling.....	31
2.8. Composite structures.....	34
2.8.1. Aluminium-concrete structural members.....	34
2.8.2. Aluminium-CFRP structural members.....	35
2.9. Connections.....	35
2.9.1. Welded.....	35
2.9.2. Bolted.....	36
2.9.3. Other studies.....	40
2.10. Summary and knowledge gap.....	41
CHAPTER 3: Methodology.....	43
3.1. Introduction.....	43
3.2. Experimental investigation.....	44
3.2.1. Material testing.....	44
3.2.2. Initial geometric imperfections.....	47
3.2.3. Fix-ended stub columns.....	48
3.2.4. Pin-ended columns.....	51
3.2.5. Simply-supported beams.....	52
3.2.6. Continuous beams.....	56
3.3. Numerical investigation.....	57
3.3.1. Finite element method.....	57
3.3.2. Elements.....	58
3.3.3. Mesh.....	60
3.3.4. Material properties.....	60
3.3.5. Initial geometric imperfections and residual stresses.....	62
3.3.6. Boundary conditions, constraints and contact interactions.....	63
3.3.7. Analysis techniques.....	64
3.3.8. Analysis output.....	65
3.3.9. Validation.....	66
3.3.10. Parametric studies.....	66
3.4. Analysis of the results and design recommendations.....	67
CHAPTER 4: Experimental investigation of aluminium alloy structural elements.....	68
4.1. Introduction.....	68

4.2. Fix-ended stub columns	70
4.2.1. Bare tubular cross-sections.....	70
4.2.2. Concrete-filled tubular cross-sections.....	77
4.2.3. Channel cross-sections.....	83
4.3. Pin-ended columns.....	87
4.3.1. Bare tubular cross-sections.....	87
4.3.2. Concrete-filled tubular cross-sections.....	94
4.3.3. Channel cross-sections.....	100
4.4. Simply-supported beams.....	108
4.4.1. Bare rectangular tubular cross-sections.....	108
4.4.2. Bare square tubular cross-sections.....	120
4.4.3. Concrete-filled tubular cross-sections.....	129
4.4.4. Channel cross-sections.....	137
4.5. Continuous beams	150
4.6. Summary	157
CHAPTER 5: Validation of the finite element models.....	157
5.1. Introduction.....	158
5.2. Fix-ended stub columns	159
5.2.1. Channel cross-sections.....	159
5.3. Pin-ended columns.....	163
5.3.1. Bare tubular cross-sections.....	163
5.3.2. Concrete-filled tubular cross-sections.....	168
5.3.3. Channel cross-sections.....	172
5.4. Simply-supported beams.....	176
5.4.1. Bare rectangular tubular cross-sections.....	176
5.4.2. Channel cross-sections.....	180
5.5. Continuous beams	185
5.6. Summary	190
CHAPTER 6: Analysis of the results and design recommendations.....	191
6.1. Introduction.....	192
6.2. Fix-ended stub columns	192
6.2.1. Concrete-filled tubular cross-sections.....	1921

6.2.2. Channel cross-sections.....	196
6.3. Pin-ended columns.....	199
6.3.1. Bare tubular cross-sections.....	199
6.3.2. Concrete-filled tubular cross-sections.....	202
6.3.3. Channel cross-sections.....	210
6.4. Simply-supported beams.....	215
6.4.1. Bare rectangular tubular cross-sections.....	215
6.4.2. Concrete-filled tubular cross-sections.....	221
6.4.3. Channel cross-sections.....	226
6.5. Continuous beams.....	250
6.5.1. Assessment of plastic design concept.....	250
6.5.2. Assessment of traditional plastic design method.....	251
6.5.3. Assessment of Eurocode 9.....	253
6.5.4. Assessment of Continuous Strength Method for indeterminate structures.....	257
6.5.5. Comparison of design codes and methods.....	260
CHAPTER 7: Conclusions and future research.....	262
7.1. Fix-ended stub columns.....	262
7.1.1. Concrete-filled tubular cross-sections.....	262
7.1.2. Channel cross-sections.....	263
7.2. Pin-ended columns.....	264
7.2.1. Bare tubular cross-sections.....	264
7.2.3. Concrete-filled tubular cross-sections.....	264
7.2.4. Channel cross-sections.....	265
7.3. Simply-supported beams.....	266
7.3.1. Bare rectangular tubular cross-sections.....	266
7.3.2. Concrete-filled tubular cross-sections.....	267
7.3.3. Channel cross-sections.....	268
7.4. Continuous beams.....	269
7.5. Research impact.....	270
7.6. Suggestions for future work.....	270
References.....	275

List of Figures

Figure 1.1: Examples of aluminium alloy structures [8-14].....	3
Figure 2.1: Stress-strain curves from corresponding tensile coupon tests [19-22].	9
Figure 2.2: Yield and tensile strengths of commonly used aluminium grades.....	10
Figure 2.3: Comparison between test results and EN 1999-1-2 [49] predictions (adapted from [48]).	13
Figure 2.4: Cross-sectional shapes employed in stub column investigations.....	16
Figure 2.5: Comparison between test results and design predictions using EN 1999-1-1[5].....	28
Figure 2.6: Investigated cross-sections of aluminium-concrete composite members [140-144,146-148].....	34
Figure 2.7: Configuration of investigated bolted connections.	37
Figure 3.1: Adopted methodology for the execution of the experimental tests and finite element modelling studies.	44
Figure 3.2: Tensile coupon specimens.	45
Figure 3.3: Experimental stress-strain curves.....	45
Figure 3.4: Typical concrete cube after compression test.	46
Figure 3.5: Measurements of initial geometric imperfections of a typical concrete-filled tubular specimen.....	48
Figure 3.6: Schematic illustration of a typical fix-ended stub concrete-filled tubular column test arrangement and instrumentation.....	50
Figure 3.7: Schematic illustration of a typical pin-ended concrete-filled tubular column test arrangement and instrumentation.....	52
Figure 3.8: Schematic illustration of a typical three-point bending test arrangement and instrumentation of bare tubular cross-section.....	53
Figure 3.9: Schematic illustration of a typical four-point bending test arrangement and instrumentation of bare tubular cross-section.....	55
Figure 3.10: Schematic illustration of the continuous beam test arrangement and instrumentation of bare tubular cross-section.....	56
Figure 3.11: Most commonly applied element types [196].....	59
Figure 3.12: Stress-strain responses considered in the FE simulations.....	62

Figure 3.13: Typical local and global buckling modes of bare tubular pin-ended columns.	63
Figure 4.1: Geometric properties of the BAT sections of the fix-ended stub columns..	71
Figure 4.2: Stress-strain curves of the BAT/CFAT sections of the fix-ended stub columns.	71
Figure 4.3: Schematic illustration of the BAT/CFAT fix-ended stub column test arrangement and instrumentation.	72
Figure 4.4: Typical BAT/CFAT fix-ended stub column test set-up.....	72
Figure 4.5: Typical failure modes of BAT fix-ended stub column specimens.....	74
Figure 4.6: Load-end shortening curves of the BAT fix-ended stub column specimens.	75
Figure 4.7: Geometric properties of the CFAT sections of the fix-ended stub columns.	77
Figure 4.8: Schematic illustration of the CFAT fix-ended stub column test arrangement and instrumentation.	78
Figure 4.9: Typical failure modes of CFAT fix-ended stub column specimens.	79
Figure 4.10: Crack patterns of the infill for typical CFAT fix-ended stub column specimens.....	80
Figure 4.11: Load-end shortening curves of the CFAT fix-ended stub column specimens.	81
Figure 4.12: Adopted notation for the C-sections of the fix-ended stub columns.....	84
Figure 4.13: Stress-strain curves of the C-sections of the fix-ended stub columns.....	84
Figure 4.14: Schematic illustration of the fix-ended stub column test arrangement and instrumentation.	86
Figure 4.15: Typical fix-ended stub column test setup.	86
Figure 4.16: Load-end shortening curves obtained from C-section fix-ended stub column tests.....	87
Figure 4.17: Failure modes obtained from C-section fix-ended stub column tests.....	88
Figure 4.18: Geometric properties of the BAT sections of the pin-ended columns.....	88
Figure 4.19: Stress-strain curves of the BAT/CFAT sections of the pin-ended columns	89

Figure 4.20: Schematic illustration of the BAT pin-ended column test arrangement and instrumentation.	92
Figure 4.21: Typical BAT/CFAT pin-ended column test set-up.....	92
Figure 4.22: Load–mid-height lateral deflection curves obtained from BAT pin-ended column tests.....	93
Figure 4.23: Obtained failure mode for 50.8×50.8×1.6 specimen.	94
Figure 4.24: Geometric properties of the CFAT sections of the pin-ended columns.....	95
Figure 4.25: Schematic illustration of the CFAT pin-ended column test arrangement and instrumentation.	97
Figure 4.26: Load–mid-height lateral deflection curves obtained from CFAT pin-ended column tests.....	98
Figure 4.27: Obtained failure mode for 76.2×38.1×3.3-C specimen.	98
Figure 4.28: Adopted notation for the C-sections of the pin-ended columns.....	100
Figure 4.29: Sign convention for measured initial global geometric imperfection amplitude ω_g of C-section pin-ended columns.....	100
Figure 4.30: Stress-strain curves of the C-sections of the pin-ended columns.....	102
Figure 4.31: Schematic illustration of the pin-ended column test arrangement and instrumentation.	103
Figure 4.32: Typical pin-ended column test setup.	104
Figure 4.33: Sign convention for actual initial load eccentricity e_0 of C-section pin-ended column tests.....	104
Figure 4.34: Load-mid-height lateral deflection curves obtained from pin-ended column tests.....	106
Figure 4.35: Typical failure modes obtained from pin-ended column tests.....	107
Figure 4.36: Geometric properties of the BAT sections of the simply-supported beams.	108
Figure 4.37: Stress-strain curves of the BAT sections of the simply-supported beams.	110
Figure 4.38: Schematic illustration of the three-point bending test arrangement and instrumentation.	112
Figure 4.39: Schematic illustration of the four-point bending test arrangement and instrumentation.	112

Figure 4.40: Typical three-point bending test set-up.....	113
Figure 4.41: Typical four-point bending test set-up.....	113
Figure 4.42: Normalised moment–rotation responses of BAT beam specimens obtained from three-point bending tests.....	115
Figure 4.43: Normalised moment–curvature responses of BAT beam specimens obtained from four-point bending tests.....	115
Figure 4.44: Failure modes of BAT beam specimens obtained from three-point and four-point bending tests.....	118
Figure 4.45: Failure modes of BAT beam specimens obtained from three-point bending tests.....	119
Figure 4.46: : Geometric properties of the BAT sections of the simply-supported beams.	120
Figure 4.47: Stress-strain curves of the BAT/CFAT sections of the simply-supported beams.....	121
Figure 4.48: Schematic illustration of the three-point bending test arrangement and instrumentation.....	122
Figure 4.49: Typical three-point bending test set-up.....	123
Figure 4.50: Failure modes of BAT beam specimens obtained from three-point bending tests.....	124
Figure 4.51: Bending moment–midspan deflection curves of BAT beam specimens obtained from three-point bending tests.....	125
Figure 4.52: Bending moment–rotation curves of BAT beam specimens obtained from three-point bending tests.....	126
Figure 4.53: Bending moment–longitudinal strain curves of BAT beam specimens obtained from three-point bending tests.....	128
Figure 4.54: Geometric properties of the CFAT sections of the simply-supported beams.	129
Figure 4.55: Schematic illustration of the three-point bending test arrangement and instrumentation.....	130
Figure 4.56: Typical three-point bending test set-up.....	131
Figure 4.57: Failure modes of CFAT beam specimens obtained from three-point bending tests.....	132

Figure 4.58: Crack patterns of the 50.8×50.8×4.8-C specimen.....	133
Figure 4.59: Bending moment–midspan deflection curves of CFAT beam specimens obtained from three-point bending.	134
Figure 4.60: Bending moment–rotation curves of CFAT specimens beam obtained from three-point bending.....	134
Figure 4.61: Bending moment–longitudinal strain curves of CFAT beam specimens obtained from three-point bending tests.	137
Figure 4.62: Adopted notation of the C-sections of the simply-supported beams.	138
Figure 4.63: Stress-strain curves of the C-sections of the simply-supported beams....	138
Figure 4.64: Schematic illustration of the four-point bending test setup.	141
Figure 4.65: Typical four-point bending test setup.	142
Figure 4.66: Normalised moment–curvature responses of C-section beam specimens obtained from four-point bending tests.	147
Figure 4.67: Typical failure modes of C-section beam specimens obtained from four-point bending tests.....	148
Figure 4.68: Failure modes of C-section beam specimens obtained from four-point bending tests.	150
Figure 4.69: Schematic illustration of the continuous beam test arrangement and instrumentation.	152
Figure 4.70: Typical continuous beam test set-up.....	153
Figure 4.71: Load–displacement responses of BAT specimens obtained from continuous beam tests.	155
Figure 4.72: Normalised load–end rotation responses of BAT specimens obtained from continuous beam tests.....	155
Figure 4.73: Failure modes of BAT specimens obtained from continuous beam tests.	156
Figure 4.74: Evolution of the support to span moment ratio with increasing displacement.	156
Figure 5.1: Modelled geometry of a typical of C-section fix-ended stub column specimen and the corresponding applied constraints and boundary conditions.	160
Figure 5.2: Comparison between typical FE and experimental load-deformation curves for 38.1×38.1×4.76-L115 specimen.....	161

Figure 5.3: Comparison between typical experimental (left) and FE (right) failure modes for 50.8×50.8×6.35-L150 specimen.....	162
Figure 5.4: Modelled geometry of a typical BAT pin-ended column specimen and the corresponding applied constraints and boundary conditions.....	164
Figure 5.5: Experimental and numerical load–mid-height lateral deflection curves for BAT pin-ended columns.....	166
Figure 5.6: Experimental and numerical failure modes for 50.8×50.8×1.6 specimen.	167
Figure 5.7: Modelled geometry of a typical CFAT pin-ended column specimen and the corresponding applied constraints and boundary conditions.....	169
Figure 5.8: Experimental and numerical load–mid-height lateral deflection curves for CFAT pin-ended columns..	171
Figure 5.9: Experimental and numerical failure modes for 76.2×76.2×4.8-C specimen.	171
Figure 5.10: Modelled geometry of a typical C-section pin-ended column specimen and the corresponding applied constraints and boundary conditions.....	173
Figure 5.11: Comparison between typical FE and experimental load-deformation curves for 50.8×50.8×6.35-L500 specimen.....	174
Figure 5.12: Comparison between typical experimental (left) and FE (right) failure modes for 76.2×76.2×6.35-L300 specimen.....	175
Figure 5.13: Modelled geometry of a typical C-section simply supported beam specimen and the corresponding applied boundary conditions.	177
Figure 5.14: Comparison between typical numerical and experimental responses for BAT simply-supported beams.....	179
Figure 5.15: Comparison between typical numerical and experimental failure modes for BAT simply-supported beams.....	180
Figure 5.16: Modelled geometry of a typical C-section simply supported beam specimen and the corresponding applied boundary conditions.	181
Figure 5.17: Comparison between typical FE and experimental normalised moment-curvature curves for C-section simply-supported beams.	183
Figure 5.18: Comparison between typical FE and experimental failure modes for C-section simply-supported beams.....	183

Figure 5.19: Modelled geometry of a typical BAT continuous beam specimen and the corresponding applied boundary conditions and constraints.....	186
Figure 5.20: Comparison between typical numerical and experimental response of 50.8×38.1×3.25 specimen.....	188
Figure 5.21: Comparison between typical numerical and experimental failure mode of 38.1×25.4×3.25 specimen.....	188
Figure 5.22: Load configurations considered in parametric studies for BAT continuous beams.....	190
Figure 6.1: Effect of the concrete infill on the CFAT fix-ended stub column specimens compared with the BAT fix-ended stub column specimens, based on average values between the two replicates.....	194
Figure 6.2: Comparison of experimental and FE results with EC9 [5] design strengths for fix-ended stub columns.....	197
Figure 6.3: Comparison of experimental and FE results with DSM [228] design strengths for fix-ended stub columns.....	199
Figure 6.4: Comparison of experimental and numerical results with European and proposed design strengths for BAT columns.	201
Figure 6.5: Comparison of experimental and numerical ultimate loads with design strengths based on European standards and proposed equations for BAT columns.	202
Figure 6.6: Typical load-mid-height lateral deflection curves for CFAT pin-ended columns from FE studies.....	204
Figure 6.7: Effects of concrete compressive strengths f_{ck} on the ultimate strength of CFAT columns ($L_e=1000$ mm).....	206
Figure 6.8: Comparison of experimental and numerical results with proposed design strengths for CFAT columns.	208
Figure 6.9: Comparison of experimental and numerical ultimate loads with proposed design strengths for CFAT columns.....	209
Figure 6.10: Comparison of experimental and FE results with EC9 [5] design strengths for pin-ended columns.....	211
Figure 6.11: Comparison of experimental and FE results with DSM [228] design strengths for pin-ended columns.....	214

Figure 6.12: Assessment of EC9 [5] slenderness limits for internal elements in compression.....	216
Figure 6.13: Base curve and material model adopted by CSM [66].	219
Figure 6.14: Effect of the depth-to-thickness ratio D/t of the aluminium tube on the flexural behaviour of CFAT simply-supported specimens.....	222
Figure 6.15: Effect of the concrete infill on the CFAT simply-supported beam specimens compared with the BAT simply-supported beam specimens.	224
Figure 6.16: Normalised bending moment capacity $M_{u,FE}/M_{pl}$ of C-sections under “n” bending orientation.....	227
Figure 6.17: Normalised bending moment capacity $M_{u,FE}/M_{pl}$ of C-sections under “u” bending orientation.....	228
Figure 6.18: Assessment of Class 2 slenderness limits for outstand elements under stress gradient.	229
Figure 6.19: Assessment of Class 3 slenderness limits for outstand elements under stress gradient.	229
Figure 6.20: Assessment of Class 2 slenderness limits for internal elements in compression.....	230
Figure 6.21: Assessment of Class 3 slenderness limits for internal elements in compression.....	231
Figure 6.22: Assessment of EN 1999-1-1 [5] design strength predictions.....	232
Figure 6.23: Assessment of CSM design strength predictions.....	234
Figure 6.24: Assessment of DSM design strength predictions.....	235
Figure 6.25: Longitudinal stress distribution over the flange at mid-span of the slenderest 6082-T6 and 6063-T5 C-sections under “u” bending configuration.....	237
Figure 6.26: Longitudinal stress distribution over the flange at mid-span of the slenderest 6082-T6 and 6063-T5 C-sections under “n” bending configuration.....	238
Figure 6.27: Plastic Effective Width Method - Strain and stress distribution profiles of the outstand flanges of a C-section under “u” bending orientation.....	240
Figure 6.28: Assessment of Plastic Effective Width Method design strength predictions for Class 4 C-sections under “u” bending orientation.	241
Figure 6.29: Strain coefficient $C_{y,FE}$ derived from FE results.....	242

Figure 6.30: Comparison between FE and calculated stress distribution for typical 6082-T6 and 6063-T5 C-sections under "u" bending orientation.....	243
Figure 6.31: Plastic Effective Width Method-Strain and stress distribution profiles of the outstand flanges of a C-section under "n" bending orientation.....	244
Figure 6.32: Assessment of Plastic Effective Width Method design strength predictions for Class 4 C-sections under "n" bending orientation.	245
Figure 6.33: Comparison between FE and calculated stress distribution for typical 6082-T6 and 6063-T5 C-sections under "n" bending orientation.....	246
Figure 6.34: Comparison between elastic and plastic design concept.	251
Figure 6.35: Assessment of traditional plastic design method.	252
Figure 6.36: Assessment of EC9 [5] using global elastic analysis.	254
Figure 6.37: Assessment of European design provisions using plastic hinge method from Annex-H [5].....	256
Figure 6.38: Assessment of CSM.....	259

List of Tables

Table 1.1: International Design Specifications for Aluminium Alloy Structures.	2
Table 2.1: Summary of basic tempers for wrought alloys and the corresponding subdivisions (adapted from [16]).....	8
Table 2.2: Mechanical properties of commonly investigated aluminium alloys.....	10
Table 2.3: Summary of tests on material properties of aluminium alloys under cyclic loading.....	12
Table 2.4: Summary of aluminium alloy stub column tests.....	17
Table 2.5: Material groups based on temper designation. (adapted from Wang et al. [60])	19
Table 2.6: Summary of aluminium alloy column experiments.	21
Table 2.7: Summary of tests on columns at elevated temperatures.....	23
Table 2.8: Summary of numerical investigations on columns at elevated temperatures.	23
Table 2.9: Summary of investigations on beams.....	26
Table 2.10: Summary of web crippling tests.	33
Table 2.11: Summary of aluminium alloy bolted connection tests.	38
Table 2.12: Summary of recommended future work.....	41
Table 4.1: Mean measured geometrical dimensions and local geometric imperfections of the tested BAT fix-ended stub columns.	71
Table 4.2: Material properties of BAT/CFAT cross-sections obtained from the tensile coupon tests.	72
Table 4.3: Results obtained from BAT fix-ended stub column tests.....	77
Table 4.4: Mean measured geometrical dimensions of the tested CFAT fix-ended stub columns.....	77
Table 4.5: Measured compressive strength of concrete cubes for the CFAT fix-ended stub columns.....	82
Table 4.6: Results obtained from the CFAT fix-ended stub column tests.	83
Table 4.7: Mean measured geometrical dimensions and local geometric imperfections of the tested C-section fix-ended stub columns.	83
Table 4.8: Material properties of C-sections obtained from tensile coupon tests.	85

Table 4.9: Summary of key results obtained from C-section fix-ended stub column tests.	86
Table 4.10: Mean measured geometrical dimensions of the tested BAT pin-ended columns.....	88
Table 4.11: Mean measured geometric imperfections of the tested BAT pin-ended columns.....	88
Table 4.12: Material properties of BAT/CFAT sections obtained from tensile coupon tests.....	90
Table 4.13: Key results obtained from BAT fix-ended column tests.....	94
Table 4.14: Mean measured geometrical dimensions of the tested CFAT pin-ended columns.....	95
Table 4.15: Mean measured geometric imperfections of the tested CFAT pin-ended columns.....	96
Table 4.16: Measured compressive strength of concrete cubes for the CFAT pin-ended columns.....	99
Table 4.17: Key results obtained from CFAT pin-ended column tests.....	99
Table 4.18: Mean measured geometrical dimensions of the tested C-section pin-ended columns.....	100
Table 4.19: Mean measured geometric imperfections of the tested C-section pin-ended columns.....	101
Table 4.20: Material properties of C-sections obtained from tensile coupon tests.	102
Table 4.21: Summary of key results obtained from pin-ended column tests.	105
Table 4.22: Mean measured geometrical dimensions and local geometric imperfections of the tested BAT simply-supported beams.	110
Table 4.23: Material properties of BAT sections obtained from the tensile coupon tests.	111
Table 4.24: Key results obtained from three-point and four-point bending tests.....	116
Table 4.25: Key results obtained from three-point and four-point bending tests.....	116
Table 4.26: Mean measured geometrical dimensions and local geometric imperfections of the tested BAT simply-supported beams.	121
Table 4.27: Material properties of BAT/CFAT sections obtained from the tensile coupon tests.....	121

Table 4.28: Key results obtained from three-point bending tests.....	123
Table 4.29: Mean measured geometrical dimensions of the tested CFAT simply-supported beams.	130
Table 4.30: Key results obtained from three-point bending tests.....	132
Table 4.31: Mean measured geometrical dimensions and local geometric imperfections of the tested C-section simply-supported beams.	138
Table 4.32: Material properties of C-sections obtained from tensile coupon tests.	140
Table 4.33: Key results obtained from the four-point bending tests.	143
Table 4.34: Key results obtained from the four-point bending tests (continued).....	143
Table 4.35: Mean measured geometrical dimensions and local geometric imperfections of the tested BAT continuous beams.	151
Table 4.36: Key results obtained from continuous beam tests.....	154
Table 5.1: Comparison between the FE and experimental ultimate loads for C-section fix-ended stub columns.....	161
Table 5.2: List of key parameters considered in parametric studies for C-section fix-ended stub columns.....	162
Table 5.3: Comparison of test and FE results for varying imperfection amplitudes for BAT pin-ended columns.....	165
Table 5.4: List of key parameters considered in parametric studies for BAT pin-ended columns.....	168
Table 5.5: Comparison of test and FE results for varying imperfection amplitudes for CFAT pin-ended columns..	170
Table 5.6: List of key parameters considered in parametric studies for CFAT pin-ended columns.....	172
Table 5.7: Comparison between the FE and experimental ultimate loads for C-section pin-ended columns for local imperfection amplitude $t_f/15$	174
Table 5.8: List of key parameters considered in parametric studies for C-section pin-ended columns.	175
Table 5.9: Comparison of numerical and experimental ultimate loads for BAT simply-supported beams.	178
Table 5.10: Comparison between the FE and experimental bending moment capacities for C-section simply-supported beams.....	182

Table 5.11: List of key parameters considered in parametric studies for C-section simply-supported beams.	184
Table 5.12: Material properties for 6082-T6 and 6063-T5 [98] aluminium alloys considered in parametric studies.....	185
Table 5.13: Comparison of numerical and experimental ultimate loads for BAT continuous beams.	187
Table 5.14: List of examined parameters in parametric studies for BAT continuous beams.....	189
Table 5.15: Material properties for 6082-T6, 6061-T6 [98] and 6063-T5 [98] aluminium alloys adopted in parametric studies.....	190
Table 6.1: Effect of the concrete infill on the CFAT fix-ended stub column specimens compared with the BAT fix-ended stub column specimens.....	193
Table 6.2: Proposed design strengths for CFAT cross-sections.....	196
Table 6.3: Predicted strength ratios for both experimental and numerical results for fix-ended stub columns.	198
Table 6.4: Predicted strength ratios for both experimental and numerical results for BAT columns.....	202
Table 6.5: Effect of the concrete infill on the CFAT pin-ended column specimens compared with the BAT pin-ended column specimens.....	203
Table 6.6: Predicted strength ratios for both experimental and numerical results for CFAT columns.....	209
Table 6.7: Predicted strength ratios for both experimental and numerical results for pin-ended columns.	213
Table 6.8: Assessment of EC9 [5] and CSM design predictions for BAT simply-supported beams.	218
Table 6.9: Percentage increase in ultimate strength, displacement and rotation at failure due to infill.....	223
Table 6.10: Proposed design strengths for GCFAT and CFAT beams.	226
Table 6.11: Assessment of design strength predictions for C-sections under “n” bending orientation.....	248
Table 6.12: Assessment of design strength predictions for C-sections under “u” bending orientation.....	249

Table 6.13: Assessment of design methods for aluminium alloy continuous beams...261
Table 7.1: Summary of recommended future work.....274

Nomenclature

Latin characters

1D	One-dimensional
2D	Two-dimensional
AA	Aluminium Association
AAG joints	Aluminium alloy gusset joints
A	Cross-sectional area of aluminium
A_c	Cross-sectional area of concrete
A_{eff}	Effective cross-sectional area of aluminium
AIJ	Architectural Institute of Japan
B	Outer flange width
B/t	Width-to-thickness ratio
b	Flat flange width
b_e	Effective flange width
C-	Channel cross-section
C_y	Strain coefficient according to Plastic Effective Width Method
$C_{y,FE}$	Strain coefficient obtained numerically
CFAT	Concrete-filled aluminium tube
CFDT	Concrete-filled double-skin tube
CFRP	Carbon fibre reinforced polymer
CFST	Concrete-filled steel tube
CHS	Circular hollow section
COV	Coefficient of variation
CSM	Continuous Strength Method
D	Outer web depth
d	Flat web depth
DSM	Direct Strength Method
E	Young's modulus of aluminium
E_c	Young's modulus of concrete
EI	Flexural rigidity

EC3	Eurocode 3
EC4	Eurocode 4
EC9	Eurocode 9
ENA	Elastic neutral axis
EOF	End-one-flange
E_{sh}	Strain hardening modulus of aluminium
ETF	End-two-flange
e_m	Combined equivalent global imperfection and applied eccentricity
e_0	Actual initial load eccentricity
F	Load
F_0	Initial experimental load
F_{coll}	Theoretical collapse load
F_{cre}	Elastic flexural buckling stress
F_{crl}	Critical elastic local column buckling load
F_{CSM}	Ultimate load predicted by CSM
F_{EC9-el}	Ultimate load predicted by EC9 applying global elastic design
F_{EC9-H}	Ultimate load predicted by Annex H of EC9
F_{ne}	Flexural buckling strength
$F_{pl,Rk}$	Plastic cross-sectional resistance
F_{pred}	Ultimate cross-sectional load predicted by codes/methods
$F_{pred,DSM}$	Ultimate cross-sectional load predicted by DSM
$F_{pred,EC9}$	Ultimate cross-sectional load predicted by EC9
$F_{pred,EC9,prop}$	Ultimate cross-sectional load predicted by modified EC9
$F_{pred,cs,EC9}$	Ultimate cross-sectional load predicted by EC9
$F_{pred,cs,DSM}$	Ultimate cross-sectional load predicted by DSM
$F_{prop,CFAT}$	Ultimate load for CFAT section proposed by design equations
F_u	Ultimate load
$F_{u,prop}$	Ultimate load calculated by proposed design equations
$F_{u,Exp}$	Ultimate experimental load
$F_{u,BAT}$	Ultimate experimental load of BAT section
$F_{u,C30}$	Ultimate load of CFAT columns with C30 concrete grade
$F_{u,C50/70}$	Ultimate load of CFAT columns with C50 or C70 concrete grade

$F_{u,CFAT}$	Ultimate experimental load of CFAT section
$F_{u,FE}$	Ultimate numerical load
f_{ck}	Compressive cylinder strength of concrete
$f_{ck,cube}$	Compressive cube strength of concrete
$F_{tr-pl-d}$	Ultimate load predicted by traditional plastic design method.
FE	Finite Element
FRP	Fibre reinforced polymer
FSA	Fast-Simulated Annealing
h	Distance between the strain gauges
h_n	Location of neutral axis
HAZ	Heat-Affected Zone
HBJ	Hexagonal bolted joint
I	Second moment of area of aluminium
I_c	Second moment of area of concrete
IOF	Interior-one-flange
ITF	Interior-two-flange
k_e	Correction factor for concrete
L	Column/beam length
L_e	Effective column length
LVDT	Linear variable displacement transducers
LBF	Local buckling of the upper flange
M	Bending moment
M_{CSM}	Ultimate bending moment predicted by CSM
M_{EC9}	Ultimate bending moment predicted by EC9
M_{EC9-H}	Ultimate bending moment predicted by Annex H of EC9
M_{EC9-F}	Ultimate bending moment predicted by Annex F of EC9
M_{el}	Elastic moment resistance
M_{pl}	Plastic moment resistance
M_{pred}	Ultimate bending moment predicted by design codes
$M_{pred,pl-eff-w}$	Ultimate bending moment predicted by Plastic Effective Width Method
M_{span}	Bending moment at the central support

M_{sup}	Bending moment at the midspan
M_u	Ultimate experimental/numerical bending moment
$M_{u,Exp}$	Ultimate experimental bending moment
$M_{u,prop}$	Ultimate bending moment calculated by proposed design equations
MY	Material yielding
n	Hardening exponent (Ramberg-Osgood coefficient)
NA	Neutral axis
NAS	North American Specification
$N_{pred.}$	Load predicted by design codes
NSA	Numerical Slenderness Approach
PNA	Plastic neutral axis
r	Radius of gyration of the aluminium tube
r_{int}	Internal corner radius of the aluminium tube
RHS	Rectangular hollow section
R_m	Rotational capacity
SHS	Square hollow section
t	Thickness
t_f	Flange thickness
t_w	Web thickness
TF	Tensile fracture
W	Vertical deflection
W_{eff}	Effective elastic section modulus of aluminium
W_{el}	Elastic section modulus of aluminium
W_{pl}	Plastic section modulus of aluminium
$W_{pl,n}$	Net plastic section modulus of aluminium
W_{plc}	Plastic section modulus of concrete
$W_{plc,n}$	Net plastic section modulus of concrete
W_u	Ultimate experimental/numerical vertical deflection
WASA	Weighted Average Stress Approach

Greek characters

α	Imperfection factor
α_5	Generalised shape factor for brittle alloys
α_{10}	Generalised shape factor for ductile alloys
$\alpha_{M,j}$	Correction factor
β/ε	Cross-sectional slenderness ratio
β	Flat web depth or flange width
β_f/ε	Slenderness ratio of the flange
β_f	Flat flange width
δ	End shortening
$\delta_{u,Exp}$	Ultimate experimental end shortening
$\delta_{u,Exp,BAT}$	Ultimate experimental end shortening of BAT section
$\delta_{u,Exp,CFAT}$	Ultimate experimental end shortening of CFAT section
Δ	Lateral deflection
Δ_u	Ultimate experimental/numerical lateral deflection
ε	Material coefficient
$\varepsilon_{0.2}$	strain corresponding to 0.2% proof stress ($\sigma_{0.2}$)
ε_{CSM}	Maximum attainable strain according to CSM
ε_f	Strain at fracture
ε_{max}	Maximum recorded compressive strain
ε_{min}	Minimum recorded compressive strain
$\varepsilon_{nom}(\varepsilon)$	Engineering (nominal) strain
ε_{true}^{pl}	Logarithmic plastic strain (true)
ε_u	Ultimate tensile strain
θ	Rotation
θ_m	Rotation at ultimate load
θ_{pl}	Elastic rotation
κ	Curvature
κ_m	Curvature at ultimate load
κ_{pl}	Elastic curvature
$\kappa_{u,Exp}$	Ultimate experimental curvature
$\bar{\lambda}$	Member slenderness

$\bar{\lambda}_0$	Horizontal plateau
λ_c	Column slenderness parameter
$\bar{\lambda}_{cs}$	Cross-sectional slenderness calculated according to CSM
λ_l	Cross-sectional slenderness calculated according to DSM
ρ_c	Reduction factor
$\sigma_{0.01}$	Stress corresponding at 0.01% strain
$\sigma_{0.1}$	Stress corresponding at 0.1% strain
$\sigma_{0.2}$	Stress corresponding at 0.2% strain (proof stress)
σ_{cr}	Elastic critical buckling stress
$\sigma_{nom}(\sigma)$	Engineering (nominal) stress
σ_{true}	True stress
σ_u	Ultimate stress
φ	Buckling coefficient
χ	Buckling reduction factor
ω_g	Global geometric imperfections
ω_l	Local geometric imperfection

CHAPTER 1

Introduction

1.1. Background

The research and application of aluminium alloys as a structural material has increased over the last years owing to its advantageous properties. Today, 25% of the global aluminium production is used in the construction sector [1]. Aluminium alloys are characterised by a wide variety of advantages, such as high strength-to-weight ratio, ease of fabrication, high degree of workability, excellent electrical and thermal conductivity, high corrosion resistance and attractive appearance at its natural finish. Its ease of extrusion which is advantageous for a wide scope of cross-sectional shapes makes aluminium alloy a versatile structural material, suitable for structures that cannot be developed from steel, wood or reinforced concrete. Its prominent corrosion resistance makes it well-suited for applications in marine environments without surface protection and with low maintenance cost. Aluminium is also characterised by great durability, as aluminium structures can be designed with minimum service life of 80 years and within this timespan the dominant material can maintain its inert properties in large temperature variations [1]. Within the framework of sustainability, recent technological advances led to innovative aluminium structural systems that are more efficient from an environmental and economical point of view compared to steel and concrete. In particular, advances on its manufacturing process reduced the required energy more than 75% since 1995, reducing the industry's carbon footprint by almost 40% [2] whilst it has been stated that “aluminum made in North

America is more sustainable today than ever before” [2]. Further to the decrease in carbon dioxide emissions, structural aluminium alloys are 100% recyclable, thereby arguably winning the title of “green metal” [3].

The advantageous features have contributed to increased usage of aluminium in structural applications. Aluminium alloys have been applied in high-rise buildings and roofs, reducing the total weight of the structure, while ensuring adequate bearing capacity. Typical structural aluminium applications along with brief information are presented in Figure 1.1. As with all structural materials, structural design codes are warranted for aluminium alloys. The history of the design codes for aluminium alloy structures is definitely shorter than the corresponding ones for steel structures, as engineers have started widely using aluminium alloys in the construction field over the last 20 years. Currently there are four international design specifications for the structural design of aluminium alloys, listed in Table 1.1.

Table 1.1: International Design Specifications for Aluminium Alloy Structures.

Standard ID	Standard Title
Chinese Standard: GB 50429-2007 [4]	Code for design of aluminium structures
European Committee for Standardization: BS EN 1999:2007 [5]	Design of aluminium structures
Australian/New Zealand Standard: AS/NZS 1664:1997 [6]	Aluminium structures
The Aluminum Association: AA 2020 [7]	Aluminum Design Manual

Based on past research, aluminium alloys could be an alternative structural material, capable of efficiently responding to the challenges encountered in real-life structures, while allowing for sustainable design solutions. Potential applications of aluminium alloys as primary structural material include high-rise buildings, skyscrapers, pavilions, exhibition centres, sports facilities, roof systems and footbridges.

However, as has been reported, many of these codified design rules do not provide accurate predictions, as they are based on limited research work and they sometimes adopt the same assumptions as their steel structural counterparts.

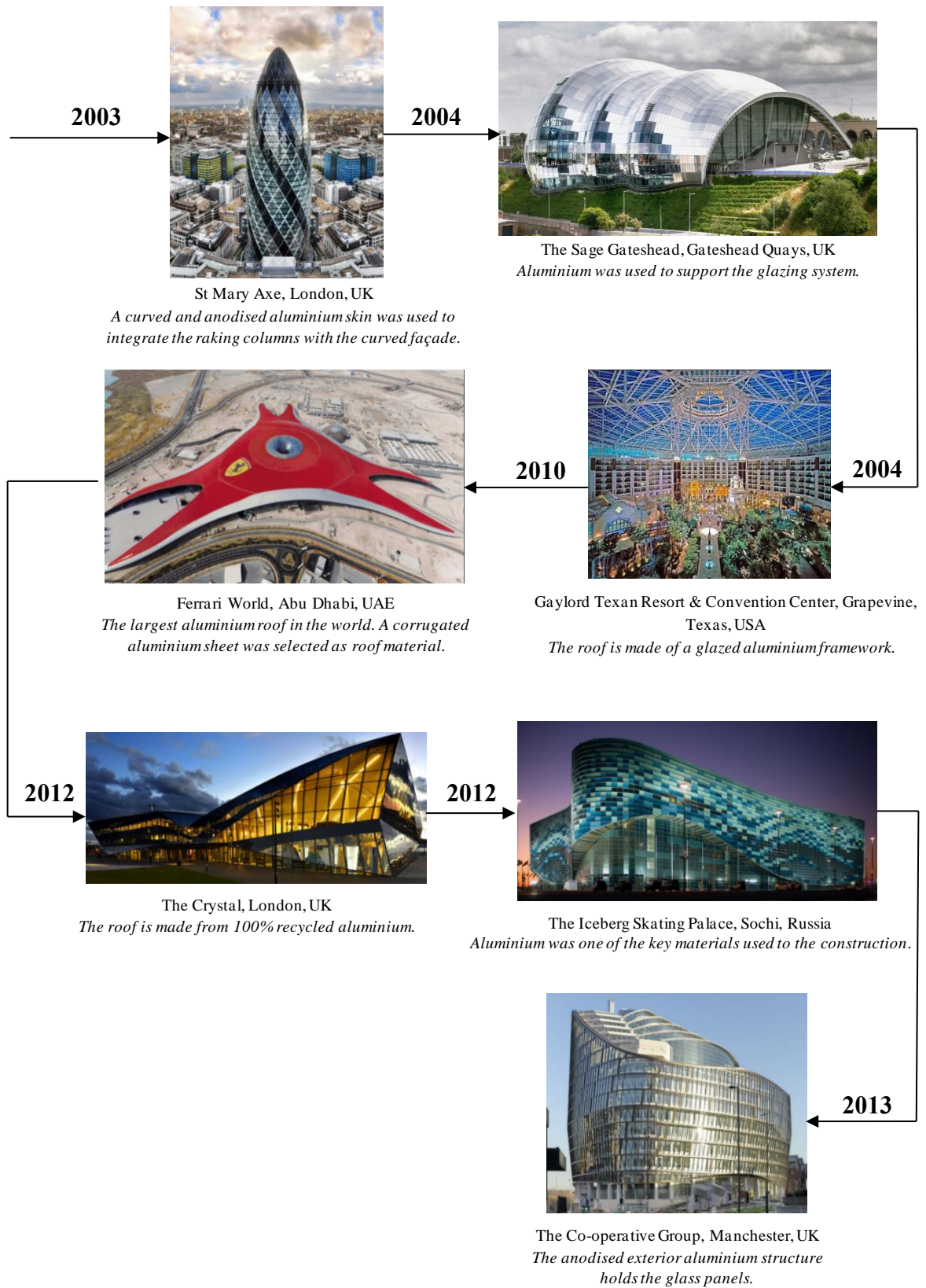


Figure 1.1: Examples of aluminium alloy structures [8-14].

1.2. Aim

The current study aims to investigate the structural behavior of 6xxx series aluminium alloys, with particular emphasis on the relatively new 6082-T6 aluminium alloy, that are the most attractive for structural engineering applications [15-17]. This study will enhance the comprehension of structural aluminium alloys' response and design, thereby also increasing structural engineers' confidence towards a more frequent employment of this material in modern structures.

1.3. Objectives

The objectives towards achieving the research aim set above are described as follows:

- To investigate the cross-sectional behaviour of 6082-T6 fix-ended stub columns employing bare and concrete-filled square/rectangular hollow, and channel sections with varying cross-sectional aspect ratios and cross-sectional slendernesses.
- To study the buckling behaviour of 6082-T6 pin-ended columns employing bare and concrete-filled square/rectangular hollow, and channel sections with varying cross-sectional aspect ratios and cross-sectional and member slendernesses.
- To examine the flexural response of 6082-T6 simply-supported beams employing bare and concrete-filled square/rectangular hollow, and channel sections with varying cross-sectional aspect ratios and cross-sectional slendernesses.
- To investigate the ultimate response of 6082-T6 continuous beams employing stocky bare rectangular hollow sections.
- To assess current design specifications and methods and recommend proper modifications in line with the obtained research outcomes.

1.4. Outline of thesis

In this chapter an introduction on aluminium alloys as structural material is presented, whilst the project's research aim and objectives are provided. The outline of the thesis is given hereafter.

In Chapter 2, a comprehensive literature review of the experimental, numerical and theoretical research works to date on the structural performance and design of aluminium alloy structures is carried out and thus identify existing knowledge gaps.

The methodology followed to investigate experimentally and numerically the structural performance of aluminium alloy cross-sections and members is described thoroughly in Chapter 3, Note that some general experimental techniques and numerical modelling assumptions performed throughout this study are also incorporated in this chapter.

Chapter 4, describes in detail the experimental investigation of the structural response of aluminium alloy structural elements. Series of structural tests comprising fix-ended stub column tests, pin-ended column tests, simply-supported beam tests and continuous beam tests are presented in order to address the compressive and flexural performance of bare tubular, concrete-filled tubular and channel cross-sections. Prior to structural testing, material testing including tensile tests on coupons and compressive tests on concrete cubes was also performed to determine the mechanical properties of the examined aluminium alloy and concrete, respectively.

Chapter 5 focuses on the numerical investigation of the structural response of aluminium alloy structural elements. Series of FE modelling studies are carried out to supplement the experimentally obtained data sets providing a deeper understanding about the structural response of the considered cross-sections.

Having examined experimentally and numerically the structural response of aluminium alloy cross-sections and members, Chapter 6 analyses the results obtained from the testing programme in conjunction with those generated from the parametric studies to examine the influence of the considered parameters on the behaviour of aluminium alloy structural elements. Moreover, in this chapter, the experimental and numerical ultimate strengths are utilised to assess the applicability and accuracy of the existing design specifications and methods and propose safe and economically efficient design recommendations.

A summary of the research outcomes accompanied with some recommendations for future research is given in Chapter 7.

CHAPTER 2

Literature review

2.1. Introduction

The purpose of this chapter is to provide a comprehensive review of the experimental, numerical and theoretical research works to date on the structural performance and design of aluminium alloy structures and thus identify existing knowledge gaps. The material properties of aluminium alloys are discussed in Section 2.2. In Sections 2.3., 2.4. and 2.5. studies focussing on the structural performance of columns, beams and beam-columns are presented, respectively. Reported works on residual stresses and web crippling of aluminium sections are summarised in Sections 2.6. and 2.7. Studies on aluminium-concrete composite structures are outlined in Section 2.8. Reported research on connections are presented in Section 2.9. Concluding remarks on the overall investigation accompanied by suggestions for future work are finally presented in Section 2.10.

2.2. Material properties

Aluminium alloys are divided into two basic categories: wrought and cast alloys. The former comprises alloys which are melted in a furnace and then poured into moulds, whereas the latter includes alloys treated in a solid form. Depending on the strengthening working conditions aluminium alloys can be classified as heat-treatable and not heat-treatable. The Aluminum Association Inc. classifies the wrought alloys into 9 series using

a four-digit system and each series comprises different combinations of alloying additions [2]. The first digit (Xxxx) indicates the principal constituent alloy, whereas the second digit (xXxx) indicates the modifications made in the original alloy. The last two digits (xxXX) are arbitrary numbers so that the specific alloy can be identified in the series. Thus, the material properties can vary offering several options for applications. Research on aluminium alloys in terms of their structural response has focussed on wrought alloys and particularly on 5xxx and 6xxx series that are the most attractive for structural engineering applications due to their mechanical properties [15-17]. 5xxx series alloys are based on magnesium and they are strain hardenable, but not heat treatable. Magnesium additions to aluminium provide among the highest strength non-heat-treatable alloys. These alloys are exceptionally tough, absorbing lots of energy during fracture, and so can be used in critical applications where superior toughness is vital. Generally, 5xxx series alloys have excellent resistance to atmospheric and seawater corrosion to the point that they may be used in severe marine environments. 6xxx series alloys have both magnesium and silicon as their main alloying elements, which combine as magnesium silicide (Mg_2Si) following solid solution. Alloys in this series are heat treatable. These alloys have modestly higher strengths than possible with non-heat-treatable alloys, combined with generally excellent corrosion resistance. 6xxx series alloys are amongst the easiest of aluminium alloys to extrude, and are thus widely used for complex shapes produced in this manner. The alloy classification is also followed by the temper designation in order to provide more information about the fabrication treatment. The temper designation consists of five basic tempers; F, O, H, W, or T, accompanied by additional digits for more details about the fabrication treatment, as described in Table 2.1.

Table 2.1: Summary of basic tempers for wrought alloys and the corresponding subdivisions
(adapted from [16]).

Basic tempers for wrought alloys		Subdivisions of basic tempers
F (fabricated)	The thermal conditions during working or strain-hardening process to obtain specific material properties do not demand any special control.	-
O (annealed)	Treatment under high-temperature conditions in order to achieve maximum workability, toughness and ductility.	-
H (strain-hardened)	Used for non-heat-treatable alloys cold worked by strain-hardening method in order to stabilise their strength.	The first digit indicates the type of the thermal treatment and the second the amount of strain-hardening.
W (solution heat treated)	Applied to alloys subjected to natural aging after the solution heat treatment. Rather limited designation.	-
T (thermally treated)	Used for heat-treatable alloys subjected to natural or artificial aging in order stable tempers different than F, O, or H to be elaborated.	The first digit indicates the main type of heat treatment and the second to fifth [if they exist] the amount of stress release and other special treatments.

2.2.1. Material properties under monotonic loading

A series of tensile coupon tests have been conducted in a wide spectrum of aluminium alloys available in the market, aiming to investigate their material properties. Typical engineering stress-strain curves of commonly investigated structural aluminium alloys are presented in Figure 2.1 and typical mechanical properties are summarised in Table 2.2. In this table, E is the Young's Modulus, $\sigma_{0.2}$ is the stress at 0.2% strain (also known as proof stress), σ_u is the ultimate stress and n is the hardening exponent according to Ramberg – Osgood constitutive model [18]. A stress-strain curve of conventional structural carbon steel [19] is also included in Figure 2.1 for comparison purposes. As it can be seen in Figure 2.1, the stress-strain relationship of the aluminium alloys is

characterised by a rounded curve without a distinct yielding point contrary to carbon steel. The initial material behaviour is linear elastic and is defined to relatively low stress, $\sigma_{0.01}$, that corresponds to strain of 0.01%. After this point the material exhibits non-linear elastic behaviour up to $\sigma_{0.2}$ stress, whilst beyond this point, plastic strains occur. Note that the $\sigma_{0.2}$ or proof stress constitutes a threshold after which the stress-strain curve presents a “knee” followed by a strain-hardening branch. On the other hand, carbon steel behaves similarly at the elastic range but with larger and stiffer slope, followed by a clearly defined yield plateau and strain-hardening branch. Comparing the stress-strain curves from different aluminium series in Figure 2.1, it is apparent that 7xxx series have higher yield stress, but lower ductility compared to 6xxx series. It can also be seen from Table 2.2 that more pronounced ductility is observed for 6063-T5 and 6082-T4 and more evident strain-hardening is exhibited by 6082-T4 with $\sigma_{0.2}/\sigma_u$ equal to 0.54. The yield and tensile strengths of additional commonly used structural aluminium grades are presented for reference in Figure 2.2, where $\sigma_{0.2}$ and σ_u have been reported in the range of 80 to 275 MPa and 160 to 350 MPa, respectively [5].

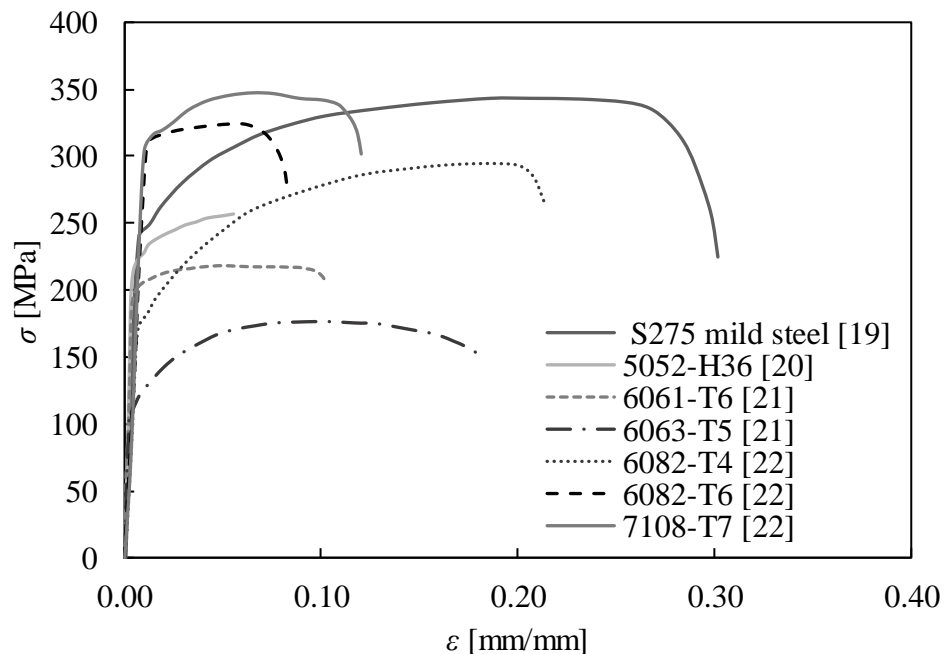


Figure 2.1: Stress-strain curves from corresponding tensile coupon tests [19-22].

Table 2.2: Mechanical properties of commonly investigated aluminium alloys.

Author(s) (date) [Reference]	Aluminium m grade	$\sigma_{0.2}$ [MPa]	σ_u [MPa]	E [GPa]	$\sigma_{0.2}/\sigma_u$	n
Alsanat et al. (2019) [20]	5052-H36	211.6	257.8	64.2	0.82	-
Su et al. (2014) [21]	6061-T6	234.0	248.0	66.0	0.94	12
Su et al. (2014) [21]	6063-T5	179.0	220.0	69.0	0.81	10
Moen et al. (1999) [22]	6082-T4	120.1	221.0	66.9	0.54	26
Moen et al. (1999) [22]	6082-T6	312.2	324.2	66.7	0.96	74
Moen et al. (1999) [22]	7108-T7	314.0	333.4	66.9	0.94	65

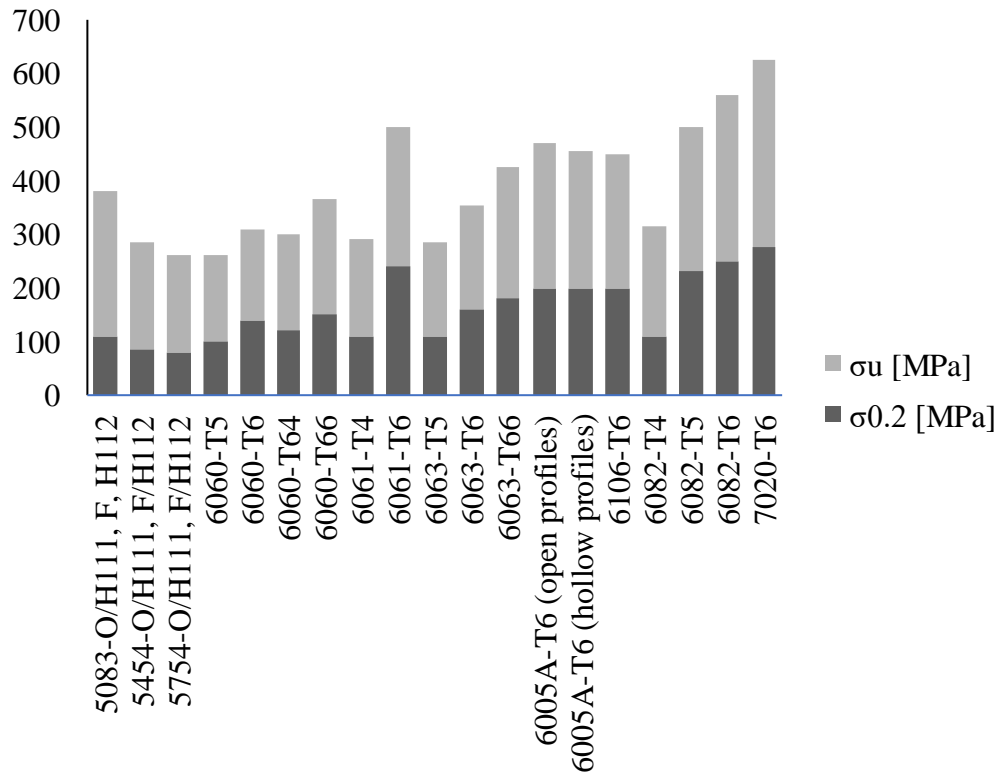


Figure 2.2: Yield and tensile strengths of commonly used aluminium grades.

In order to simulate the stress-strain response of aluminium alloys, the Ramberg-Osgood model [18] can be applied. Further to this, Baehre [23] proposed a satisfactory analytical approach, but was unable to capture the observed “knee” of the experimental stress-strain curves. De Matteis et al. [24] modified Baehre’s law on the basis of experimental evidence improving its suitability. Guo et al. [25] investigated the material properties of

6061-T6 aluminium alloy and found that the stress-strain relationship derived from the Ramberg-Osgood model [18] combined with the Steinhardt Suggestion [26] allowed precise capture of its mechanical behaviour. It is noteworthy that the Steinhardt Suggestion [26] greatly simplifies the description of the constitutive relationship as it determines the hardening exponent n without considering the 0.1% stress $\sigma_{0.1}$. Wang et al. [27] performed a series of tensile coupon tests on 6082-T6 aluminium alloys and proposed a constitutive model based on the Ramberg-Osgood law, combined with the application of the fast-simulated annealing method for the calculation of n .

2.2.2. Material properties under cyclic loading

The ductility and energy dissipation of structural materials are of great significance for the response of structural members subjected to seismic loading. As can be seen in Table 2.3, there is lack of reported works on the cyclic behaviour of aluminium alloys, which sets limitations on their usage in earthquake prone areas. Early attempts to obtain an understanding of the hysteretic behaviour of aluminium alloys date back to 1990s. Hopperstad et al. [28] performed uniaxial cycling tests on specimens made from 6060 in tempers T4 and T5 under constant and varying strain amplitudes. They suggested an amendment to the cyclic plasticity model of Chaboche [29], so that the Bauschinger effect of temper T4 is precisely considered. Aiming to further investigate T4 aluminium alloys, the same authors conducted biaxial proportional and non-proportional cycling tests and extended the previous constitutive model to capture the observed influence of the strain range and the strain path shape on the material hardening [30]. The aforementioned tests could not clarify the presence of hardening behaviour, due to the low strain amplitudes (<2%) during the cyclic tests. To this end, Dusicka & Tinker [31] investigated the hysteretic response of coupons generated by 6061-T6/511 alloys subjected to constant strain amplitudes beyond 2%. The observed slight increase of the cyclic softening behaviour indicated its potential for seismic retrofit applications. De Matteis et al. [24] conducted cyclic tests on coupons of an almost pure aluminium alloy coded 1050A-H24 and found that it has substantial dissipative capacity largely for higher applied strain levels. More recently, Guo et al. [32] proposed a new constitutive model for the hysteretic behaviour of 6082-T6 and 7020-T6 on the basis of the monotonic curve

and the reduction factor method. Based on the above, more cyclic tests are suggested to be performed to cover a wider range of aluminium alloys available in the market.

Table 2.3: Summary of tests on material properties of aluminium alloys under cyclic loading.

(in chronological order from most recent research)

Author(s) (date) [Reference]	Aluminium grade	Strain range [%]
Guo et al. (2018) [32]	6082-T6, 7020-T6	up to 4
Dusicka & Tinker (2013) [31]	6061-T6/511	2-4
De Matteis et al. (2012) [24]	1050A-H24	-
Hopperstand et al. (1995) [28,30]	6060-T4, 6060-T5	up to 1.2

2.2.3. Material properties of Heat-Affected Zone

A noteworthy characteristic of aluminium is that when high strength heat-treated aluminium alloys (6xxx series) are welded in order to be joined with adjacent structural members, the strength in the vicinity of the welded region is decreased significantly. This is an important demerit of these particular aluminium alloys which cannot be neglected during the design. The inferior material properties of this localised region around the welds, known as Heat-Affected Zone (HAZ), are considered through the application of softening factors. According to AA 2020 [7], the HAZ extends about 25.4 mm around the weld. The influence of the HAZ on the structural behaviour of beams and columns was demonstrated by Lai & Nethercot [33] using numerical analysis. Mazzolani [34] determined that the parent metal strength can be reduced almost 50% due to the presence of HAZ in 6xxx series aluminium alloys, whereas Zhu & Young [35] found that the proof stress can undergo a decrease up to 70%.

2.2.4. Material properties at elevated temperatures

Since 1990s a remarkable amount of studies on the material properties of aluminium alloys under fire conditions has been reported. Kaufman [36] significantly contributed to this research field by conducting steady state tests on 158 different aluminium alloys and found that the Young's Modulus E is independent of the heating rate. Langhelle [37] and Hepples & Wale [38] investigated the structural response of 6082 subjected to steady state thermal conditions. Faggiano et al. [39] emphasised on the way that elevated temperatures affect the material hardening factor and proposed a modified stress-strain

relationship based on the Ramberg-Osgood expression. Maljaars et al. [40] performed tests on 5083-O/H111 and 6060-T66 and modified the Dorn-Harmathy creep model [41,42] so that to be applicable for 6xxx series aluminium alloys. Furthermore, Kandare et al. [43] modified the Larson-Miller model [44] on the basis of fire tests on coupons formed by 5083-H116. The reported test results were used for the assessment of a thermo-mechanical model developed by Kandare et al. [45] as well as an advanced modelling approach for fire conditions proposed by Feih et al. [46]. More recently, Chen et al. [47] investigated experimentally the post-fire behaviour of 6061-T6 and 7075-T73 and suggested simplified design formulae. Su & Young [48] presented a series of empirical equations regarding the mechanical properties of 6063-T5 and 6061-T6 exposed to fire. In the same study, design specifications were assessed, showing that the present partial factors lead to conservative design predictions. This is shown in Figure 2.3, where the test results from both steady and transient tests appear far from the EN 1992-1-2 [49] design curve. The studies also concluded that the behaviour under fire conditions is complex and dependent on the chemical composition of each aluminium alloy. Additional tests that will allow more accurate design models for each aluminium alloy ensuring both economy and safety are necessary.

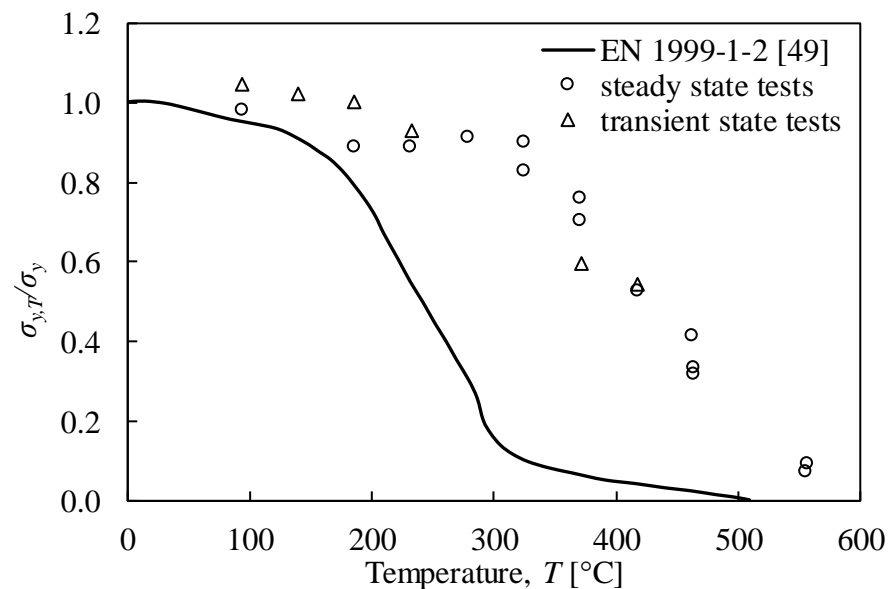


Figure 2.3: Comparison between test results and EN 1999-1-2 [49] predictions (adapted from [48]).

2.3. Columns

2.3.1. Local buckling

The design resistance of an aluminium structural member under compression is governed by the cross-section classification. This is a codified procedure that implicitly treats local buckling phenomenon, i.e. the buckling of the constituent plate elements of a cross-section under compression. EN 1999-1-1 [5] classifies the cross-sections in four classes, using cross-section slenderness limits (dependent on the boundary conditions of the constituent plate elements of a cross-section), the plate element stress distribution and the heat-treatment method. Classes 1, 2 and 3 comprise cross-sections capable of yielding without failing due to local buckling, while in Class 4 sections local buckling occurs in the elastic range and thus a reduced cross-sectional area is considered for the evaluation of the cross-sectional resistance.

Aiming to study local buckling and the cross-sectional performance, early tests on stub columns have been reported [50-54]. More recently, a considerable amount of stub column tests have been conducted in a wide range of cross-sectional shapes (Figure 2.4), aluminium grades and width-to-thickness ratios of the most slender constituent plate element. Zhu et al. [55] investigated the behaviour of plain and lipped channel (C-) stub columns, whereas Mazzolani et al. [56] tested angles and proposed an empirical equation about the local buckling resistance. Liu et al. [57,58] studied the local buckling behaviour of stiffened and irregular-shaped cross-sections and Yuan et al. [59] evaluated experimentally the post-buckling behaviour of slender (i.e. large width to thickness ratio) I-sections. Wang et al. [60] conducted stub columns tests on circular hollow sections CHSs made from 6082-T6, whilst Feng & Young [61] dealt with perforated cross-sections. Following, Feng et al. [62,63] determined the reduced load-bearing capacity due to the presence of holes by testing perforated stub columns with rectangular hollow sections (RHSs), square hollow sections (SHSs) and CHSs. Upon experimental testing on tubular sections, Su et al. [21] highlighted the significant contribution of the material strain-hardening on the cross-section capacity and assessed the applicability of the Continuous Strength Method (CSM) [64,65], that was originally developed for stainless steel stocky (i.e. small width to thickness ratio) cross-sections. Su et al. [66,67] extended

the CSM to cover aluminium sections and proposed new slenderness limits as well as an effective thickness formula on the basis of collected data. The studies are listed in Table 2.4, where the design code assessment is also shown. The mean values and coefficient of variations (COVs) of ratios of the reported test strength F_u to the code predicted strength N_{pred} are included. For mean ratios F_u/F_{pred} higher than unity (>1.05), the predictions are conservative, for lower than unity (<1.00), they are unsafe and for close to unity ($1.00 < F_u/F_{pred} < 1.05$), they are accurate. Furthermore, high values of COV suggest scattering and thus the predictions are considered as unreliable. As it can be seen, excessively conservative predictions were reported for channel sections in [55], which is opposed to an economic design process. In general, only a few studies indicated accurate cross-sectional strength predictions. The lack of accuracy is also related to the fact that the design formulae for aluminium often adopt similar principles to structural steel design, without sufficient consideration of the differences between the two materials. Modifications in line with obtained test data on aluminium are needed.

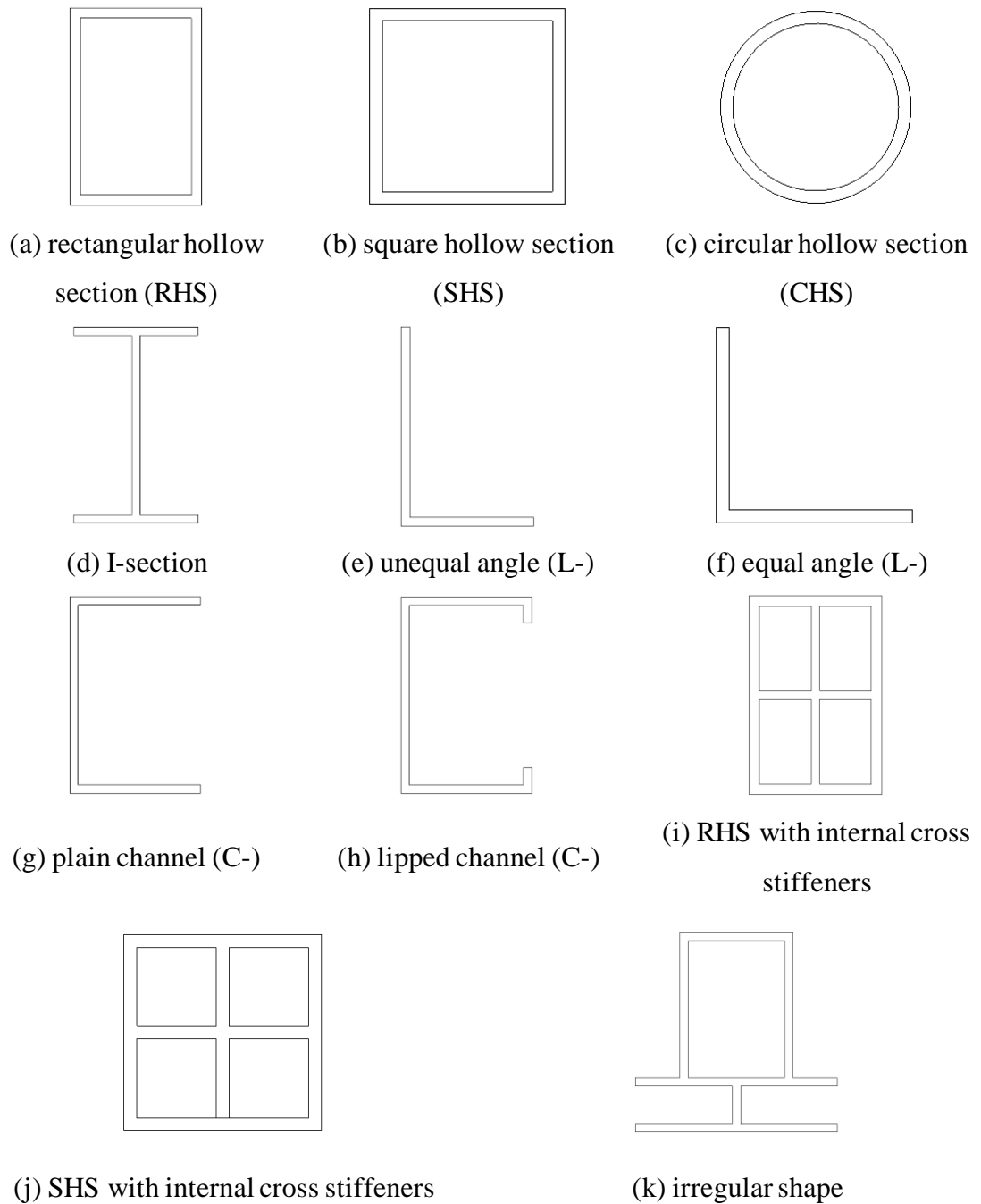


Figure 2.4: Cross-sectional shapes employed in stub column investigations.

Table 2.4: Summary of aluminium alloy stub column tests.

(in chronological order from most recent research)

Author(s) (date) [Reference]	Aluminium grade	Shape	No of tests	Width-to-thickness ratios	Design codes	F_w/F_{pred}		Assessment
						mean	COV	
Zhu et al. (2019) [55]	6063-T5, 6061-T6	plain C-, lipped C-	8	25.50-25.90	GB 50429-2007 [4]	1.65	0.06	conservative
					EN 1999-1-1:2007 [5]	1.35	0.07	conservative
					AS/NZS 1664.1:1997 [6]	1.28	0.15	conservative
					AA [7]	1.28	0.15	conservative
					NAS [131]	1.21	0.10	conservative
CSM [64,65]	1.12	0.16	conservative					
Feng et al. (2018) [62]	6063-T5, 6061-T6	perforated RHS, SHS	16	27.30-43.67	NAS [125]	0.92	0.11	unsafe
Feng et al. (2016) [63]	6063-T5, 6061-T6	perforated CHS	10	23.48-49.81	NAS [125]	1.50	0.11	conservative
Wang et al. (2015) [60]	6082-T6	CHS	9	14.00-26.70	-			
Feng & Young (2015) [61]	6061-T6	perforated SHS	28	6.20-48.30	AISI 2008 [127]	0.96	0.32	unsafe
					NAS [131]	0.95	0.33	unsafe
Yuan et al. (2015) [59]	6061-T6, 6063-T5	I-	15	35.70-71.70	GB 50429-2007 [4]	1.13	0.12	conservative
					EN 1999-1-1:2007 [5]	1.12	0.12	conservative
					AS/NZS 1664.1:1997 [6]	1.10	0.09	conservative
					AA [7]	1.06	0.09	conservative

Liu et al. (2015) [57]	6063-T5	irregular	7	-	-			
Liu et al. (2015) [58]	6063-T5	stiffened closed-sections	10	-	GB 50429-2007 [4]	0.96	0.05	unsafe
					EN 1999-1-1:2007 [5]	1.01	0.04	accurate
					AA [7]	0.94	0.08	unsafe
					DSM [72]	0.83	0.04	unsafe
					AISI 2008 [127]	0.98	0.08	accurate
Su et al. (2014) [21]	6061-T6, 6063-T5	SHS, RHS (with and without internal stiffeners)	15	3.20-20.70	EN 1999-1-1:2007 [5]	1.07	0.09	conservative
					AS/NZS 1664.1:1997 [6]	1.34	0.16	conservative
					AA [7]	1.19	0.16	conservative
					CSM [64,65]	1.04	0.06	accurate
Mazzolani et al. (2011) [56]	6xxx	angles	64	2.90-35.40*	-			

*calculated according to available data.

2.3.2. Flexural buckling

The flexural buckling behaviour of aluminium alloy columns has been under thorough investigation, being one of the primary constituents for the assurance of the structural integrity. According to the current design guidelines, buckling classes are determined by two material groups based on the temper designation, as shown in Table 2.5.

Table 2.5: Material groups based on temper designation. (adapted from Wang et al. [60])

Specifications	Material group 1	Material group 2
GB 50429-2007 [4]	T6	Other tempers
EN 1999-1-1:2007 [5]	T6, H14/24/34	Other tempers
AS/NZS 1664.1:1997 [6]	T5, T6, T7, T8, T9	O, H, T1, T2, T3, T4
AA 2020 [7]	T5, T6, T7, T8, T9	O, H, T1, T2, T3, T4

Note: Material groups 1 and 2 refer to buckling curves A and B in EC9, respectively.

In order to comprehend the ultimate performance of aluminium alloy columns, early studies have been reported by Hopperstad et al. [52] who tested 6082-T4 and 6082-T6 columns, and Manevich [68] who numerically investigated the influence of the material strain-hardening on the critical buckling stress. Over the last years, a considerable amount of experimental studies has been performed, as summarised in Table 2.6. In this table, the test boundary conditions and the slenderness ratio L_e/r of the specimens are also included (L_e is the effective buckling length and r the radius of gyration of the cross-section). Wang et al. [60] focussed on the reliability level of current design rules on CHSs columns, while Adeoti et al. [69] expanded the investigation on columns formed by H-sections and RHSs. Wang et al. [70] studied L-shaped columns manufactured by 7A04 high-strength aluminium alloy, whereas Wang et al. [71] focussed on I-section columns. Feng et al. [63] investigated the buckling behaviour of perforated columns, suggesting that a properly modified Direct Strength Method (DSM) [72] a design approach suggested for cold-formed steel sections, could be suitable for the design of CHS columns with circular openings. After two years, Feng et al. [62] reported that the DSM cannot be applied for the design of perforated RHS and SHS columns. The aforementioned test results were also used by Feng & Liu [73] to conduct an extensive parametric study and adjust the EN 1999-1-1 [5] equations, taking into account the reduced cross-sectional area due to perforation. A numerical study on irregular-shaped sections was carried out by Chang et al. [74] who concluded that the DSM is able to predict the interactive

buckling failure mode accurately but not in every case. Recently, Wang et al. [75] tested columns with large RHS and I- sections and Zhu et al. [55,76] presented their test results on plain and lipped channel columns. As shown in Table 2.6, the reported test data have been used to assess current design rules and it can be concluded that the international guidelines are overly conservative and confirm the need for further research into this field. In addition, many of past studies have focussed on hollow sections, which are less prone to torsional failure. Hence, despite the exhaustive experimental and numerical investigation on the structural response of columns, test data on interactive torsional-flexural buckling behaviour are relatively limited and further research is recommended.

Table 2.6: Summary of aluminium alloy column experiments.

(in chronological order from most recent research)

Author(s) (date) [Reference]	Aluminium grade	Shape	No of tests	Boundary conditions	Slenderness ratio [L_e/r]	Design codes	F_u/F_{pred}		Assessment
							mean	COV	
Zhu et al. (2019) [76]	6063-T5, 6061-T6	plain C-, lipped C-	20	fixed ends	-	GB 50429-2007 [4]	1.38	0.20	conservative
						EN 1999-1-1:2007 [5]	1.45	0.14	conservative
						AS/NZS 1664.1:1997 [6]	1.23	0.16	conservative
						AA [7]	1.23	0.16	conservative
						NAS [131]	1.21	0.15	conservative
Wang et al. (2018) [71]	6061-T6	I-, RHS	7	pinned ends	28.96-116.74	GB 50429-2007 [4]	1.55	0.25	conservative
						EN 1999-1-1:2007 [5]	1.30	0.22	conservative
						AA [7]	1.06	0.19	conservative
Feng et al. (2018) [62]	6063-T5, 6061-T6	perforated RHS, SHS	21	pinned ends	13.94-93.22	NAS [131]	0.97	0.07	accurate
Wang et al. (2017) [75]	6063-T5, 6061-T6	I-	11	fixed-pinned ends	46.90-67.50	GB 50429-2007 [4]	1.45	0.13	conservative
						EN 1999-1-1:2007 [5]	1.45	0.11	conservative
						AS/NZS 1664.1:1997 [6]	1.27	0.09	conservative
						AA [7]	1.13	0.13	conservative
Feng et al. (2016) [63]	6063-T5, 6061-T6	perforated CHS	8	pinned ends	28.84-58.88	NAS [125]	1.27	0.12	conservative
Wang et al. (2016) [70]	7A04	L-	42	pinned ends	15.00-100.00	GB 50429-2007 [4]	2.76	0.27	conservative
						EN 1999-1-1:2007 [5]	1.21	0.21	conservative
						AA [7]	1.19	0.34	conservative
Adeoti et al. (2015) [69]	6082-T6	H-, RHS	30	pinned ends	22.36-163.01	GB 50429-2007 [4]	1.14	0.09	conservative
						EN 1999-1-1:2007 [5]	1.14	0.09	conservative
						AA [7]	1.20	0.09	conservative
						GB 50017-2003 [110]	1.21	0.10	conservative
Wang et al. (2015) [60]	6082-T6	CHS	15	pinned ends	24.42-73.99*	EN 1999-1-1:2007 [5]	1.10	0.08	conservative
						AS/NZS 1664.1:1997 [6]	0.97	0.13	accurate
						AA [7]	1.14	0.13	conservative

*calculated according to available data.

2.3.3. Welded columns

As mentioned in Subsection 2.2.4. the reduced strength of the HAZ affects the structural response of the structural member and thus it should be considered during the design process. To this end, Zhu & Young [35,77-81] examined the buckling behaviour of RHSs, SHSs and CHSs columns with and without transverse welds. They proposed new design criteria for the ultimate strength based on the DSM and new values for HAZ softening factors. Zhu et al. [82] extended this investigation to channel sections and modified the DSM and the CSM approach to make them applicable to welded channel columns. Feng et al. [62] dealt with perforated RHS and SHS columns incorporating welded and non-welded specimens. Their experimental outcomes demonstrated the applicability of the design criteria proposed by Zhu & Young [79] to welded columns.

2.3.4. Columns at elevated temperatures

In order to comprehend the buckling response and design of columns at elevated temperatures, experimental and numerical work has been performed, as listed in Table 2.7 and Table 2.8, respectively. Langhelle & Amdahl [83] performed column buckling tests to clarify the consequences of the viscoplastic behaviour at elevated temperatures. Suzuki et al. [84] conducted a series of column tests under fire conditions and extended the simple plastic theory to estimate the critical temperature beyond which column failure occurs. Maljaars et al. [85,86] carried out axial compression tests and FE analyses on slender SHSs and angles under steady and transient state conditions and proposed new less conservative cross-section classification limits for EN 1999-1-2 [49]. In a following numerical work, Maljaars et al. [87,88] pointed out that the stress-strain relationships at elevated temperatures are more curved than at ambient temperature and that the buckling resistance is directly linked to the inelastic critical stress. Liu et al. [89] determined the buckling behaviour of columns with irregular-shaped cross sections by numerical means and suggested a modification to the equations provided by EN 1999-1-2 [49]. In a more recent study, Jiang et al. [90] performed tests and FE models on RHS and CHS columns and modified the stability coefficient of EN 1999-1-1 [5] and GB 50429 [4] to take into account the effect of the elevated temperatures on the normalised slenderness and the imperfection parameter.

Table 2.7: Summary of tests on columns at elevated temperatures.

(in chronological order from most recent research)

Author(s) (date) [Reference]	Type of test	Aluminium grade	Shape	No of tests	Temperature [°C]	Design codes	Assessment
Jiang et al. (2018) [90]	axial compression	6061-T66	RHS, CHS	108	up to 400	-	
Maljaars et al. (2009) [85]	axial compression	5083-H11, 6060-T66	SHS, L-	55	up to 330	EN 1999-1-2 [49]	conservative
Suzuki et al. (2005) [84]	fire resistance test	5083-O, 5083-H112	box, H-	23	up to 850	-	
Langhelle & Amdahl (2001) [83]	axial compression	6082	-	31	-	-	

Table 2.8: Summary of numerical investigations on columns at elevated temperatures.

(in chronological order from most recent research)

Author(s) (date) [Reference]	Type of test	Aluminium grade	Shape	No of analyses	Temperature [°C]	Design codes	Assessment
Jiang et al. (2018) [90]	axial compression	6063-T5, 6061-T6, 6063-T6, 6061-T4	RHS, CHS, J-, T-, L-, C-, Z-, T- [one sym. axis]	8829	up to 400°C	-	
Liu et al. (2016) [89]	axial compression	6061-T6	irregular shaped	300	up to 500°C	GB 50429-2007 [4] EN 1999-1-1:2007 [5] EN 1999-1-2 [49] AA [7] DSM [72] AISI 2008 [127]	conservative conservative conservative conservative conservative
Maljaars et al. (2009) [86,87,88]	axial compression	5083-O/H111, 6060-T66	SHS, I-	48	200,300	EN 1999-1-2 [47]	conservative

2.4. Beams

2.4.1. Flexural resistance

The flexural resistance and rotational capacity of beams are of significant importance in order to ensure the safe transfer of the vertical loads to the foundation. This is one of the earliest research topics, since the first experimental works date back to 1950s, when Panlilo [91] investigated the behaviour of two-span statically indeterminate beams. Later, Mazzolani et al. [92] extended the plastic design to aluminium alloy structures and Welo [93] performed tests under uniform moment and determined the moment-curvature behaviour. Thereon, numerous experimental and numerical investigations have been carried out on aluminium beams under three-, four- and five-point bending conditions, as summarised in Table 2.9. Opheim [94] conducted 4-point bending tests and found that there is no significant difference between tensile and compressive behaviour of 6060-T4 beams. Moen et al. [22,95] demonstrated through experimental and numerical studies that the rotational capacity is dependent on the material strain-hardening and the magnitude of the moment gradient. Their test results [22] were used by De Matteis et al. [96] who proposed new limits on the cross-section classification of EN 1999-1-1 [5], considering the material strain-hardening. The importance of the material strain-hardening was also highlighted by Su et al. [97-100]. In another study, Zhu & Young [101] modified the current DSM achieving more accurate and reliable design provisions for flexural SHS members. Kim & Peköz [102] developed a new formulation for the stress at ultimate limit state based on test results of doubly symmetric I-section beams. Kim & Peköz [103] also presented a simplified design approach named Numerical Slenderness Approach in order to determine the nominal stresses of each constituent plate element of a complex section under flexure. The reliability of the proposed method was evaluated by performing a series of tests on beams with mullion sections. Castaldo et al. [104] numerically studied the ultimate behaviour of RHS beams under non-uniform bending and proposed multivariate non-linear equations for their ultimate flexural resistance and rotational capacity. Piluso et al. [105] extended the aforementioned study to I-sections fabricated by 6082-T4 and 6063-T5. Experimental and numerical studies on perforated CHS beams subjected to gradient and constant moments were reported by

Feng et al. [106,107]. They found that the presence of holes, their size and number reduce the flexural capacity. Recently, Montuori et al. [108] reported a thorough FE investigation on I-beams formed by high-yielding low-hardening aluminium alloys. The outcomes denoted that the increased values of slenderness parameter and shear length ratio reduce the rotational capacity. Focussing on lateral-torsional buckling, Cheng et al. [109] investigated numerically the lateral stability of I-section beams and suggested a modification to the GB 50017-2003 [110]. The proposed modified design methodology was assessed by Wang et al. [111] concluding that it provides more accurate predictions compared to EN 1999-1-1 [5]. A few years later, Wang et al. [112] extended their investigation conducting experiments on I-beams including specimens with and without intermediate stiffeners subjected to concentrated loads.

Table 2.9 summarises the studies and the design code assessment by providing the mean and COV values of the reported obtained ultimate flexural strengths M_u over design strengths predicted by the international design codes M_{pred} . The overall high M_u/M_{pred} ratios reveal largely conservative design estimations. The latter can also be visualised in Figure 2.5, which presents reported M_u values normalised by M_{pred} of EN 1999-1-1 [5], and plotted against the cross-sectional slenderness parameter (b/t , i.e. width to thickness ratio). In addition, as shown in Table 2.9, there are only a few reported studies on five-point bending tests and hence additional experiments are suggested to better evaluate the plastic performance of indeterminate beams.

Table 2.9: Summary of investigations on beams.

(in chronological order from most recent research)

Author(s) (date) [Reference]	Type of study	Aluminium grade	Type of bending test	Shape	No of tests	Design codes	M_u/M_{pred}		Assessment
							mean	COV	
Montuori et al. (2020) [108]	FE	6061-T6, 6082-T6	three-point	H-, I-	240	-			
Feng et al. (2020) [107]	Exp	6061-T6, 6063-T5	three-point, four-point	perforated CHS	8	NAS [131]	1.20	0.23	conservative
Feng et al. (2019) [106]	FE	6061-T6, 6063-T5	three-point, four-point	perforated CHS	408	-			
Piluso et al. (2019) [105]	FE	6082-T4, 6063-T5	three-point	H-, I-	240	-			
Kim & Peköz (2018) [103]	Exp & FE	6063-T5	four-point	mullion	2 & -	AA [7]			conservative
Castaldo et al. (2017) [104]	FE	6082-T6	three-point	RHS	252	-			
Wang et al. (2016) [112]	Exp & FE	6061-T6, 6063-T5	simply supported	I-	10 & 24	EN 1999-1-1:2007 [5]	1.40	0.10	conservative
Su et al. (2016) [100]	Exp & FE	6063-T5, 6063-T6	three-point, four-point, five-point	SHS, RHS with internal stiffeners	30 & 150	EN 1999-1-1:2007 [5]	1.41	0.11	conservative
						AS/NZS 1664.1:1997 [6]	2.11	0.21	conservative
						AA [7]	1.67	0.18	conservative
						CSM [64,65]	1.30	0.10	conservative
Su et al. (2015) [98,99]	Exp & FE	6061-T6, 6063-T5	five-point	SHS, RHS	27 & 120	EN 1999-1-1:2007 [5]	1.82	0.23	conservative
						AS/NZS 1664.1:1997 [6]	2.26	0.23	conservative
						AA [7]	2.02	0.26	conservative
						CSM [64,65]	1.39	0.16	conservative
Su et al. (2014) [97]	Exp & FE	6061-T6, 6063-T5	three-point, four-point	SHS, RHS	29 & 132	EN 1999-1-1:2007 [5]	1.17	0.11	conservative
						AS/NZS 1664.1:1997 [6]	1.54	0.16	conservative
						AA [7]	1.38	0.14	conservative
						CSM [64,65]	1.11	0.11	accurate
Wang et al. (2012) [111]	Exp	6061-T6, 6063-T5	simply supported	I-	40	EN 1999-1-1:2007 [5]	0.92	0.13	unsafe
Kim & Peköz (2010) [102]	Exp & FE	6063-T6	four-point	I-	3 & -	AA [7]	1.21	0.06	conservative

Zhu & Young (2009) [101]	Exp & FE	6061-T6, 6063-T5	four-point	SHS	10 & 60	EN 1999-1-1:2007 [5] AS/NZS 1664.1:1997 [6] AA [7] DSM [72]	1.31 1.38 1.35 1.21	0.11 0.20 0.20 0.07	conservative conservative conservative conservative
Cheng et al. (2006) [109]	FE	-	simply supported	I-	250	-			
De Matteis et al. (2001) [96]	FE	6082-T4, 6082-T6	four-point	RHS	-	EN 1999-1-1 [5]			conservative
Moen et al. (1999) [95]	FE	6082-T4, 6082-T6, 7108-T7	four-point	unwelded I, welded I, box	19	-			
Moen et al. (1999) [22]	FE	6082-T4, 6082-T6, 7108-T7	four-point	unwelded I, welded I, box	38	EN 1999-1-1 [5]	1.15	0.11	conservative
Opheim (1996) [94]	Exp & FE	6060-T4, 6064-T6	four-point	SHS	-	-			

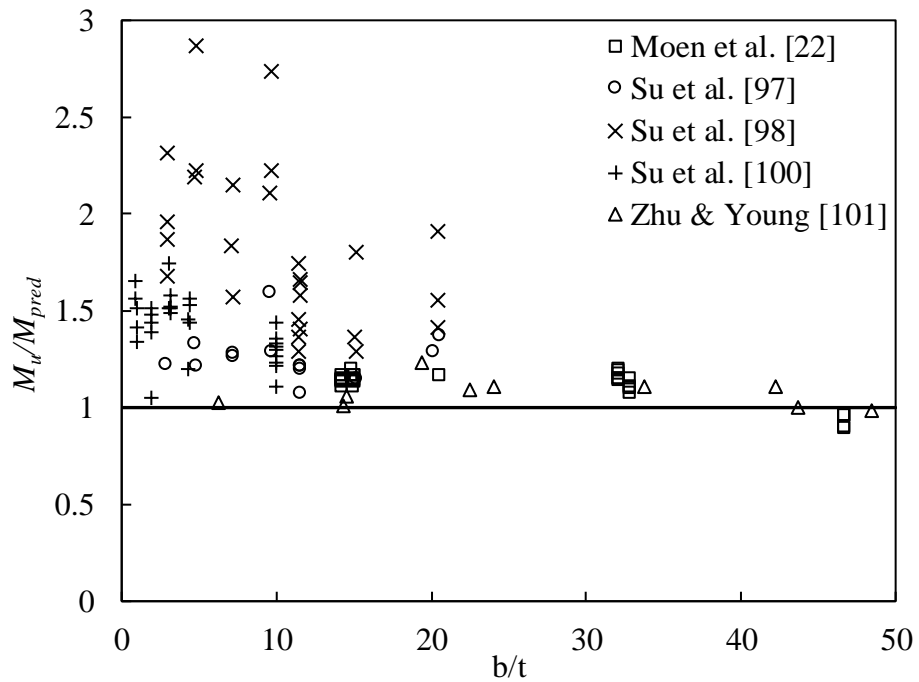


Figure 2.5: Comparison between test results and design predictions using EN 1999-1-1 [5].

2.4.2. Welded beams

Until now relatively little attention has been given at the behaviour of aluminium alloy welded beams. Thus, the existing design approaches adopt the same principles to the corresponding ones for steel welded beams, leading to gross approximations, since the two materials differ considerably. Moen et al. [22,95] and Matusiak [113] presented their studies on welded I-beams highlighting the significant reduction on rotational capacity due to welding. The reported results by the latter were used by Wang et al. [114] who focussed on the vicinity of the weld and determined its impact on the total strength and ductility of the beams. The authors proposed a new modelling methodology for the region around the weld, assuming shell elements, geometric imperfections, plastic anisotropy, inhomogeneous material properties and ductile failure. The actual structural performance of welded beams is still ambiguous and thus more experimental research needs to be carried out.

2.4.3. Beams at elevated temperatures

A few studies have been carried out on the structural behaviour of beams exposed to fire. Suzuki et al. [84] performed fire resistance tests and proposed fire design formulae,

whereas more recently, Meulen et al. [115] performed 3-point bending steady and transient state tests up to 300°C in order to assess the EN 1999-1-2 [49]. The experimental and numerical studies on aluminium beams at elevated temperatures are limited and thus more three-, four- and five- point bending tests on different cross-sectional shapes in a wide range of applied strain rates are necessary. Data from these experiments will form a database that can be used for the development of more accurate design models and more reliable design provisions for aluminium alloys.

2.5. Beam-columns

The behaviour of aluminium alloy members under combined compression and bending has also been reported. Clark [116], Klöppel & Bärsch [117] and Gilson & Cescotto [118] performed tests on RHS, I- and T stocky sections. Zhu & Young [118,119] presented their experimental work on SHS, RHS and CHS specimens under combined axial compression and bending about the weak axis. The obtained outcomes demonstrated that the predicted beam-column strengths are underestimated by the current design guidelines. Zhao et al. [120-122] reviewed the Chinese Standards and proposed new values for certain design parameters. Furthermore, Zhu et al. [123] tested eccentrically compressed I-shaped members under elevated temperatures and presented a simplified correlation curve able to predict the bearing capacity of columns subjected to eccentric compression up to 300°C.

2.6. Residual stresses

The residual stresses developed during the manufacturing process can have a significant impact on the overall structural response of a member. According to Mazzolani [17], the residual stresses are quite low for extruded profiles, heat treated or not, and thus can be ignored, contrary to welded profiles, where the residual stresses can have a significant impact on the load-bearing capacity of the structure. Aiming for a better understanding of the residual stress distribution in aluminium sections, Huynh et al. [124] investigated the residual stresses of cold-rolled aluminium channel sections using the sectioning method. It was shown that the in-plane residual stresses were significant only in the corner parts of the smallest and thinnest C-section, whereas the out-of-plane residual

stresses were considerable (up to 30% of yield stress) for all the investigated sections. Similar findings for cold-formed steel open sections have been reported by Moen et al. [125] and Gardner & Cruise [126]. There is a need to extend this investigation in various cold-formed, hot-rolled and welded cross-sections, so that the effect of residual stresses will be adequately considered in the design process.

2.7. Web crippling

Web crippling is specified as localised buckling and yielding of the web in the vicinity of the applied concentrated load. Research works examining the web crippling of a plethora of sections including end-two-flange (ETF), interior-two-flange (ITF), end-one-flange (EOF) and interior-one-flange (IOF) loading and boundary conditions, as defined in AISI 2008 [127], have been reported and summarised in Table 2.10. The first reported work was presented by Tryland et al. [128] who found that the web thickness and the flange stiffness considerably affects the ultimate capacity. Later Zhou & Young [129,130] conducted an extensive investigation on SHSs and RHSs in a wide slenderness range and suggested modified design formulae to the North American Specification (NAS) [131]. Zhou et al. [132] tested SHSs under concentrated bearing loads and proposed threshold slenderness values beyond which the web buckling becomes the predominant failure mode. Zhou & Young [133] extended their investigation on SHSs with perforated webs proposing a strength reduction factor and a new web crippling design equation for SHSs with circular web holes. Chen et al. [134] studied further the web crippling behaviour of SHSs proposing new equations for the ultimate capacity. In another study, Su & Young [135] proposed a more accurate and reliable design methodology for the web bearing capacity of stocky sections which takes into account the significant effect of the material strain-hardening. Alsanat et al. [20,136] tested for first time roll-formed aluminium lipped channel sections under ETF and ITF conditions and proposed modified rules on the basis of the obtained test data. Recently, Zhou & Young [137] carried out tests on plain and lipped channel sections with restrained flanges. The assessment of the design specifications based on the most crucial loading-boundary condition are also summarised in Table 2.10, revealing the current lack of accuracy and reliability in the design predictions of the web crippling phenomenon. Contrary to the cross-sectional (Table 2.4), column (Table 2.6) and flexural strengths

(Table 2.9) that are generally underestimated by the codes, Table 2.10 shows that overall the codified capacities against web crippling are not safely estimated.

Table 2.10: Summary of web crippling tests.

(in chronological order from most recent research)

Author(s) (date) [Reference]	Aluminium grade	Shape	No of tests	Loading- boundary conditions	Web slenderness ratios (b/t)	Design codes	N_u/N_{pred}		Assessment					
							mean	COV						
Zhou & Young (2020) [137]	6063-T5, 6061-T6	lipped C- plain C-	52	ETF, ITF	43.00-58.00	EN 1999-1-1:2007 [5]	0.75	0.26 (ETF)	unsafe					
							1.18	0.32 (ITF)						
						AS/NZS 1664.1:1997 [6]	1.00	0.47 (ETF)	conservative					
							1.06	0.28 (ITF)						
						AA [7]	1.00	0.47 (ETF)	conservative					
	1.06	0.28 (ITF)												
				NAS [131]	1.12	0.36 (ETF)	unsafe							
					0.62	0.40 (ITF)								
Alsanat et al. (2019) [20]	5052-H36	lipped C-	40	ETF, ITF	3.33-10.00*	AS/NZS 1664.1:1997 [6]	0.50	0.37 (ETF)	unsafe					
							0.88	0.24 (ITF)						
						EN 1993-1-3:2005 [138]	0.49	0.06 (ETF)	unsafe					
					0.60	0.07 (ITF)								
Su & Young (2018) [135]	6063-T5, 6061-T6	SHS, RHS	34	ETF, ITF, EOF, IOF	2.80-28.00			0.53	0.23 (EOF)	unsafe				
								0.78	0.19 (IOF)					
							EN 1999-1-1:2007 [5]	0.87	0.14 (ETF)					
								1.16	0.11 (ITF)					
												0.62	0.32 (EOF)	unsafe
											AS/NZS 1664.1:1997 [6]	0.78	0.30 (IOF)	
												0.96	0.14 (ETF)	
												1.00	0.16 (ITF)	
												0.47	0.20 (EOF)	unsafe
											AA [7]	0.78	0.30 (IOF)	
					0.96	0.14 (ETF)								
					1.00	0.16 (ITF)								
					3.14	0.31 (EOF)	conservative							
				EN 1993-1-3:2005 [138]	1.01	0.21 (IOF)								
					5.05	0.30 (ETF)								

							8.04	0.24 (ITF)	
							0.54	0.25 (EOF)	
						AISC [139]	0.88	0.22 (IOF)	unsafe
							0.87	0.12 (ETF)	
							1.19	0.12 (ITF)	
							2.45	0.53 (EOF)	
						EN 1993-1-3:2005 [138]	1.47	0.33 (IOF)	conservative
Chen et al. (2015) [134]	-	SHS	48	ETF, ITF, EOF, IOF	30.00-88.00		2.26	0.52 (ETF)	
							1.34	0.33 (IOF)	
						GB 50017 [110]	0.29	0.54 (EOF)	unsafe
							0.42	0.39 (IOF)	
							0.28	0.53 (ETF)	
							0.38	0.44 (IOF)	
						EN 1999-1-1:2007 [5]	0.75	0.23 (ETF)	unsafe
Zhou & Young (2010) [133]	6061-T6	perforated SHS	84	ETF, ITF	6.20-49.50		0.95	0.15 (ITF)	
						AA [7]	0.95	0.47 (ETF)	accurate
							0.97	0.29 (ITF)	
						EN 1999-1-1:2007 [5]	1.04	0.25 (EL)	accurate
Zhou et al. (2009) [132]	6061-T6	SHS	64	ETF, ITF	6.20-48.30		1.05	0.20 (IL)	
						AA [7]	1.86	0.37 (EL)	conservative
							1.46	0.25 (IL)	
Zhou & Young (2008) [129]	6063-T5, 6061-T6	SHS, RHS	150	EF**, IF***	6.30-74.50	-			
Tryland et al. (1999) [128]	6082-T6	SHS, I-	52	-	-	-			

*calculated according to available data.

EF: **End-bearing Loading

*IL: ***Interior-bearing Loading

2.8. Composite structures

2.8.1. Aluminium-concrete structural members

Following similar concept and principles with the composite steel-concrete structures and in particular with the concrete-filled steel tubes (CFST), the possibility of combining aluminium with concrete has been investigated. Research work on the structural response of concrete-filled aluminium tubes (CFAT) with typical cross-sections shown in Figure 2.6 has been reported.

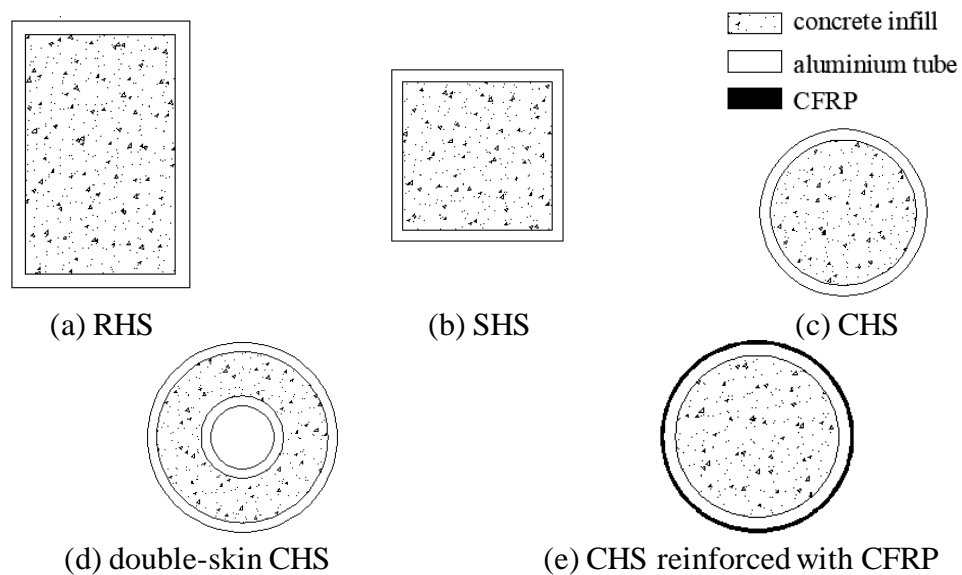


Figure 2.6: Investigated cross-sections of aluminium-concrete composite members [140-144,146-148].

Zhou & Young [140] conducted axial compression tests on concrete-filled aluminium stub columns with SHSs and RHSs and concluded that the AS/NZS 1664.1:1997 [6] and AA [7] design codes are generally unconservative. Later, Zhou & Young [141,142] extended their experimental investigation on CHS stub columns filled with concrete and developed design criteria considering the observed material interaction. In a more recent study, Zhou & Young [143] assessed experimentally the compressive response of concrete-filled double-skin tubes and suggested formulae for their ultimate capacity. Wang et al. [144] used the data reported by Zhou & Young [141] and evaluated whether the “nominal yield strength” method adopted by GB 50936 [145] for CFST is applicable to CFAT, concluding that it provides conservative but reliable predictions.

Feng et al. [146] tested simply-supported concrete-filled SHS and RHS beams, whereas Chen et al. [147] performed 4-point bending tests on concrete-filled CHS beams. In both investigations, the ultimate strength almost doubled thanks to the concrete infill, which prevented premature failure due to local buckling. Chen et al. [148] investigated the flexural behaviour of concrete-filled CHSs strengthened by carbon fibre-reinforced polymer (CFRP). It was observed that the slightly improved ultimate capacity was accompanied by a reduction in the ductility. Modifications on the Architectural Institute of Japan (AIJ) standards [149] so as to consider the contribution of the CFRP reinforcement were also presented.

More research on this field should be carried out in order to adequately determine the structural behaviour of CFATs and propose design criteria able to achieve efficient exploitation of both materials. Future studies could include flexural buckling tests on CFATs with and without CFRP strengthening, beam-column tests, stub columns under eccentric compression and investigation of their behaviour at elevated temperatures.

2.8.2. Aluminium-CFRP structural members

Wu et al. [150] were at the forefront of strengthening aluminium alloy tubular sections against web crippling using CFRP, finding that the web crippling capacity can experience almost a four-fold increase due to the CFRP. Islam & Young [151] focussed on the effect of the application of six different types of adhesives and fibre-reinforced polymers (FRPs) on the web crippling capacity of SHSs and RHSs. It was shown that the higher the web slenderness ratio, the greater the enhancement of the web crippling strength. This was confirmed at their following experimental work [152] and the reported results were used in a recent numerical study where the NAS [131] design equations were modified in order to consider the contribution of both the CFRP-strengthening and the adhesive to the web crippling capacity [153].

2.9. Connections

2.9.1. Welded

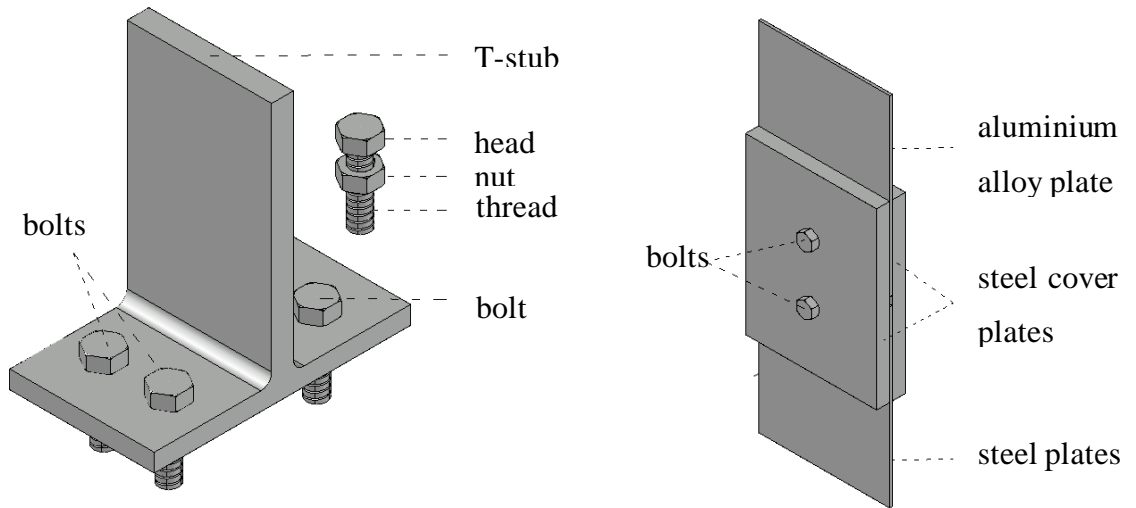
Owing to the difficulties related to the weldability of aluminium [154], only limited work has been reported to date on aluminium welded connections. Early attempts for a

comprehensive understanding of the behaviour of welded connections were made by Soetens [155], who investigated experimentally and numerically the structural response of welded connections in RHSs fabricated by 6063-T5 and 7020-T6. His findings were incorporated in the international specifications for the design of aluminium alloy structures (ECCS [156], NEN 3854 [157], CP 118 [158]). Another research study on welded connections was performed by Chan & Porter Goff [159] who evaluated experimentally the effects of the reduced strength zone on the ultimate capacity, ductility and failure mode of 7xxx series aluminium alloys. The structural response of welded T-stub joints under monotonic tensile loading was examined by De Matteis et al. [160] and it was shown that EN 1999-1-1 [5] equations provide reliable although slightly underestimated design predictions. The scarcity of the reported data reveals the need of additional experiments on aluminium welded connections to enable a better understanding of their behaviour.

2.9.2. Bolted

Over the last two decades, a series of studies have been performed on bolted connections under various arrangements and load cases, as illustrated in Figure 2.7. Table 2.11 summarises the reported experimental work. De Matteis et al. [160,161] conducted a thorough experimental and numerical work on T-stub connections under monotonic and cyclic loading. Kim [162] carried out tests on single shear bolted connections and found that the curling effect (out-of-plane deformation) reduces suddenly the ultimate capacity. These findings were used by Cho & Kim [163] who modified the strength equations for block shear fracture and bearing factor, taking into account the curling effect. In a more recent study by Wang et al. [164], twenty bolted connections were tested under tensile loading and the obtained results were used for the assessment of GB 50429 [4], EN 1999-1-1 [5] and AA [7] design codes, concluding that the aforementioned design specifications lead to conservative predictions. De Matteis et al. [165] carried out an extensive parametric study on the structural behaviour of T-stub joints showing that the material strain-hardening and the ductility considerably affect the strength of the joint. Brando et al. [166] determined the ultimate capacity of the web in beam-to-column joints subjected to tension and adjusted the design criteria developed for steel joints by using correction factors that consider the mechanical characteristics of aluminium alloys.

Recently, Adeoti et al. [167] reported a study dealing with the flexural behaviour of hexagonal bolted joints underling the importance of considering all the parameters with great impact on the structural behaviour and stiffness in order to design joints with high performance.



(a) T-stub bolted connection under monotonic and cyclic loading (adapted from De Matteis et al. [160,161])

(b) Bolted connection under tensile loading (adapted from Wang et al. [164])

Figure 2.7: Configuration of investigated bolted connections.

Table 2.11: Summary of aluminium alloy bolted connection tests.

(in chronological order from most recent research)

Author(s) (date) [Reference]	Aluminium grade	Connection type	No of tests	Design codes	N_u/N_{pred}		Assessment
					mean	COV	
Adeoti et al. (2019) [167]	6082-T6	hexagonal bolted joints	6	-			
Wang et al. (2018) [164]	6061-T6, 6063-T5	shear connection in single shear with two bolts	20	EN 1999-1-1:2007 [5]	1.36	0.03	conservative
				AA [7]	1.42	0.11	conservative
				GB 50429-2007 [4]	2.78	0.12	conservative
Kim (2012) [162]	6061-T6	shear connection in single shear with four bolts	10	-			
De Matteis et al. (2004) [160]	6061-T6, 6082-T6, 7020-T6	welded plates with holes	26	-			

Over the last five years, there is also a wide usage of aluminium alloy gusset (AAG) pinned, rigid or semi-rigid joints in practice. Guo et al. [168,169] performed a series of tests on fourteen AAG joints in order to define their out-of-plane flexural response. The results were used to elaborate simplified design formulae about the resistance against block tearing and local buckling. Guo et al. [170] adapted the component method included in EN 1993-1-8 [171] for AAG steel joints system and proposed suitable expressions for their bending behaviour. Guo et al. [172] investigated the flexural response of AAG joints exposed up to 300°C and proposed design criteria for the bearing capacity and the non-linear flexural stiffness. In a further study by Guo et al. [173], the hysteretic behaviour of AAG joints was assessed through cycling loading tests. Shi et al. [174] conducted experiments on two-way AAG joints subjected to pure bending and shear loading and they proposed a theoretical model able to accurately capture the mechanical behaviour of these joint systems. Liu et al. [175] determined experimentally the flexural behaviour of double- and single- layer AAG joints. Comparisons between the two types of the investigated joints demonstrated the superior structural response of the former.

Additional research in order to obtain a better understanding of the structural response of bolted connections under various configurations, loading cases (static, cyclic and fatigue) and aluminium alloy types, is recommended. This will allow for design criteria able to take into account this complex behaviour and lead to safe and economic design solutions.

2.9.3. Other studies

Kesawan et al. [176] conducted experimental work on the flexural response of mullions caused by wind pressure and suction, whereas the following year a numerical study on long span mullions with complex-shape sections under wind suction was presented by them [177]. Scheperboer et al. [178] studied numerically the buckling behaviour of perforated steel and aluminium plates and suggested that the design rules for steel perforated plates are applicable to aluminium alloy plates. Pursuing optimised cross-sectional shape with efficient exploitation of the material distribution, Tsavdaridis et al. [179] applied Structural Topology Optimization in aluminium cross-sections. They concluded that further research should be conducted including more global and local failure modes. Ampatzis et al. [180] suggested a useful methodology for determining the

safety factor of spatial aluminium frame structures against elastoplastic collapse. He et al. [181] proposed a novel modular support structure assembled by a foldable plane frame and joints suitable for temporary structures. Finally, the hysteresis behaviour of aluminium shear panels has been investigated, demonstrating their potential as dissipative devices in seismic resistant structures [182-184]. Related to this, it is noteworthy that studies on the seismic behaviour of columns and beams remain scarce. Therefore, a series of tests on structural members subjected to cyclic loading would be an interesting future research field in terms of the investigation of their ductility and energy dissipation capacity.

2.10. Summary and knowledge gap

This study reviewed the reported research work on structural aluminium alloys, providing a complete view of their mechanical properties, structural response and design of basic structural elements. The history of structural aluminium's investigation is relatively short and thus more research is needed in order to obtain a thorough understanding of its behaviour. On the basis of the reviewed papers, the following conclusions can be drawn:

- (1) Overall the current design guidelines do not provide accurate strength predictions, which are opposed to an economical and efficient design philosophy. This is related to the fact that their formulae are based on limited amount of experimental and numerical results. Design codes sometimes adopt similar principles to their steel structure counterparts, without sufficient consideration of the differences between the two materials.
- (2) Despite the advantageous features of structural aluminium alloys members, the investigation revealed that there are still limitations in their design, forcing the designers to favour more conventional materials.
- (3) Topics with limited number of studies that have been mentioned throughout this work are summarised in Table 2.12 as future recommendations. Additional research work can lead to modifications of the existing design codes and potentially increase structural engineers' confidence towards a more frequent employment of aluminium alloys.

- (4) Finally, scope of future work is to bridge the gap between theoretical and real world, making aluminium alloy an alternative construction material, capable of efficiently responding to the challenges encountered in real-life structures.

Table 2.12: Summary of recommended future work.

Investigation topic	Methods of investigation (experimental & numerical)
Cross-sectional response of aluminium elements	Fix-ended stub columns tests employing bare square/rectangular hollow and channel sections.
Cross-sectional response of concrete-aluminium elements	Fix-ended stub columns tests employing concrete-filled square/rectangular hollow sections.
Buckling behaviour of aluminium elements	Pin-ended columns tests employing bare square/rectangular hollow and channel sections.
Buckling behaviour of concrete-aluminium elements	Pin-ended columns tests employing concrete-filled square/rectangular hollow sections.
Flexural response of aluminium elements	Bending tests employing bare square/rectangular hollow and channel sections.
Flexural response of concrete-aluminium elements	Bending tests employing concrete-filled square/rectangular hollow sections.
Ultimate response of statically indeterminate aluminium structures.	Continuous beam tests employing stocky bare rectangular hollow sections.

CHAPTER 3

Methodology

3.1. Introduction

In order to investigate the structural response of aluminium alloy elements, a series of experimental tests combined with FE modelling studies have been conducted adopting the methodology presented in Figure 3.1. The current chapter describes in detail the adopted methodology for the execution of the experimental testing and FE modelling. Material testing including tensile tests on coupons and compressive tests on concrete cubes was conducted to determine the mechanical properties of the examined aluminium alloy and concrete, respectively. Series of structural tests were performed to study the compressive and flexural performance of bare tubular, concrete-filled tubular and channel cross-sections. Particularly, three series of fix-ended stub columns were executed to study the cross-sectional response of bare tubular, concrete-filled tubular and channel cross-sections. The same type of cross-sections were also employed to perform pin-ended column tests to investigate their minor-axis buckling behaviour. Moreover, two sets of bare tubular and one set of concrete-filled tubular cross-sections were tested under three-point bending, whilst one set of bare tubular and channel cross-sections were tested under four-point bending to quantify their moment resistance and rotational capacity. Finally, a series of two-span continuous beam tests employing bare tubular cross-sections was also executed to estimate the rotational capacity and the potential for moment redistribution of aluminium alloy indeterminate beams. Subsequent parametric studies were carried out to supplement the experimentally obtained data sets providing a

deeper understanding about the structural response of the considered cross-sections. Particularly, an extensive numerical modelling study was performed to investigate further the cross-sectional response of channel cross-sections. Parametric studies were also undertaken to generate additional structural performance data for the buckling behaviour of bare tubular, concrete-filled tubular and channel cross-sections. Moreover, the flexural behaviour of channel cross-sections under four-point bending configuration was better clarified through an extensive series of numerical analyses. Finally, the experimental results for the bare tubular cross-sections obtained from the three- and four-point bending tests as well as the two-span continuous beam tests were utilised for a comprehensive parametric study aimed to extend the pool of performance data for aluminium alloy indeterminate structures.

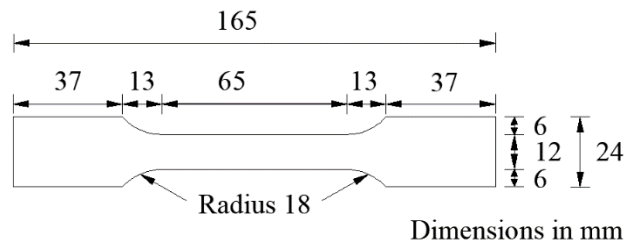
Methodology	Experimental investigation	Material testing	tensile coupon tests	[Number of tests/ numerical analyses]	
			compressive tests on concrete cubes		
		Fix-ended stub column tests			Bare tubular [8] Concrete-filled tubular [8] Channel [6]
		Pin-ended column tests			Bare tubular [8] Concrete-filled tubular [8] Channel [8]
		Simply-supported beam tests	three-point bending		Bare rectangular tubular [5] Bare square tubular [4] Concrete-filled tubular [4]
		four-point bending	Bare rectangular tubular [5] Channel [14]		
	Continuous beam tests		Bare tubular [5]		
	Numerical investigation	Fix-ended stub columns		Channel [47]	
		Pin-ended columns		Bare tubular [54] Concrete-filled tubular [54] Channel [45]	
		Simply-supported beams	four-point bending	Channel [140]	
Continuous beams			Bare rectangular tubular [108]		

Figure 3.1: Adopted methodology for the execution of the experimental tests and FE modelling studies.

3.2. Experimental investigation

3.2.1. Material testing

The examined cross-sections were fabricated by extrusion of 6082-T6 heat-treated aluminium alloy. 6082-T6 has the highest strength amongst 6,000 series (aluminium-magnesium-silicon family) alloys, known as “structural” alloys, and is rapidly employed in structural applications [34,185]. In order to determine the mechanical properties of the 6082-T6 heat-treated aluminium alloy, tensile tests were performed on flat coupons. Prior to testing, the geometric dimensions of each coupon were measured using a Vernier digital calliper. For each employed cross-section, two flat coupons were cut with a nominal width of 12 mm and gauge length of 100 mm as shown in Figure 3.2(a). Afterwards, the coupons were placed between the jaws of a 50 kN Tinius Olsen testing machine and were loaded with 0.2 mm/min displacement rate up to fracture. Moreover, a calibrated extensometer was attached onto the mid-length of the coupon specimens to measure the longitudinal strains during testing (Figure 3.2(b)). The average measured material properties, including the initial modulus of elasticity E , the 0.1 % proof stress $\sigma_{0.1}$, the 0.2 % proof stress $\sigma_{0.2}$, the ultimate tensile stress σ_u , the strain corresponding to ultimate tensile stress ε_u , the strain at fracture ε_f , the strain hardening exponent n [18,186] and the strain hardening ratio $\sigma_u/\sigma_{0.2}$ are summarised in the relevant tables for each experimental series. Figure 3.3 shows a typical experimental stress-strain (σ - ε) curve. As can be seen, the investigated 6082-T6 aluminium alloy exhibits a round stress-strain behaviour without a clearly defined yield point due to continuous strain hardening.



(a) Geometry

(b) During testing

Figure 3.2: Tensile coupon specimens.

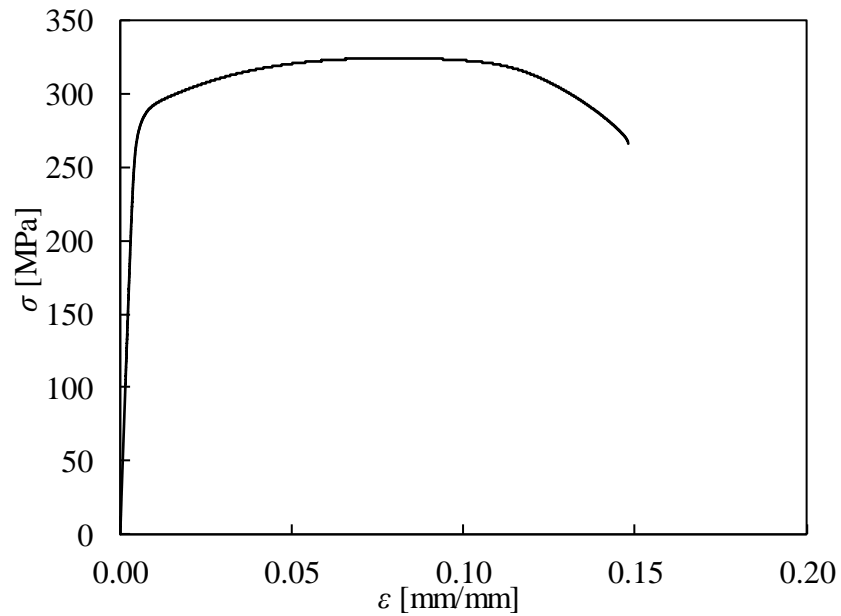


Figure 3.3: Experimental stress-strain curves.

The compressive strength of the concrete mix used to fill the aluminium tubes of the concrete-filled tubular specimens was also determined through compressive tests in standardised concrete cubes. The concrete mix was produced using ordinary Portland cement, fine and coarse aggregates as well as free water as listed below in Table 3.1.

Moreover, $100 \times 100 \times 100 \text{ mm}^3$ standard concrete cubes were cast from the same concrete mix to determine the maximum compressive strength of the concrete infill. After casting, the cubes were kept in rest period for 24 hours. Following, the cubes were demoulded and were placed in a water tank at ambient temperature for curing. Upon 28 days of curing, the concrete cubes were tested under axial compression. A typical tested concrete cube is shown in Figure 3.4. This concrete mix was used to fill the aluminium tubes of the concrete-filled tubular specimens, which were left to cure for 28 days before the execution of the structural testing. It is also noted that the vibration method in stages was used for compacting the concrete infill during casting. The average compressive strength $f_{ck,cube}$ of the tested cubes for each experimental series is reported in the relevant subsections.

Table 3.1: Properties of concrete mix of CFAT specimens.

Specimens	Concrete class	Cement (kg/m ³)	Fine Aggregates (kg/m ³)	Coarse Aggregates (kg/m ³)	Water/Cement ratio
Fix-ended stub columns and simply-supported beams	C30/37	434	635	1081 (maximum size 10 mm)	0.53
Pin-ended columns	C25/30	434	635	1081 (maximum size 5 mm)	0.53



Figure 3.4: Typical concrete cube after compression test.

3.2.2. Initial geometric imperfections

Most metallic structural members have initial geometric imperfections as a result of the manufacturing, transporting, and handling processes. Initial geometric imperfections can be classified into two main categories, which are local and overall (bow, global, or out-of-straightness) imperfections. Initial local geometric imperfections can be found in any region of the outer or inner surfaces of metallic structural members and are in the perpendicular directions to the structural member surfaces. On the other hand, initial global geometric imperfections are global profiles for the whole structural member along the member length in any direction [187].

The presence of initial geometric imperfections may significantly affect the structural response and strength of metallic structural members, precipitating the occurrence of buckling. Therefore, the initial local and global geometric imperfection amplitudes of each specimen were measured before the execution of the tests. Aiming to obtain a representative geometric imperfection pattern, each specimen was secured to a flat surface table and a ball probe attached onto the scribing jaw was moving along a line inscribed over the full specimen length. Measurements were taken for each face using a Mitutoyo linear height gauge at 20 mm intervals as shown in Figure 3.5. For each measuring point, the maximum deviation from a datum plane was assumed as local imperfection amplitude. The maximum measured local imperfection amplitude for each specimen is taken as the maximum value of the measured local imperfection amplitudes of all faces. With regards to the initial global imperfection amplitudes, the deviation of each measuring point at the mid-height from a linear reference line connecting the corresponding measuring points at both ends was recorded and the maximum of the recorded values for each face was defined as the initial global geometric imperfection amplitude of the specimen.



Figure 3.5: Measurements of initial geometric imperfections of a typical concrete-filled tubular specimen.

3.2.3. Fix-ended stub columns

Fix-ended stub column tests were performed to investigate the cross-sectional response and obtain the load-carrying capacity of bare tubular, concrete-filled tubular and channel cross-sections. The specimens' nominal length was set equal to three times the maximum cross-sectional dimension enabling for pure local buckling behaviour without any coupled instability phenomena [188]. The specimens were cut roughly to length and then were milled flat at both ends to a tolerance of ± 0.02 mm to achieve uniform distribution of the applied compressive loading. Figure 3.6 shows the schematic illustration of a typical fix-ended stub concrete-filled tubular column test arrangement and instrumentation. A Mayes servo-controlled hydraulic testing machine with 600 kN maximum capacity was used for the execution of the tests under displacement control. The end platens of the testing machine were fixed flat and parallel. Alignment of the examined specimens was deemed necessary to ensure that the compressive loading is applied concentrically. To do so, special wooden cut-outs were placed at both ends. Following, an initial compressive loading approximately equal to 15% of the predicted load-carrying capacity [189] was applied and the variation in strains taken from the affixed strain gauges (Tokyo Sokki Kenkyujo) at the mid-length of the specimen was observed. In all tested specimens, the variation between strains from the average strain

was less than 5% [190] confirming that the compressive loading was applied concentrically. Moreover, linearity of the stress-strain curve was utilised to verify that the initial compressive loading was below to the proportional limit. The compressive loading was applied at a cross-head displacement rate of 0.2 mm/min. Two Micro-Measurements linear variable displacement transducers (LVDTs) were located between the end platens to determine the end shortening of the stub column. The applied loading was measured using the load cell of the machine. The applied loading, end shortening and strain values were monitored through a data acquisition equipment (Micro-Measurements-model 8000) with sampling frequency of 10 Hz.

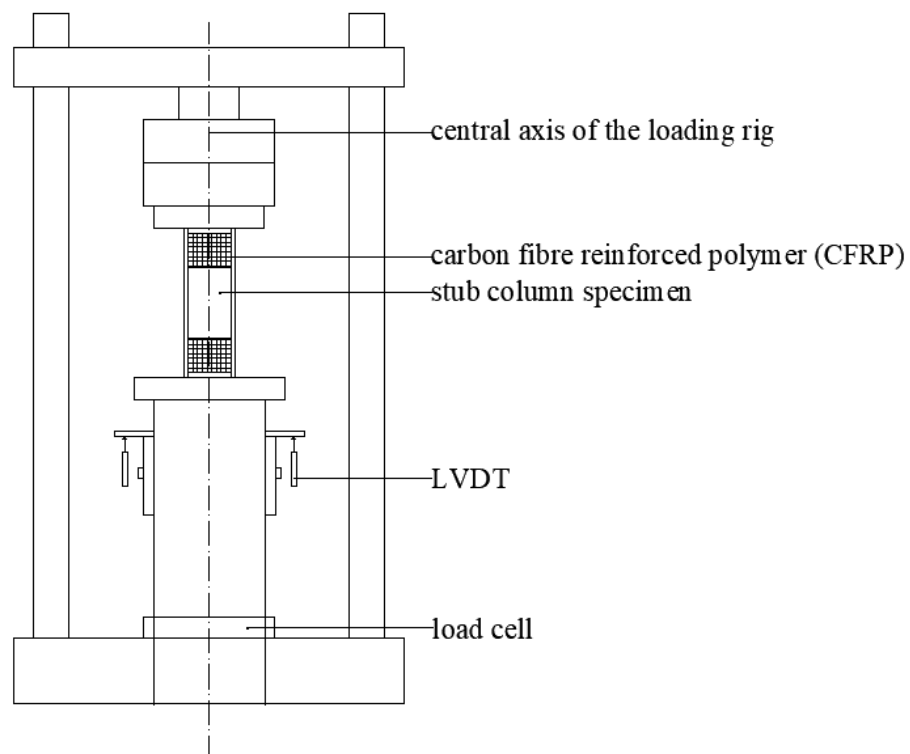


Figure 3.6: Schematic illustration of a typical fix-ended stub concrete-filled tubular column test arrangement and instrumentation.

3.2.4. Pin-ended columns

Aiming to investigate the minor-axis buckling behaviour of aluminium alloy bare tubular, concrete-filled tubular and channel cross-sections, concentric axial compression tests were performed employing pin-ended support conditions. The considered column lengths L were ranging from 300 mm to 1000 mm. Similar to fix-ended stub columns, the specimens were roughly cut to length and then were milled flat at both ends to ensure uniform distribution of the applied compressive loading. Figure 3.7 shows the schematic illustration of a typical pin-ended concrete-filled tubular column test arrangement and instrumentation. An assembly of a pit plate with V-shaped grooves and a wedge plate with a single knife-edge wedge was used to simulate the pin-ended support conditions allowing rotation around the minor axis. Moreover, steel C-sections were loosely bolted through steel plates at both edges to clamp both specimen's ends and prevent twisting and warping. Four LVDTs were placed; two at the mid-length to record the lateral deflection and two bilateral at the bottom edge to monitor the end rotation. Moreover, strain gauges were attached longitudinally at the mid-length to measure the compressive strains. The same Mayes servo-controlled hydraulic testing machine was used to perform the compression tests applying loading under displacement control at a cross-head displacement rate of 0.2 mm/min. Each specimen was placed carefully between the two pit plates and centralised in an accurate position, i.e., aimed eccentricity equal to zero. An initial compressive loading of approximately equal to 15% of the predicted load-carrying capacity [189] was also applied to ease the specimen's alignment into accurate position. It worth noting that the distance from the rotation centre of the knife-edge wedge to the end of the specimen was equal to 32 mm. Thus, the effective column length of each column was $L_e = L + 64$ mm. The applied loading was measured using the load cell of the testing machine. Upon specimen's alignment, compressive loading was applied again until failure occurs. The applied loading, end shortening and strain values were monitored through a data acquisition equipment with sampling frequency of 10 Hz.

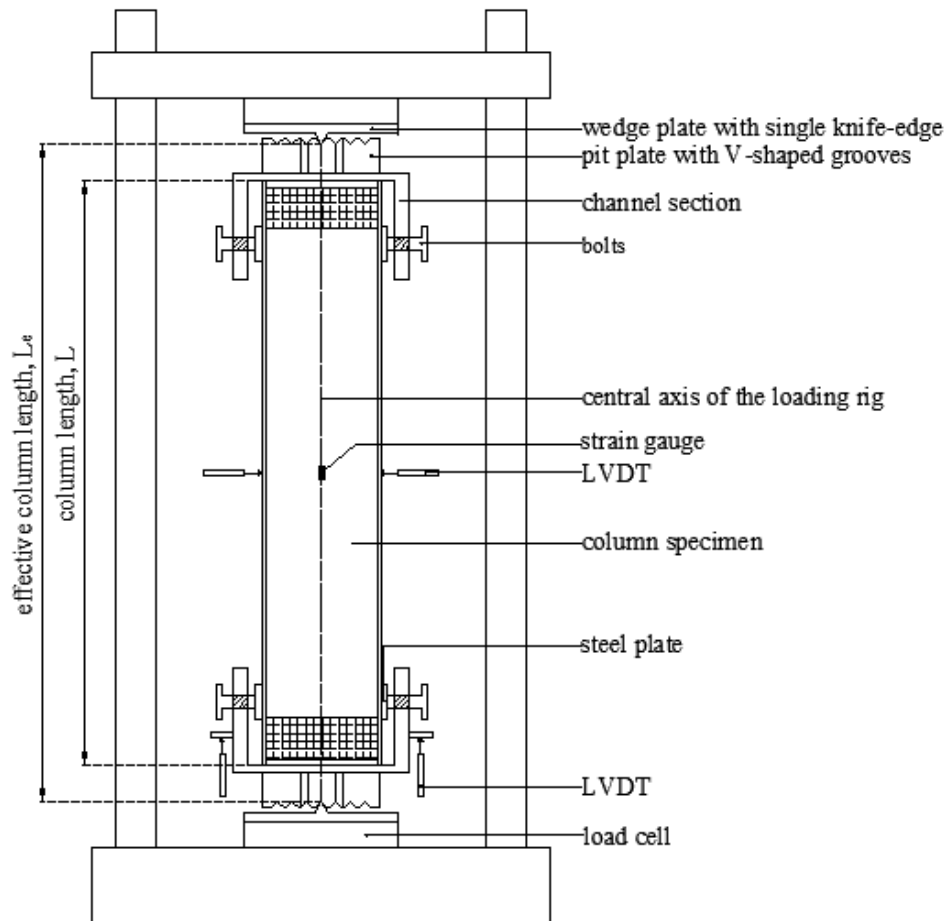


Figure 3.7: Schematic illustration of a typical pin-ended concrete-filled tubular column test arrangement and instrumentation.

3.2.5. Simply-supported beams

Series of symmetric bending tests on simply-supported beams were performed aiming to quantify the moment resistance and rotational capacity of bare tubular, concrete-filled tubular and channel cross-sections. Three-point and four-point bending configurations were adopted to explore the cross-sectional response under moment gradient and constant moment, respectively. The considered cross-sections were tested under in-plane bending about the major axis. Figure 3.8 and Figure 3.9 show the schematic illustration of a typical three-point and four-point bending test arrangement and instrumentation of bare tubular cross-sections, respectively. The total length of the beam specimens was ranging between 600 mm and 1000 mm, whilst they overhung each end by 50 mm beyond the centerlines of the supports. The span-to-height ratio ranged from 10 to 23 representing the proportions of actual beams and being sufficiently high to preclude any shear

dominance on the flexural response. The simply-supported boundary conditions were elaborated using steel rollers which allowed free rotation about the major axis as well as free longitudinal displacement of the specimen's ends. A Mayes servo-controlled hydraulic testing machine with 600 kN capacity was used to apply load under displacement control and at 0.8 mm/min cross-head displacement rate. The load was applied symmetrically at midspan in three-point bending tests and at third-points in four-point bending tests via a spreader beam located between the two steel rollers and the hydraulic jack of the machine. Linear electrical resistance strain gauges were attached at top and bottom flanges of each cross-section to measure the extreme compressive and tensile strains during testing. In addition, in three-point bending tests, one LVDT was located at the midspan to record the vertical displacement, whilst two inclinometers (Siko-model IK360L) were positioned at the support locations to measure the end rotations. In four-point bending tests, three LVDTs were attached at both midspan and loading points to monitor the vertical displacements and determine the curvature in the constant moment area. The applied load, strains, displacements and end rotations were recorded using a data acquisition system at 2 s intervals.

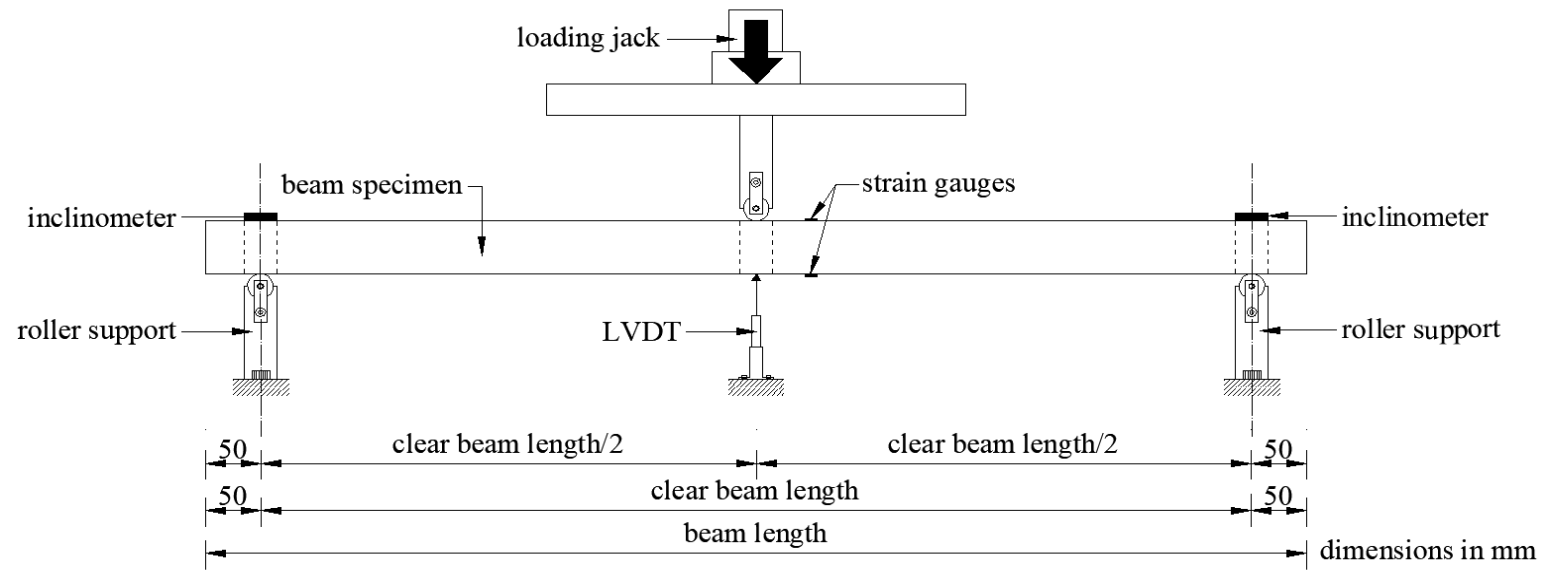


Figure 3.8: Schematic illustration of a typical three-point bending test arrangement and instrumentation of bare tubular cross-section.

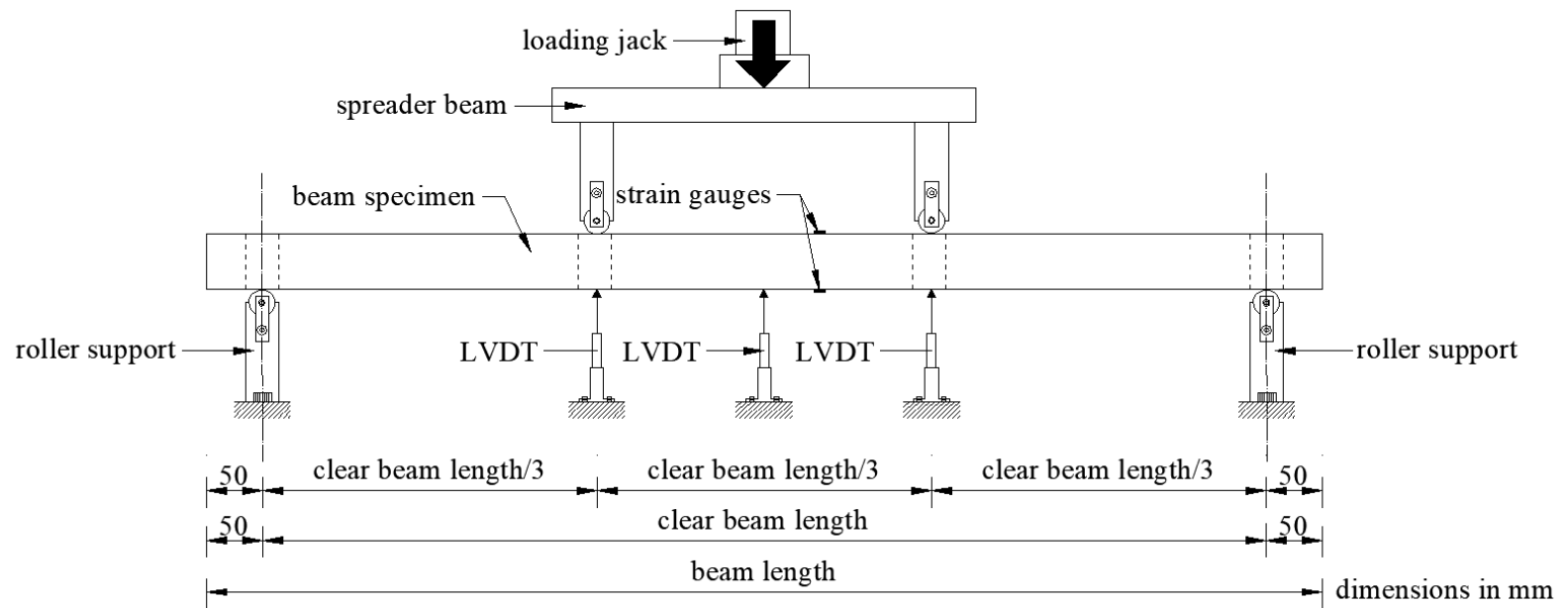


Figure 3.9: Schematic illustration of a typical four-point bending test arrangement and instrumentation of bare tubular cross-section.

3.2.6. Continuous beams

Aiming to estimate the rotational capacity and the potential for moment redistribution of aluminium alloy indeterminate beams, bare tubular cross-sections were subjected to five-point bending. Figure 3.10 shows the schematic illustration of a typical five-point bending test arrangement and instrumentation of bare tubular cross-section. The investigated specimens were two-span continuous beams with a total length of 2000 mm. Each specimen overhung each end by 100 mm beyond the centerlines of the supports. Following the same methodology with simply-supported beam tests, the support conditions were formed using steel rollers. The load was applied through a hydraulic testing machine with 150 kN capacity under displacement control and at 0.8 mm/min cross-head displacement rate. The beams were loaded symmetrically at both midspans using a spreader beam placed between the two steel rollers and the hydraulic jack of the machine. The employed instrumentation consisted of four load cells located at the supports and underneath the ram of the hydraulic jack to measure the reaction forces (unknown due to statical indeterminacy) and the overall applied loading, respectively. Two LVDTs were also placed at both midspans to monitor the corresponding vertical displacements. Two inclinometers were attached to the end supports and two additional to the either side of the central support to record the rotations during testing. Furthermore, six linear electrical resistance strain gauges were affixed to the top and bottom flange of the cross-section to ensure that the end rollers did not provide any axial restraint. The applied load, reaction forces, strains, displacements and end rotations were all recorded using a data acquisition system at 2 s intervals.

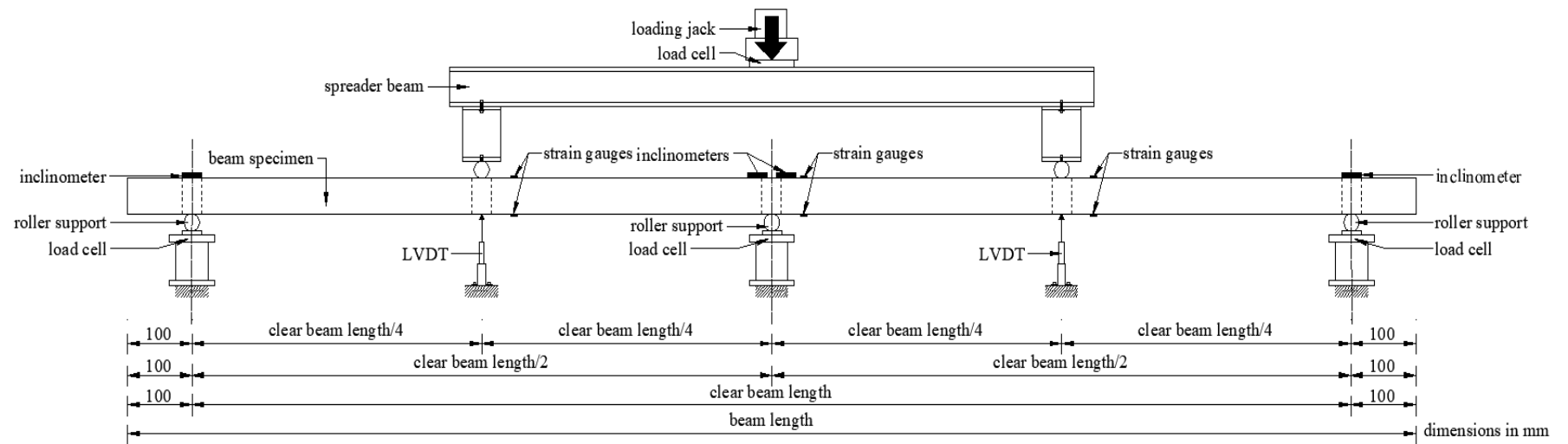


Figure 3.10: Schematic illustration of the continuous beam test arrangement and instrumentation of bare tubular cross-section.

3.3. Numerical investigation

3.3.1. Finite element method

The development of the FE method in the field of structural engineering was credited to the numerical investigations performed by Hrennikoff [191] and McHenry [192]. These investigations were limited to the use of one-dimensional (1D) elements for the evaluation of stresses in continuous structural beams. Two-dimensional (2D) elements were first introduced by Clough et al. [193] where stiffness matrices were derived for truss, beam, and 2D triangular and rectangular elements in plane stress conditions. This study has outlined the fundamentals of the stiffness method for predicting the structure stiffness matrix. The development of the FE method was first introduced by Clough [194] where triangular and rectangular elements were used for the analysis of structures under plane stress conditions.

Most of the initial investigations addressed structures under small strains and small displacements, elastic material, and static loading. Improved numerical techniques for the solution of FE equations were first addressed by Belytschko [195]. Recent developments in computers have resulted in the FE method being used to describe complicated structures associated with large number of equations. Numerous special-purpose and general-purpose programs have been written to analyse various complicated structures with the advent of computers and computational programs. However, to successfully use computers in FE analyses, it is important to understand the fundamentals of developing FE models comprising the definition of nodal coordinates, finite elements and how they are connected, material properties of the elements, applied loads, boundary conditions, and the kind of analysis to be performed.

The FE method is based on modeling the structure using small, interconnected elements called finite elements with defined points forming the element boundaries called nodes. There are numerous finite elements analysed in the literature such as bar, beam, frame, solid, and shell elements. The use of any element depends on the type of the structure, geometry, type of analysis, applied loads and boundary conditions, computational time, and data required from the analysis. Each element has its own displacement function that describes the displacement within the element in terms of nodal displacement. Every

interconnected element has to be linked to other elements simulating the structure directly by sharing the exact boundaries or indirectly through the use of interface nodes, lines, or elements that connect the element with the other elements. The element stiffness matrices and finite element equations can be generated by making use of the commonly known stress strain relationships and direct equilibrium equations. By solving the FE equations, the unknown displacements can be determined and used to predict different straining actions such as internal forces and bending moments. For the execution of the FE analyses for the nonlinear problems presented in the current study, the general purpose FE package Abaqus [196] has been used.

3.3.2. Elements

Abaqus [196] provides a wide range of element types for the development of the FE models. Each element is characterised by its family from a structural point of view (solid or continuum, shell, beam, truss etc.), the number of nodes (linear or first-order, quadratic or second-order, cubic or third-order), the degrees of freedom, the formulation and the integration scheme (full, reduced).

The most commonly applied element types are displayed in Figure 3.11. Continuum or solid elements simply model small blocks of material in a component. Shell elements approximate a three-dimensional continuum with a surface model and are used to model structures in which the one dimension (the thickness) is significantly smaller than the other dimensions and the stresses in the thickness direction are negligible. In beam elements, one dimension (the length) is significantly greater than the other two dimensions and the longitudinal stress is most important. Truss elements are rods that can carry only tensile or compressive loads and have no resistance to bending.

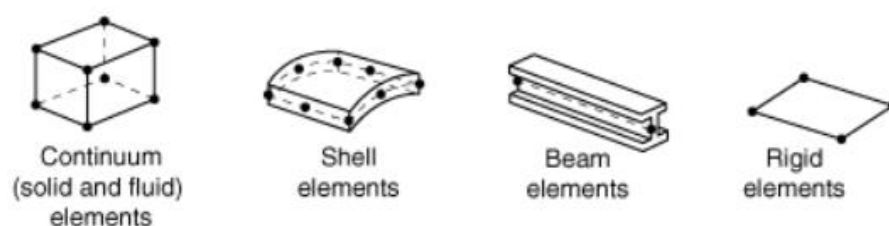


Figure 3.11: Most commonly applied element types [196].

The elements primarily applied within the present research study are the following [196]:

- S4R: Four-noded shell element with reduced integration rule and hourglass control. This type of shell element has three translational and three rotational degrees of freedom. It is a general-purpose conventional shell element, as its mathematical formulation allows transverse shear deformation and changes in the shell thickness as a function of the membrane strain (using thick shell or Kirchoff theory depending on the shell thickness). Furthermore, it is suitable for materially and geometrically nonlinear problems, as it accounts for arbitrarily large rotations and finite membrane strains.
- C3D8R: Eight-noded general purpose first-order solid element with one integration point and hourglass control in order to avoid uncontrolled mesh distortion. This type of element has only translational degrees of freedom at each node.

3.3.3. Mesh

Meshing is one of the key components to obtaining accurate results from a FE model. The elements in the mesh must take many aspects into account to be able to discretise stress gradients accurately. In general, the finer the mesh size, the more accurate the solution as the design is better sampled across the physical domains. However, the higher the accuracy, the larger the simulation become and thus the computational time is extended. Keeping these in mind and aiming to obtain the optimal balance between accuracy and computational time, convergence studies from coarser to finer mesh were performed for the developed FE models.

3.3.4. Material properties

The accuracy of material modelling is considered as one of the most important aspects of FE simulations significantly affecting the performance of the FE models. A bilinear elastic-plastic behaviour associated with isotropic hardening and von Mises yield criterion was adopted for the aluminium alloys. In the linear analyses stage, the material properties were defined by the Young's modulus E , the Poisson's ratio ν and the yield stress (0.2% proof stress). In the nonlinear stage, aluminium alloy's plasticity was

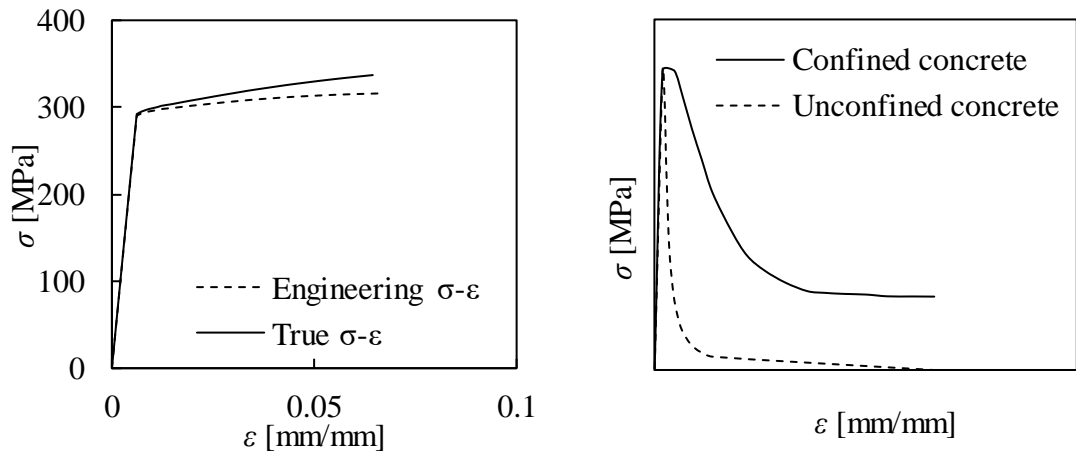
included in the FE models by specifying sets of values of true stress σ_{true} and logarithmic plastic strain ε_{true}^{pl} to define a piecewise linear response. To do so, the engineering (nominal) stress σ_{nom} and strain ε_{nom} for the aluminium alloy obtained from the coupon tests were converted to true stress σ_{true} and logarithmic plastic strain ε_{true}^{pl} using the Equations (3.2) and (3.3) (see Figure 3.12(a)). The true stress-strain curve was discretised and represented by approximately 20 points in the FE models.

$$\sigma_{true} = \sigma_{nom}(1 + \varepsilon_{nom}) \quad (3.2)$$

$$\varepsilon_{true}^{pl} = \ln(1 + \varepsilon_{nom}) - \frac{\sigma_{nom}}{E} \quad (3.3)$$

The concrete damaged plasticity model from Abaqus [196] material library was employed to simulate concrete infill's plasticity. The Young's modulus E was calculated according to European standards [197]. The value of the dilation angle was taken equal to 40° as suggested by Tao et al. [198] for infilled concrete. The default values of the viscosity parameter and flow potential eccentricity were taken as 0 and 0.1 respectively, as they have no significant influence on concrete-filled tubes [198]. The ratio of the compressive strength under biaxial loading to uniaxial compressive strength and the compressive meridian were determined according to [199]. When a CFAT member is axially compressed, the concrete infill expands laterally and interacts with the aluminium tube. To account for the composite action between the concrete infill and the aluminium tube, an equivalent uniaxial compressive stress-strain model of confined concrete [198-201] was considered. In this model, the ascending part of the stress-strain response of the confined concrete is taken similar to that of the unconfined concrete, considering no interaction. After the peak strength, the lateral strain of concrete increases and the concrete interacts with the hollow tube. Consequently, confining pressure develops between the two materials, improving the compressive strength of concrete. The beneficial effect of confinement in concrete's strength and ductility is simulated by considering the confined model shown in Figure 3.12(a). Based on the material test data, the compressive cylinder strength was taken equal to 80% of the cube strength. The tensile behaviour of concrete was assumed to be linear up to 10% of compressive cylinder strength [198]. The inelastic region of the concrete tensile stress-strain curve was defined

according to the stress-crack opening displacement relationship [202], as a function of the fracture energy which was determined in line with [203,204].



(a) Typical stress-strain response of 6082-T6 aluminium alloy.

(b) Stress-strain model for confined concrete proposed by Tao et al. [198].

Figure 3.12: Stress-strain responses considered in the FE simulations.

3.3.5. Initial geometric imperfections and residual stresses

As has already been referred in Subsection 3.2.2. the initial geometric imperfections present on metallic structural members may significantly affect their structural response and strength, and thus they should be incorporated in the FE models. The initial local and global geometric imperfection patterns were predicted from FE models by conducting eigenvalue buckling analysis to extract the local and global buckling modes (see Figure 3.13). These local and global buckling modes were factored by the magnitudes measured in tests or determined by additional imperfection sensitivity analysis. A following superposition was applied to predict the final combined local and global buckling modes compliant with the observed failure modes in tests. The resulting combined buckling modes were then added to the initial coordinates of each one of the investigated structural members. The final coordinates will be used in the subsequent nonlinear analysis.

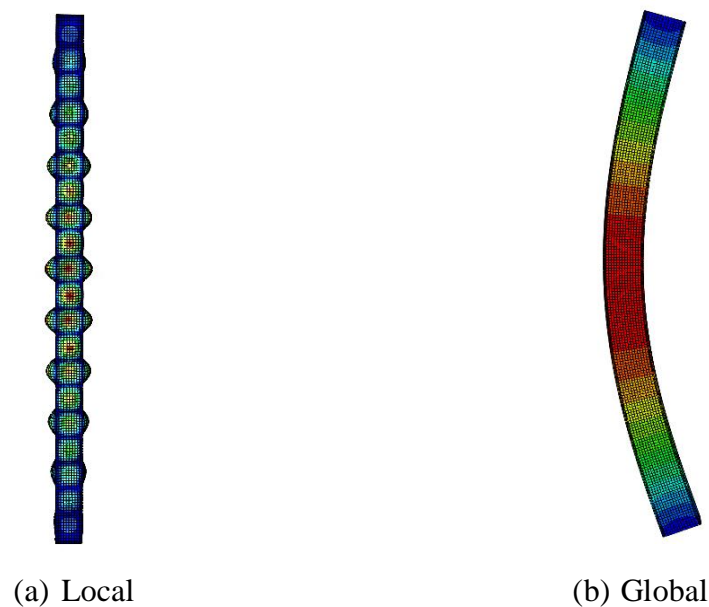


Figure 3.13: Typical local and global buckling modes of bare tubular pin-ended columns.

Residual stresses are initial stresses existing in cross-sections without application of an external load such as stresses resulting from manufacturing processes of metallic structural members. The residual stresses caused by the heat-treatment of aluminium alloys were not explicitly incorporated into the simulations [73,205] for the following two reasons. Firstly, the presence of bending residual stresses, which can be reflected by pronounced curving of the tensile coupons [206,207], was not observed herein. Secondly, the residual stresses of extruded aluminium alloy cross-sections have been shown to have a negligible influence on the ultimate strength [34].

3.3.6. Boundary conditions, constraints and contact interactions

Supports and applied loading in tests of metallic structural members must be simulated accurately in the FE models. Any assumptions or simplifications in actual supports and loads could affect the accuracy of the results. The exact test conditions were captured by appropriately restraining the translational and rotational degrees of freedom, whilst suitable constraints were used. Examples of applied constraints are the following:

- rigid body which allows constraining the motion of regions of an assembly to the motion of a reference point

- kinematic coupling which limits the motion of a group of nodes (coupling nodes) to the rigid body motion defined by a reference node, and
- tie constraint which allows fusing together permanently two surfaces so that there is no relative motion between them, using a master-slave formulation.

The interaction between the aluminium tube and the concrete infill was simulated using the surface-to-surface contact. Thus, a contact pair was defined between the inner surfaces of the aluminium tube (slave surface) and the outer surfaces of the concrete infill (master surface). A hard contact pressure-overclosure relationship was assigned in the direction normal to the plane of these surfaces to simulate the development of normal stresses between surfaces without penetration in compression and releasing stresses by separating from each other in tension. The Coulomb friction model was adopted in the tangential direction for allowing slippage between the aluminium tube and concrete. As the compressive load was applied on both the aluminium tube and the concrete simultaneously, the possibility of slippage is almost negligible. Therefore, the results are less sensitive to the values of the friction coefficient. Based on the findings reported in [208], a value of 0.3 was used for the friction coefficient, which retains sufficient accuracy and offers a quick convergence.

Boundary conditions, constraints and contact interactions are further discussed in Chapter 5, where a full description of the applied boundary conditions and constraints for each model is given.

3.3.7. Analysis techniques

Two analyses techniques have been mainly used within the current study: Linear buckling analysis and Riks analysis.

Linear buckling analysis is a linear perturbation procedure that estimates the elastic critical buckling loads of structures. The analysis searches for loads that make the model stiffness matrix become singular for nontrivial displacement solutions by solving the following Equation.

$$\left(K_0^{NM} + \lambda_i K_{\Delta}^{NM} \right) v_i^M = 0 \quad (3.4)$$

where K_0^{NM} is the stiffness matrix corresponding to the base state, K_A^{NM} is the differential initial stress and load stiffness matrix due to incremental loading pattern, λ_i are the eigenvalues, u_i are the eigenvectors (i.e. the buckling mode shapes), i refers to the i^{th} buckling mode, whilst M and N are the degrees of freedom of the whole model. The subspace iteration method which firstly introduced by Bathe & Wilson [209] is employed to solve the Equation (3.4). The obtained mode shapes were subsequently used as a representative geometric imperfection pattern, scaled to an appropriate magnitude, as discussed in Subsection 3.3.5. whilst also provide an estimate of the collapse failure mode. In case a negative eigenvalue is reported, this indicates that the structure would buckle if the load was applied in the opposite direction.

The Riks method provided by Abaqus [196] is an efficient method that is generally used to predict unstable, geometrically nonlinear collapse of a structure. The method can include nonlinear materials and boundary conditions. The method commonly follows an eigenvalue buckling analysis to provide complete information about a structure's collapse. The Riks method treats the load magnitude as an additional unknown and solves loads and displacements simultaneously. Therefore, another quantity must be used to measure the progress of the solution. Abaqus [196] uses the arc length along the static equilibrium path in load displacement domain. Abaqus [196] uses Newton's method to solve the nonlinear equilibrium equations. The Riks procedure uses very small extrapolation of the strain increment. An initial increment should be provided in arc length along the static equilibrium path when defining the step. After that, Abaqus [196] computes subsequent steps automatically. Since the loading magnitude is part of the solution, a method is needed to specify when the step is completed. It is common that one can specify a maximum displacement value at a specified degree of freedom. The step will terminate once the maximum value is reached. Otherwise, the analysis will continue until the maximum number of increments specified in the step definition is reached.

3.3.8. Analysis output

Upon solving the boundary value problem and completing the analysis, output data including stresses, strains and displacements (both translational and rotational) and forces in locations of interest were derived and visualised.

3.3.9. Validation

In order to verify that the developed FE models are able to precisely capture the structural performance of the tested specimens, the numerically derived response was compared with the experimental one on the basis of the following criteria.

- (1) Initial stiffness of the structural system (i.e. the initial linear part of the load-deformation curve obtained from the experiments was compared with the numerical one).
- (2) Ultimate capacity (i.e. the maximum load achieved during testing was compared with the numerical one - the latter is defined separately in each chapter).
- (3) Failure mode (i.e. the shape of the experimentally failed specimen was compared with the numerical one).
- (4) Overall load-deformation response (i.e. the overall experimental load-deformation response from the beginning of loading up to strains beyond the failure load was compared with the numerical one).

As explained in Subsection 3.3.5. the developed FE models were calibrated against the test results, considering different magnitudes for the initial geometric imperfections. The calibration was based on the satisfaction of the aforementioned four criteria. The results of the imperfection sensitivity analysis performed during the validation of the FE models along with typical graphs of the load-deformation response and representative failure modes are shown in the following chapters. Moreover, the comparison ratios of ultimate loads together with statistical quantities are also presented, thus allowing the selection of the imperfection magnitude that successfully captured the experimental performance.

3.3.10. Parametric studies

Upon establishing a successful validation, the FE models were used to investigate further the considered structural response and evaluate the influence of key parameters on the structural response.

For the fix-ended stub columns, different aspect ratios D/B were considered, where D is the outer web and B is the outer flange of the studied cross-sections. Note that the considered aspect ratios were resulted by maintaining the outer web D , while changing

the outer flange B . Moreover, the cross-sectional thickness was appropriately varied to encompass a wide range of cross-sectional slenderness ratios β/ε of the web, where $\beta = (D-2t)/t$ and t is the web/flange thickness for the tubular cross-sections and β_f/ε of the outstand flange, where $\beta_f = (B-t_w/2)/t_f$, t_w is the web thickness and t_f is the flange thickness) for the channel cross-sections, whilst $\varepsilon = \sqrt{250/\sigma_{0.2}}$ is the material coefficient. The specimens' nominal length was set equal to three times the maximum cross-sectional dimension enabling for pure local buckling behaviour without any coupled instability phenomena [188].

For the pin-ended columns, different aspect ratios D/B and cross-sectional thicknesses were considered allowing to study the buckling behaviour over a wide range of cross-sections. Moreover, the members' length L was ranging providing a broad range of member slendernesses $\bar{\lambda}$, where $\bar{\lambda} = \sqrt{A\sigma_{0.2}/F_{cr}}$, A is the cross-sectional area and F_{cr} is the elastic critical buckling load of the column according to EN 1999-1-1 [5]. For bare and concrete-filled tubular pin-ended columns both major and minor axis buckling behaviour were investigated, whilst for channel pin-ended columns only the minor axis buckling behaviour was investigated. For the concrete-filled pin-ended columns, different concrete cylinder strengths were also considered in the parametric studies, to study their influence on the buckling performance.

For the simply-supported beams, the parametric studies emphasised on the influence of key parameters on the flexural performance of channel cross-sections. Different aspect ratios D/B and cross-sectional thicknesses ($t_w = t_f$) were considered, extending the experimental data to a broad range of plate slendernesses. Aiming to extend the study to an additional structural aluminium alloy, two types of heat-treated aluminium alloys were investigated, namely 6082-T6 and 6063-T5, representing a typical high and normal strength heat-treated aluminium alloy, respectively. All beam specimens were examined under both the “u” and “n” orientations (see Subsection 4.4.4.).

For continuous beams, a series of parametric studies was carried out to generate further data on aluminium alloy two-span continuous beams. Different aspect ratios D/B and cross-sectional thicknesses t were studied, extending the experimental results to a broad

range of plate slendernesses. Moreover, three aluminium alloy types were considered within the investigation, namely 6082-T6, 6061-T6 and 6063-T5.

The examined parameters considered in the parametric studies for each investigation are listed in relevant tables in Chapter 5.

3.4. Analysis of the results and design recommendations

On the basis of the experimental and the numerical results, guidelines for the design of bare tubular and channel section members were assessed. Particular emphasis was placed upon the accuracy of the current European specification for aluminium alloy structural elements EC9 [5], whereas relevant design recommendations were made, where appropriate. The applicability of the Continuous Strength Method and the Direct Strength Method to aluminium alloy structural elements was also evaluated. In absence of codified design rules for the prediction of the capacities of composite aluminium-concrete cross-sections and members, design recommendations on the basis of the design formulae for composite steel-concrete cross-sections available in EC4 [210] were provided. Note that for all the comparisons, safety factors were taken equal to unity.

CHAPTER 4

Experimental investigation of aluminium alloy structural elements

4.1. Introduction

The current chapter describes in detail the experimental investigation of the structural response of aluminium alloy structural elements. Material testing including tensile tests on coupons and compressive tests on concrete cubes was conducted to determine the mechanical properties of the examined aluminium alloy and concrete, respectively. Series of structural tests were performed in the Light Structures and Materials Laboratory of the School of Civil Engineering and Built Environment at Liverpool John Moores to study the compressive and flexural performance of bare tubular, concrete-filled tubular and channel cross-sections. Particularly, 22 fix-ended stub columns (Section 4.2.) were executed to study the cross-sectional response of bare tubular, concrete-filled tubular and channel cross-sections. The same type of cross-sections were also employed to perform 24 pin-ended column tests (Section 4.3.) to investigate their minor-axis buckling behaviour. Moreover, 9 bare tubular and 4 concrete-filled tubular cross-sections were tested under three-point bending (Section 4.4.) whilst 5 bare tubular and 14 channel cross-sections were tested under four-point bending (Section 4.4.) to quantify their moment resistance and rotational capacity. Finally, 5 two-span continuous beam tests (Section 4.5.) employing bare tubular cross-sections were

also executed to estimate the rotational capacity and the potential for moment redistribution of aluminium alloy indeterminate structures.

4.2. Fix-ended stub columns

4.2.1. Bare tubular cross-sections

Four different SHSs made from 6082-T6 heat-treated aluminium alloy were examined in the present study. All cross-sections had nominal outer depth D and width B of 50.8 mm. Four nominal thicknesses t namely 1.6, 2.7, 3.3 and 4.8 mm were considered enabling to investigate the cross-sectional response in a broad range of width-to-thickness ratio B/t values varying from 10.37 to 31.63 (see Table 4.1). Following the technical memorandum for fix-ended stub column tests [188] as explained in Subsection 3.2.3. the specimens were cut in nominal length L equal to three times the maximum cross-sectional dimension. Each fix-ended stub column test was executed twice resulting in total 8 fix-ended stub column tests. Table 4.1 presents the measured dimensions for all the investigated bare aluminium tubular (BAT) specimens using the nomenclature depicted in Figure 4.1. The specimens were designated according to their nominal geometric dimensions. The designation was also followed by the letter “a” or “b” to distinguish the specimens employed in the first and repeated test, respectively. For instance, the label “50.8×50.8×3.3-a” defines a fix-ended stub column specimen with outer depth $D=50.8$ mm, outer width $B=50.8$ mm and thickness $t=3.3$ mm, whilst the letter “a” signifies that this specimen was tested first. The engineering stress–strain curves (σ – ε) obtained from the tensile coupon tests for each examined cross-section are depicted in Figure 4.2. Moreover, the average measured material properties, are listed in Table 4.2.

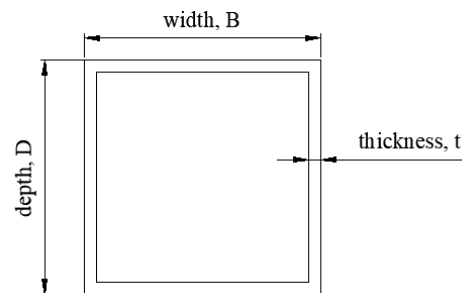


Figure 4.1: Geometric properties of the BAT sections of the fix-ended stub columns.

Table 4.1: Mean measured geometrical dimensions and local geometric imperfections of the tested BAT fix-ended stub columns.

Specimen	D (mm)	B (mm)	t (mm)	B/t	L (mm)
50.8×50.8×1.6-a	51.04	50.80	1.62	31.36	153.00
50.8×50.8×1.6-b	50.89	50.36	1.64	30.71	152.90
50.8×50.8×2.7-a	50.86	50.82	2.68	18.96	153.00
50.8×50.8×2.7-b	50.78	50.10	2.71	18.49	153.00
50.8×50.8×3.3-a	51.32	50.70	3.27	15.50	153.00
50.8×50.8×3.3-b	51.49	51.20	3.25	15.75	152.90
50.8×50.8×4.8-a	51.22	51.00	4.79	10.65	153.00
50.8×50.8×4.8-b	51.06	50.79	4.73	10.74	153.00

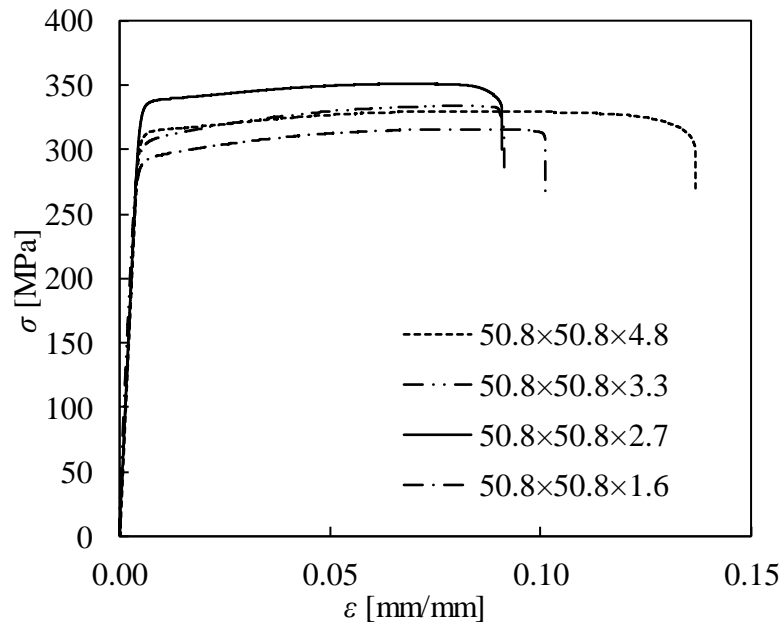


Figure 4.2: Stress-strain curves of the BAT/CFAT sections of the fix-ended stub columns.

Table 4.2: Material properties of BAT/CFAT cross-sections obtained from the tensile coupon tests.

	E (MPa)	$\sigma_{0.1}$ (MPa)	$\sigma_{0.2}$ (MPa)	σ_u (MPa)	ϵ_u (mm/mm)	ϵ_f (mm/mm)	n	$\sigma_u/\sigma_{0.2}$
50.8×50.8×1.6	65000	283	289	315	0.08	0.11	34.8	1.09
50.8×50.8×2.7	72200	330	337	352	0.07	0.10	31.2	1.04
50.8×50.8×3.3	71700	296	302	330	0.08	0.09	30.9	1.09
50.8×50.8×4.8	67500	300	306	325	0.09	0.16	34.4	1.06

In line with similar studies [140,142,143] the BAT specimens, prior to testing, were also strengthened with carbon fibre reinforced polymer strips at both ends to prevent any localised failure. Figure 4.3 shows a schematic illustration of the fix-ended stub column test arrangement along with the corresponding employed instrumentation, whilst Figure 4.4 illustrates a typical fix-ended stub column test set-up.

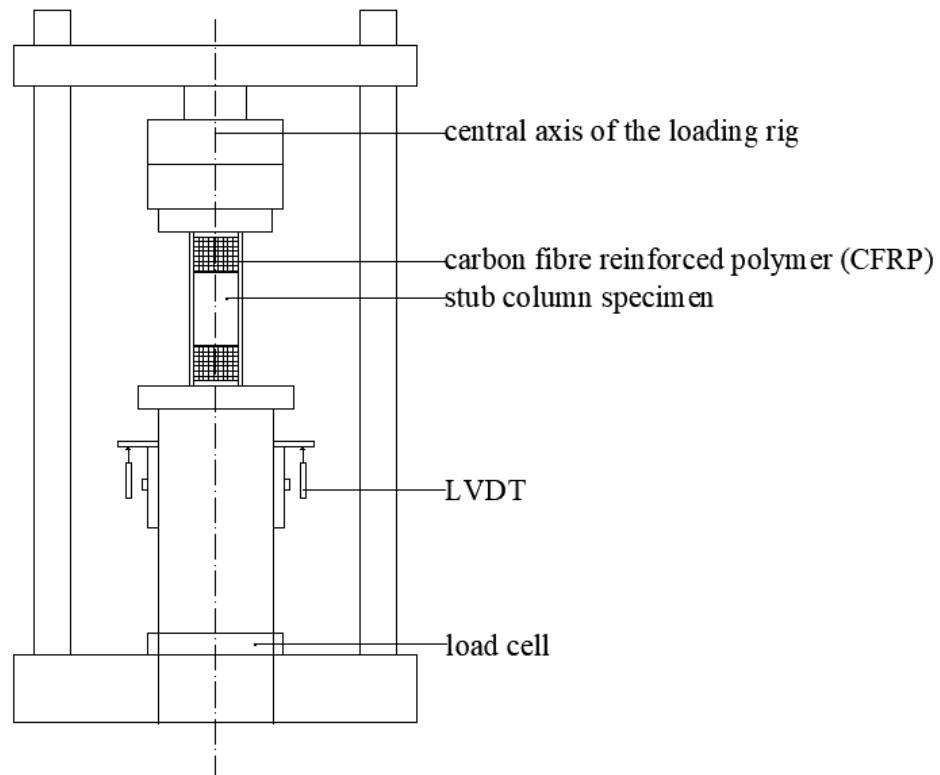


Figure 4.3: Schematic illustration of the BAT/CFAT fix-ended stub column test arrangement and instrumentation.



Figure 4.4: Typical BAT/CFAT fix-ended stub column test set-up.

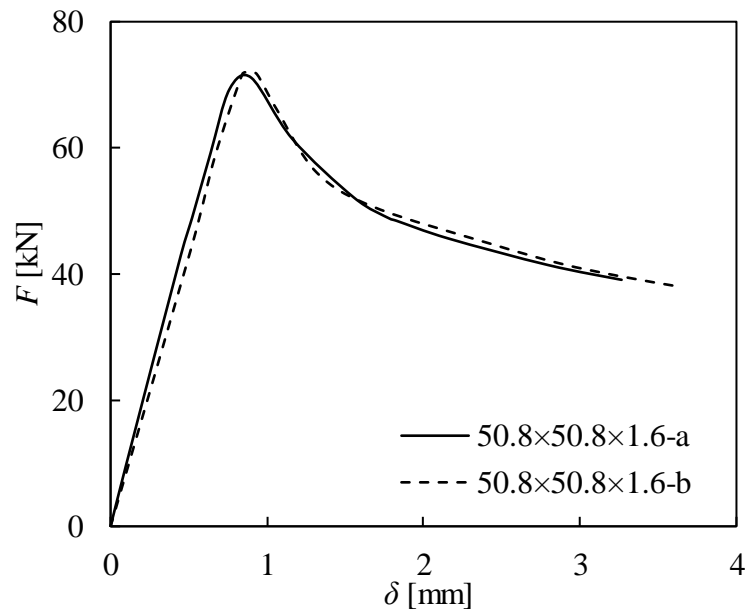
For the tested BAT fix-ended stub columns, the governing failure mode was local buckling. Typical failure modes are shown in Figure 4.5. Figure 4.5(a) displays the $50.8 \times 50.8 \times 1.6$ -a specimen which failed due to elastic local buckling. This was expected, since $50.8 \times 50.8 \times 1.6$ specimen consisted of the most slender cross-section, and thus its cross-sectional capacity was limited by local buckling. Note that a slender cross-section (higher B/t) fails due to local buckling before the attainment of its yield strength, whilst a stocky cross-section (lower B/t) is capable of reaching its yield strength without presence of local instabilities. As can be seen from Figure 4.5(a), alternate inward and outward local buckling shapes occurred almost in the mid-height of the specimen, where the existing local geometric imperfections might have larger magnitude and thus triggering local buckling of the constituent plates. Another example of local buckling on a stockier BAT specimen is shown in Figure 4.5(b).



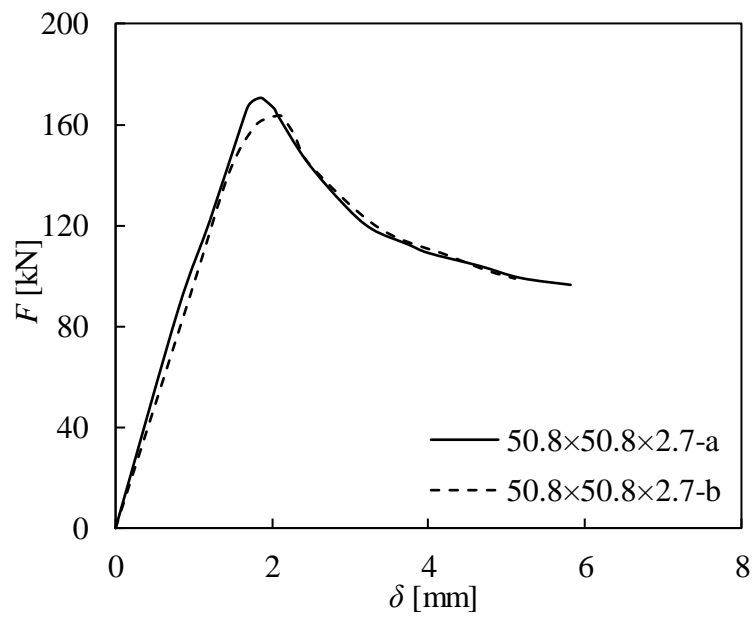
Figure 4.5: Typical failure modes of BAT fix-ended stub column specimens.

The obtained load–end shortening (F – δ) curves of the tested specimens are plotted in Figure 4.6, where the horizontal axis represents the end shortening δ as average value measured from both LVDTs and the vertical axis represents the applied load F . The key experimental results including the maximum recorded load $F_{u,Exp}$ and the corresponding end shortening $\delta_{u,Exp}$ are summarised in Table 4.3.

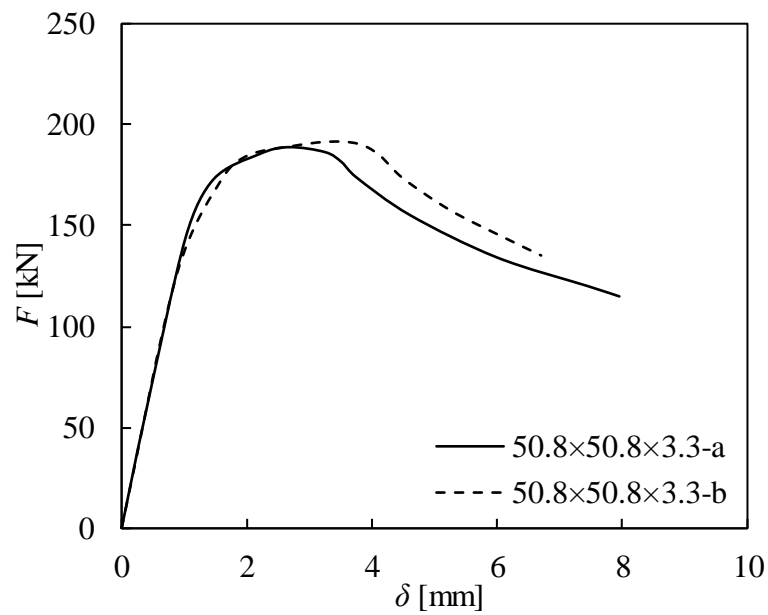
As can be seen, the initial behaviour of the BAT fix-ended stub column specimens is linear elastic. This is followed by a nonlinear elastic region up to yielding. Upon the attainment of the ultimate strength, the curves' slope decreases with increasing end shortening. The 50.8x50.8x1.6 specimen comprising the slenderest cross-section (i.e., higher B/t), exhibited its ultimate load level at the lowest δ due to local buckling failure occurrence. In specimens with stockier cross-sections (i.e., lower B/t), the delay of local buckling allowed for deformation into the strain-hardening range and the achievement of ultimate loads higher than the theoretically calculated yield load. In the case of the stockiest 50.8x50.8x4.8 specimen, the obtained ultimate load was even higher than the yield load owing to the increased cross-sectional areas arising from the Poisson' effect [211].



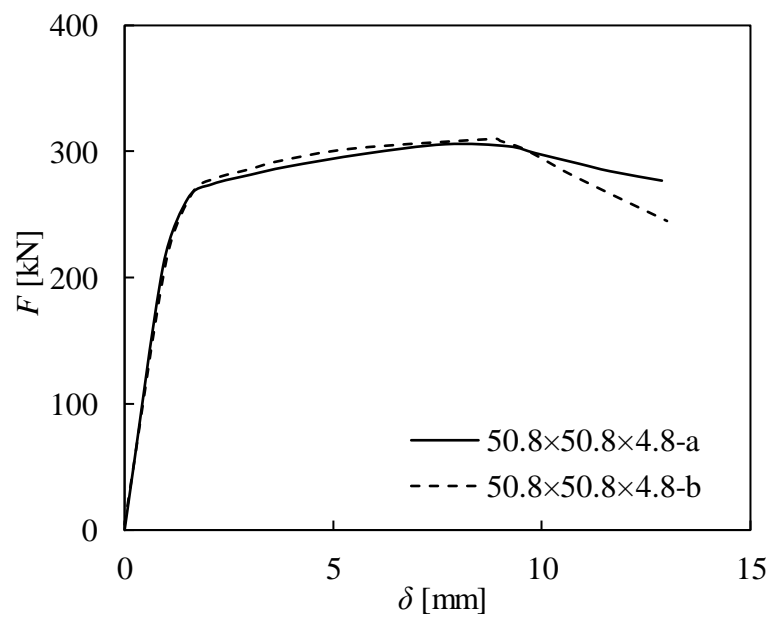
(a) 50.8x50.8x1.6



(b) 50.8x50.8x2.7



(c) 50.8x50.8x3.3



(d) 50.8x50.8x4.8

Figure 4.6: Load-end shortening curves of the BAT fix-ended stub column specimens.

Table 4.3: Results obtained from BAT fix-ended stub column tests.

Specimen	$F_{u,Exp}$ (kN)	$\delta_{u,Exp}$ (mm)
50.8×50.8×1.6-a	71.12	0.90
50.8×50.8×1.6-b	71.98	0.88
50.8×50.8×2.7-a	170.47	1.84
50.8×50.8×2.7-b	163.18	2.04
50.8×50.8×3.3-a	188.83	2.67
50.8×50.8×3.3-b	191.55	3.12
50.8×50.8×4.8-a	305.81	7.69
50.8×50.8×4.8-b	310.15	8.90

4.2.2. Concrete-filled tubular cross-sections

The cross-sections presented in Subsection 4.2.1. were also investigated infilled with concrete. Following the same procedure with the BAT fix-ended stub column specimens, the geometric dimensions of the examined specimens were measured prior to testing. Table 4.4 presents the measured dimensions for all the investigated CFAT specimens using the nomenclature depicted in Figure 4.7. The specimens were designated according to their nominal geometric dimensions and the presence of the concrete “C” infill. The designation was also followed by the letter “a” or “b” to distinguish the specimens employed in the first and repeated test, respectively. For instance, the label “50.8×50.8×3.3-C-a” defines a fix-ended stub column specimen with outer depth $D=50.8$ mm, outer width $B=50.8$ mm and thickness $t=3.3$ mm, whilst the letters “C” indicate that the specimen is infilled with concrete. Letter “a” signifies that this specimen was tested first. The average material properties were the same as those shown in Figure 4.2 and in Table 4.2. The average compressive strength $f_{ck,cube}$ of the tested cubes was 37.55 MPa. Table 4.5 summarises the compressive strength $f_{ck,cube}$ of the concrete cubes along with the corresponding standard deviation.

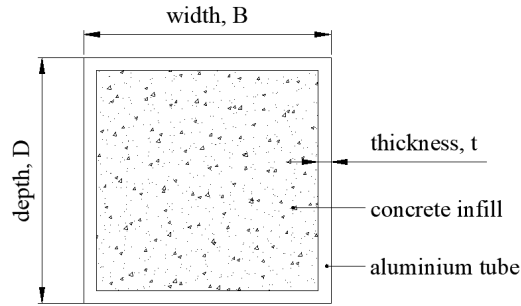


Figure 4.7: Geometric properties of the CFAT sections of the fix-ended stub columns.

Table 4.4: Mean measured geometrical dimensions of the tested CFAT fix-ended stub columns.

Specimen	D (mm)	B (mm)	t (mm)	B/t	L (mm)
50.8×50.8×1.6-C-a	50.92	50.44	1.69	29.85	152.90
50.8×50.8×1.6-C-b	50.66	50.55	1.66	30.45	152.90
50.8×50.8×2.7-C-a	51.13	51.00	2.65	19.25	152.90
50.8×50.8×2.7-C-b	51.11	50.28	2.59	19.41	152.90
50.8×50.8×3.3-C-a	50.89	50.63	3.33	15.20	152.90
50.8×50.8×3.3-C-b	50.33	50.29	3.36	14.97	152.90
50.8×50.8×4.8-C-a	51.36	50.89	4.78	10.65	152.90
50.8×50.8×4.8-C-b	51.47	51.32	4.80	10.69	152.90

Table 4.5: Measured compressive strength of concrete cubes for the CFAT fix-ended stub columns.

Specimen	$f_{ck,cube}$ (MPa)
C301	35.90
C30-2	37.59
C30-3	37.56
C30-4	39.15
mean	1.15
Standard deviation	1.14

Prior to testing, the top infill surface of the CFAT specimens was roughened with a wire brush and then was cast in plaster to fill the longitudinal gap. This practice allowed for simultaneous loading of both infill and aluminium tube. Prior to testing and similarly to their BAT counterparts, the CFAT specimens were also strengthened with carbon fibre reinforced polymer strips at both ends to prevent any localised failure. Figure 4.8 shows

a schematic illustration of the fix-ended stub column test arrangement along with the corresponding employed instrumentation, whilst Figure 4.4 illustrates a typical fix-ended stub column test set-up.

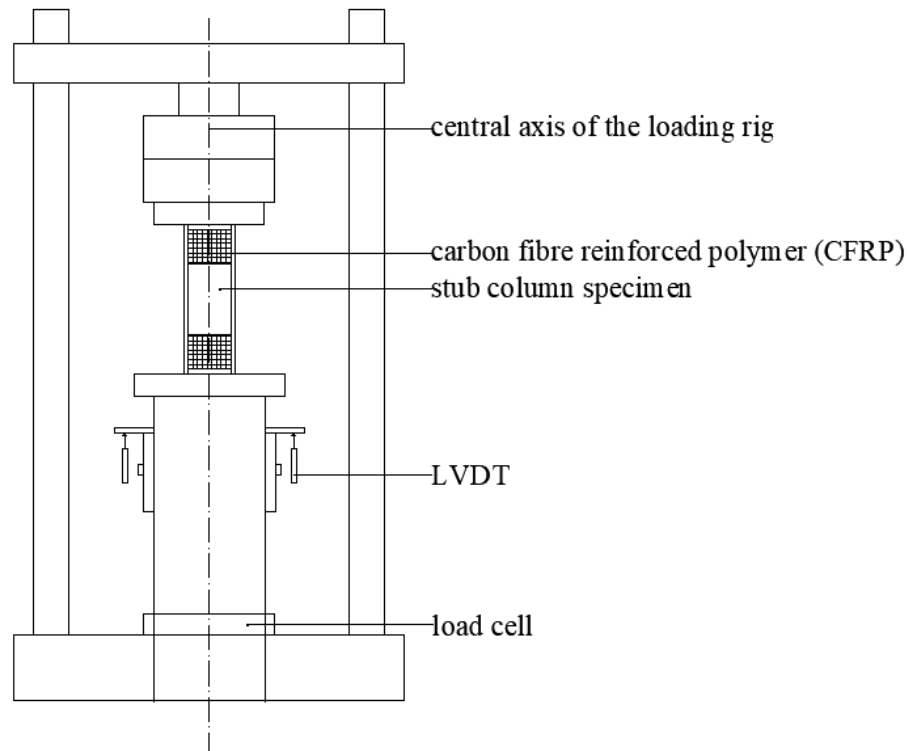


Figure 4.8: Schematic illustration of the CFAT fix-ended stub column test arrangement and instrumentation.

Similarly to BAT fix-ended stub columns, the governing failure mode for the CFAT fix-ended stub columns was local buckling. Typical failure modes are shown in Figure 4.9. It is noteworthy that for some specimens, the observed local buckling deformation was closer to specimens ends and was followed by splitting of the aluminium tube along the corner due to exceedance of the aluminium alloy's tensile fracture strain ε_f (see Figure 4.9(b)).

After the execution of the tests, the aluminium tube was removed to inspect the crack patterns of the infill. Generally, the presence of the infill delayed the occurrence of local buckling, bracing the aluminium tubes to resist the developed local transverse deformations and thus allowing for full development of aluminium alloy's plasticity. Figure 4.10 depicts the resulting crack patterns in 50.8×50.8×1.6-C-a and 50.8×50.8×4.8-

C-a specimens. For most specimens, infill crushing was mainly observed at the locations that the aluminium tube buckled, i.e., top end and mid-height, respectively. Moreover, the aluminium constituent plates were separated from the infill in the locations where buckling occurred. It is noteworthy that similar failure modes were also observed by other researchers for concrete-filled steel tubes [212-214].

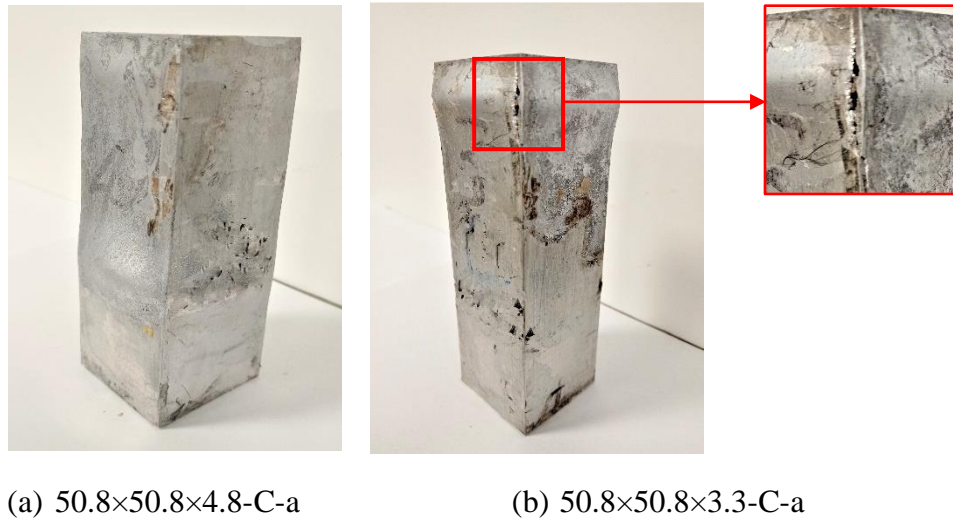


Figure 4.9: Typical failure modes of CFAT fix-ended stub column specimens.

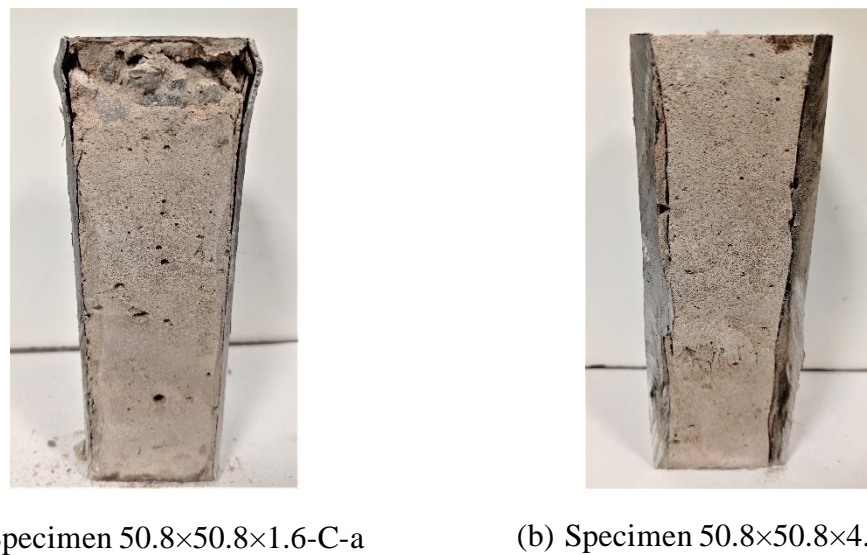
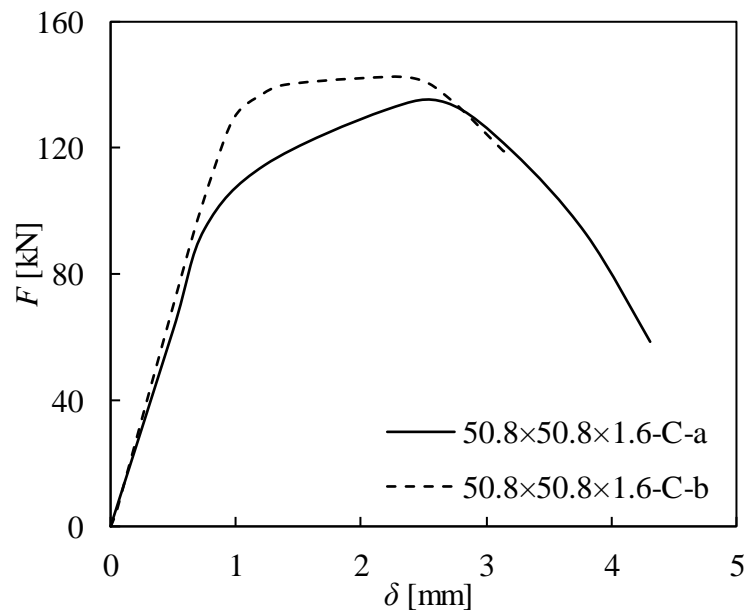


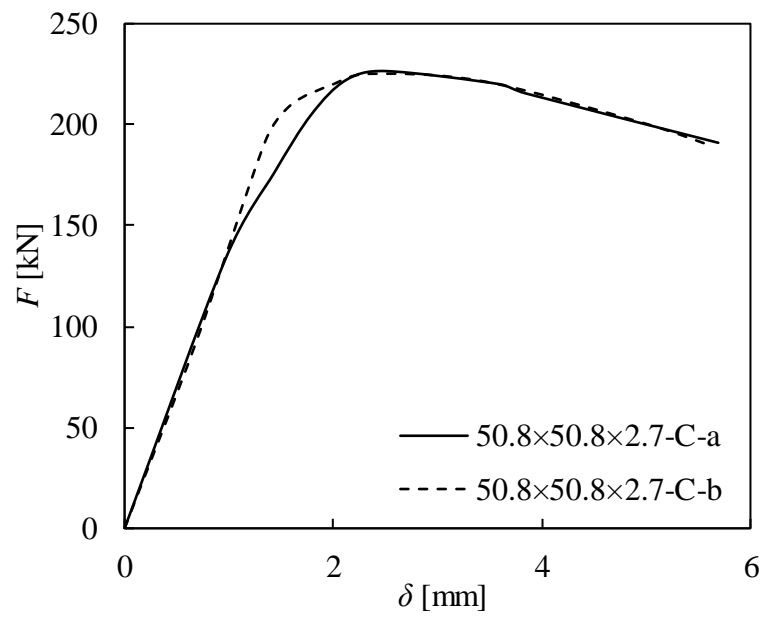
Figure 4.10: Crack patterns of the infill for typical CFAT fix-ended stub column specimens.

The obtained $F-\delta$ curves of the tested specimens are plotted in Figure 4.11. The key experimental results are summarised in Table 4.6. The cross-sectional response of both CFAT fix-ended stub column specimens was quite similar to their BAT counterparts

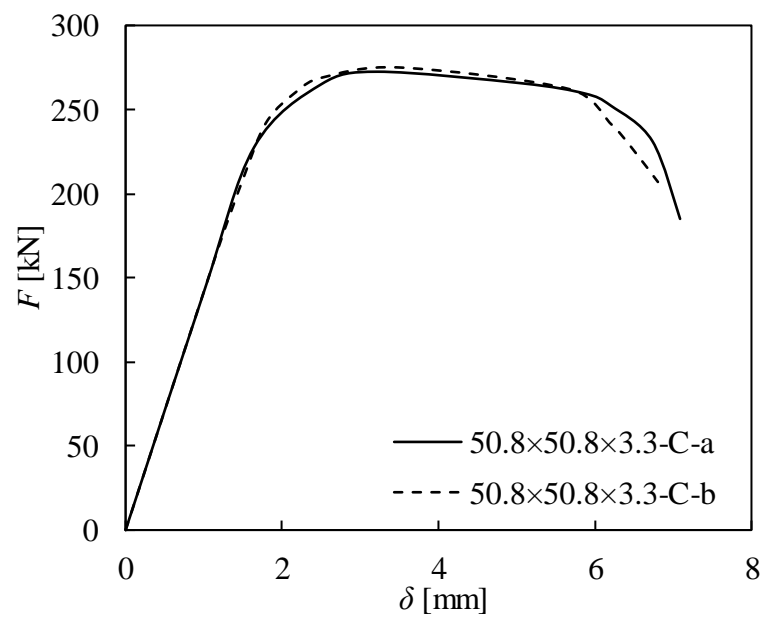
consisting of three stages. During the first stage (elastic), there is no interaction between the aluminium tube and the concrete infill and thus both components endure the applied load independently. Moreover, a small gap may appear between the aluminium tube and the concrete infill since the initial lateral expansion of the infill is smaller than that of the aluminium tube owing to the difference in Poisson's ratio of the two materials. In the following stage (elastic-plastic), as the loading increases, the lateral expansion of the infill gradually becomes greater than that of the aluminium tube until both components contact each other. That moment, interaction between the aluminium tube and the concrete develops and particularly the aluminium tube provides confining pressure to the infill. In the third stage (strain-hardening/softening), the CFAT fix-ended stub columns continue to endure loading for increasing deformation owing to the confinement effect. Similarly to BAT fix-ended stub column specimens, it can be observed that the CFAT counterparts with stockier aluminium cross-sections, exhibited higher ductility, since they failed at larger end shortening values. Moreover, specimens with thicker cross-sections exhibited quite higher elastic stiffness compared to their thinner counterparts since the slope of the initial elastic branch of the load-end-shortening curves for these specimens (with thicker cross-sections) is larger.



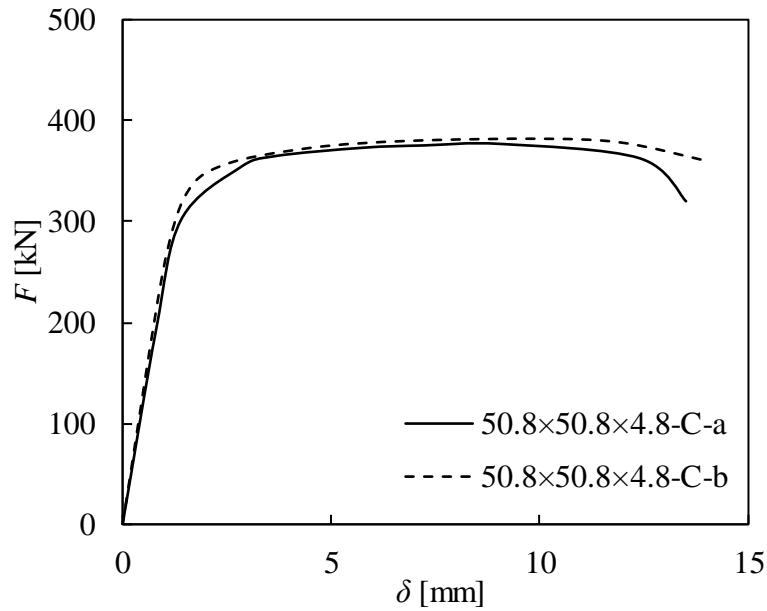
(a) 50.8x50.8x1.6-C



(b) 50.8x50.8x2.7-C



(c) 50.8x50.8x3.3-C



(d) 50.8×50.8×4.8-C

Figure 4.11: Load-end shortening curves of the CFAT fix-ended stub column specimens.

Table 4.6: Results obtained from the CFAT fix-ended stub column tests.

Specimen	$F_{u,Exp}$ (kN)	$\delta_{u,Exp}$ (mm)
50.8×50.8×1.6-C-a	134.33	2.68
50.8×50.8×1.6-C-b	142.00	2.43
50.8×50.8×2.7-C-a	226.54	2.50
50.8×50.8×2.7-C-b	225.16	2.34
50.8×50.8×3.3-C-a	272.48	3.22
50.8×50.8×3.3-C-b	275.00	3.50
50.8×50.8×4.8-C-a	375.43	9.08
50.8×50.8×4.8-C-b	382.00	10.10

4.2.3. Channel cross-sections

A series of fix-ended stub column tests was carried out employing 6 different cross-sections to study the cross-sectional behaviour of channels. Particularly, the slenderness ratio β_f/ϵ (defined in Subsection 3.3.10. was ranging from 5.46 to 11.94, whilst as mentioned in Subsection 3.2.3. the specimens' nominal length L was set equal to three times the maximum cross-sectional dimension. Figure 4.12 depicts the adopted notation for the examined C-sections. Prior to testing, the geometrical dimensions of the examined specimens were measured and are listed in Table 4.7, where D is the outer web depth.

The specimens were labelled according to the nominal geometric dimensions ($D \times B \times t-L$ where t is the nominal thickness of both web and flanges) followed by the specimen's nominal length. The measured initial local ω_l geometric imperfection amplitudes are also listed in Table 4.7. The engineering stress–strain curves ($\sigma-\varepsilon$) obtained from the tensile coupon tests for each examined cross-section are depicted in Figure 4.13 and in Table 4.8.

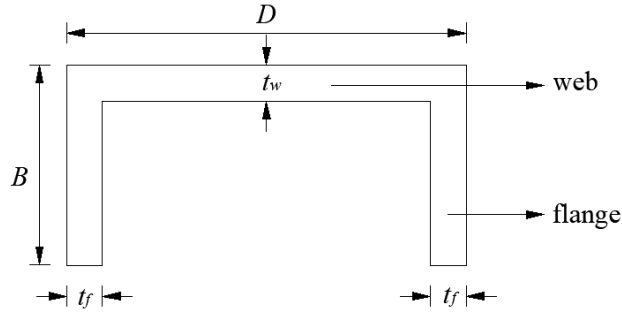


Figure 4.12: Adopted notation for the C-sections of the fix-ended stub columns.

Table 4.7: Mean measured geometrical dimensions and local geometric imperfections of the tested C-section fix-ended stub columns.

Specimen	D (mm)	B (mm)	t_w (mm)	t_f (mm)	β_f/ε	L (mm)	ω_l (mm)
50.8×50.8×6.35-L150	50.92	50.84	6.28	6.32	7.49	152.76	0.28 ($t_f/23$)
50.8×50.8×4.76-L150	50.89	50.56	4.62	4.75	10.42	152.67	0.30 ($t_f/16$)
50.8×38.1×6.35-L150	50.89	38.23	6.32	6.35	5.46	152.66	0.35 ($t_f/18$)
50.8×38.1×3.18-L150	50.81	37.75	3.13	3.13	11.94	152.42	0.26 ($t_f/12$)
50.8×25.4×3.18-L150	50.68	25.85	3.17	3.11	7.62	152.03	0.27 ($t_f/12$)
38.1×38.1×4.76-L115	37.97	37.97	4.68	4.64	7.84	113.92	0.31 ($t_f/15$)

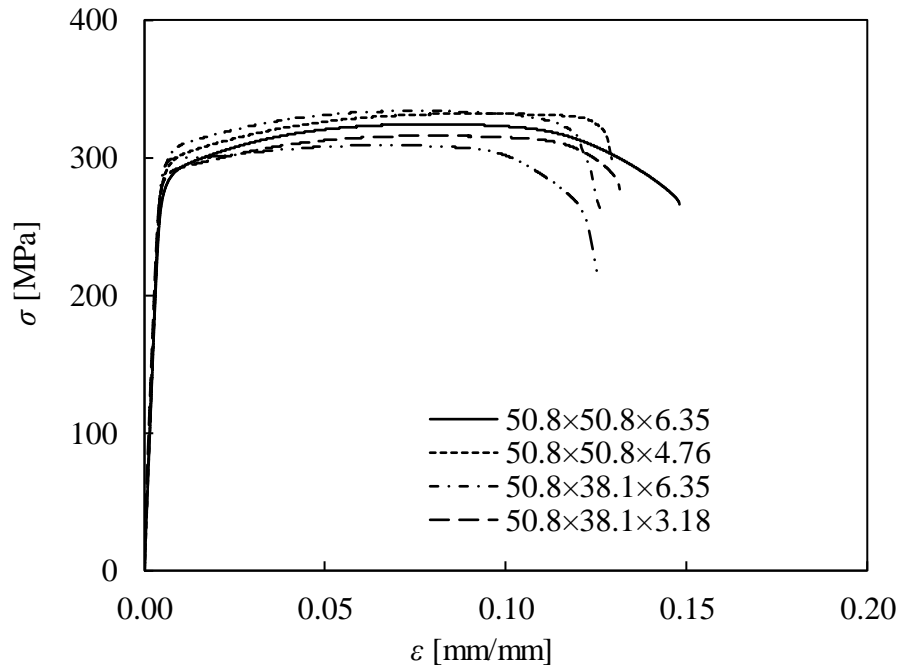


Figure 4.13: Stress-strain curves of the C-sections of the fix-ended stub columns.

Table 4.8: Material properties of C-sections obtained from tensile coupon tests.

Specimen	E (MPa)	$\sigma_{0.1}$ (MPa)	$\sigma_{0.2}$ (MPa)	σ_u (MPa)	ϵ_u (mm/mm)	ϵ_f (mm/mm)	n	$\sigma_u/\sigma_{0.2}$
50.8×50.8×6.35	66729	275	282	324	0.08	0.14	27.6	1.15
50.8×50.8×4.76	69302	284	292	332	0.09	0.13	25.0	1.14
50.8×38.1×6.35	67009	290	298	334	0.08	0.13	25.5	1.12
50.8×38.1×3.18	67500	280	287	316	0.08	0.13	28.1	1.10
50.8×25.4×3.18	66408	276	282	295	0.06	0.11	32.2	1.05
38.1×38.1×4.76	68744	290	297	309	0.07	0.13	29.1	1.04

A total of 6 fix-ended stub column tests were performed to investigate the cross-sectional response of aluminium alloy C-sections. Figure 4.14 illustrates a schematic illustration of the test arrangement and the corresponding employed instrumentation. Underpinning bolts were inserted between the flanges and G-clamps were located onto the outer faces of the flanges at both ends to prevent any localised failure [215]. The experimental setup for a typical fix-ended stub column test is depicted in Figure 4.15. Two LVDTs were located between the end plates to determine the end shortening of the fix-ended stub column. In addition, three linear electrical resistance strain gauges were affixed longitudinally at the mid-length of the specimen to measure the compressive strains.

Particularly, the two strain gauges were affixed at both flanges at 10 mm of the tip and the third one at the middle of the web, as shown in Figure 4.15.

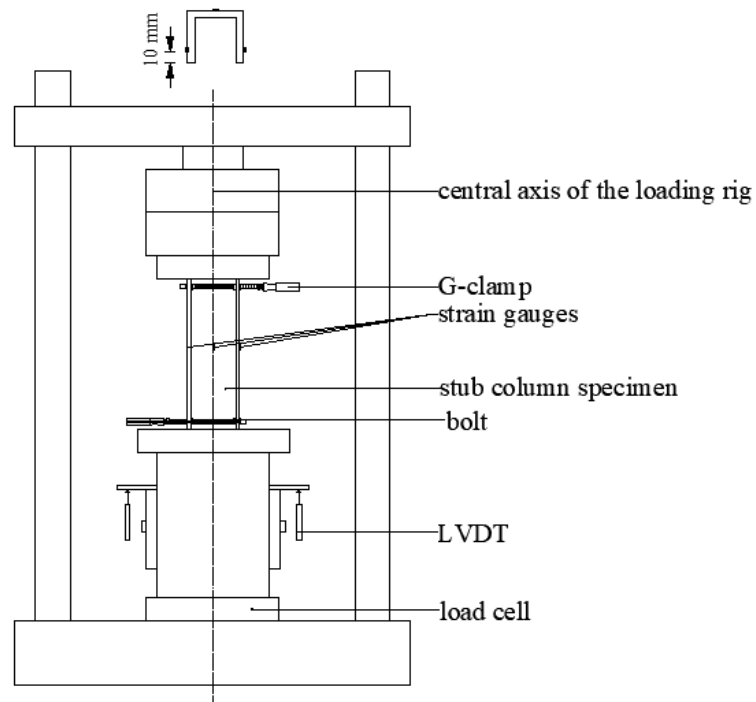


Figure 4.14: Schematic illustration of the fix-ended stub column test arrangement and instrumentation.

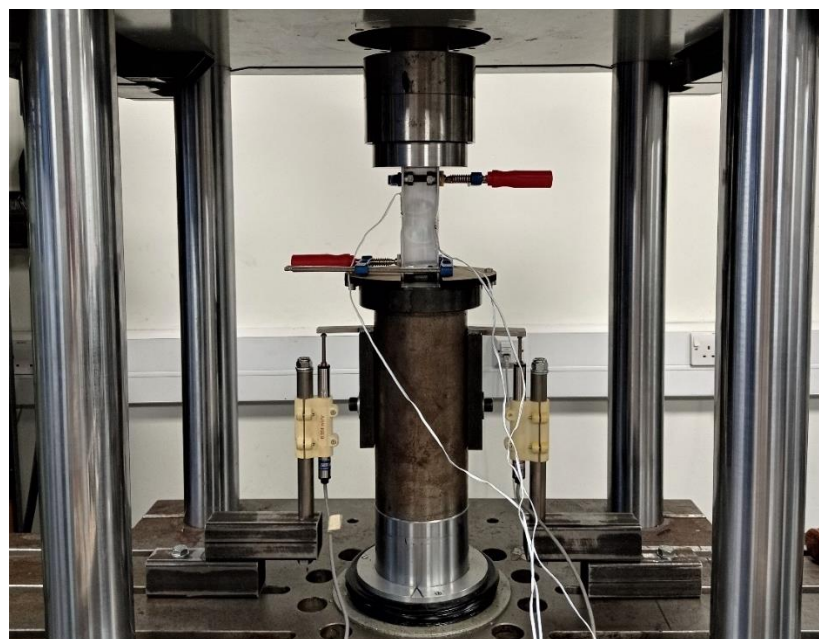


Figure 4.15: Typical fix-ended stub column test setup.

The F - δ for all tested C-section fix-ended stub column specimens are depicted in Figure 4.16, whilst the key tests results are summarised in Table 4.9. All C-section fix-ended stub column specimens failed due to local buckling with a classic “in-out” deformation mode at the mid-length, as displayed in Figure 4.17.

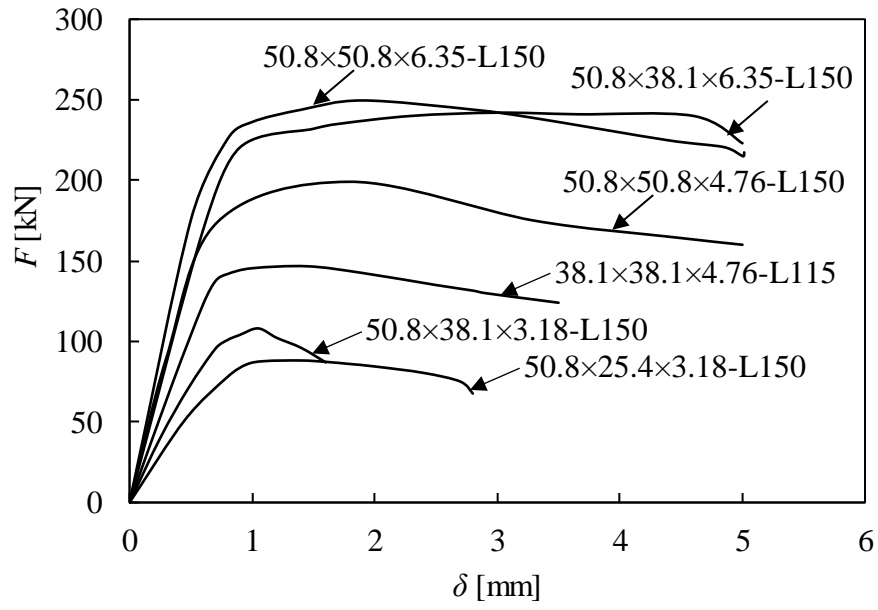


Figure 4.16: Load-end shortening curves obtained from C-section fix-ended stub column tests.

Table 4.9: Summary of key results obtained from C-section fix-ended stub column tests.

Specimen	$F_{u,Exp}$ (kN)	$\delta_{u,Exp}$ (mm)
50.8×50.8×6.35-L150	249.57	1.90
50.8×50.8×4.76-L150	199.10	1.80
50.8×38.1×6.35-L150	242.00	3.00
50.8×38.1×3.18-L150	108.07	1.05
50.8×25.4×3.18-L150	88.15	1.40
38.1×38.1×4.76-L115	146.65	1.45



Figure 4.17: Failure modes obtained from C-section fix-ended stub column tests.

4.3. Pin-ended columns

4.3.1. Bare tubular cross-sections

A total of 8 tests were carried out to examine the buckling response of BAT columns. All specimens were made of 6082-T6 heat-treated aluminium alloy and had pin-ended boundary conditions allowing rotation about the minor axis. The specimens comprised rectangular and square tubes as shown in Figure 4.18 and had a nominal length L of 1 m. The mean measured geometric dimensions of the specimens are summarised in Table 4.10, where D , B , t are the cross-sectional depth, width and thickness, respectively and the D/B the cross-sectional aspect ratio. The specimen designation is defined according to the cross-sectional dimensions and the presence of concrete infill. For example, the label “50.8×50.8×1.6” indicates a pin-ended column specimen with nominal depth of 50.8 mm, nominal width of 50.8 mm and nominal thickness of 1.6 mm. The member slenderness $\bar{\lambda}$ according to EN 1999-1-1 [5] (defined in Subsection 3.3.10) ranged from 0.76 to 1.39. The measured initial global ω_g and local ω_l geometric imperfection amplitudes are listed in Table 4.11. The engineering stress–strain curves (σ – ε) are depicted in Figure 4.19 and the average measured material properties are listed in Table 4.12.

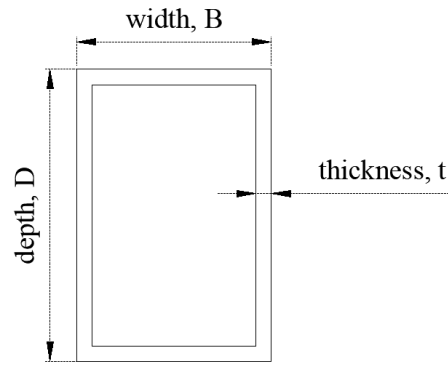


Figure 4.18: Geometric properties of the BAT sections of the pin-ended columns.

Table 4.10: Mean measured geometrical dimensions of the tested BAT pin-ended columns.

Specimen	D (mm)	B (mm)	t (mm)	D/B	L (mm)
50.8×50.8×1.6	50.68	51.00	1.61	0.99	1000.00
50.8×50.8×3.3	50.59	50.62	3.13	1.00	999.00
50.8×50.8×4.8	50.58	50.62	4.67	1.00	1000.00
76.2×76.2×3.3	76.38	76.43	3.23	1.00	1000.00
76.2×76.2×4.8	76.22	76.06	4.76	1.00	1000.00
76.2×76.2×6.4	76.31	76.27	6.28	1.00	1000.00
76.2×38.1×3.3	76.23	38.22	3.27	1.99	1000.00
76.2×50.8×3.3	76.14	50.73	3.18	1.50	1000.00

Table 4.11: Mean measured geometric imperfections of the tested BAT pin-ended columns.

Specimen	ω_g (mm)	ω_l (mm)
50.8×50.8×1.6	0.03 ($L_e/33333$)	0.11 ($t/15$)
50.8×50.8×3.3	0.04 ($L_e/24975$)	0.17 ($t/18$)
50.8×50.8×4.8	0.01 ($L_e/100000$)	0.19 ($t/25$)
76.2×76.2×3.3	0.19 ($L_e/5263$)	0.31 ($t/10$)
76.2×76.2×4.8	0.05 ($L_e/20000$)	0.08 ($t/60$)
76.2×76.2×6.4	0.04 ($L_e/25000$)	0.18 ($t/35$)
76.2×38.1×3.3	0.02 ($L_e/50000$)	0.06 ($t/55$)
76.2×50.8×3.3	0.42 ($L_e/2381$)	0.68 ($t/5$)

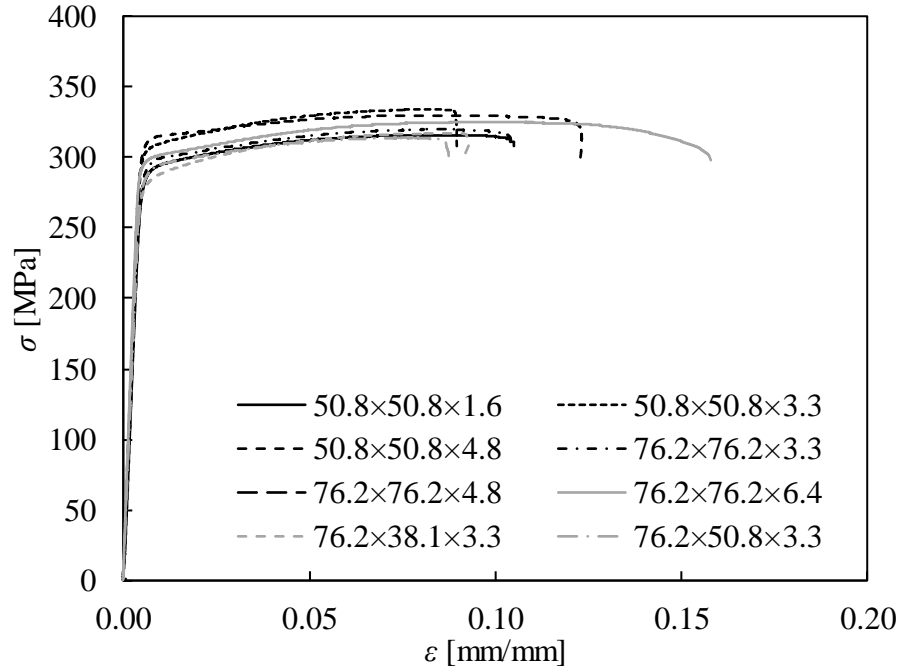


Figure 4.19: Stress-strain curves of the BAT/CFAT sections of the pin-ended columns.

Table 4.12: Material properties of BAT/CFAT sections obtained from tensile coupon tests.

Specimen	E (MPa)	$\sigma_{0.1}$ (MPa)	$\sigma_{0.2}$ (MPa)	σ_u (MPa)	ϵ_u (mm/mm)	ϵ_f (mm/mm)	n	$\sigma_u/\sigma_{0.2}$
50.8×50.8×1.6	65000	284	289	315	0.08	0.11	42.3	1.09
50.8×50.8×3.3	71700	298	302	330	0.08	0.09	44.2	1.09
50.8×50.8×4.8	67500	303	306	325	0.09	0.16	68.1	1.06
76.2×76.2×3.3	66200	295	299	321	0.08	0.11	52.8	1.07
76.2×76.2×4.8	64700	304	306	316	0.06	0.10	88.1	1.03
76.2×76.2×6.4	69300	290	295	326	0.09	0.15	41.4	1.10
76.2×38.1×3.3	68500	270	277	315	0.08	0.09	29.6	1.14
76.2×50.8×3.3	67500	286	290	312	0.07	0.09	55.4	1.08

In line with similar studies [140,142,143] the BAT specimens ends, prior to testing, were also strengthened with CFRP strips at both ends to prevent any localised failure. Figure 4.20 shows a schematic illustration of the BAT pin-ended column test arrangement along with the corresponding employed instrumentation, whilst Figure 4.21 illustrates a typical BAT pin-ended column test set-up. It is noteworthy that at initial loading stage, the readings taken from the LVDTs and strain gauges for each specimen were utilised to calculate the combined equivalent global imperfection and applied eccentricity e_m which

is defined as the sum of the measured initial global geometric imperfection amplitude ω_g and the actual initial load eccentricity e_0 and is given as follows [189,216].

$$e_m = e_0 + \omega_g = \frac{EI(\varepsilon_{max} - \varepsilon_{min})}{hF_0} - \Delta \quad (4.1)$$

where EI is the flexural rigidity of the cross-section about the minor axis, ε_{max} is the maximum recorded compressive strain, ε_{min} is the maximum recorded tensile or minimum recorded compressive strain, h is the distance between the strain gauges attached on the web and flange, F_0 is the applied initial compressive load approximately equal to 15% of the predicted load-carrying capacity and Δ is the lateral deflection at the mid-height.

On the basis of similar studies, the F_0 value [189,217,218] was deemed adequate to ensure that the specimen's behaviour remains into the elastic range providing reliable lateral deflection and strain measurements. In case that the absolute value of the combined equivalent global imperfection and applied eccentricity $|e_m|$ exceeded the value of $L_e/1000$, the specimen's position was carefully re-adjusted to achieve $|e_m| \leq L_e/1000$ [189,219].

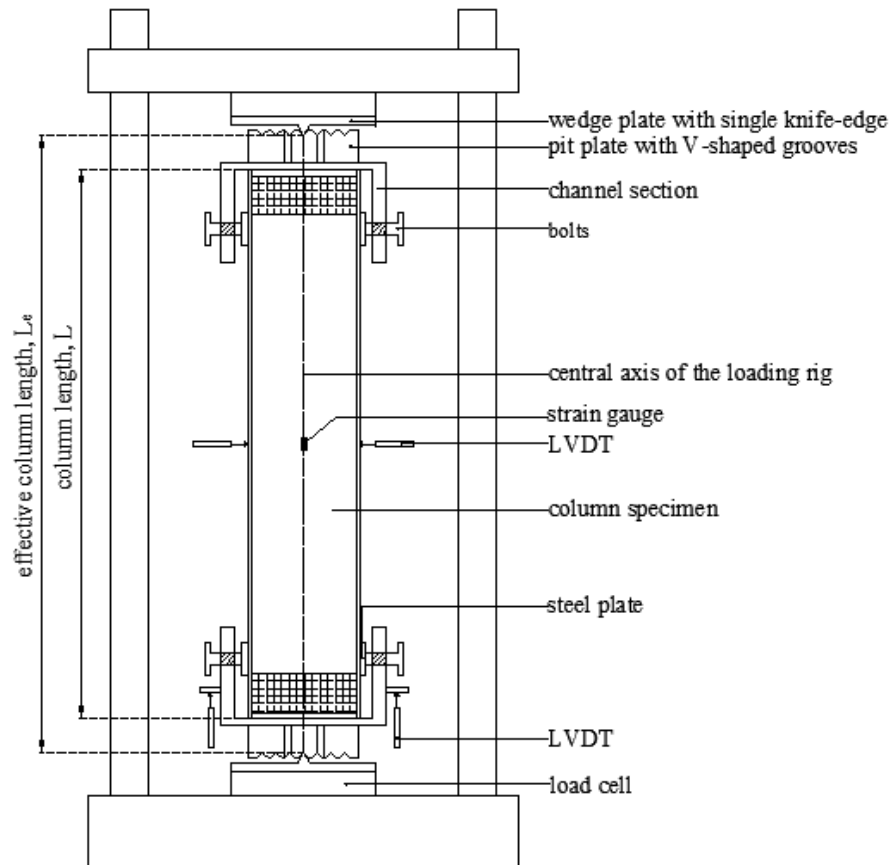


Figure 4.20: Schematic illustration of the BAT pin-ended column test arrangement and instrumentation.



Figure 4.21: Typical BAT/CFAT pin-ended column test set-up.

As expected, the knife-edges allowed rotation about the minor axis and thus all BAT columns failed due to flexural buckling about this axis. This was also confirmed by the out-of-plane strain gauge values that indicated negligible out-of-plane deformations. Figure 4.22 shows the load–mid-height lateral deflection curves for the 8 tested specimens. A typical flexural buckling mode is shown in Figure 4.23(a). In addition to the flexural buckling mode, upon the attainment of their ultimate load, the BAT specimens $50.8 \times 50.8 \times 1.6$ and $76.2 \times 76.2 \times 3.3$ with the most slender constituent plate elements also experienced local buckling at mid-height, as shown in Figure 4.23(b). Table 4.13 presents the obtained key test results including the ultimate loads $F_{u,Exp}$ and the lateral deflections at the mid-height corresponding to the ultimate loads Δ_u . The cross-sectional slenderness ratio β/ε of the web along with the member slenderness $\bar{\lambda}$ calculated according to [5] are also included in Table 4.13.

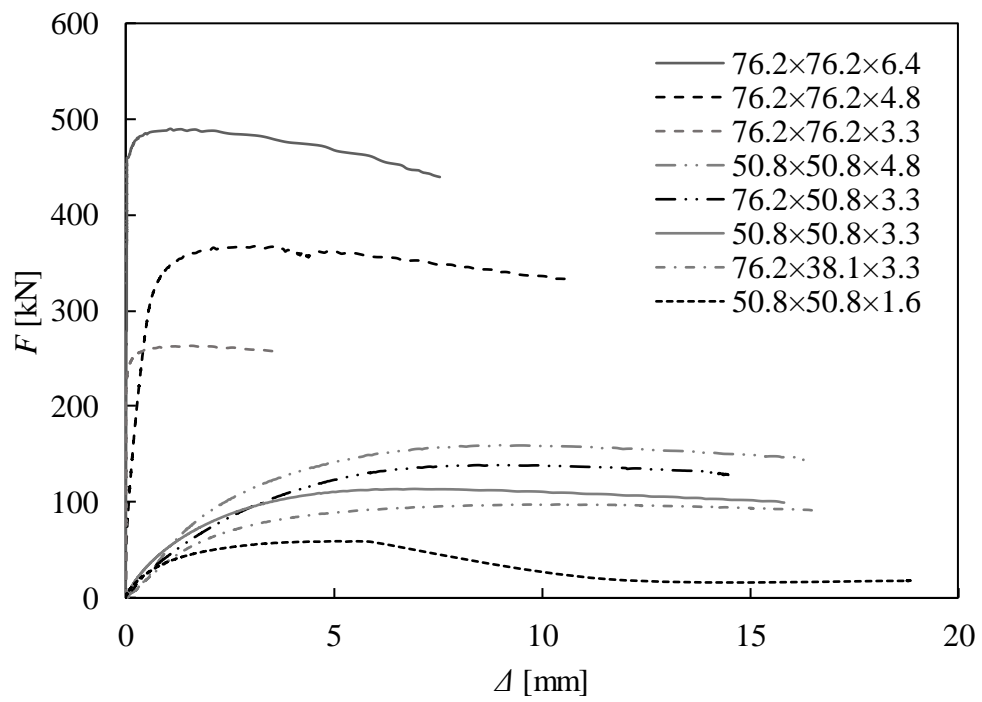


Figure 4.22: Load–mid-height lateral deflection curves obtained from BAT pin-ended column tests.

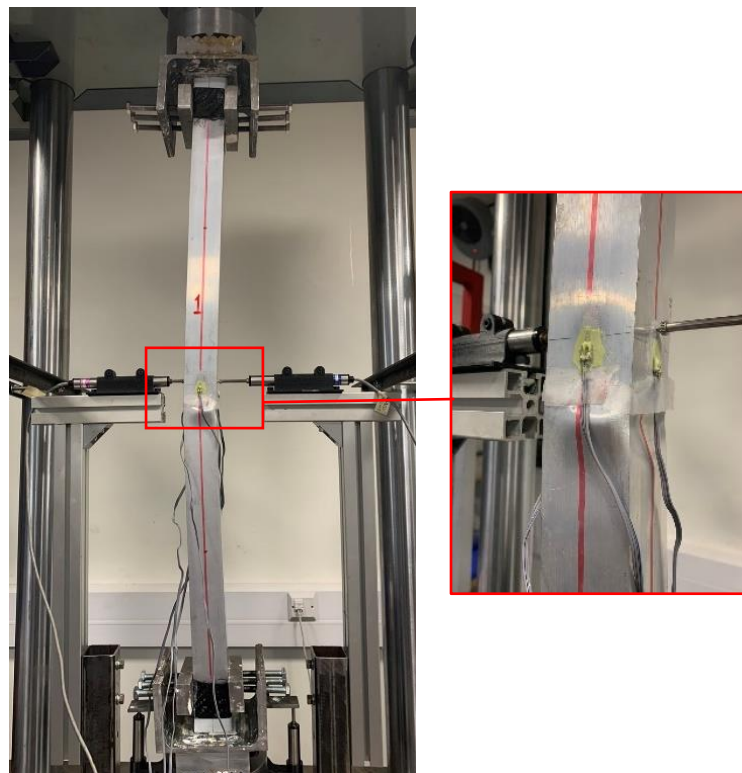


Figure 4.23: Obtained failure mode for 50.8×50.8×1.6 specimen.

Table 4.13: Key results obtained from BAT fix-ended column tests.

Specimen	$F_{u,Exp}$ (kN)	Δ_u (mm)	β/ε	$\bar{\lambda}$
50.8×50.8×1.6	60.22	5.10	34.06	1.11
50.8×50.8×3.3	113.83	6.95	17.77	1.13
50.8×50.8×4.8	161.48	8.98	11.99	1.21
76.2×76.2×3.3	263.28	1.59	25.87	0.76
76.2×76.2×4.8	367.36	3.15	17.69	0.80
76.2×76.2×6.4	489.85	1.38	13.20	0.76
76.2×38.1×3.3	97.62	10.50	12.29	1.39
76.2×50.8×3.3	138.72	8.88	17.16	1.09

4.3.2. Concrete-filled tubular cross-sections

The cross-sections presented in Subsection 4.3.1. were also investigated infilled with concrete. Following the same procedure with the BAT pin-ended column specimens, the geometric dimensions of the examined specimens were measured prior to testing. A total of 8 tests were carried out to examine the buckling response of CFAT pin-ended columns. Table 4.14 presents the measured dimensions for all the investigated CFAT pin-ended column specimens using the nomenclature depicted in Figure 4.24. All specimens had a nominal length L of 1 m. The specimen designation is defined according to the cross-sectional dimensions and the presence of concrete infill. For example, the label “50.8×50.8×1.6-C” indicates a column with nominal depth of 50.8 mm, nominal width of 50.8 mm and nominal thickness of 1.6 mm. The last letter “C” of the column label denotes the presence of concrete infill. The member slenderness $\bar{\lambda}$ as per EN 1999-1-1 [5] ranged from 0.70 to 1.38. The measured initial global ω_g and local ω_l geometric imperfection amplitudes are listed in Table 4.15. The engineering stress-strain curves (σ - ε) are presented in Figure 4.19 and the average measured material properties are listed in Table 4.12. The average compressive strength $f_{ck,cube}$ of the tested cubes was 31.57 MPa. Table 4.16 summarises the compressive strength $f_{ck,cube}$ of the concrete cubes along with the corresponding standard deviation.

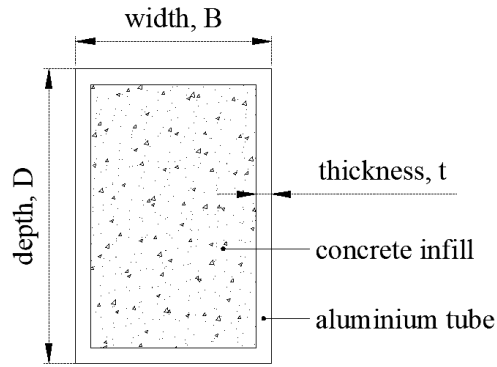


Figure 4.24: Geometric properties of the CFAT sections of the pin-ended columns.

Table 4.14: Mean measured geometrical dimensions of the tested CFAT pin-ended columns.

Specimen	D (mm)	B (mm)	t (mm)	D/B	L (mm)
50.8×50.8×1.6-C	50.72	51.04	1.61	0.99	1001.00
50.8×50.8×3.3-C	50.61	50.59	3.13	1.00	1000.60
50.8×50.8×4.8-C	50.60	50.58	4.67	1.00	999.90
76.2×76.2×3.3-C	76.40	76.42	3.23	1.00	1000.90
76.2×76.2×4.8-C	76.21	76.11	4.76	1.00	1001.00
76.2×76.2×6.4-C	76.28	76.31	6.28	1.00	1000.80
76.2×38.1×3.3-C	76.17	38.22	3.27	1.99	1001.00
76.2×50.8×3.3-C	76.11	50.68	3.18	1.50	1000.50

Table 4.15: Mean measured geometric imperfections of the tested CFAT pin-ended columns.

Specimen	ω_g (mm)	ω_l (mm)
50.8×50.8×1.6-C	0.09 ($L_e/11122$)	0.28 ($t/6$)
50.8×50.8×3.3-C	0.11 ($L_e/9096$)	0.96 ($t/3$)
50.8×50.8×4.8-C	0.08 ($L_e/12499$)	0.14 ($t/33$)
76.2×76.2×3.3-C	0.06 ($L_e/16682$)	0.80 ($t/4$)
76.2×76.2×4.8-C	0.13 ($L_e/7700$)	0.72 ($t/7$)
76.2×76.2×6.4-C	0.07 ($L_e/14297$)	0.19 ($t/33$)
76.2×38.1×3.3-C	0.18 ($L_e/5561$)	0.49 ($t/7$)
76.2×50.8×3.3-C	0.11 ($L_e/9095$)	0.38 ($t/8$)

Table 4.16: Measured compressive strength of concrete cubes for the CFAT pin-ended columns.

Specimen	$f_{ck,cube}$ (MPa)
C25-1	32.81
C25-2	32.36
C25-3	31.22
C25-4	29.87
mean	31.57
Standard deviation	1.14

Prior to testing, the top infill surface of the CFAT specimens was roughened with a wire brush and then was cast in plaster to fill the longitudinal gap. This practice allowed for simultaneous loading of both infill and aluminium tube. Prior to testing and similarly to their BAT counterparts, the CFAT specimens were also strengthened with CFRP strips at both ends to prevent any localised failure. Following the same experimental procedure with BAT pin-ended columns (see Subsection 4.3.1.) in case that the absolute value of the combined equivalent global imperfection and applied eccentricity $|e_m|$ exceeded the value of $L_e/1000$, the specimen's position was carefully re-adjusted to achieve $|e_m| \leq L_e/1000$ [189,219]. Figure 4.25 shows a schematic illustration of the CFAT pin-ended column test arrangement along with the corresponding employed instrumentation, whilst Figure 4.21 illustrates a typical CFAT pin-ended column test set-up.

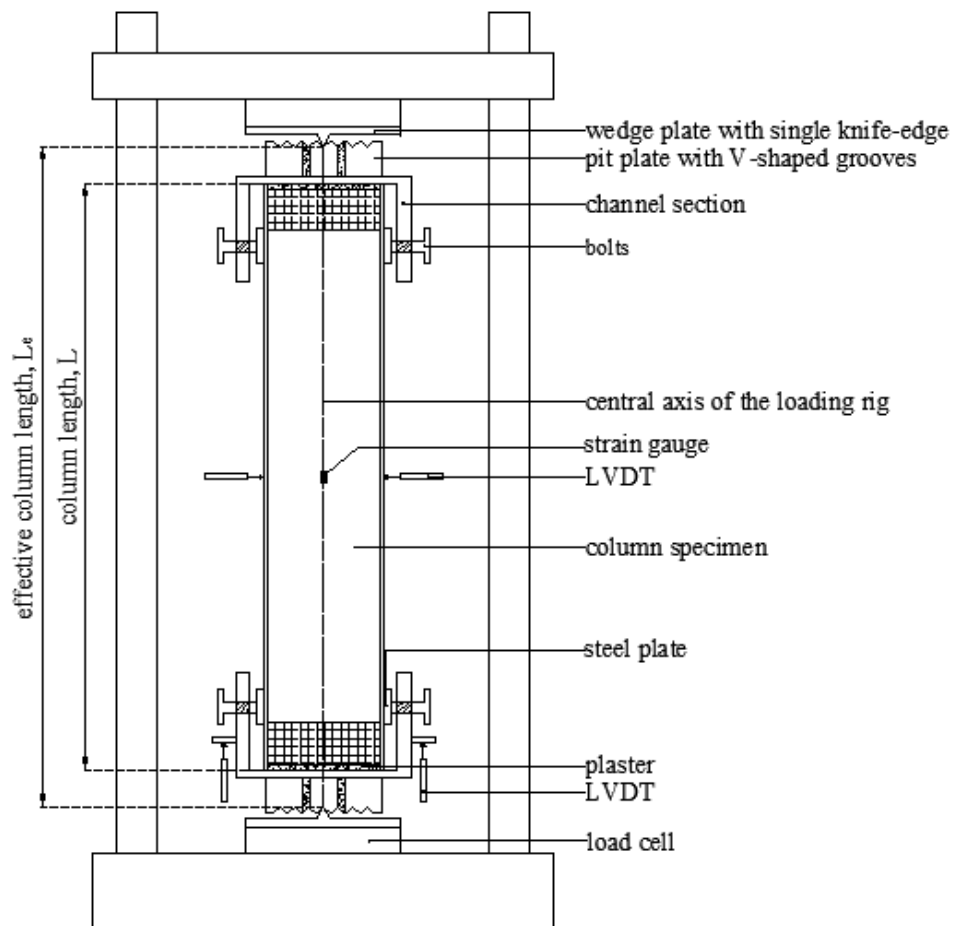


Figure 4.25: Schematic illustration of the CFAT pin-ended column test arrangement and instrumentation.

Similarly to their BAT counterparts, the CFAT columns failed due to flexural buckling about the minor axis. This was also confirmed by the out-of-plane strain gauge values that indicated negligible out-of-plane deformations. Figure 4.26 shows the load–mid-height lateral deflection curves for the 8 tested specimens. A typical flexural buckling mode is shown in Figure 4.27. Table 4.17 presents the obtained key test results. The cross-sectional slenderness ratio β/ϵ of the web along with the member slenderness $\bar{\lambda}$ calculated according to [5] are also included in Table 4.17.

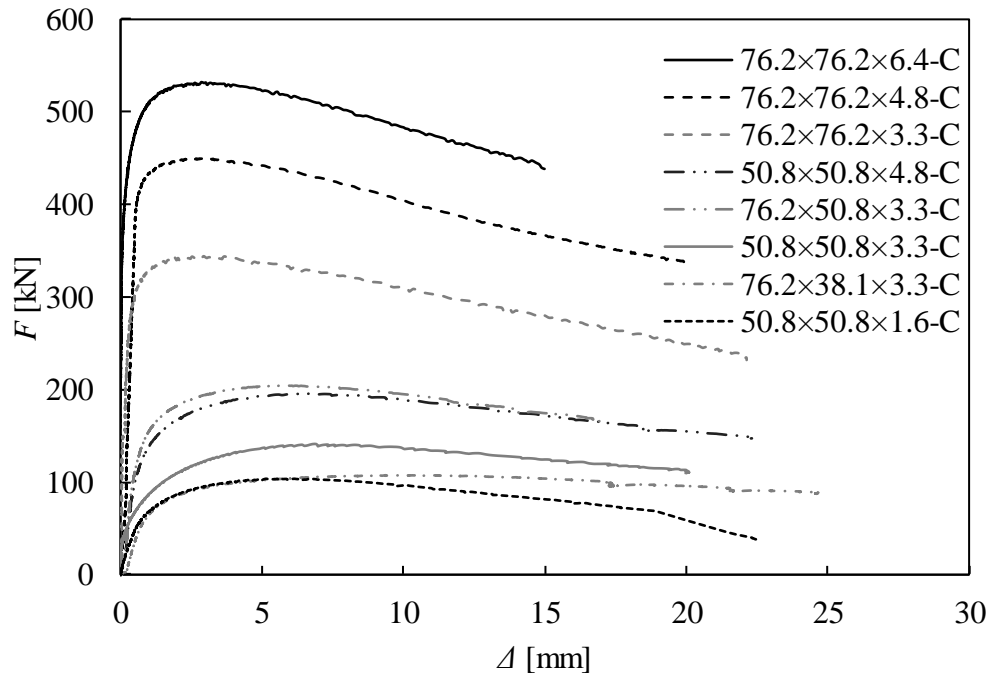


Figure 4.26: Load–mid-height lateral deflection curves obtained from CFAT pin-ended column tests.



Figure 4.27: Obtained failure mode for 76.2×38.1×3.3-C specimen.

Table 4.17: Key results obtained from CFAT pin-ended column tests.

Specimen	$F_{u,Exp}$ (kN)	Δ_u (mm)	β/ϵ	$\bar{\lambda}$
50.8×50.8×1.6-C	103.71	6.69	34.06	0.98
50.8×50.8×3.3-C	141.18	6.91	17.77	1.09
50.8×50.8×4.8-C	195.77	6.76	11.99	1.18
76.2×76.2×3.3-C	344.07	2.94	25.87	0.70
76.2×76.2×4.8-C	449.68	2.89	17.69	0.76
76.2×76.2×6.4-C	532.08	2.88	13.20	0.75
76.2×38.1×3.3-C	107.47	10.10	12.29	1.38
76.2×50.8×3.3-C	204.27	5.54	17.16	1.05

4.3.3. Channel cross-sections

A series of pin-ended column tests was carried out employing 5 different cross-sections to study the buckling behaviour of channels. Figure 4.28 depicts the adopted notation for the examined C-sections. The tests were carried out on columns in 2 different nominal lengths L , namely 300 mm and 500 mm. These lengths allowed to cover a broad range of member slendernesses $\bar{\lambda}$ as per EN 1999-1-1 [5] from 0.22-1.32. Prior to testing, the geometrical dimensions of the examined specimens were measured and are listed in Table 4.18, where D is the outer web depth. The specimens were labelled according to the nominal geometric dimensions ($D \times B \times t-L$ where t is the nominal thickness of both web and flanges) followed by the specimen's nominal length. The measured initial global ω_g and local ω_l geometric imperfection amplitudes are listed in Table 4.19. Note that the measured ω_g was considered as positive if the column specimen initially bows towards the web and negative if the column specimen initially bows towards the flange tips, as displayed in Figure 4.29. Table 4.18 also reports the effective column length values L_e and the applied eccentricities values (e_o, e_m). The engineering stress–strain curves (σ – ϵ) obtained from the tensile coupon tests for each examined cross-section are depicted in Figure 4.30. Moreover, the average measured material properties are listed in Table 4.20.

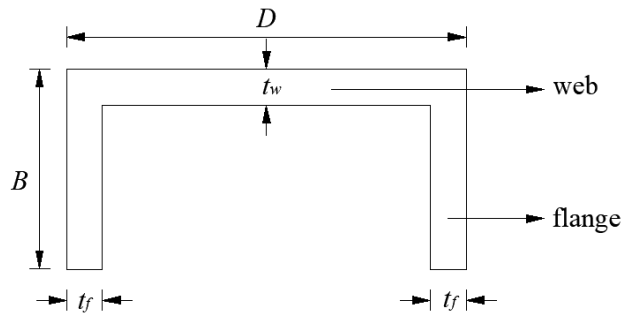


Figure 4.28: Adopted notation for the C-sections of the pin-ended columns.

Table 4.18: Mean measured geometrical dimensions of the tested C-section pin-ended columns.

Specimen	D (mm)	B (mm)	t_w (mm)	t_f (mm)	L (mm)	L_e (mm)	$\bar{\lambda}$
50.8×50.8×6.35-L500	50.92	50.84	6.35	6.32	500.50	564.50	0.63
76.2×76.2×6.35-L500	76.28	76.26	6.17	6.29	500.00	564.00	0.36
76.2×76.2×6.35-L300	76.28	76.26	6.19	6.29	300.80	364.80	0.22
50.8×38.1×6.35-L500	50.89	38.13	6.30	6.35	500.00	564.00	0.90

50.8×38.1×3.18-L500	50.81	37.95	3.08	3.13	500.50	564.50	0.79
50.8×38.1×3.18-L300	50.81	37.95	3.08	3.13	300.00	364.00	0.48
50.8×25.4×3.18-L500	50.68	25.43	3.14	3.11	500.00	564.00	1.32
50.8×25.4×3.18-L300	50.68	25.43	3.15	3.11	300.30	364.30	0.79

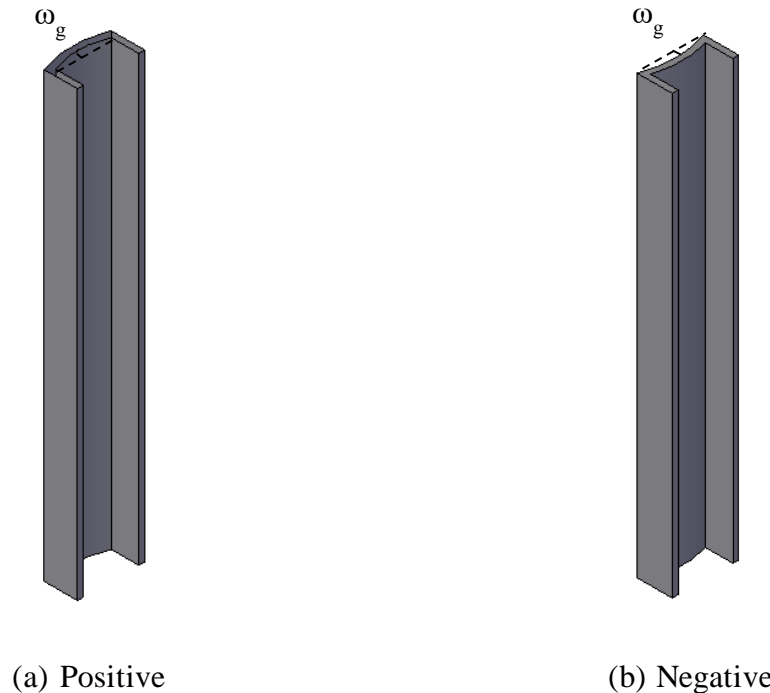


Figure 4.29: Sign convention for measured initial global geometric imperfection amplitude ω_g of C-section pin-ended columns.

Table 4.19: Mean measured geometric imperfections of the tested C-section pin-ended columns.

Specimen	ω_g (mm)	ω_l (mm)	e_0 (mm)	$e_m = \omega_g + e_0$ (mm)
50.8×50.8×6.35-L500	-0.05 ($-L_e/11290$)	0.27 ($t_f/23$)	-0.21 ($-L_e/2688$)	-0.26 ($-L_e/2171$)
76.2×76.2×6.35-L500	0.11 ($L_e/5127$)	0.33 ($t_f/19$)	0.32 ($L_e/1763$)	0.43 ($L_e/1312$)
76.2×76.2×6.35-L300	0.09 ($L_e/4053$)	0.22 ($t_f/29$)	0.26 ($L_e/1403$)	0.35 ($L_e/1042$)
50.8×38.1×6.35-L500	0.13 ($L_e/4338$)	0.20 ($t_f/32$)	0.32 ($L_e/1763$)	0.45 ($L_e/1253$)
50.8×38.1×3.18-L500	0.08 ($L_e/7056$)	0.24 ($t_f/13$)	0.17 ($L_e/3321$)	0.25 ($L_e/2258$)
50.8×38.1×3.18-L300	0.04 ($L_e/9100$)	0.18 ($t_f/17$)	0.28 ($L_e/1300$)	0.32 ($L_e/1138$)
50.8×25.4×3.18-L500	0.07 ($L_e/8057$)	0.22 ($t_f/14$)	0.20 ($L_e/2820$)	0.27 ($L_e/2089$)
50.8×25.4×3.18-L300	0.06 ($L_e/6072$)	0.26 ($t_f/12$)	0.19 ($L_e/1917$)	0.25 ($L_e/1457$)

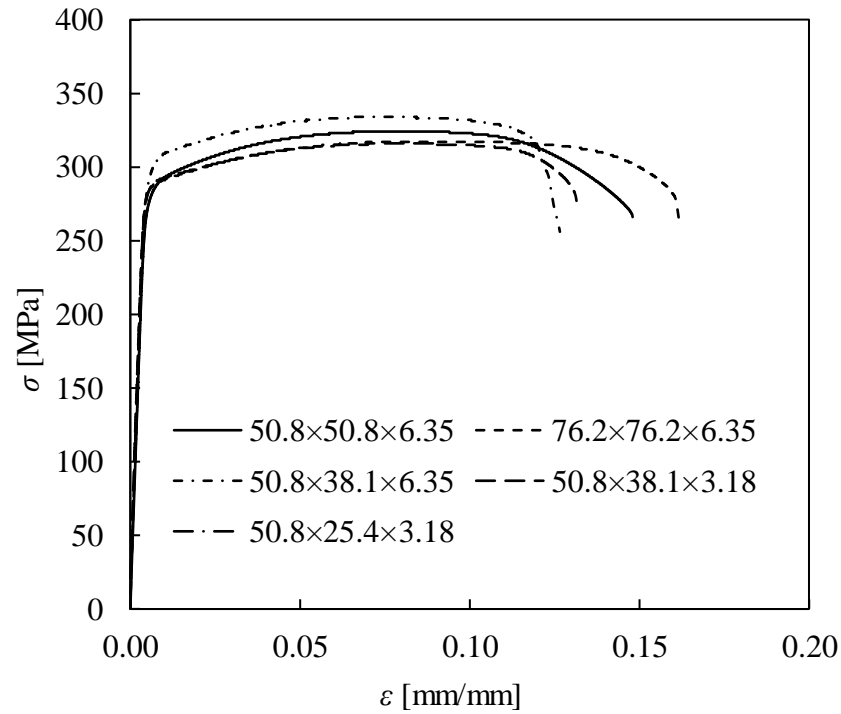


Figure 4.30: Stress-strain curves of the C-sections of the pin-ended columns.

Table 4.20: Material properties of C-sections obtained from tensile coupon tests.

Specimen	E (MPa)	$\sigma_{0.1}$ (MPa)	$\sigma_{0.2}$ (MPa)	σ_u (MPa)	ϵ_u (mm/mm)	ϵ_f (mm/mm)	n	$\sigma_u/\sigma_{0.2}$
50.8×50.8×6.35	66729	275	282	324	0.08	0.14	27.6	1.15
76.2×76.2×6.35	70885	280	286	317	0.09	0.16	32.7	1.11
50.8×38.1×6.35	67009	290	298	334	0.08	0.13	25.5	1.12
50.8×38.1×3.18	67500	280	287	316	0.08	0.13	28.1	1.10
50.8×25.4×3.18	66408	276	282	295	0.06	0.11	32.2	1.05

A total of 8 C-section columns were subjected to concentric compression under pin-ended support conditions following the methodology described in Subsection 3.2.4. Figure 4.31 illustrates a schematic diagram of the pin-ended column test arrangement and the corresponding employed instrumentation. Moreover, Figure 4.32 depicts the experimental setup for a typical pin-ended column test. Three strain gauges were also attached longitudinally at the mid-length to measure the compressive strains. Particularly, the two strain gauges were affixed at both flanges at 10 mm of the tip and the third one at the middle of the web, as shown in Figure 4.31. Note that the e_0 value was taken as positive whether the knife-edge wedges are located closer to the flange tips (resulting

initial moments lead the specimen to bow towards the web), whilst they are negative whether the knife-edge wedges are located closer to the web (resulting initial moments lead the specimen to bow towards the flange tips), as shown in Figure 4.33. Following the same experimental procedure with BAT pin-ended columns (see Subsection 4.3.1.) in case that the absolute value of the combined equivalent global imperfection and applied eccentricity $|e_m|$ exceeded the value of $L_e/1000$, the specimen's position was carefully re-adjusted to achieve $|e_m| \leq L_e/1000$ [189,219].

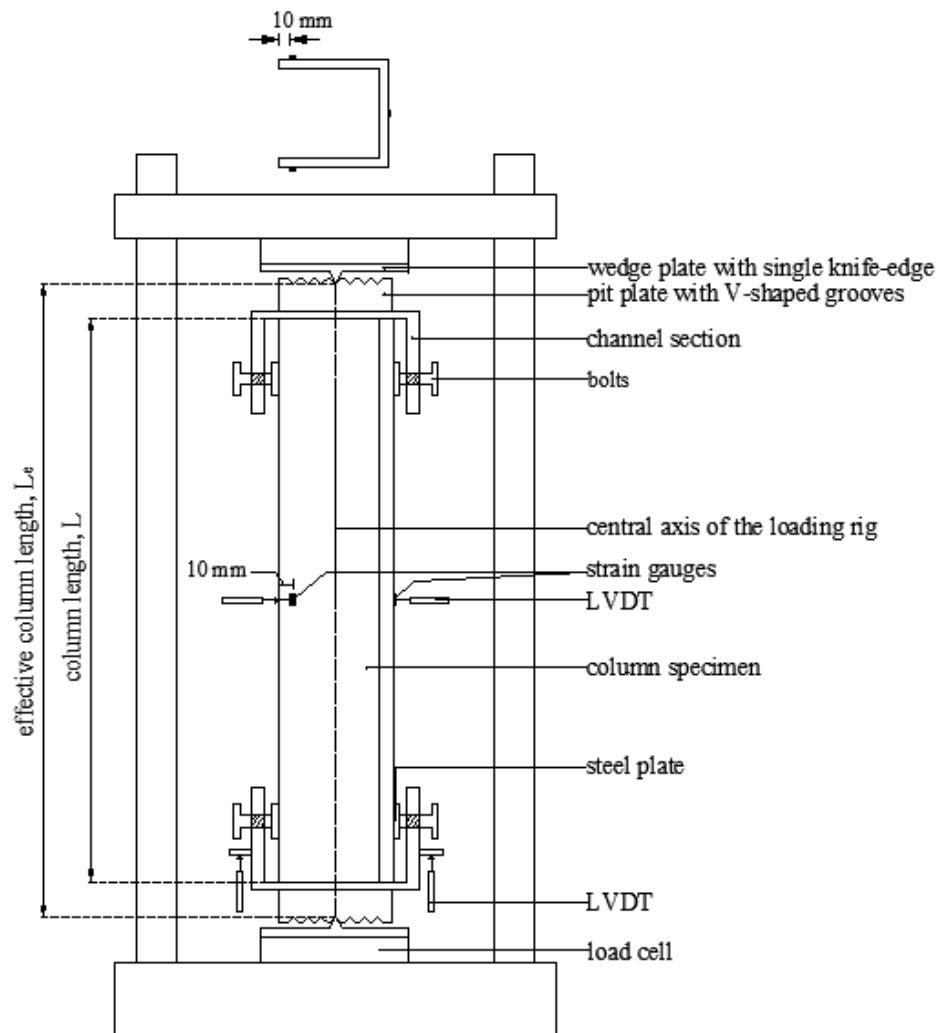


Figure 4.31: Schematic illustration of the pin-ended column test arrangement and instrumentation.



Figure 4.32: Typical pin-ended column test setup.

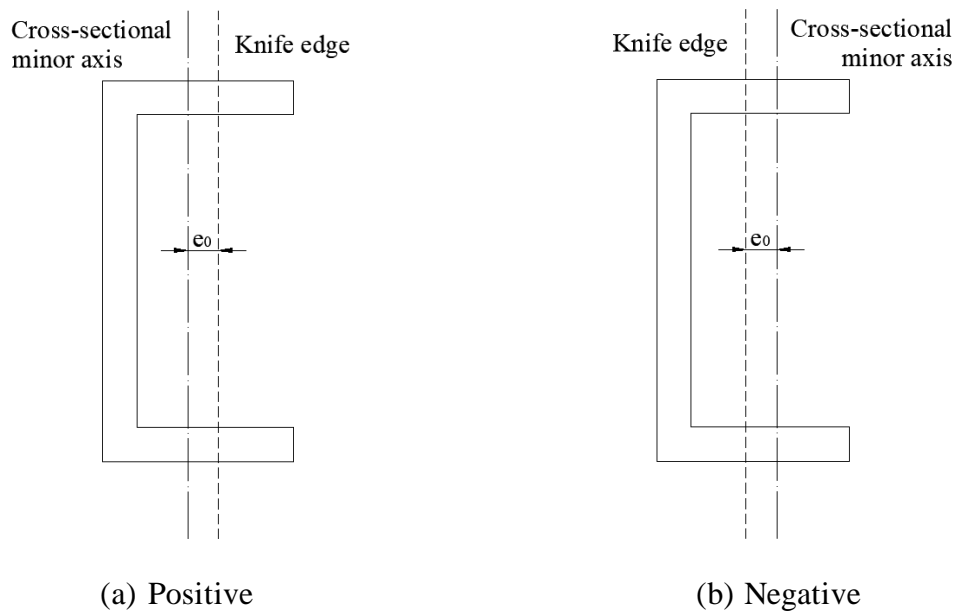


Figure 4.33: Sign convention for actual initial load eccentricity e_0 of C-section pin-ended column tests.

The recorded load–mid-height lateral deflection curves ($F-\Delta$) for all tested columns are shown in Figure 4.34. The key test results including the ultimate load $F_{u,Exp}$ and the mid-height lateral deflection at ultimate load $\Delta_{u,Exp}$ are listed in Table 4.21. The most common observed failure mode was global buckling accompanied by local buckle on the compressed flanges. All tested specimens exhibited significant mid-height lateral deflection. Two buckling orientations were observed, namely “C” orientation and “reverse C” orientation, indicating that the specimens buckled towards the web and flange tips, respectively. Typical obtained failures modes for both buckling orientations are depicted in Figure 4.35. Particularly, all specimens except from 50.8×50.8×6.35-L500 specimen, had positive combined equivalent global imperfection and applied eccentricity e_m (see Table 4.19) and thus the additional bending moments due to second order effects induced compressive stresses at the flange tips, resulting in buckling towards the web (“C” orientation). Conversely, in 50.8×50.8×6.35-L500 specimen which had negative combined equivalent global imperfection and applied eccentricity e_m , the additional bending moments induced tensile stresses at the flange tips leading to buckling towards the flange tips (“reverse C” orientation).

Table 4.21: Summary of key results obtained from pin-ended column tests.

Specimen	Orientation	$F_{u,Exp}$ (kN)	$\Delta_{u,Exp}$ (mm)
50.8×50.8×6.35-L500	"reverse C"	225.92	1.70
76.2×76.2×6.35-L500	"C"	379.63	0.20
76.2×76.2×6.35-L300	"C"	387.47	0.50
50.8×38.1×6.35-L500	"C"	200.43	8.50
50.8×38.1×3.18-L500	"C"	91.85	2.00
50.8×38.1×3.18-L300	"C"	102.50	0.50
50.8×25.4×3.18-L500	"C"	46.59	5.00
50.8×25.4×3.18-L300	"C"	81.12	1.50

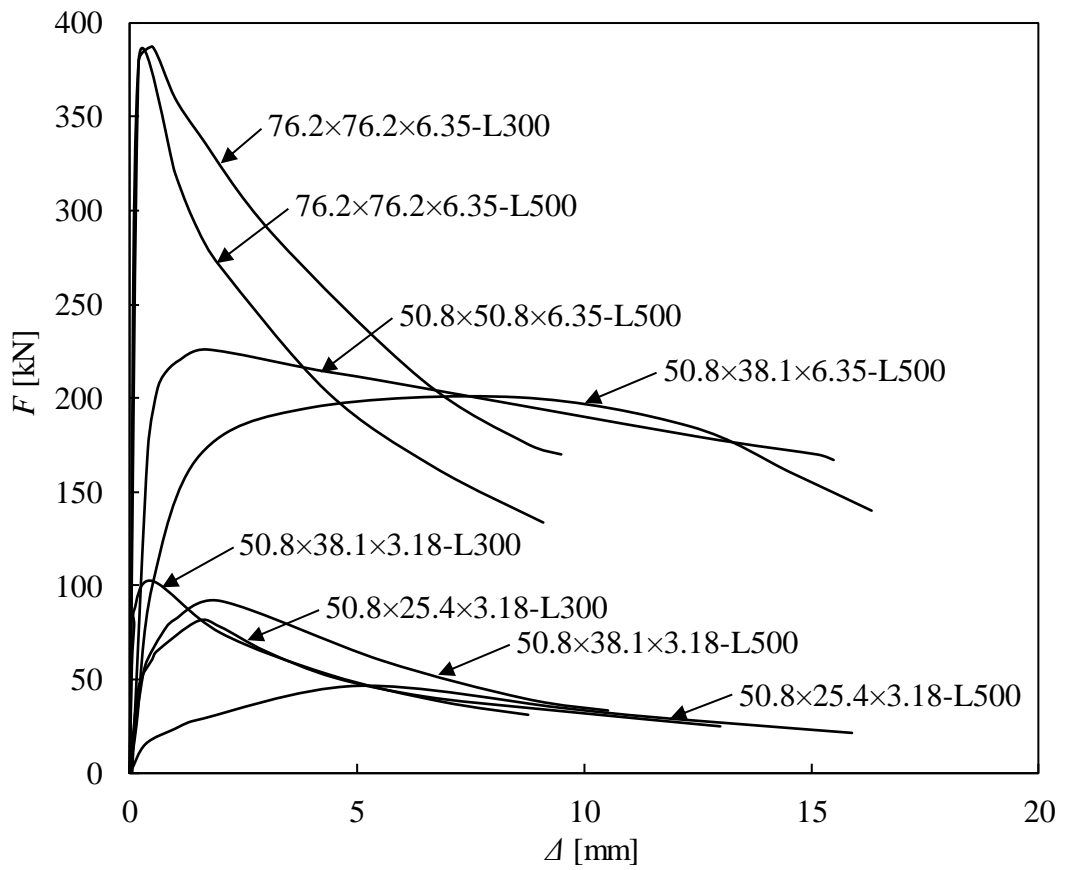
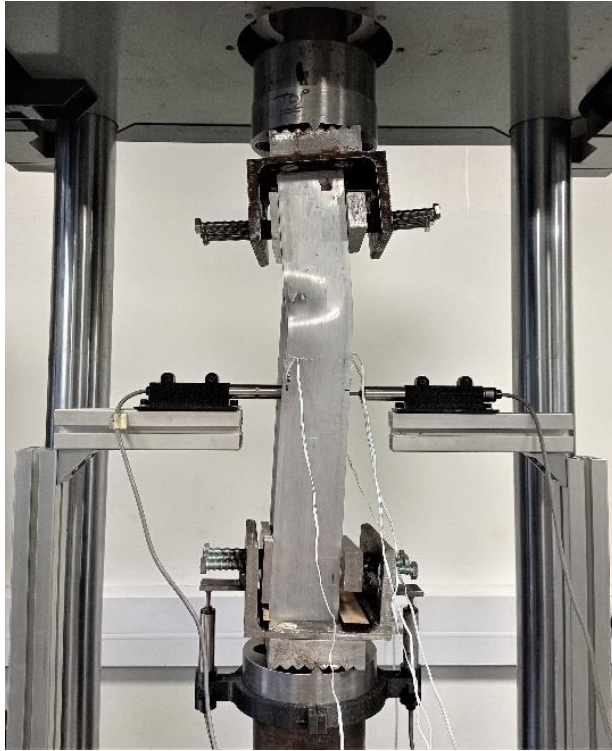
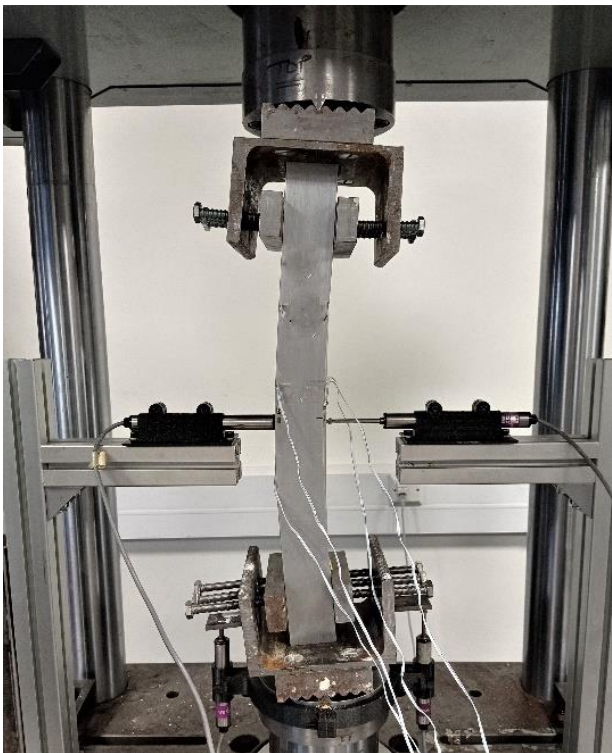


Figure 4.34: Load-mid-height lateral deflection curves obtained from pin-ended column tests.



(a) 76.2×76.2×6.35-L500 -“C” orientation



(b) 50.8×50.8×6.35-L500 -“reverse C” orientation

Figure 4.35: Typical failure modes obtained from pin-ended column tests.

4.4. Simply-supported beams

4.4.1. Bare rectangular tubular cross-sections

A series of simply-supported RHS beams were investigated under three-point and four-point bending configuration to capture their flexural response and obtain their rotational capacity. The experimental investigation comprised five 6082-T6 RHSs with geometric properties as shown in Figure 4.36. The beam specimens for each cross-section were cut from the same tube and their geometric measured dimensions are presented in Table 4.22, where D is the outer web depth, B is the outer flange width and t is the thickness. The specimens' designation is defined according to their nominal geometric dimensions. For instance, the label “63.5×38.1×3.25” refers to a beam specimen with outer depth $D=63.5$ mm, outer width $B=38.1$ mm and thickness $t=3.25$ mm. The engineering stress–strain curves (σ – ε) obtained from the tensile coupon tests for each examined cross-section are depicted in Figure 4.35. Moreover, the average measured material properties are listed in Table 4.23. In the current study, only the local geometric imperfections were measured because the investigated cross-sections have closed shape and short length, precluding the occurrence of lateral-torsional buckling. The measured local imperfection amplitudes denoted ω_l are also reported in Table 4.22.

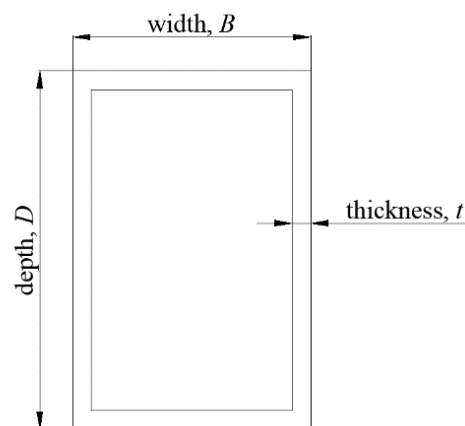


Figure 4.36: Geometric properties of the BAT sections of the simply-supported beams.

Table 4.22: Mean measured geometrical dimensions and local geometric imperfections of the tested BAT simply-supported beams.

Specimen	D (mm)	B (mm)	t (mm)	ω_l (mm)
Three-point bending				
63.5× 38.1×3.25	63.32	37.98	3.22	0.25 ($t/13$)
50.8× 38.1×3.25	50.96	38.27	3.41	0.18 ($t/19$)
50.8× 25.4×3.25	50.83	25.46	3.31	0.19 ($t/17$)
38.1×25.4×3.25	38.11	25.33	3.20	0.21 ($t/15$)
38.1× 19.1×3.25	38.07	19.05	3.28	0.32 ($t/10$)
Four-point bending				
63.5× 38.1×3.25	63.35	37.99	3.20	0.27 ($t/12$)
50.8× 38.1×3.25	50.93	38.24	3.39	0.33 ($t/10$)
50.8× 25.4×3.25	50.82	25.47	3.33	0.16 ($t/21$)
38.1×25.4×3.25	38.14	25.85	3.23	0.18 ($t/18$)
38.1× 19.1×3.25	38.17	19.05	3.24	0.21 ($t/15$)

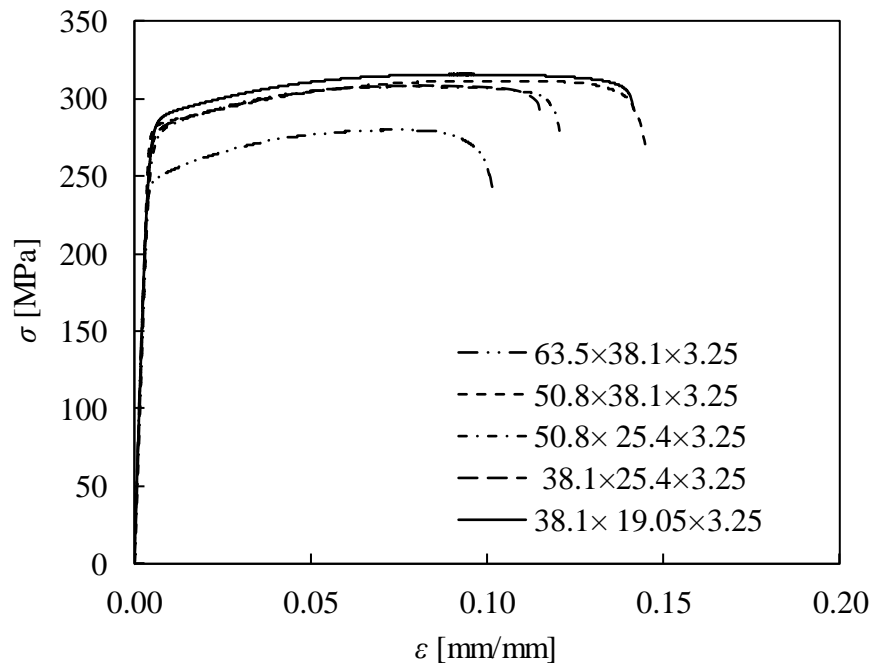


Figure 4.37: Stress-strain curves of the BAT sections of the simply-supported beams.

Table 4.23: Material properties of BAT sections obtained from the tensile coupon tests.

Specimen	E (MPa)	$\sigma_{0.1}$ (MPa)	$\sigma_{0.2}$ (MPa)	σ_u (MPa)	ε_u (mm/mm)	ε_f (mm/mm)	n	$\sigma_u/\sigma_{0.2}$
63.5×38.1×3.2	70962	242	247	280	0.08	0.10	33.8	1.13
50.8×38.1×3.2	67925	275	282	311	0.11	0.13	27.5	1.10
50.8×25.4×3.2	66280	264	271	308	0.08	0.12	26.4	1.14
38.1×25.4×3.2	67123	271	278	308	0.08	0.11	29.2	1.11
38.1×19.1×3.2	70302	275	282	316	0.09	0.14	27.5	1.12

A total of 10 symmetric bending tests on simply-supported beams were performed. Schematic illustrations of the three- and four-point test arrangements along with the corresponding employed instrumentations are depicted in Figure 4.38 and Figure 4.39, respectively. The investigated beam specimens had a total length of 1000 mm, whilst the span-to-height ratio ranged from 14 to 23. In order to prevent the occurrence of web crippling due to localised stress concentration, wooden blocks with dimensions equal to the internal ones of the tested cross-sections were inserted within the tubes at the loading points and supports. Linear electrical resistance strain gauges were attached at top and bottom flanges of each cross-section and at 50 mm distance from the midspan to measure the extreme compressive and tensile strains during testing. Photographs of both set-ups are also displayed in Figure 4.40 and Figure 4.41.

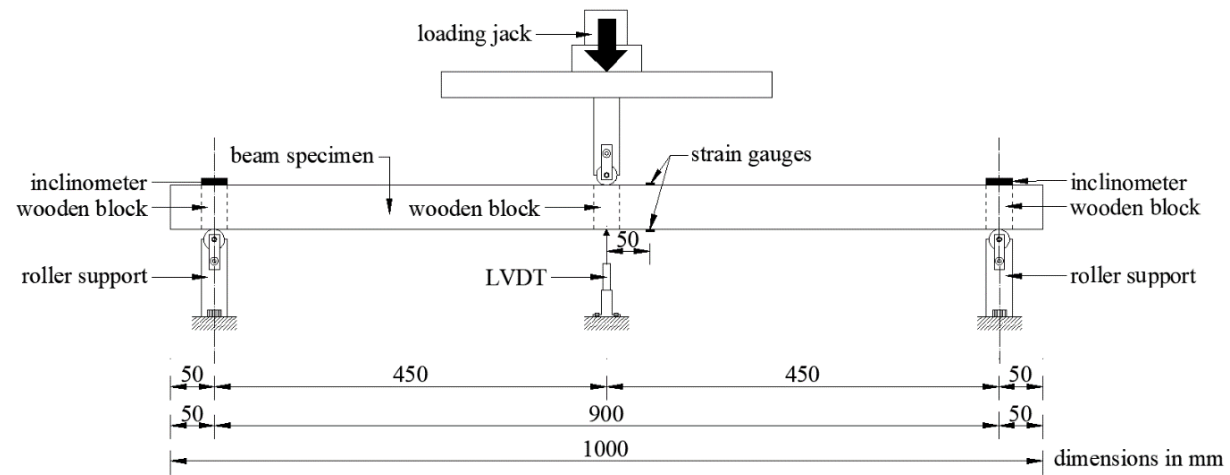


Figure 4.38: Schematic illustration of the three-point bending test arrangement and instrumentation.

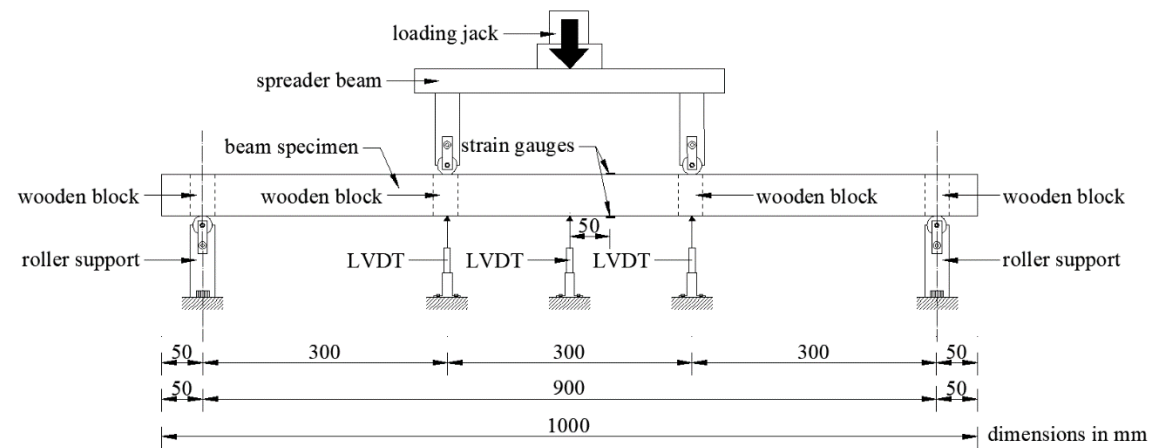


Figure 4.39: Schematic illustration of the four-point bending test arrangement and instrumentation.

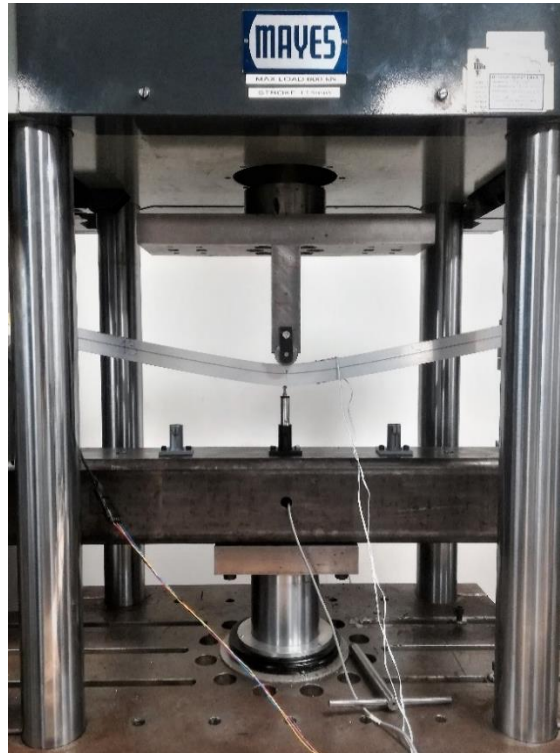


Figure 4.40: Typical three-point bending test set-up.

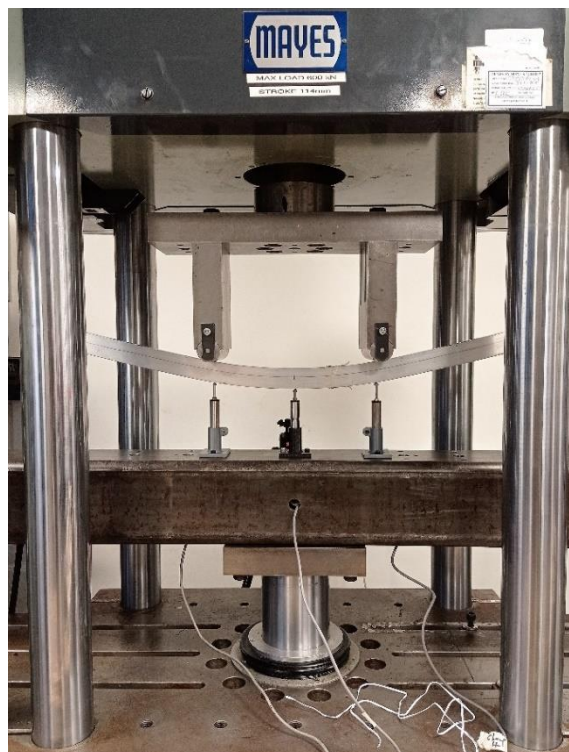


Figure 4.41: Typical four-point bending test set-up.

The moment–rotation ($M-\theta$) and moment–curvature ($M-\kappa$) responses obtained from the three-point and four-point bending tests, respectively, are depicted in Figure 4.42 and Figure 4.43, respectively. For comparison purposes, the curves are plotted in a non-dimensional format. Thus, the recorded moment M is normalised by the plastic moment resistance M_{pl} , while the rotation θ at the plastic hinge (sum of the two end rotation values measured from the inclinometers) or curvature κ at the constant moment area is normalised by θ_{pl} or κ_{pl} which is the elastic component of the rotation or curvature corresponding to M_{pl} . The terms θ_{pl} and κ_{pl} are defined in Equations (4.2) and (4.3), respectively:

$$\theta_{pl} = \frac{M_{pl}L}{2EI} \quad (4.2)$$

$$\kappa_{pl} = \frac{M_{pl}}{EI} \quad (4.3)$$

where the plastic moment resistance M_{pl} is calculated by multiplying the 0.2 % proof (yield) stress obtained from the tensile coupon tests by the plastic section modulus; L is the clear span of the beam specimen and I is the second moment of inertia of the cross-section about the major axis.

In four-point bending tests the curvature κ in the constant moment area of the beam was determined using Equation (4.4) considering that the deformed shape of the central span of length L_2 represents a segment of a circular arc of radius r [220].

$$\kappa = \frac{1}{r} = \frac{8(\delta_M - \delta_L)}{4(\delta_M - \delta_L)^2 + L_2^2} \quad (4.4)$$

where δ_M is the midspan vertical displacement and δ_L is the average vertical displacement taken at the two loading points.

As shown from Figure 4.42 and Figure 4.43, all specimens at the initial loading stage exhibit a linear response. As the loading increases, the specimens exceed their plastic moment resistance and maintain it throughout large inelastic deformations denoting high deformation capacity. It is noteworthy that the specimens under four-point bending configuration possess higher deformation capacity, as they reached larger inelastic deformations.

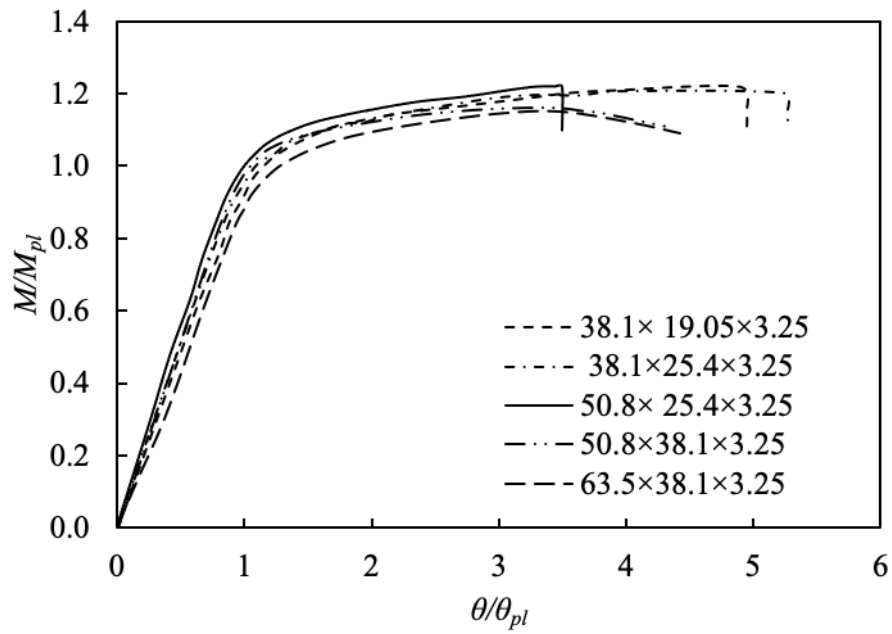


Figure 4.42: Normalised moment–rotation responses of BAT beam specimens obtained from three-point bending tests.

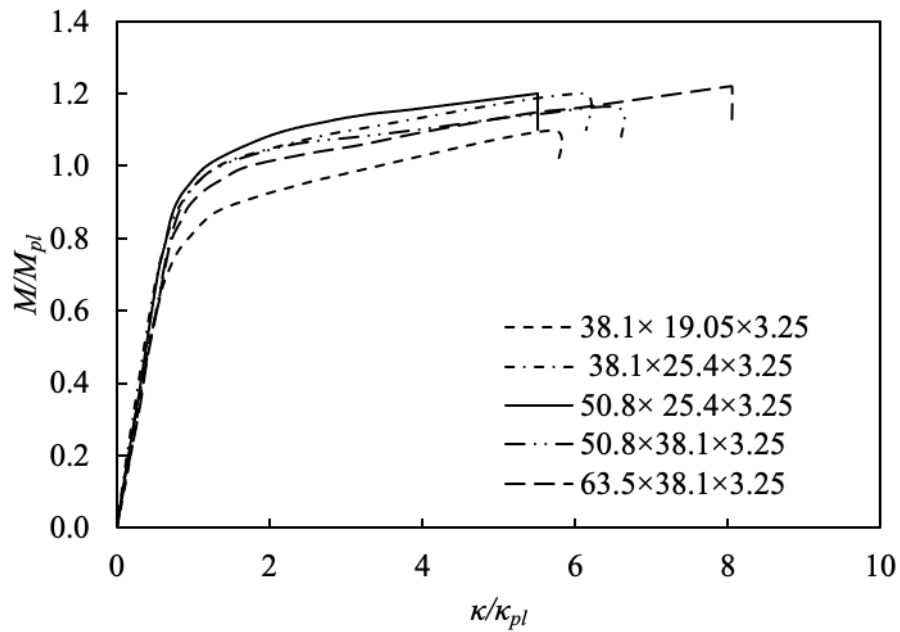


Figure 4.43: Normalised moment–curvature responses of BAT beam specimens obtained from four-point bending tests.

The key response characteristics including the ultimate bending moment $M_{u,Exp}$, which is the maximum bending moment recorded during testing, the elastic moment resistance M_{el} and the plastic moment resistance M_{pl} are listed in Table 4.24. The obtained normalised rotation θ_m/θ_{pl} and curvature κ_m/κ_{pl} for each beam specimen, where θ_m (κ_m) is the rotation (curvature) value corresponding to bending moment $M_{u,Exp}$, are also reported in Table 4.25. Note that some tests were discontinued before reaching the full moment-rotation/curvature potential due to either limited vertical displacement capacity of the test rig or excessive vertical deflection of the beam specimen. In these cases, the maximum recorded moment and rotation/curvature values are reported. On the basis of the recorded moment-rotation and moment-curvature responses, the rotational capacity R_m of the tested beam specimens under three-point and four-point cases was defined using the Equations (4.5) and (4.6), respectively, and are listed in Table 4.24.

$$R_m = \frac{\theta_m}{\theta_{pl}} - 1 \quad (4.5)$$

$$R_m = \frac{\kappa_m}{\kappa_{pl}} - 1 \quad (4.6)$$

Table 4.24: Key results obtained from three-point and four-point bending tests.

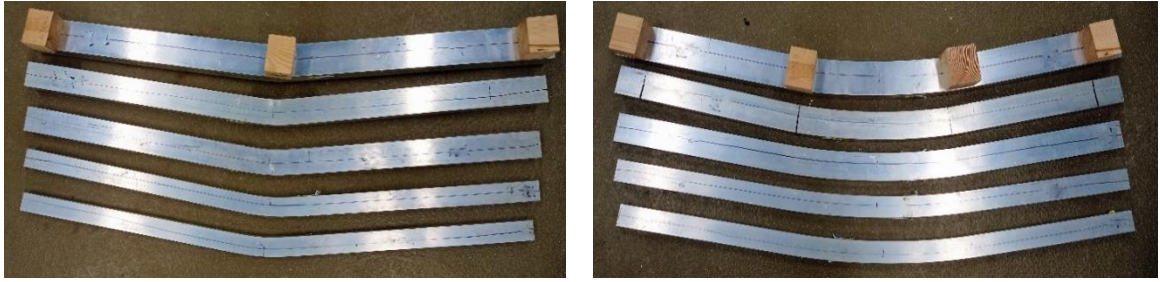
Specimen	M_{el} (kNm)	M_{pl} (kNm)	M_{pl}/M_{el}	$M_{u,Exp}$ (kNm)	$M_{u,Exp}/M_{el}$	$M_{u,Exp}/M_{pl}$
Three-point bending						
63.5× 38.1×3.25	2.53	3.15	1.24	3.57	1.41	1.13
50.8× 38.1×3.25	2.20	2.72	1.24	3.12	1.42	1.15
50.8× 25.4×3.25	1.56	2.01	1.29	2.39	1.53	1.19
38.1×25.4×3.25	1.00	1.28	1.27	1.49	1.49	1.17
38.1× 19.1×3.25	0.83	1.10	1.32	1.31	1.57	1.19
Four-point bending						
63.5× 38.1×3.25	2.53	3.15	1.24	3.77	1.49	1.20
50.8× 38.1×3.25	2.20	2.72	1.24	3.10	1.41	1.14
50.8× 25.4×3.25	1.56	2.01	1.29	2.36	1.52	1.18
38.1×25.4×3.25	1.00	1.28	1.27	1.49	1.49	1.17
38.1× 19.1×3.25	0.83	1.10	1.32	1.18	1.42	1.08

Table 4.25: Key results obtained from three-point and four-point bending tests.

Specimen	θ_m/θ_{pl}	κ_m/κ_{pl}	R_m
Three-point bending			
63.5× 38.1×3.25	4.42	-	3.42
50.8× 38.1×3.25	4.30	-	3.30
50.8× 25.4×3.25	3.50	-	2.50
38.1×25.4×3.25	5.27	-	4.27
38.1× 19.1×3.25	4.95	-	3.95
Four-point bending			
63.5× 38.1×3.25	-	8.05	7.05
50.8× 38.1×3.25	-	6.60	5.60
50.8× 25.4×3.25	-	5.51	4.51
38.1×25.4×3.25	-	6.15	5.15
38.1× 19.1×3.25	-	5.75	4.75

Further comparisons on the responses exhibited by the cross-sections under three-point and four-point bending denoted a clear influence of the moment gradient on the ultimate bending moment and rotational capacity. This influence can be observed in Table 4.24 where in almost all cases the moment gradient allow the cross-section to sustain slightly higher loading. This behaviour which has also been observed in similar studies [97,220-225] stems from the fact that in three-point bending configuration the material surrounding the plastic hinge is stiffer and at lower stress providing a kind of restraint which delays the occurrence of local buckling.

Almost all beam specimens subjected to three-point and four-point major axis bending failed by material yielding, as shown in Figure 4.44 and Figure 4.45(a). In specimen 63.5×38.1×3.25 under both bending configurations, material yielding was accompanied with pronounced inelastic local buckling of the compression flange and the upper part of the web (Figure 4.45(b)). It is also noteworthy that the specimen 50.8×25.4×3.25 under three-point bending configuration failed by material fracture at the tension flange at the midspan, due to exceedance of the material fracture strain ε_f (Figure 4.45(c)).



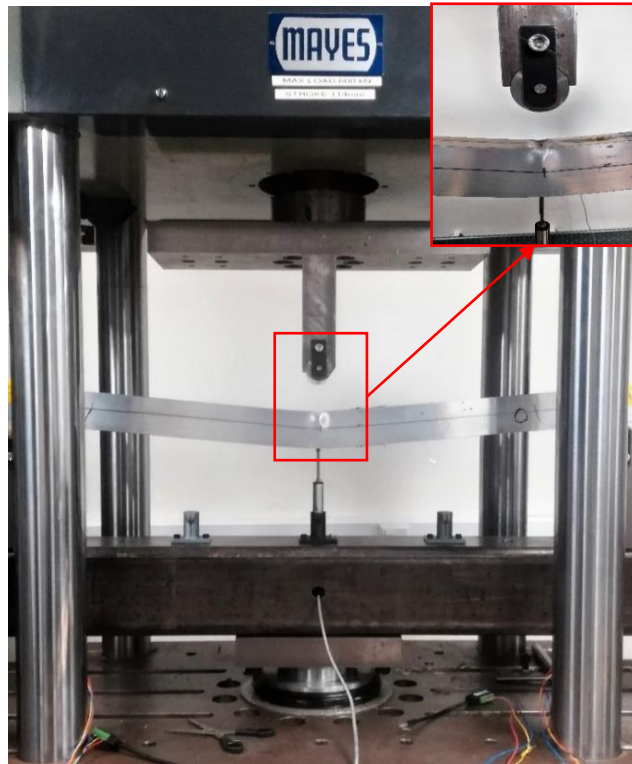
(a) Three-point bending tests

(b) Four-point bending tests

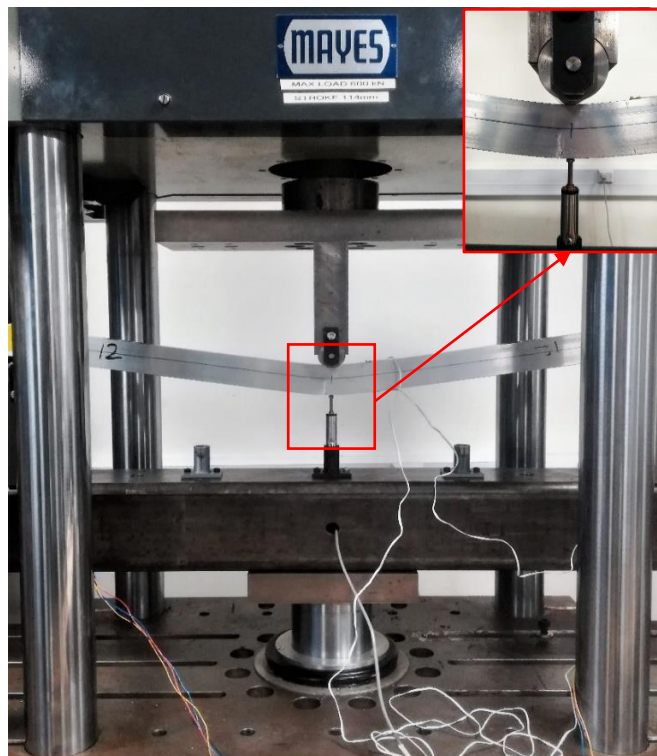
Figure 4.44: Failure modes of BAT beam specimens obtained from three-point and four-point bending tests.



(a) Material yielding of $38.1 \times 25.4 \times 3.25$



(b) Material yielding and inelastic local buckling of $63.5 \times 38.1 \times 3.25$ specimen



(c) Tensile fracture of $50.8 \times 25.4 \times 3.25$ specimen

Figure 4.45: Failure modes of BAT beam specimens obtained from three-point bending tests.

4.4.2. Bare square tubular cross-sections

A second series of simply-supported SHS beams were investigated under three-point bending configuration to capture their flexural response and obtain their rotational capacity. The results were utilised for reference purposes regarding the experimental series described in Subsection 4.4.3. Four 6082-T6 SHSs were considered in this study with geometric properties shown in Figure 4.46. The examined cross-sections had the same outer dimensions but different thicknesses resulting in various depth-to-thickness ratio D/t values ranging from 10.66 to 31.89 (see Table 4.24). The beam specimens had a nominal length L of 600 mm. Their measured geometric dimensions are reported in Table 4.26, where D is the outer web depth, B the outer flange width and t the thickness of the aluminium alloy tube (Figure 4.46). The specimens' designation is defined according to their nominal geometric dimensions. For instance, the label “50.8×50.8×1.6” refers to a beam specimen with outer depth $D=50.8$ mm, outer width $B=50.8$ mm and thickness $t=1.6$ mm. The engineering stress–strain curves (σ – ε) obtained from the tensile coupon tests for each examined cross-section are depicted in Figure 4.47. Moreover, the average measured material properties are listed in Table 4.27. In the current study, only the local geometric imperfections of the specimens were measured because the examined cross-sections have closed shape (tubular) and short length, precluding the occurrence of lateral-torsional buckling [21,221,226].

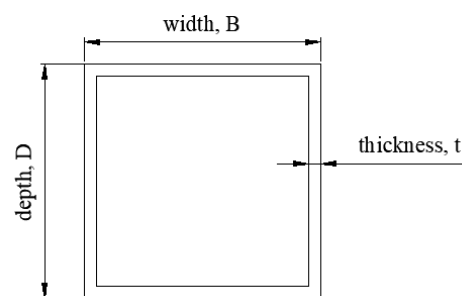


Figure 4.46: Geometric properties of the BAT sections of the simply-supported beams.

Table 4.26: Mean measured geometrical dimensions and local geometric imperfections of the tested BAT simply-supported beams.

	D (mm)	B (mm)	t (mm)	D/t	L (mm)	ω_l (mm)
50.8×50.8×1.6	51.02	50.70	1.60	31.89	599.05	0.21 ($t/10$)
50.8×50.8×2.7	51.02	50.70	2.64	19.33	599.06	0.33 ($t/9$)
50.8×50.8×3.3	50.64	50.60	3.25	15.58	599.07	0.25 ($t/13$)
50.8×50.8×4.8	50.63	50.60	4.75	10.66	599.05	0.19 ($t/25$)

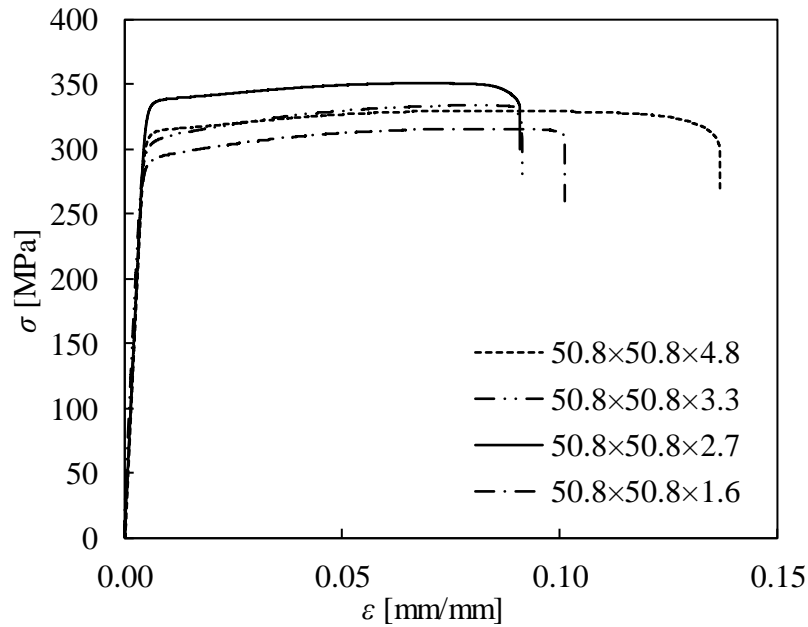


Figure 4.47: Stress-strain curves of the BAT/CFAT sections of the simply-supported beams.

Table 4.27: Material properties of BAT/CFAT sections obtained from the tensile coupon tests.

Specimen	E (MPa)	$\sigma_{0.1}$ (MPa)	$\sigma_{0.2}$ (MPa)	σ_u (MPa)	ϵ_u (mm/mm)	ϵ_f (mm/mm)	n	$\sigma_u/\sigma_{0.2}$
50.8×50.8×1.6	65000	283	289	315	0.08	0.11	34.8	1.09
50.8×50.8×2.7	72200	330	337	352	0.07	0.10	31.2	1.04
50.8×50.8×3.3	71700	296	302	330	0.08	0.09	30.9	1.09
50.8×50.8×4.8	67500	300	306	325	0.09	0.16	34.4	1.06

A total of 4 three-point bending tests on simply-supported beams were performed aiming to capture their flexural response and quantify the bending moment capacity of the cross-sections presented in Subsection 4.4.1. Figure 4.48 displays a schematic illustration of the three-point test arrangement along with the corresponding employed instrumentation.

The investigated beam specimens had a clear beam span of 500 mm whilst the span-to-height ratio was fixed and equal to 10. Moreover, wooden blocks with dimensions equal to the internal ones of the considered cross-sections were inserted within the tubes at the loading point and at both supports to prevent the occurrence of web crippling due to localised stress concentration. Linear electrical resistance strain gauges were attached at top and bottom flanges of each cross-section and at 20 mm distance from the midspan to measure the extreme compressive and tensile strains during testing. A photograph of a typical three-point bending test set-up is depicted in Figure 4.49.

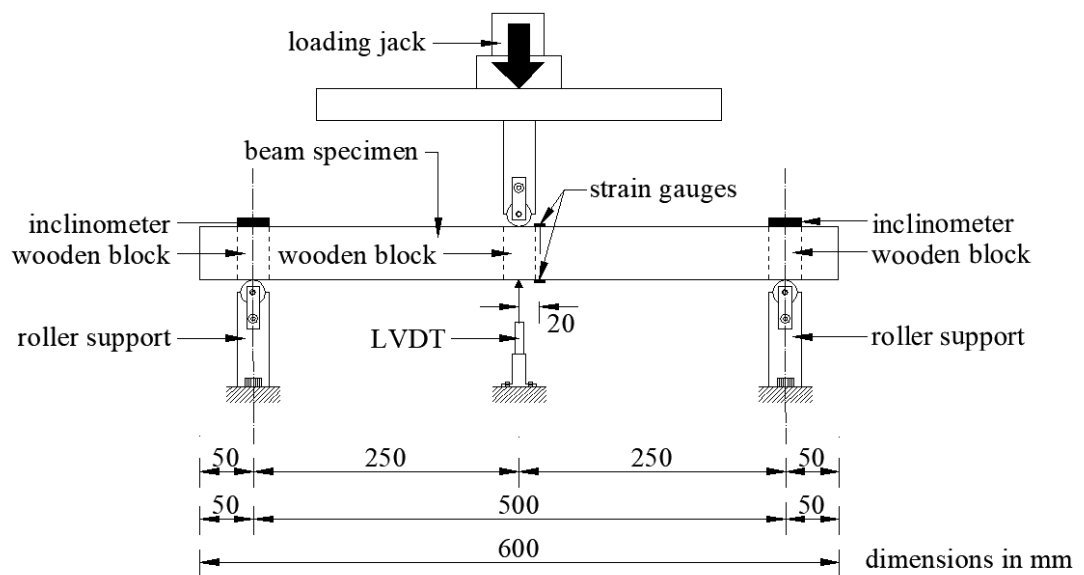


Figure 4.48: Schematic illustration of the three-point bending test arrangement and instrumentation.

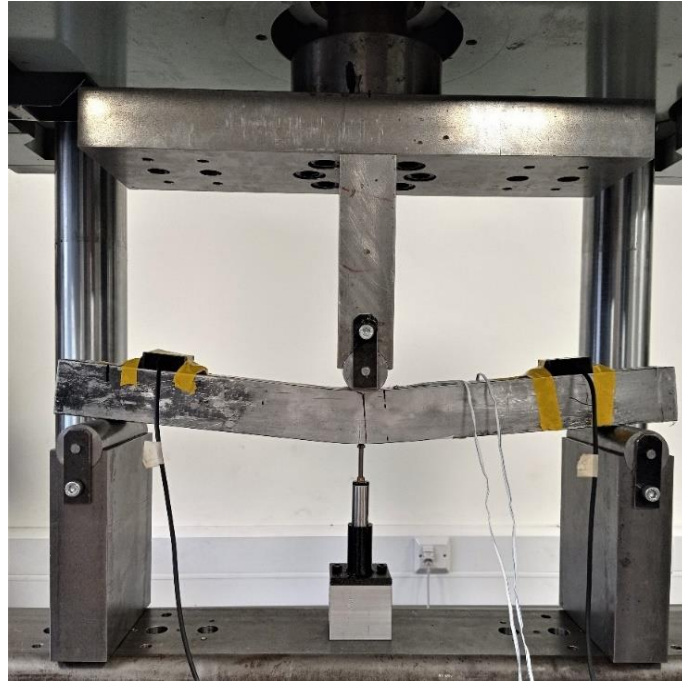
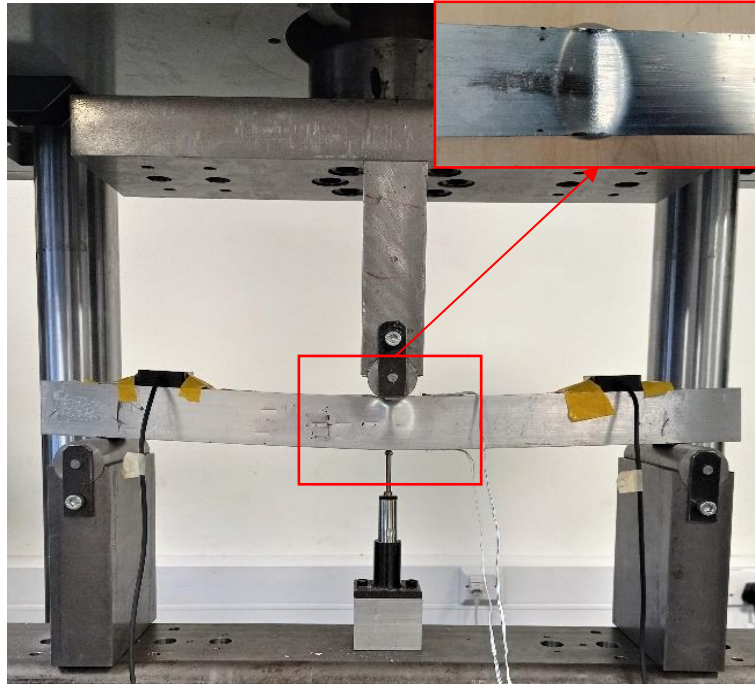


Figure 4.49: Typical three-point bending test set-up.

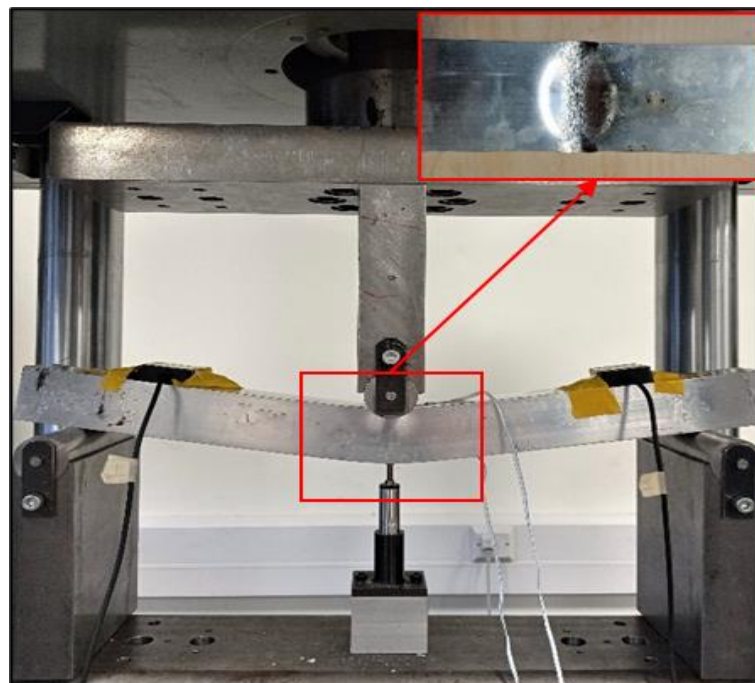
The observed predominant failure modes were due to material yielding (MY) and local buckling on the upper flange (LBF). In particular, the $50.8 \times 50.8 \times 1.6$ specimen failed due to elastic local buckling on the upper flange (LBF). This was expected, since $50.8 \times 50.8 \times 1.6$ specimen comprised the slenderest cross-section, i.e., cross-section with higher cross-sectional slenderness ratio β/ϵ . Thus, its cross-sectional bending moment capacity was limited by local buckling. As can be seen from Figure 4.50(a), local buckling occurred at the vicinity of the loading point at the midspan where the stress concentration was higher due to the presence of the moment gradient. The remaining specimens failed due to material yielding (MY) accompanied by inelastic local buckling on the upper flange (LBF), as can be seen in Figure 4.50(b). Table 4.28 summarises the obtained failure modes for all tested specimens.

Table 4.28: Key results obtained from three-point bending tests.

Specimen	Failure mode	M_u (kNm)	W_u (mm)	θ_u (deg)
$50.8 \times 50.8 \times 1.6$	LBF	1.43	4.60	1.03
$50.8 \times 50.8 \times 2.7$	MY+LBF	3.11	8.72	2.14
$50.8 \times 50.8 \times 3.3$	MY+LBF	3.40	10.85	2.40
$50.8 \times 50.8 \times 4.8$	MY+LBF	5.05	17.44	3.95



(a) Specimen $50.8 \times 50.8 \times 1.6$ – Elastic local buckling on the upper flange of the aluminium tube (LBF)



(b) Specimen $50.8 \times 50.8 \times 4.8$ – Material yielding (MY) and inelastic local buckling on the upper flange of the aluminium tube (LBF)

Figure 4.50: Failure modes of BAT beam specimens obtained from three-point bending tests.

The obtained bending moment–midspan deflection (M – W) curves of the tested specimens are plotted in Figure 4.51. In these graphs, the horizontal axis represents the vertical deflection W at the midspan measured from the LVDT and the vertical axis represents the bending moment M at the midspan of the specimen calculated as follows:

$$M = \frac{PL_e}{4} \quad (4.7)$$

where P is the applied load and L_e is the length of the clear span ($L_e=500$ mm in this study).

As can be seen, initially the specimens exhibit a linear elastic behaviour followed by a nonlinear region up to the plastic moment resistance. Upon the attainment of the ultimate bending moment M_u , the curves' slope decreases with increasing vertical deflections. It is noteworthy that the curve's slope of the $50.8 \times 50.8 \times 1.6$ specimen is comparatively steeper owing to the LBF failure occurrence which led to significant and rapid loss of strength by the end of the test. The key experimental results including the ultimate bending moment M_u and the midspan deflection W_u corresponding to M_u are summarised in Table 4.30.

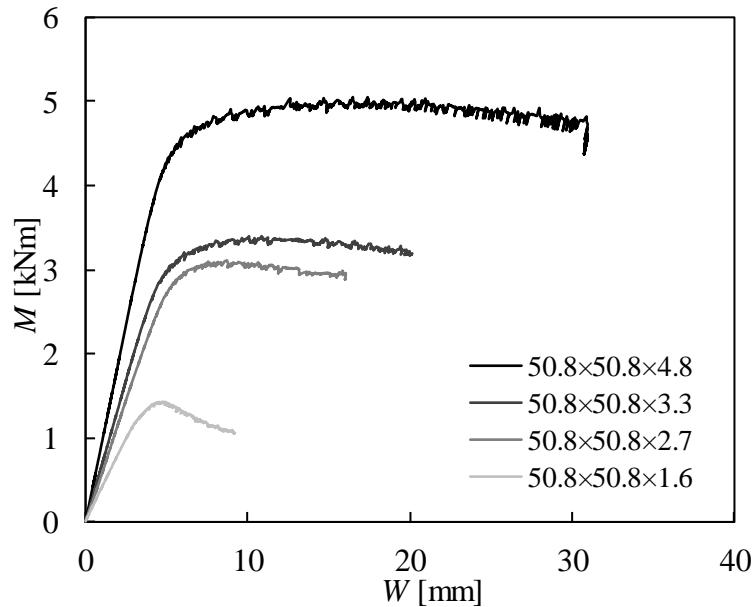


Figure 4.51: Bending moment–midspan deflection curves of BAT beam specimens obtained from three-point bending tests.

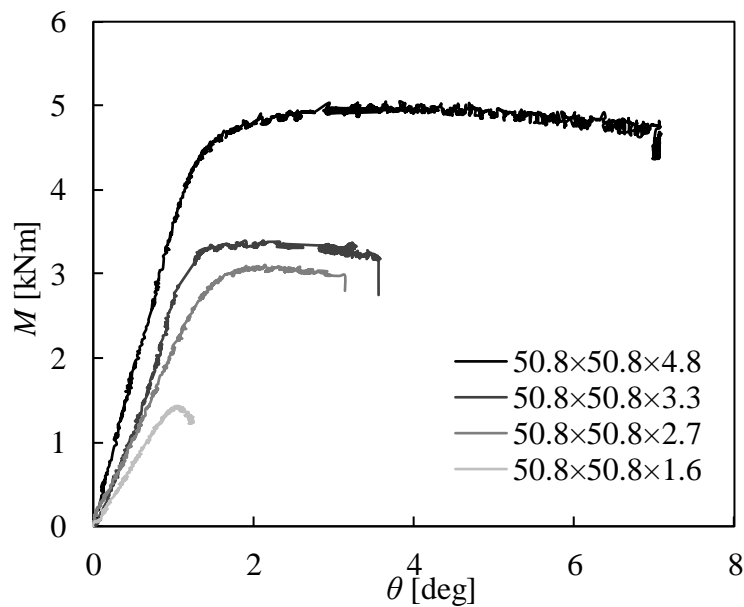
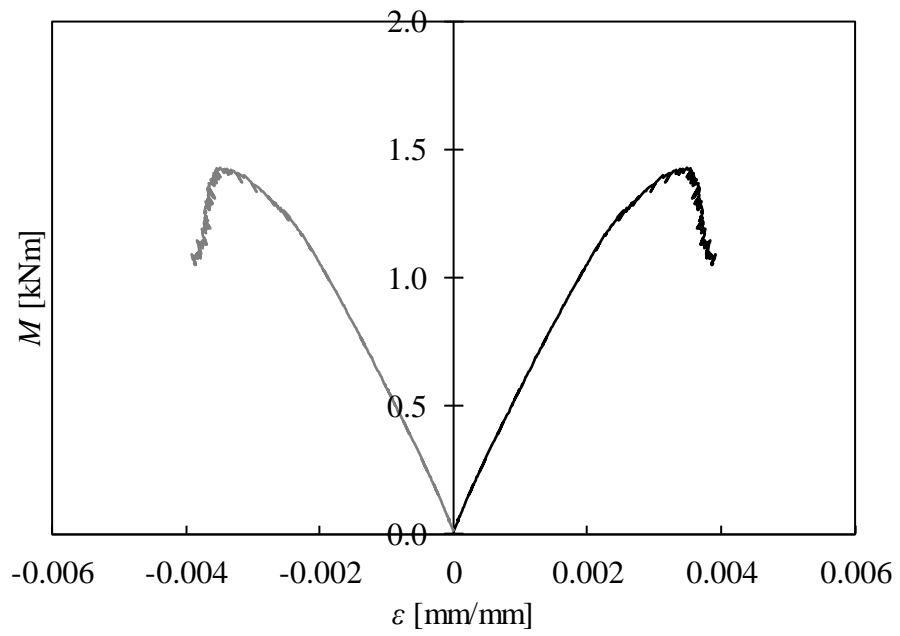
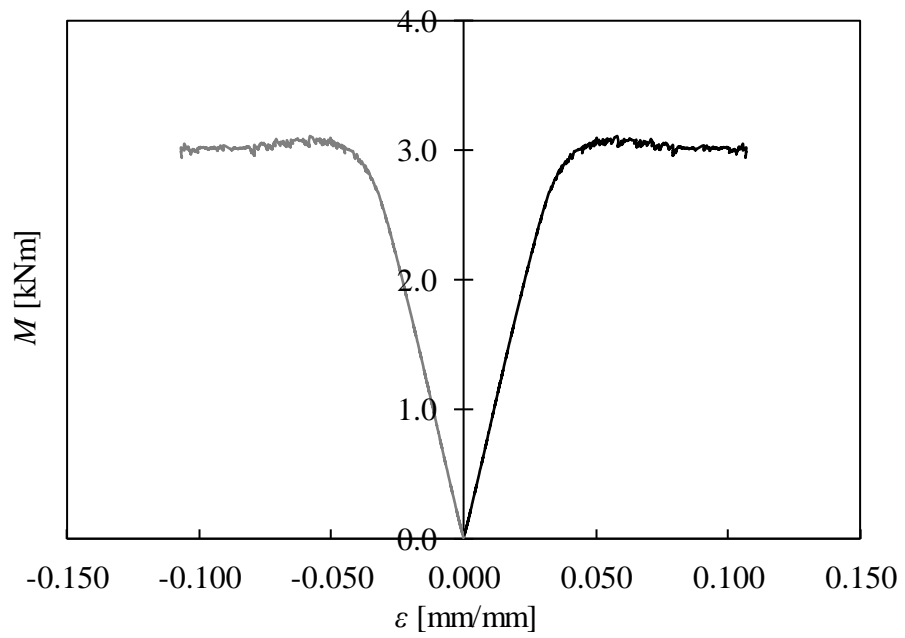


Figure 4.52: Bending moment–rotation curves of BAT beam specimens obtained from three-point bending tests.

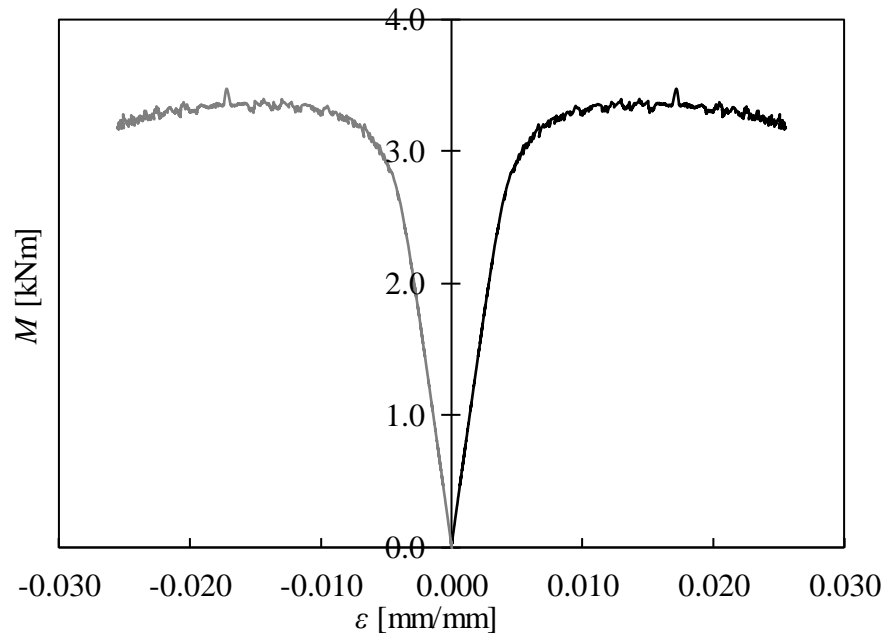
The obtained bending moment–longitudinal strain (M – ε) curves of the tested specimens are plotted in Figure 4.53. In these graphs, the horizontal axis represents the longitudinal strains ε obtained from the strain gauges attached at the top and bottom flanges of the aluminium tube at the midspan. It is noted that the compressive (measured by the strain gauge at the top flange) and tensile strains (measured by the strain gauge at the bottom flange) are defined as negative and positive strains, respectively. The plotted curves show that the compressive and tensile strains are symmetrical with respect to the vertical axis, denoting that the neutral axis coincides with the centroid of the cross-section.



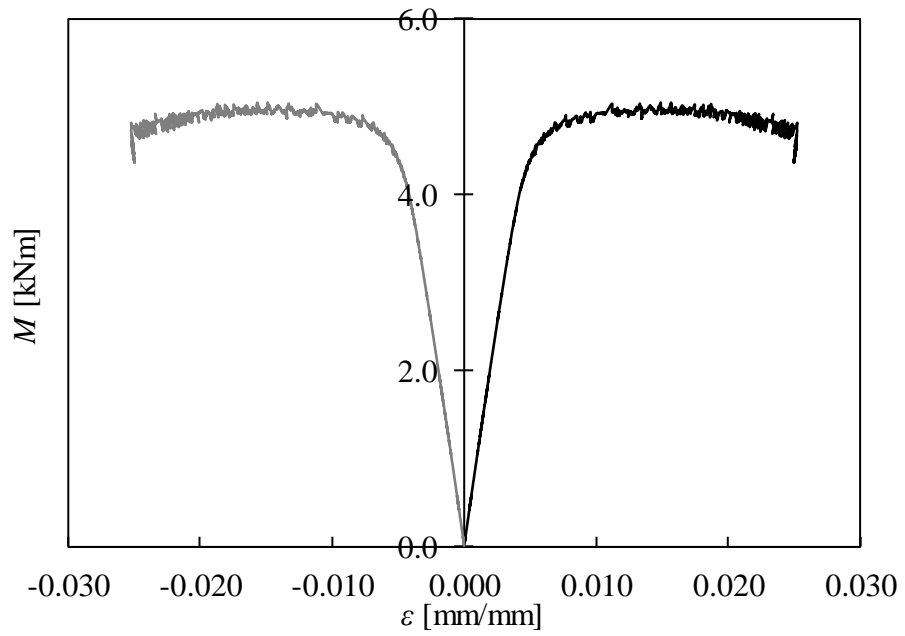
(a) 50.8×50.8×1.6



(b) 50.8×50.8×2.7



(c) 50.8×50.8×3.3



(d) 50.8×50.8×4.8

Figure 4.53: Bending moment–longitudinal strain curves of BAT beam specimens obtained from three-point bending tests.

4.4.3. Concrete-filled tubular cross-sections

The cross-sections presented in Subsection 4.4.2. were also, investigated infilled with concrete. Following the same procedure with the BAT specimens, the geometric dimensions of the examined specimens were measured prior to testing. The measured geometric dimensions are reported in Table 4.29, where D is the outer web depth, B the outer flange width and t the thickness of the aluminium alloy tube (Figure 4.54). The examined cross-sections had the same outer dimensions but different thicknesses resulting in various depth-to-thickness ratio D/t values ranging from 10.57 to 31.80 (see Table 4.29). The beam specimens had a nominal length L of 600 mm. The specimens' designation is defined according to their nominal geometric dimensions and the presence of the concrete "C" infill. For instance, the label "50.8×50.8×1.6-C" refers to a beam specimen with outer depth $D=50.8$ mm, outer width $B=50.8$ mm and thickness $t=1.6$ mm filled with concrete. The engineering stress–strain curves (σ – ε) obtained from the tensile coupon tests for each examined cross-section are depicted in Figure 4.37. Moreover, the average measured material properties are listed in Table 4.27. The average compressive strength $f_{ck,cube}$ of the tested cubes was 37.55 MPa. Table 4.5 summarises the compressive strength $f_{ck,cube}$ of the concrete cubes along with the corresponding standard deviation. In the current study, the initial global geometric imperfections were not measured because the examined cross-sections have closed shape (tubular) and short length, precluding the occurrence of lateral-torsional buckling [21,221,226]. Regarding the initial local geometric imperfections, they were not also measured since their effect on the flexural response is negligible due to the presence of the infill [146-148].

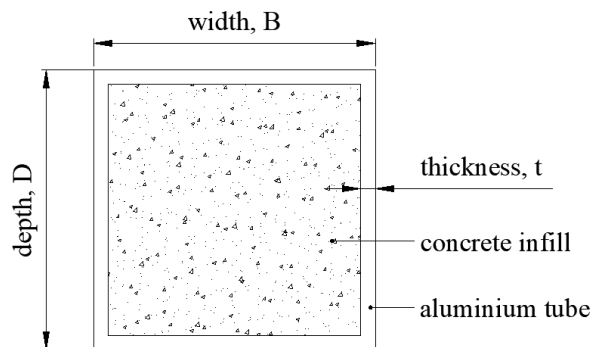


Figure 4.54: Geometric properties of the CFAT sections of the simply-supported beams.

Table 4.29: Mean measured geometrical dimensions of the tested CFAT simply-supported beams.

Specimen	D (mm)	B (mm)	t (mm)	D/t	L (mm)
50.8×50.8×1.6-C	50.88	50.65	1.60	31.80	599.08
50.8×50.8×2.7-C	50.79	50.79	2.63	19.31	599.05
50.8×50.8×3.3-C	50.96	50.84	3.22	15.83	599.05
50.8×50.8×4.8-C	50.86	50.82	4.81	10.57	599.05

A total of 4 three-point bending tests on simply-supported CFAT beams were performed aiming to capture their flexural response and quantify the bending moment capacity of the investigated cross-sections. Figure 4.55 displays a schematic illustration of the three-point test arrangement along with the corresponding employed instrumentation. The investigated beam specimens had a clear beam span of 500 mm whilst the span-to-height ratio was fixed and equal to 10. Linear electrical resistance strain gauges were attached at top and bottom flanges of each cross-section and at 20 mm distance from the midspan to measure the extreme compressive and tensile strains during testing. A photograph of a typical three-point bending test set-up is depicted in Figure 4.56.

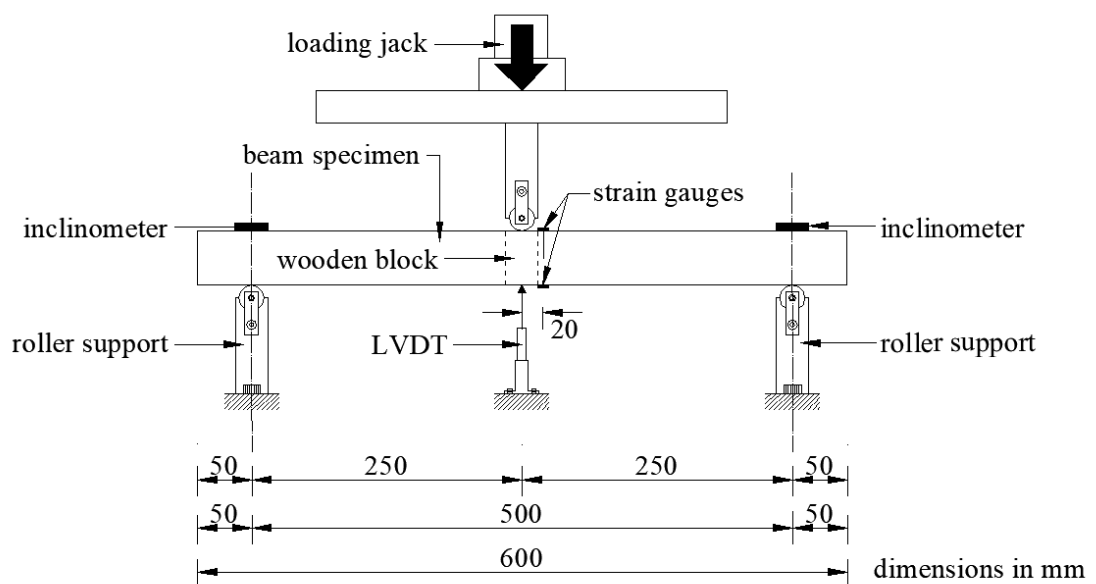


Figure 4.55: Schematic illustration of the three-point bending test arrangement and instrumentation.

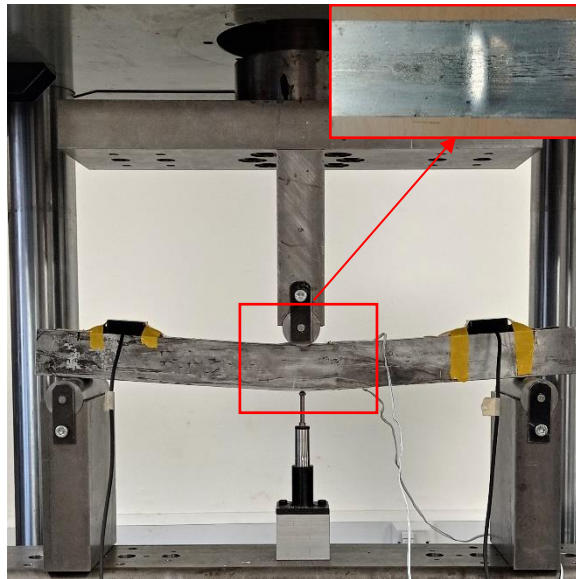


Figure 4.56: Typical three-point bending test set-up.

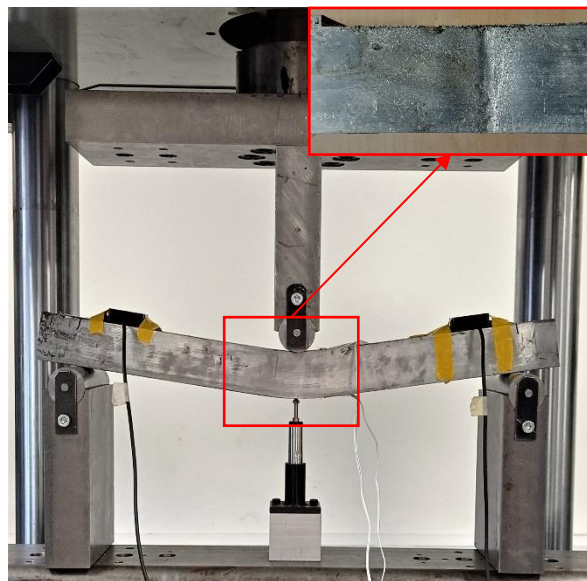
All CFAT specimens exhibited significant inelastic in-plane deformations and failed by tensile fracture (TF) at the lower flange of the aluminium tube at the midspan due to exceedance of the aluminium alloy's tensile fracture strain ε_f . The presence of the infill helped the aluminium tubes to resist the developed local transverse deformations allowing for full development of aluminium alloy's plasticity. Moreover, in specimens with slenderer cross-sections, pronounced inelastic outward local buckling on the upper flange (LBF) of the aluminium tube was observed prior to failure by tensile fracture. Figure 4.57 presents the obtained failure modes of CFAT specimens with the slenderest (50.8×50.8×1.6-C) and stockiest (50.8×50.8×4.8-C) cross-sections. After the execution of the tests of the CFAT beams, the aluminium tube around the midspan was removed to inspect the crack patterns of the infill. Figure 4.58 shows the resulting crack patterns in 50.8×50.8×4.8-C specimen. As can be observed, the flexural cracks are uniformly distributed around the midspan and along the concrete tensile fibre of the specimen. Table 4.30 summarises the obtained failure modes for all tested specimens.

Table 4.30: Key results obtained from three-point bending tests.

Specimen	Failure mode	M_u (kNm)	W_u (mm)	θ_u (deg)
50.8×50.8×1.6-C	TF	2.13	15.04	3.37
50.8×50.8×2.7-C	TF	3.78	20.17	4.97
50.8×50.8×3.3-C	TF	4.11	24.96	4.59
50.8×50.8×4.8-C	TF	5.57	29.15	7.27



(a) 50.8×50.8×1.6-C



(b) 50.8×50.8×4.8-C

Figure 4.57: Failure modes of CFAT beam specimens obtained from three-point bending tests.

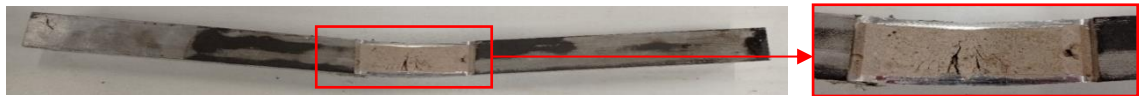


Figure 4.58: Crack patterns of the 50.8×50.8×4.8-C specimen.

The obtained flexural response of CFAT specimens was quite similar to their BAT counterparts consisting of three stages. During the first stage (elastic), the aluminium tube and the concrete infill bear load independently. Yielding of the aluminium tube also occurs at this stage. In the following stage (elastic-plastic), as the bending moment increases, the infill cracks and its volume gradually becomes greater. After some time, the two components come in contact and the aluminium tube provides confining pressure to the infill. Expansion of infill cracking at the tensile side results in degradation of the flexural stiffness. However, interaction between the aluminium tube and the infill effectively hinders the development of infill cracking along the cross-sectional depth offering effective support and thus leading to high deformation capacity of the CFAT beams. In the third stage (plastic), the CFAT beams continue to sustain bending moment for increasing deformation owing to the confinement provided by the aluminium tube to the cracked infill. Finally, failure occurs when the developed strains at the tensile (lower) flange of the aluminium tube at the midspan exceed the aluminium alloy's tensile fracture strain ε_f . Similar observations can be made from Figure 4.59, where the bending moment is plotted versus the end rotation, as obtained by the inclinometers.

The key experimental results including the ultimate bending moment M_u and the midspan deflection W_u corresponding to M_u are summarised in Table 4.30. It is noted that for CFAT specimens, the reported M_u values are the maximum recorded values.

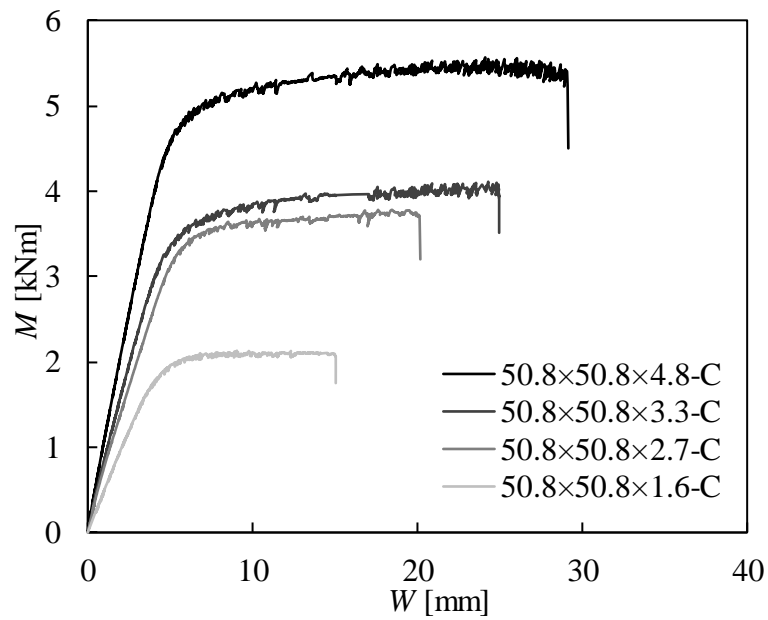


Figure 4.59: Bending moment–midspan deflection curves of CFAT beam specimens obtained from three-point bending.

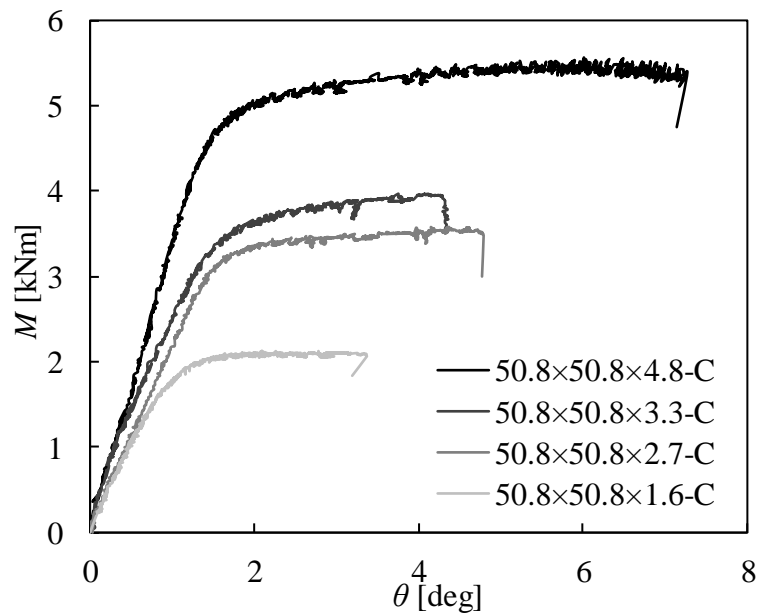
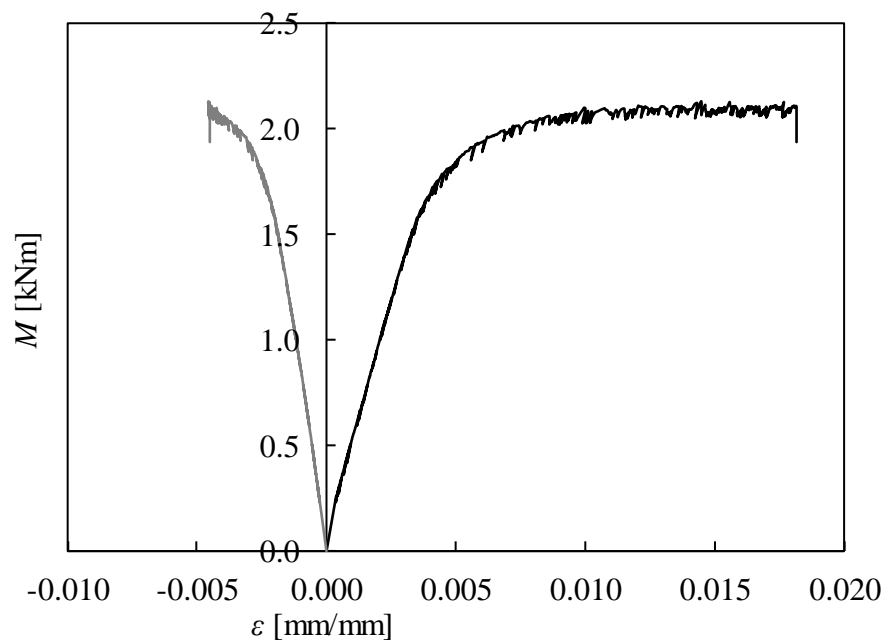
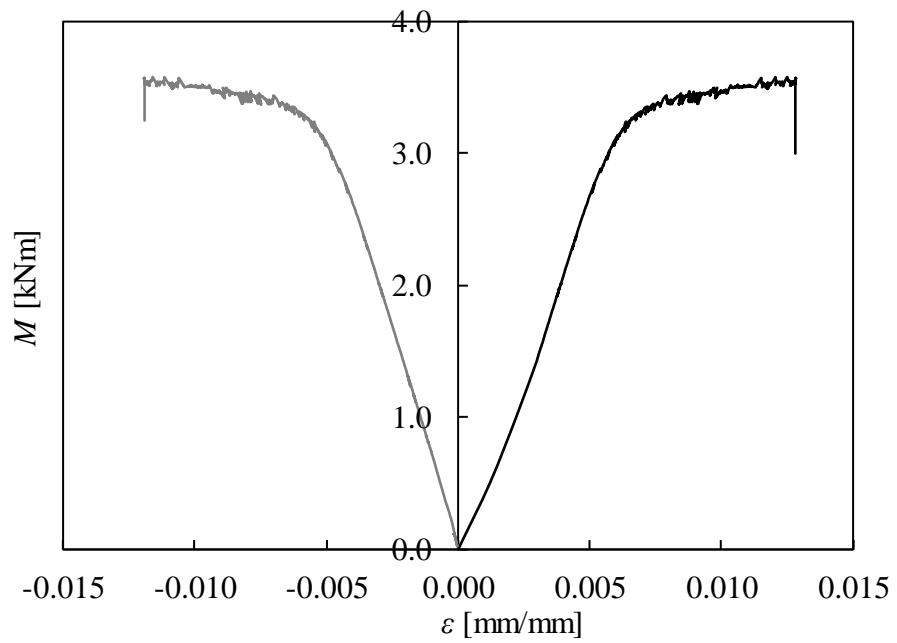


Figure 4.60: Bending moment–rotation curves of CFAT specimens beam obtained from three-point bending.

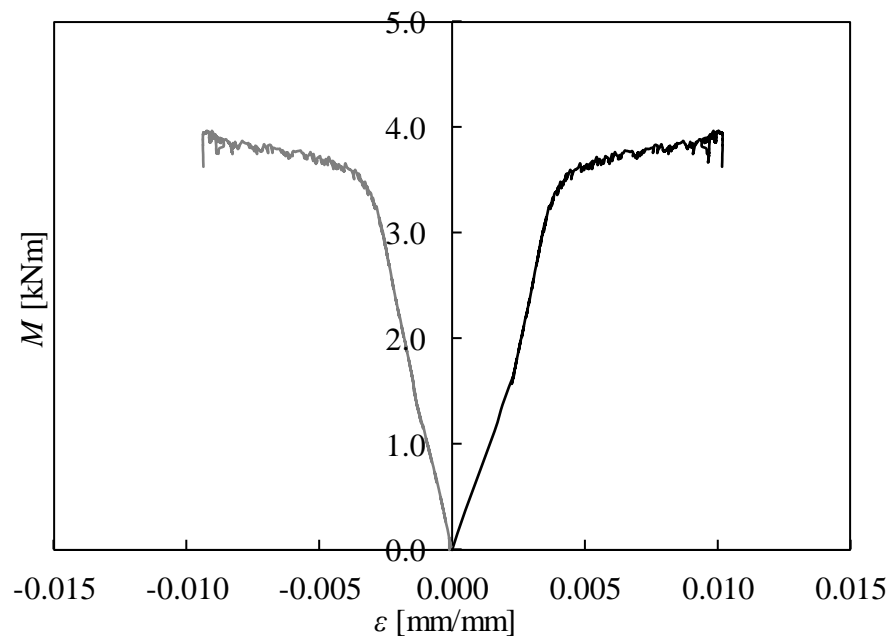
The obtained bending moment–longitudinal strain (M – ε) curves of the tested specimens are plotted in Figure 4.61. In these graphs, the horizontal axis represents the longitudinal strains ε obtained from the strain gauges attached at the top and bottom flanges of the aluminium tube at the midspan. It is noted that the compressive (measured by the strain gauge at the top flange) and tensile strains (measured by the strain gauge at the bottom flange) are defined as negative and positive strains, respectively. It can be seen that the absolute values of the tensile strains are higher than the compressive ones signifying that the neutral axis shifts upward of the centroid of the cross-section and towards the top flange of the aluminium tube. This may stem from the fact that the concrete infill significantly improves the resistance of the compressive zone of the cross-section. Therefore, the neutral axis shifts towards to the compressive fibre of the cross-section to maintain the equilibrium of the forces acting on the cross-section. The same observation is also reported in [146].



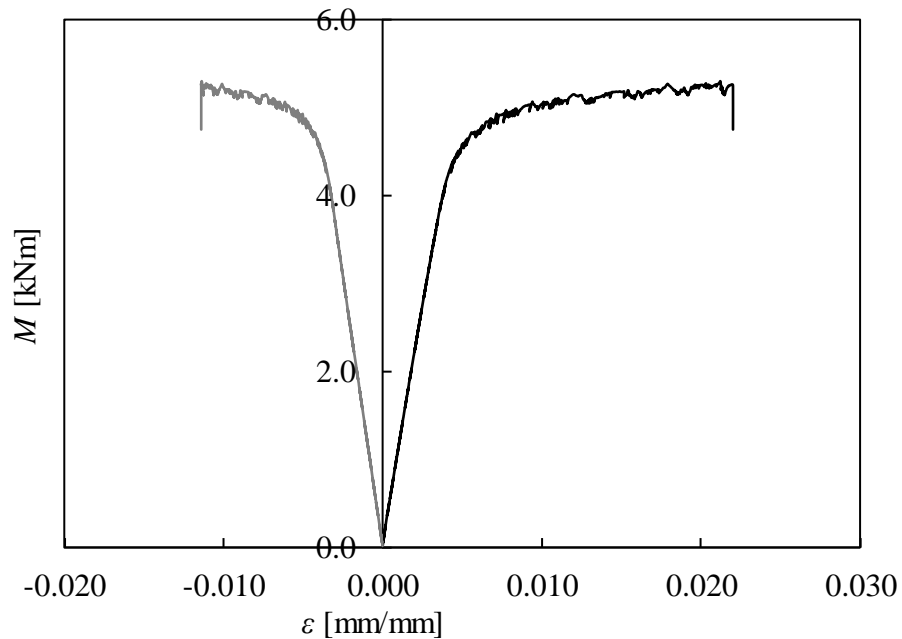
(a) 50.8×50.8×1.6-C



(b) 50.8×50.8×2.7-C



(c) 50.8×50.8×3.3-C



(d) 50.8×50.8×4.8-C

Figure 4.61: Bending moment–longitudinal strain curves of CFAT beam specimens obtained from three-point bending tests.

4.4.4. Channel cross-sections

A total of 7 C-sections with various geometrical dimensions were considered in the present study. The geometrical dimensions of the investigated cross-sections were selected so that to cover a wide variety of plate slendernesses ranging from 1.92-8.4 (see Table 4.31). These values enabled to examine the minor axis bending behaviour of C-sections across the four cross-sectional Classes (Classes 1-4) specified in EN 1999-1-1 [5]. Each cross-section was tested in both the “n”, i.e., maximum compressive stresses in web/maximum tensile stresses in flange tips (see Figure 4.62(a)), and the “u”, i.e., maximum compressive stresses in flange tips/maximum tensile stresses in web (see Figure 4.62(b)), bending orientations. Prior to testing, the dimensions of the beam specimens were measured carefully and are set out in Table 4.31, where D is the outer web depth, B is the outer flange width, t_w is the web thickness, t_f is the flange thickness and L is the total specimen’s length. The adopted notation is also shown in Figure 4.62, where the elastic (ENA) and plastic (PNA) neutral axes are also depicted. The specimens’ designation was defined according to the nominal geometric dimensions ($D - B - t$)

followed by the letter “u” or “n” which signifies the bending orientation. The engineering stress–strain curves (σ – ε) obtained from the tensile coupon tests for each examined cross-section are depicted in Figure 4.63. Moreover, the average measured material properties are listed in Table 4.26. Since the present study deals with minor axis bending and the flanges are under stress gradient, lateral torsional buckling is precluded and thereby only the local geometric imperfections were measured. The maximum measured local imperfection amplitude ω_l for each beam specimen is taken as the maximum value of the measured local imperfection amplitudes of both flanges and web and is listed in Table 4.31.

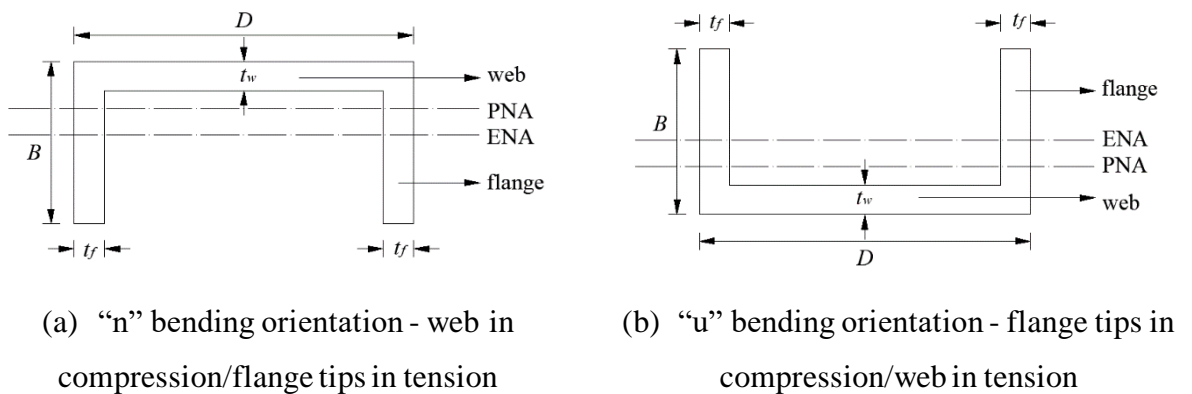


Figure 4.62: Adopted notation of the C-sections of the simply-supported beams.

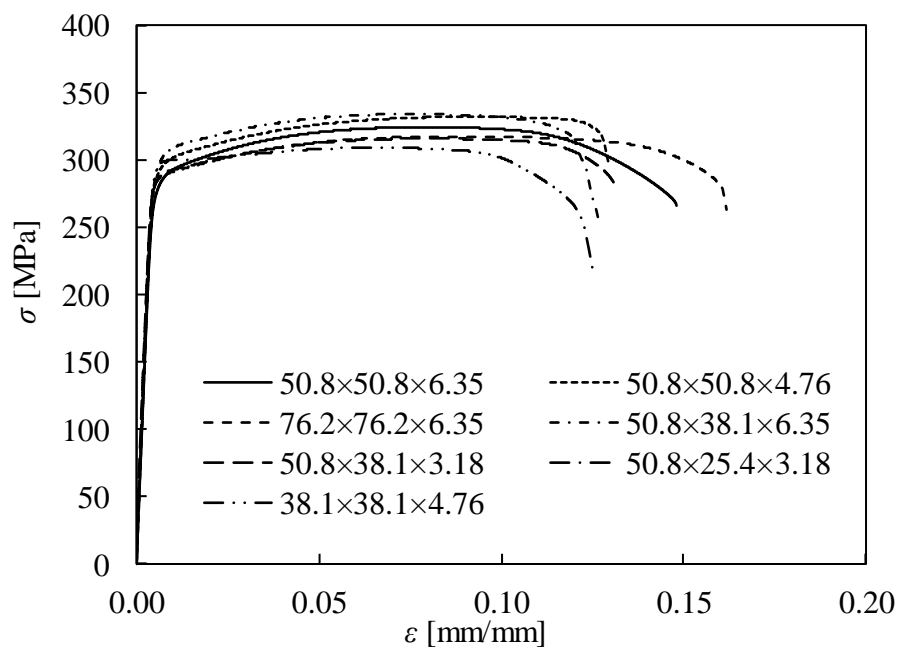


Figure 4.63: Stress-strain curves of the C-sections of the simply-supported beams.

Table 4.31: Mean measured geometrical dimensions and local geometric imperfections of the tested C-section simply-supported beams.

Specimen	orientation	D (mm)	B (mm)	t_w (mm)	t_f (mm)	L (mm)	ω_l (mm)
50.8×50.8×6.35-n	compression in web	50.92	50.84	6.34	6.29	1000.20	0.18 ($t_f/34$)
50.8×50.8×6.35-u	compression in flange tips	51.07	50.78	6.36	6.27	1000.20	0.18 ($t_f/35$)
50.8×50.8×4.76-n	compression in web	50.89	50.56	4.73	4.77	1000.80	0.30 ($t_f/16$)
50.8×50.8×4.76-u	compression in flange tips	50.88	50.62	4.73	4.77	1000.90	0.32 ($t_f/15$)
76.2×76.2×6.35-n	compression in web	76.28	76.26	6.33	6.24	1000.80	0.32 ($t_f/20$)
76.2×76.2×6.35-u	compression in flange tips	76.44	76.28	6.27	6.27	1000.80	0.27 ($t_f/23$)
50.8×38.1×6.35-n	compression in web	50.89	38.13	6.34	6.36	1001.00	0.35 ($t_f/18$)
50.8×38.1×6.35-u	compression in flange tips	50.88	38.03	6.33	6.28	1001.00	0.35 ($t_f/18$)
50.8×38.1×3.18-n	compression in web	50.81	37.95	3.15	3.11	1000.50	0.22 ($t_f/14$)
50.8×38.1×3.18-u	compression in flange tips	50.77	37.95	3.13	3.15	1000.80	0.23 ($t_f/14$)
50.8×25.4×3.18-n	compression in web	50.68	25.43	3.11	3.11	1001.00	0.24 ($t_f/13$)
50.8×25.4×3.18-u	compression in flange tips	50.71	25.31	3.21	3.17	1001.00	0.21 ($t_f/15$)
38.1×38.1×4.76-n	compression in web	37.97	37.97	4.64	4.64	1000.90	0.22 ($t_f/21$)
38.1×38.1×4.76-u	compression in flange tips	37.98	37.93	4.71	4.60	1001.00	0.16 ($t_f/29$)

Table 4.32: Material properties of C-sections obtained from tensile coupon tests.

Specimen	E (MPa)	$\sigma_{0.1}$ (MPa)	$\sigma_{0.2}$ (MPa)	σ_u (MPa)	ϵ_u (mm/mm)	ϵ_f (mm/mm)	n	$\sigma_u/\sigma_{0.2}$
50.8×50.8×6.35	66729	275	282	324	0.07	0.14	27.6	1.15
50.8×50.8×4.76	69302	284	292	332	0.09	0.13	25.0	1.14
76.2×76.2×6.35	70885	280	286	317	0.09	0.16	32.7	1.11
50.8×38.1×6.35	67009	290	298	334	0.08	0.13	25.5	1.12
50.8×38.1×3.18	67500	280	287	316	0.08	0.13	28.1	1.10
50.8×25.4×3.18	66408	276	282	295	0.06	0.11	32.2	1.05
38.1×38.1×4.76	68744	290	297	309	0.07	0.13	29.1	1.04

A series of 14 tests was performed aiming to investigate the minor axis flexural response of aluminium alloy C-sections. Figure 4.64 and Figure 4.65 illustrate a schematic diagram and a photograph of the four-point test setup, respectively. The specimens had a clear span equal to 900 mm, whilst the span-to-height ratio was over 10 [227,228]. In line with past studies [228], underpinning bolts were inserted between the flanges and G-clamps were located onto the outer faces of the flanges at the loading points and supports, to prevent web crippling occurrence. Moreover, to spread the loading uniformly and avoid local buckling of both flanges at the loading points, 100 mm × 70 mm × 10 mm steel plates were welded to the steel rollers [227,228]. During testing, the position of the neutral axis (NA) was monitored through three linear electrical resistance strain gauges attached at the midspan. Particularly, two strain gauges were affixed at both flanges at 10 mm from the tip and the third one at the middle of the web, as shown in Figure 4.64.

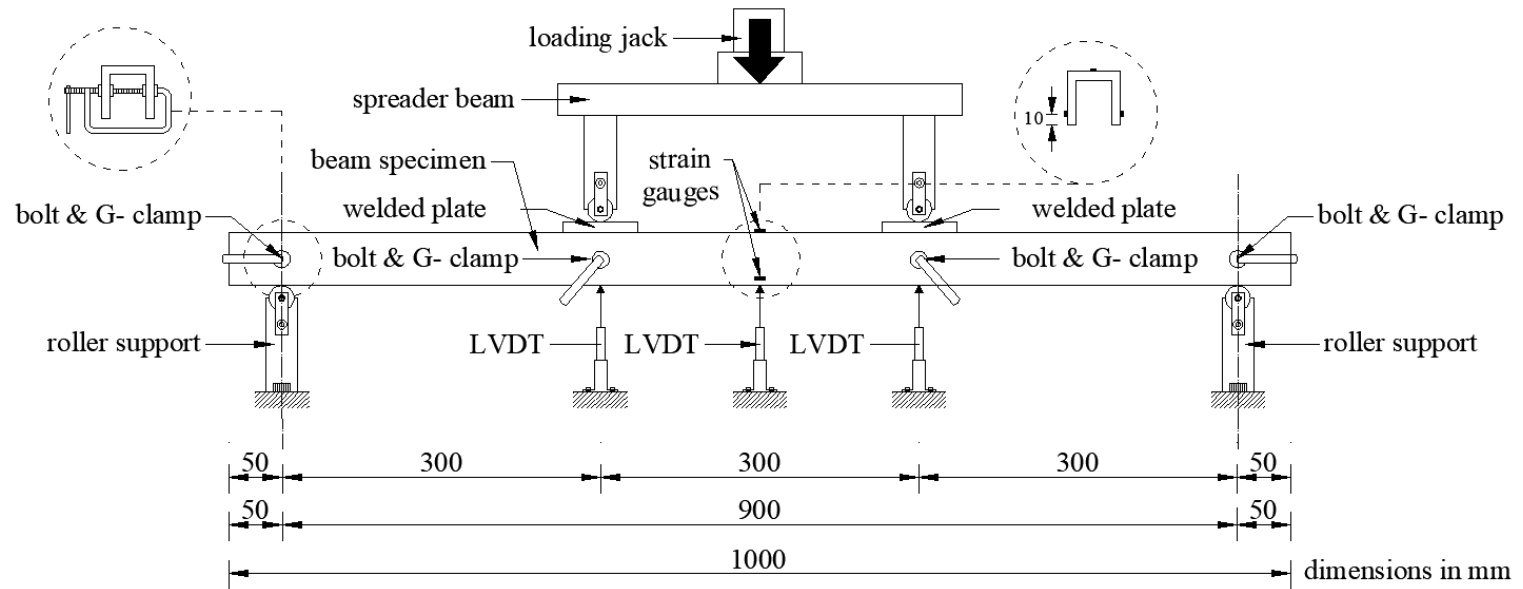


Figure 4.64: Schematic illustration of the four-point bending test setup.

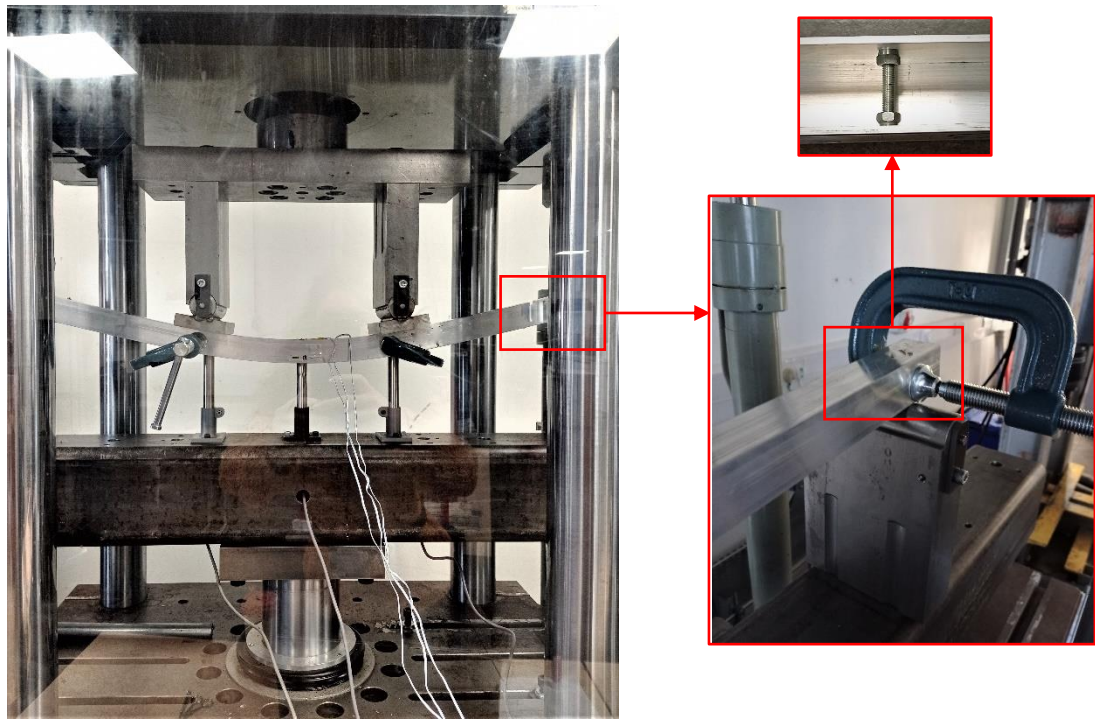


Figure 4.65: Typical four-point bending test setup.

Table 4.33 reports the key results of C-section beams obtained from four-point bending tests, including the ultimate experimental bending moment $M_{u,Exp}$ and the calculated elastic M_{el} and plastic M_{pl} cross-sectional bending moment resistances. To facilitate the comparison, the moment-curvature responses derived from tests are plotted in a non-dimensional format, as shown in Figure 4.66; the moment in the midspan is normalised by the plastic moment resistance M_{pl} , which is taken by multiplying the 0.2 % proof (yield) stress acquired from the tensile coupon tests by the plastic section modulus about the minor axis (also shown in Figure 4.62). The curvature κ in the constant moment area of the beam is determined according to [226] and is normalised by κ_{pl} which is the elastic component of the curvature corresponding to M_{pl} .

The experimentally obtained normalised curvature $\kappa_{u,Exp}/\kappa_{pl}$ for each tested beam is also listed in Table 4.33. The same table also provides the cross-sections' Class according to EN 1999-1-1 [5] and the corresponding slenderness ratios β_w/ε and β_f/ε for internal web in compression and outstand flange in bending, respectively. In the slenderness ratios expressions, $\beta_w=d/t_w$ and $\beta_f=0.7b/t_f$, are the slenderness parameters where d is the compressed flat web width and b is the flat flange width. It is noteworthy that the difference in response of the specimen $50.8\times 50.8\times 6.35$ (Figure 4.66(a)) under the two

different bending orientations can be attributed to the fact that it is classified as Class 2 in “n” bending orientation and as Class 3 in “u” orientation, hence reaching larger normalised moment in the first case.

Table 4.33: Key results obtained from the four-point bending tests.

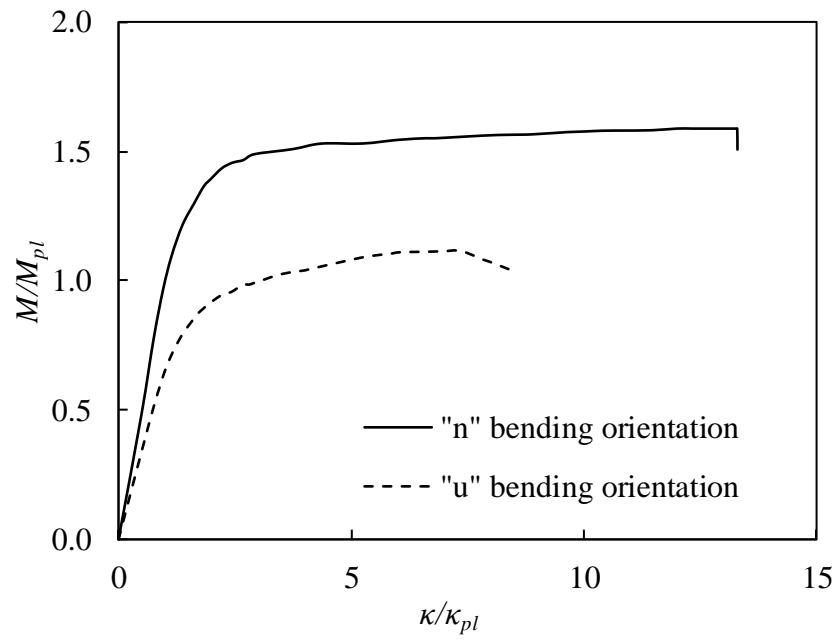
Specimen	Internal web in compression		Outstand flange in bending		M_{el} (kNm)	M_{pl} (kNm)	M_{pl}/M_{el}
	β_w/ε	Class	β_f/ε	Class			
50.8×50.8×6.35-n	2.11	1	4.31	2	2.03	3.49	1.73
50.8×50.8×6.35-u	-*	-*	5.22	3	2.02	3.49	1.73
50.8×50.8×4.76-n	3.26	1	6.29	4	1.58	2.76	1.74
50.8×50.8×4.76-u	-*	-*	7.32	4	1.50	2.64	1.75
76.2×76.2×6.35-n	2.38	1	4.58	3	4.48	7.86	1.76
76.2×76.2×6.35-u	-*	-*	8.39	4	4.20	7.45	1.77
50.8×38.1×6.35-n	1.92	1	2.81	1	1.23	2.18	1.78
50.8×38.1×6.35-u	-*	-*	3.81	2	1.21	2.16	1.78
50.8×38.1×3.18-n	5.28	1	7.23	4	0.58	1.05	1.81
50.8×38.1×3.18-u	-*	-*	8.27	4	0.55	1.00	1.81
50.8×25.4×3.18-n	4.65	1	4.46	3	0.28	0.51	1.80
50.8×25.4×3.18-u	-*	-*	5.19	3	0.28	0.51	1.80
38.1×38.1×4.76-n	2.23	1	4.59	3	0.87	1.51	1.73
38.1×38.1×4.76-u	-*	-*	5.51	3	0.88	1.51	1.73

* Internal web is tension in the “u” bending orientation

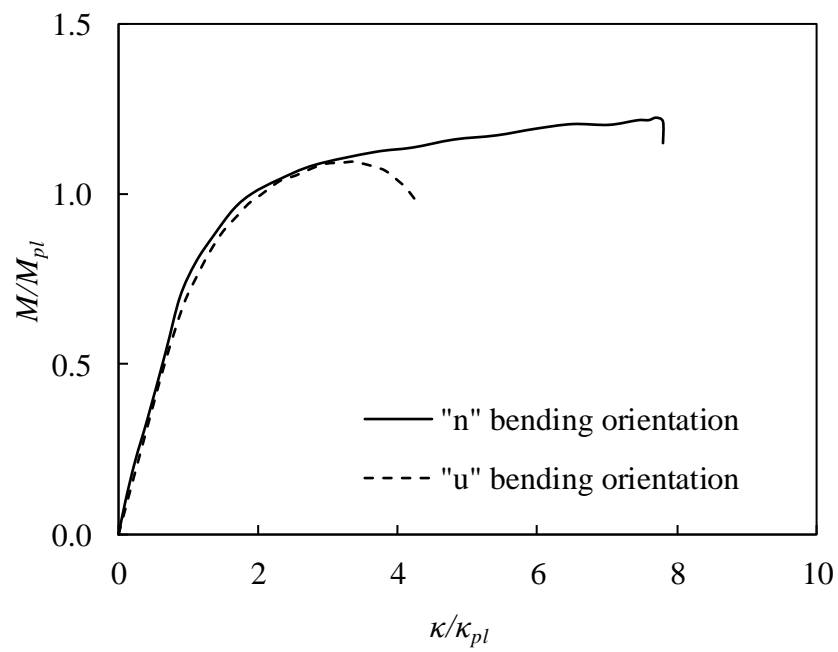
Table 4.34: Key results obtained from the four-point bending tests (continued).

Specimen	$M_{u,Exp}$ (kNm)	$M_{u,Exp}/M_{el}$	$M_{u,Exp}/M_{pl}$	$\kappa_{u,Exp}/\kappa_{pl}$
50.8×50.8×6.35-n	5.56	2.74	1.59	13.30
50.8×50.8×6.35-u	3.91	1.93	1.12	8.39
50.8×50.8×4.76-n	3.36	2.12	1.22	7.80
50.8×50.8×4.76-u	2.90	1.93	1.10	4.30
76.2×76.2×6.35-n	10.30	2.30	1.31	24.00
76.2×76.2×6.35-u	8.19	1.95	1.10	5.60
50.8×38.1×6.35-n	2.83	2.10	1.30	11.40
50.8×38.1×6.35-u	2.75	2.19	1.17	7.15
50.8×38.1×3.18-n	1.35	2.31	1.28	6.41
50.8×38.1×3.18-u	1.12	2.03	1.12	2.79
50.8×25.4×3.18-n	0.59	2.11	1.17	7.60
50.8×25.4×3.18-u	0.56	1.98	1.10	5.66
38.1×38.1×4.76-n	1.69	1.93	1.12	7.15
38.1×38.1×4.76-u	1.63	1.86	1.08	5.50

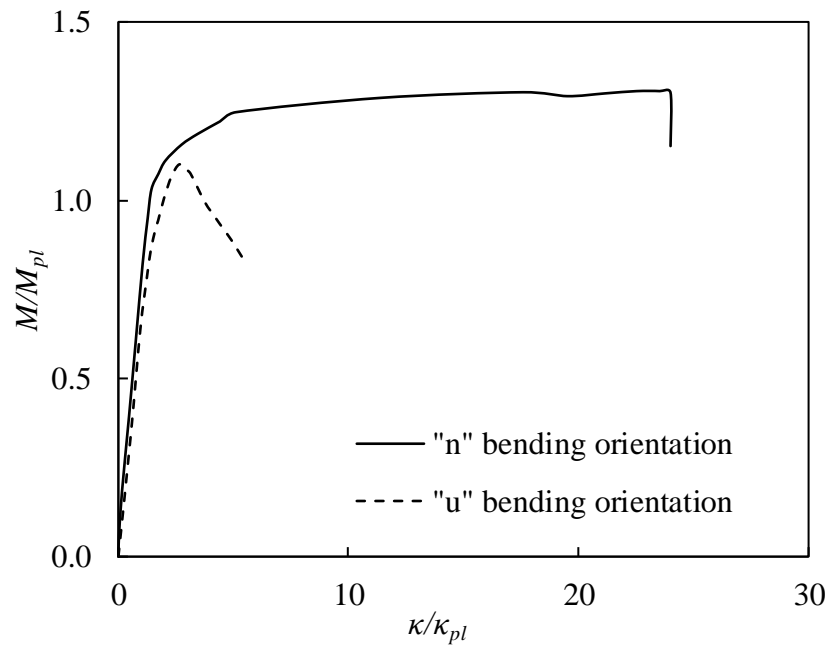
* Internal web is tension in the “u” bending orientation



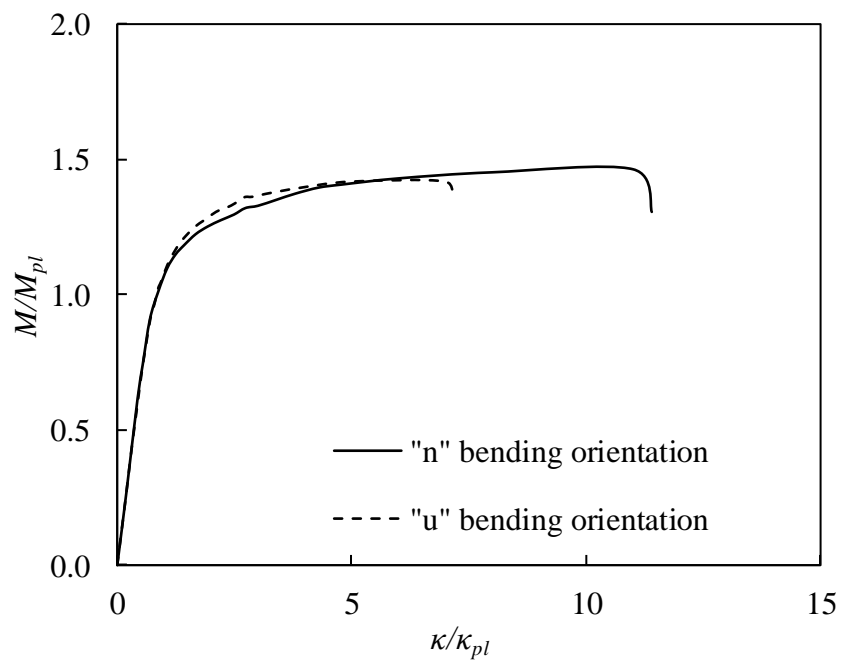
(a) $50.8 \times 50.8 \times 6.35$



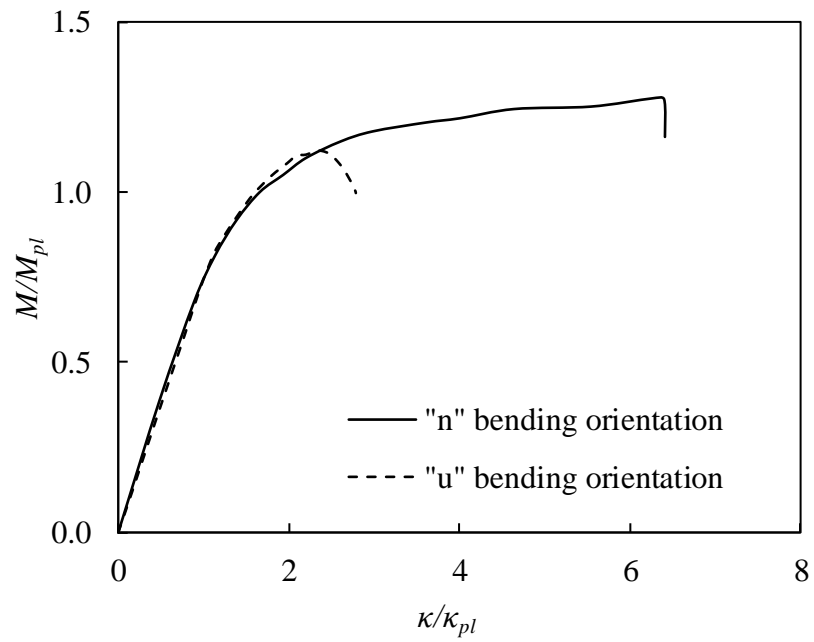
(b) $50.8 \times 50.8 \times 4.76$



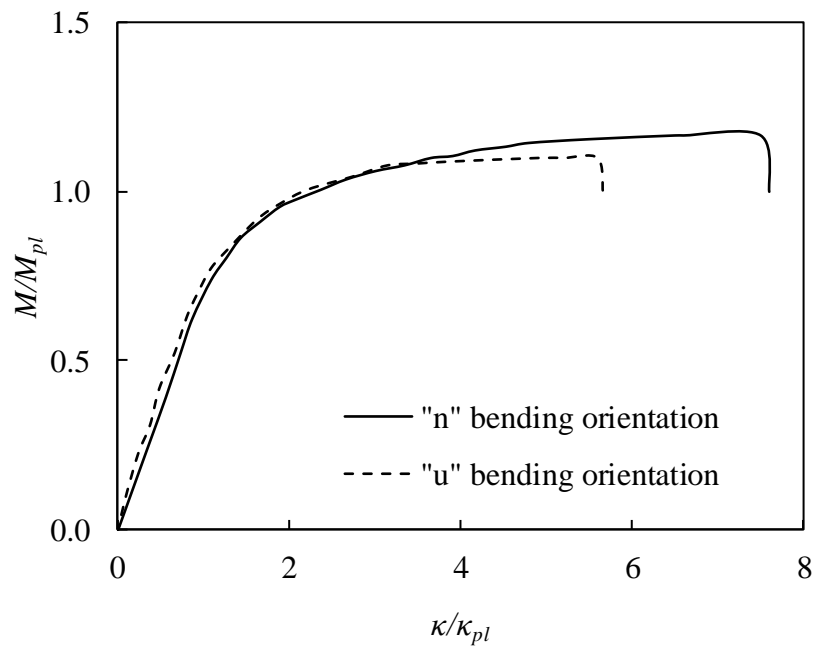
(c) $76.2 \times 76.2 \times 6.35$



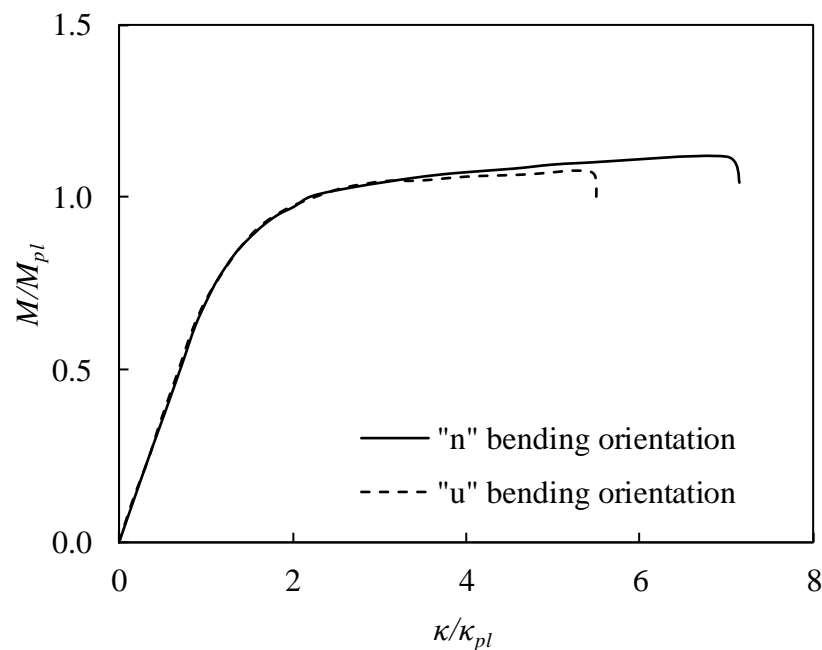
(d) $50.8 \times 38.1 \times 6.35$



(e) 50.8×38.1×3.18



(f) 50.8×25.4×3.18

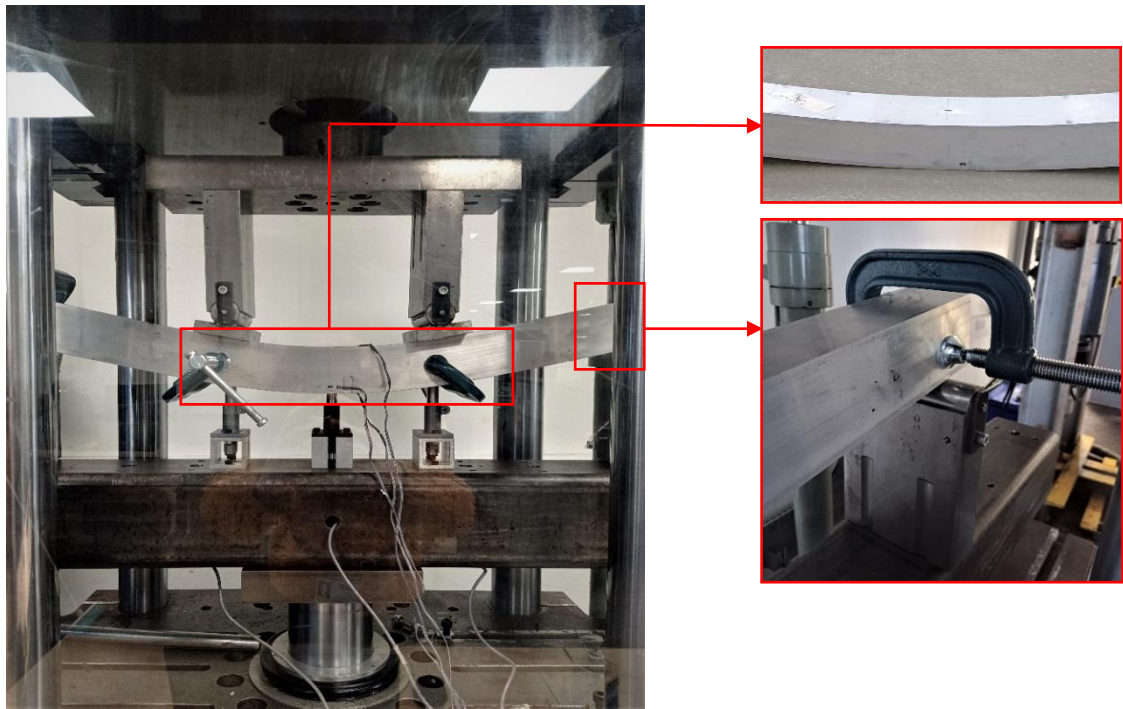


(g) 38.1×38.1×4.76

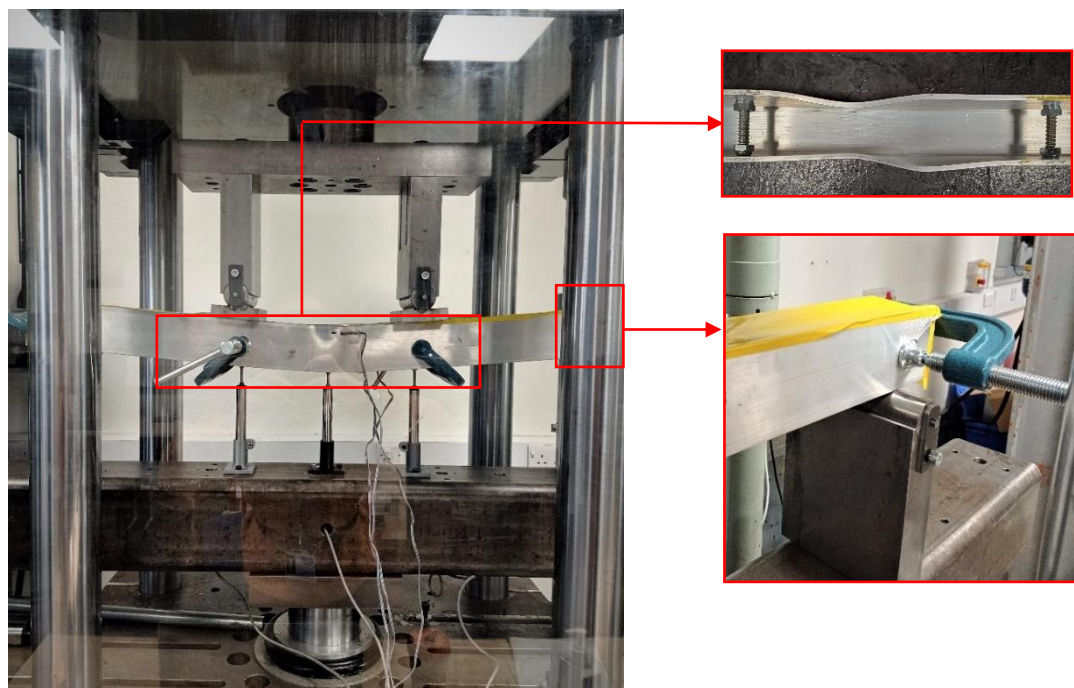
Figure 4.66: Normalised moment–curvature responses of C-section beam specimens obtained from four-point bending tests.

The governing failure modes for beam specimens under “n” and “u” bending orientation were material yielding (Figure 4.67(a)) and local buckling (Figure 4.67(b)), respectively. The failure modes of all beam specimens are presented in Figure 4.68. As can be seen, all specimens exhibited significant in-plane bending deformations prior to failure. In the specimens under “n” orientation, the stockier web is in compression and the slenderest constituent element, i.e., outstand flanges, are subjected to stress gradient with the tips in tension. This results in higher deformations without any evidence of local buckling and higher curvature values compared to their counterparts bent in the “u” orientation (see also Figure 4.66) and the failure occurs due to material yielding. In specimens under “u” orientation, the stockier web is in tension and the slenderer outstand flange tips in compression, thereby leading to failure due to pronounced local buckling of both outstand flanges. The same was also observed in similar past studies conducted on stainless and high strength steel C-sections [215,226-228]. Moreover, the quite steep softening branch of the curves of the 50.8×50.8×4.76-u, 76.2×76.2×6.35-u and 50.8×38.1×3.18-u specimens indicates a brittle post-ultimate behaviour, i.e., low

capability for inelastic deformations with significant loss of strength. This was anticipated since these beam specimens comprised slender sections.



(a) Material yielding of 76.2×76.2×6.35-n specimen



(b) Local buckling in the flanges of 76.2×76.2×6.35-u specimen

Figure 4.67: Typical failure modes of C-section beam specimens obtained from four-point bending tests.



(a) $50.8 \times 50.8 \times 6.35$ -n



(b) $50.8 \times 50.8 \times 6.35$ -u



(c) $50.8 \times 50.8 \times 4.76$ -n



(d) $50.8 \times 50.8 \times 4.76$ -u



(e) $76.2 \times 76.2 \times 6.35$ -n



(f) $76.2 \times 76.2 \times 6.35$ -u



(g) $50.8 \times 38.1 \times 6.35$ -n



(h) $50.8 \times 38.1 \times 6.35$ -u



(i) $50.8 \times 38.1 \times 3.18$ -n



(j) $50.8 \times 38.1 \times 3.18$ -u



(k) $50.8 \times 25.4 \times 3.18$ -n



(l) $50.8 \times 25.4 \times 3.18$ -u



(m) $38.1 \times 38.1 \times 4.76$ -n



(n) $38.1 \times 38.1 \times 4.76$ -u

Figure 4.68: Failure modes of C-section specimens obtained from four-point bending tests.

4.5. Continuous beams

Aiming to estimate the rotational capacity and the potential for moment redistribution of aluminium alloy indeterminate beams, the BAT cross-sections employed for the simply-supported beam tests, reported in Subsection 4.4.1. were subjected to five-point bending. It is noteworthy that since the objective of this study is to explore the possibility of plastic design in aluminium alloy indeterminate structures, the examined cross-sections were chosen to be Class 1, i.e., capable of developing their collapse resistance without presence

of local instabilities, according to EN 1999-1-1 [5]. The geometric measured dimensions for each tested cross-section are presented in Table 4.35, where D is the outer web depth, B is the outer flange width and t is the thickness. The specimens' designation is defined according to their nominal geometric dimensions. For instance, the label “63.5×38.1×3.25” refers to a beam specimen with outer depth $D=63.5$ mm, outer width $B=38.1$ mm and thickness $t=3.25$ mm. The engineering stress–strain curves (σ – ε) obtained from the tensile coupon tests for each examined cross-section are depicted in Figure 4.37. Moreover, the average measured material properties are listed in Table 4.23. In the current study, only the local geometric imperfections were measured because the investigated cross-sections have closed shape and short length, precluding the occurrence of lateral-torsional buckling. The measured local imperfection amplitudes denoted ω_l are also reported in Table 4.35.

Table 4.35: Mean measured geometrical dimensions and local geometric imperfections of the tested BAT continuous beams.

Specimen	D (mm)	B (mm)	t (mm)	ω_l (mm)
63.5×38.1×3.25	63.57	38.04	3.25	0.21 ($t/15$)
50.8×38.1×3.25	50.99	38.30	3.45	0.14 ($t/24$)
50.8×25.4×3.25	51.15	25.48	3.36	0.20 ($t/16$)
38.1×25.4×3.25	38.22	25.47	3.31	0.17 ($t/19$)
38.1×19.1×3.25	38.11	19.05	3.37	0.50 ($t/7$)

The continuous beam tests were executed following the methodology described in Subsection 3.2.6. The investigated specimens were two-span continuous beams with a total length of 2000 mm. Each specimen overhung each end by 100 mm beyond the centerlines of the supports, resulting in a clear beam span of 900 mm. Furthermore, six linear electrical resistance strain gauges were affixed to the top and bottom flange of the cross-section at 50 mm distance from the loading points and the central supports to ensure that the end rollers did not provide any axial restraint. Figure 4.69 illustrates a schematic view of the test arrangement and the corresponding employed instrumentation. It's worth mentioning that wooden blocks were inserted into the tubular specimens at the loading points and the supports to prevent web crippling occurrence (Figure 4.69). A photograph of the overall set-up is also displayed in Figure 4.70.

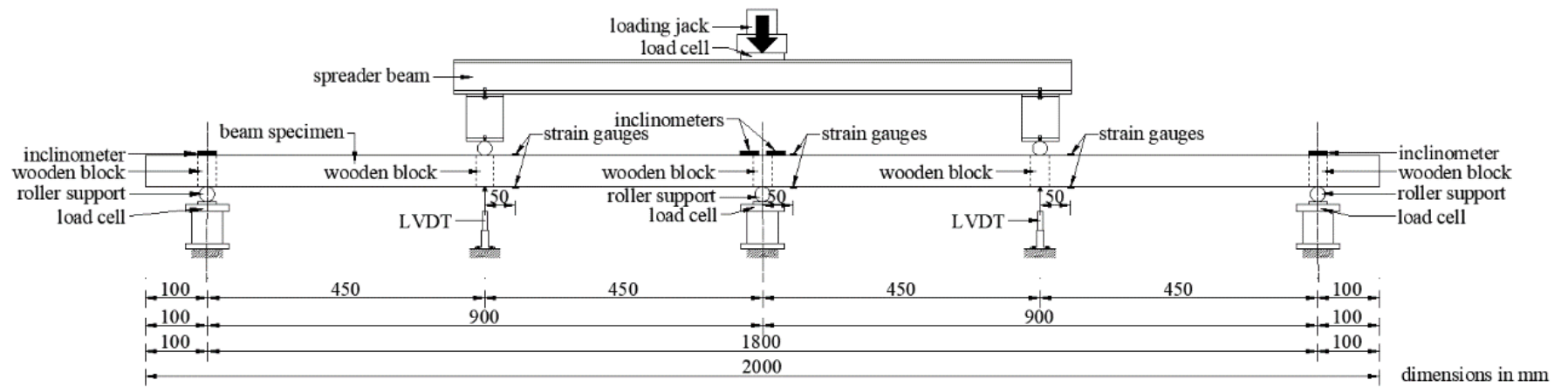


Figure 4.69: Schematic illustration of the continuous beam test arrangement and instrumentation.

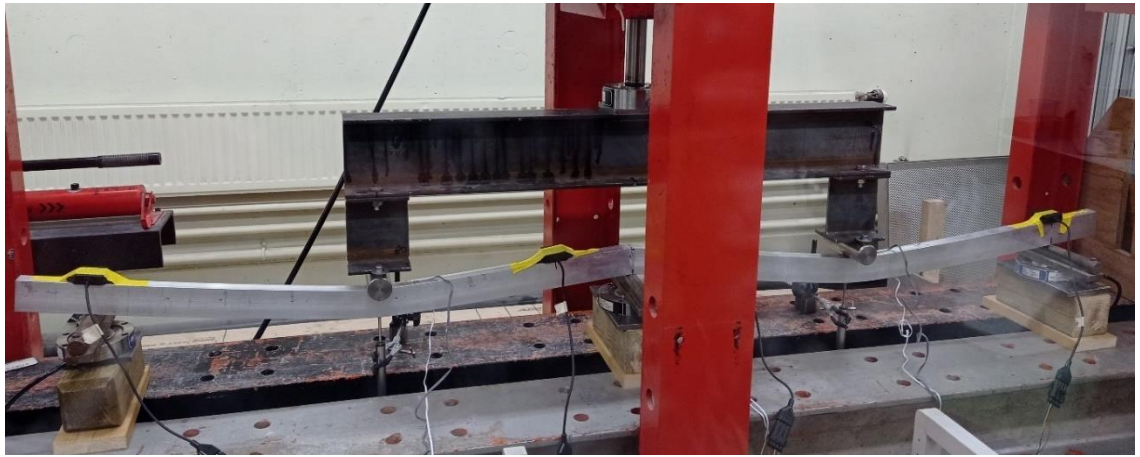


Figure 4.70: Typical continuous beam test set-up.

The test key response characteristics are summarised in Table 4.36, where $F_{u,Exp}$ is the ultimate load at collapse stage, W_u is the midspan deflection at collapse stage, taken as average value of both LVDTs, and θ_u is the end rotation at collapse stage, arisen in the most heavily stressed cross-section. In the same table, the theoretical collapse load F_{coll} which was determined using classical plastic analysis theory, is also reported. The experimental response for each tested beam specimen is depicted in Figure 4.71, where the applied load is plotted against the average measured midspan deflection W . Moreover, in Figure 4.72, the applied load normalised by the theoretical collapse load F_{coll} is plotted against the average measured end rotation θ . According to the obtained curves plotted in Figures 4.71 and 4.72, all specimens initially exhibit a linear response. Following, they exceed their plastic moment resistance and almost all (except from $63.5 \times 38.1 \times 3.25$ specimen) maintain it throughout large inelastic deformations denoting high deformation capacity.

The observed failure mechanism of all the investigated specimens consisted of three distinct plastic hinges. As was expected the first plastic hinge was formed at the central support which was the most heavily stressed cross-section. Further spread of plasticity and moment redistribution occurrence resulted in two additional plastic hinges at both loading points, as shown in Figure 4.73. Figure 4.74 presents the evolution of the M_{sup}/M_{span} ratio with increasing average vertical displacement for the $63.5 \times 38.1 \times 3.25$ and $50.8 \times 38.1 \times 3.25$ specimens. The M_{sup}/M_{span} ratio corresponds to the experimental bending moment of the central support over the bending moment of the midspan. This

ratio is utilised to evaluate whether the theoretical response based on elastic-perfectly plastic analysis is in line with the experimental response. In Figure 4.74, the horizontal lines of 1.2 and 1.0 which correspond to the theoretical moment ratios derived from elastic and rigid plastic analysis, respectively, are also included. As can be observed, the initial experimental moment ratio is equal to the theoretical moment ratio evaluated from elastic analysis (i.e., horizontal line of the elastic limit). For increasing deformation, the experimental moment ratio shifts towards the theoretical plastic ratio (i.e., horizontal line of the plastic limit) after yielding, spread of plasticity and moment redistribution occurrence. Within the same graphs, the displacement at which collapse occurs is also noted with the vertical dotted lines. The results demonstrate the initially elastic distribution of the bending moments changing to significant redistribution with increasing displacement towards equal moments at collapse.

Table 4.36: Key results obtained from continuous beam tests.

Specimen	$F_{u,Exp}$ (kN)	F_{coll} (kN)	W_u (mm)	θ_u (deg)
63.5× 38.1×3.25	43.98	42.01	18.60	3.95
50.8× 38.1×3.25	39.38	36.26	48.53	7.89
50.8× 25.4×3.25	30.70	26.76	36.99	6.60
38.1×25.4×3.25	19.80	17.01	66.16	11.20
38.1× 19.1×3.25	17.20	14.63	61.92	9.45

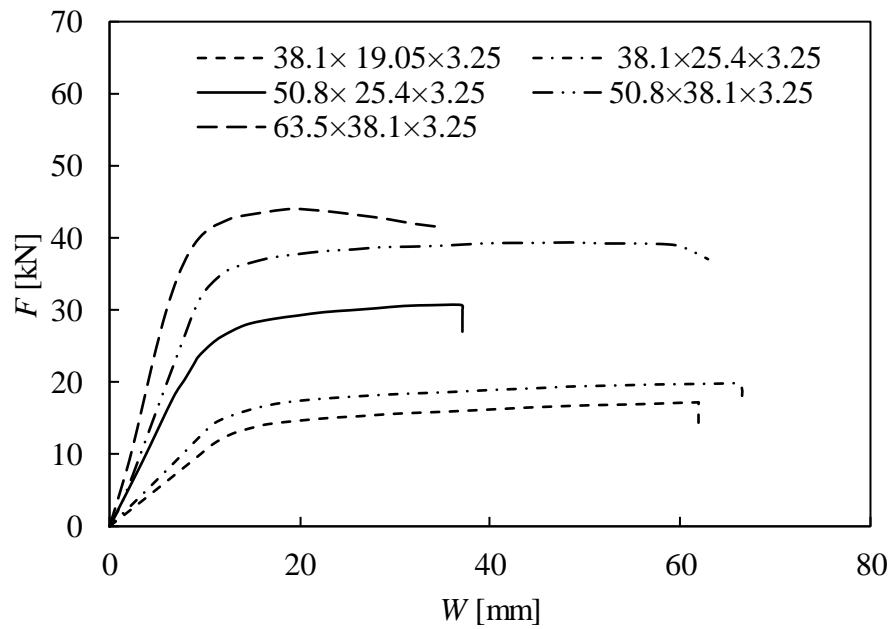


Figure 4.71: Load–displacement responses of BAT specimens obtained from continuous beam tests.

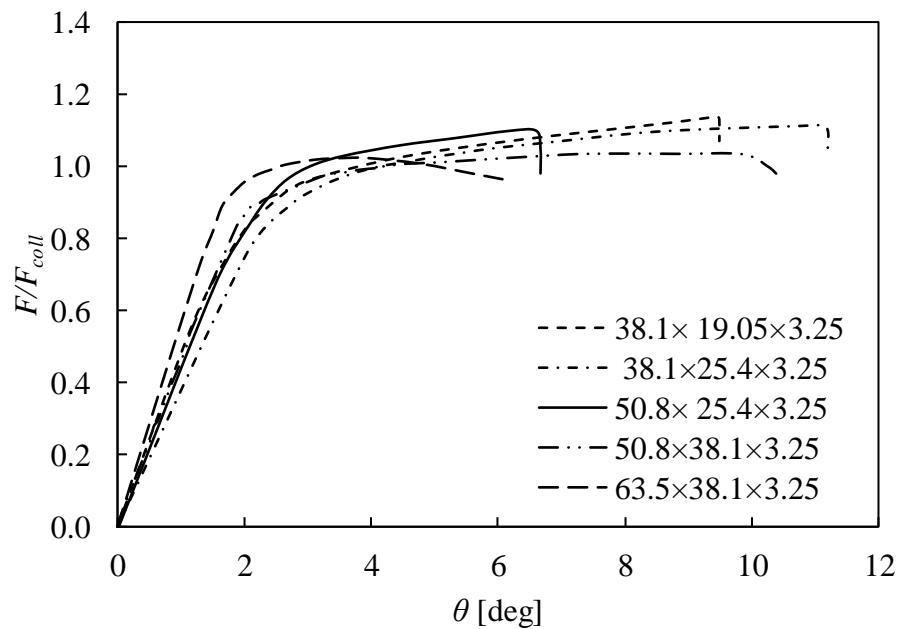


Figure 4.72: Normalised load–end rotation responses of BAT specimens obtained from continuous beam tests.

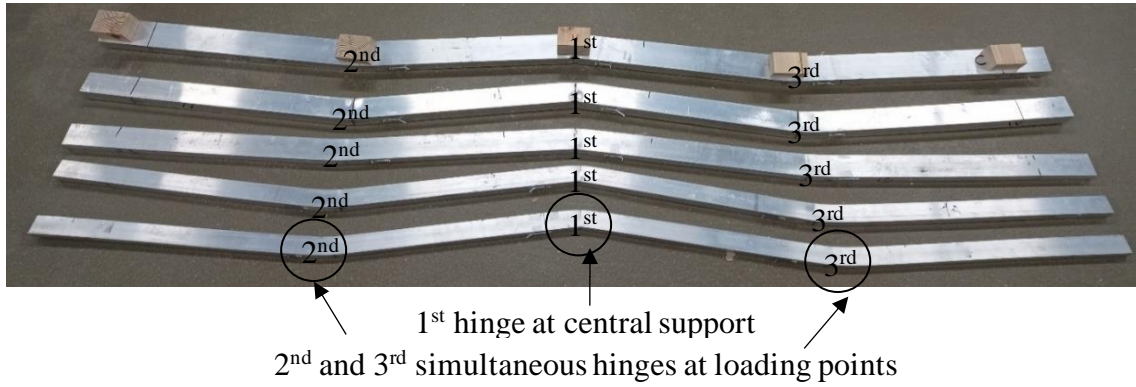
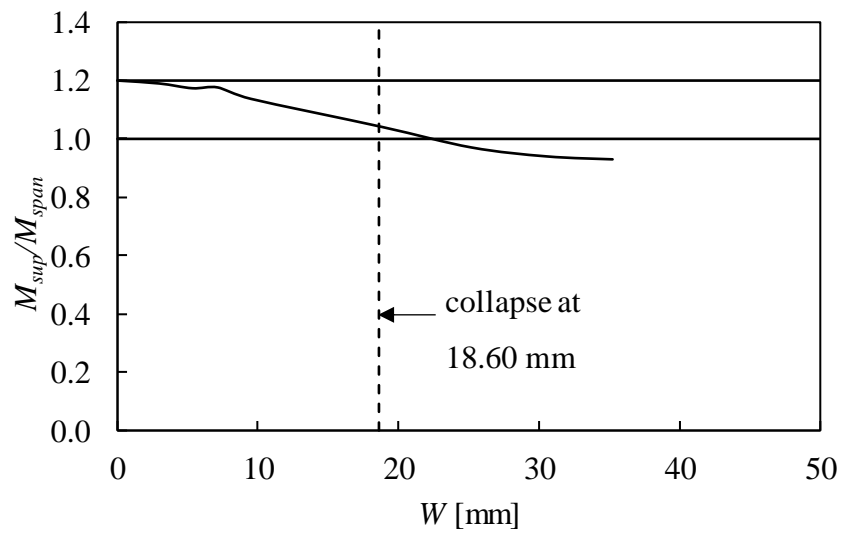
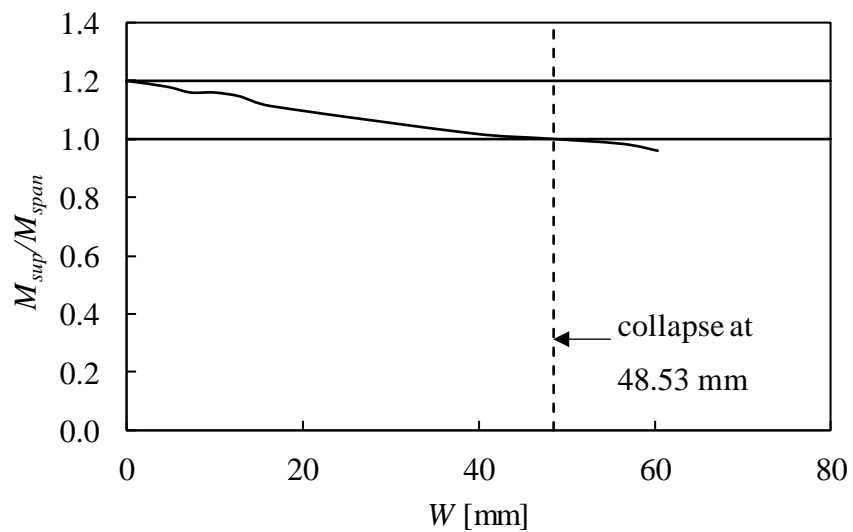


Figure 4.73: Failure modes of BAT specimens obtained from continuous beam tests.



(a) 63.5×38.1×3.25



(b) 50.8×38.1×3.25

Figure 4.74: Evolution of the support to span moment ratio with increasing displacement.

Summary

This chapter presented the experimental investigation on the behaviour of aluminium alloy structural elements. A total of

- 22 fix-ended stub columns (8 having BAT sections, 8 having CFAT sections and 6 having C-sections),
- 24 pin-ended columns (8 having BAT sections, 8 having CFAT sections and 8 having C-sections),
- 32 simply-supported beams (9 having BAT sections under three-point bending configuration, 5 having BAT sections under four-point bending configuration, 4 having CFAT sections under three-point bending configuration and 14 having C-sections under four-point bending configuration) and
- 5 BAT continuous beams.

A number of tensile coupon tests and compressive tests on concrete cubes were also conducted to determine the mechanical properties of the examined 6082-T6 heat-treated aluminium alloy and the concrete infill of the CFAT specimens, respectively. The experimental ultimate strengths in combination with those obtained numerically and are reported in Chapter 5, were used to assess the accuracy and applicability of the current design rules and methods and suggest design recommendations.

CHAPTER 5

Validation of the finite element models

5.1. Introduction

The current chapter describes in detail the numerical investigation of the structural response of aluminium alloy structural elements. In parallel with the experimental studies, series of FE modelling studies were carried out to supplement the experimentally obtained data sets providing a deeper understanding about the structural response of the considered cross-sections. Particularly, an extensive parametric study was performed to investigate further the cross-sectional response of channel cross-sections (Section 5.2.). FE modelling studies were also undertaken to generate additional structural performance data for the buckling behaviour of bare tubular, concrete-filled tubular and channel cross-sections (Section 5.3.). Moreover, the flexural behaviour of channel cross-sections under four-point bending configuration was better clarified through an extensive series of numerical analyses (Section 5.4.). Finally, the experimental results for the bare tubular cross-sections obtained from the three- and four-point bending tests as well as the two-span continuous beam tests were utilised for a comprehensive parametric study aimed to extend the pool of performance data for aluminium alloy indeterminate structures (Section 5.5.).

5.2. Fix-ended stub columns

It was decided to investigate further through a numerical modelling study only the cross-sectional response of C-sections. The reason for this was to generate additional data across a wide range of cross-sectional slenderness ratios β_f/ϵ (covering the four Classes of EC9) and thus gaining a better understanding of the cross-sectional response of C-sections.

5.2.1. Channel cross-sections

FE models of C-section fix-ended stub column specimens were developed adopting the assumptions described in Subsection 3.3. An average element size of 3 mm was applied resulted from a mesh sensitivity study achieving accurate numerical results with a reasonable computational time. To simulate the fix-ended boundary conditions, a reference point was created on the centroid of the cross-section for each column end. All degrees of freedom were restrained at both reference points, apart from the vertical translation at the loaded end. The stiffening effect provided by the underpinning bolts and the G-clamps was also taken into consideration assigning distributing coupling constraints at both end cross-sections to ensure that they remain undeformed during loading. Figure 5.1 displays the modelled geometry of a typical of C-section fix-ended stub column specimen along with the corresponding applied constraints and boundary conditions. An imperfection sensitivity study was also conducted to determine the suitable amplitude values to be adopted in the following parametric studies. For the local geometric imperfection amplitudes, three different fractions of the cross-sectional flange thickness t_f namely $t_f/15$ (average measured), $t_f/50$ and $t_f/100$ were considered.

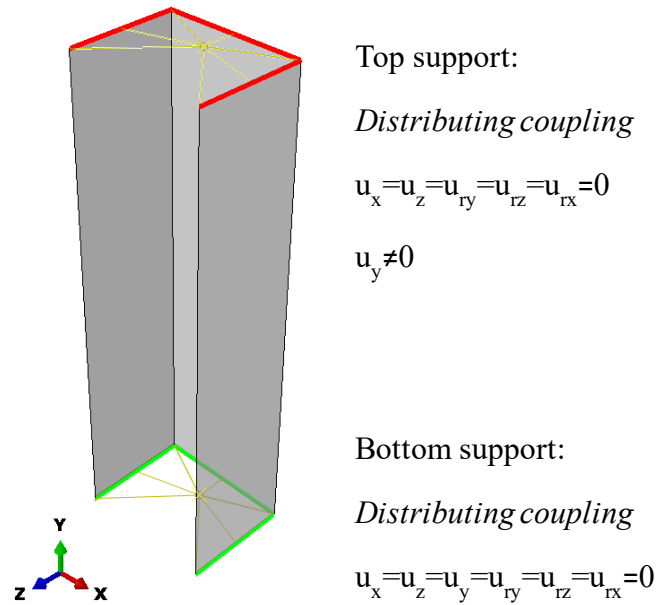


Figure 5.1: Modelled geometry of a typical of C-section fix-ended stub column specimen and the corresponding applied constraints and boundary conditions.

The specimens investigated experimentally (see Subsection 4.2.3.) were utilised to validate the developed FE models based on the assumptions mentioned in Subsection 3.3. Aiming to assess the accuracy of the developed FE models and verify their suitability for the conduction of parametric studies, the numerical results were compared with those obtained from tests. Table 5.1 presents the ratios of the experimental $F_{u,Exp}$ over the FE $F_{u,FE}$ ultimate strengths for the considered imperfection amplitudes. It can be seen that the values of the initial imperfection amplitudes slightly influence the $F_{u,Exp}/F_{u,FE}$ ratio. The most accurate and consistent prediction of the experimental response is obtained for the average measured local imperfection amplitude $t_f/15$ which resulted in mean value and COV of the $F_{u,Exp}/F_{u,FE}$ ratio of 1.02 and 0.03, respectively. A typical load-deformation curve obtained from test and FE analysis is depicted in Figure 5.2. It can be seen that the compressive behaviour was accurately predicted throughout the loading history, including the initial stiffness, ultimate load, displacement corresponding to ultimate load and inelastic response exhibited during the tests. Moreover, a good agreement was achieved between the experimental and FE failure modes, as shown in Figure 5.3. It can be concluded that the developed FE models can accurately replicate the cross-sectional response of aluminium alloy C-sections.

Table 5.1: Comparison between the FE and experimental ultimate loads for C-section fix-ended stub columns.

Specimen	$F_{u,Exp}/F_{u,FE}$		
	$t_f/15$	$t_f/50$	$t_f/100$
50.8×50.8×6.35-L150	0.97	0.99	1.0
50.8×50.8×4.76-L150	1.03	1.05	1.1
50.8×38.1×6.35-L150	1.05	1.08	1.1
50.8×38.1×3.18-L150	1.02	1.01	1.0
50.8×25.4×3.18-L150	1.05	1.10	1.1
38.1×38.1×4.76-L115	1.01	1.02	1.03
mean	1.02	1.04	1.06
COV	0.03	0.04	0.03

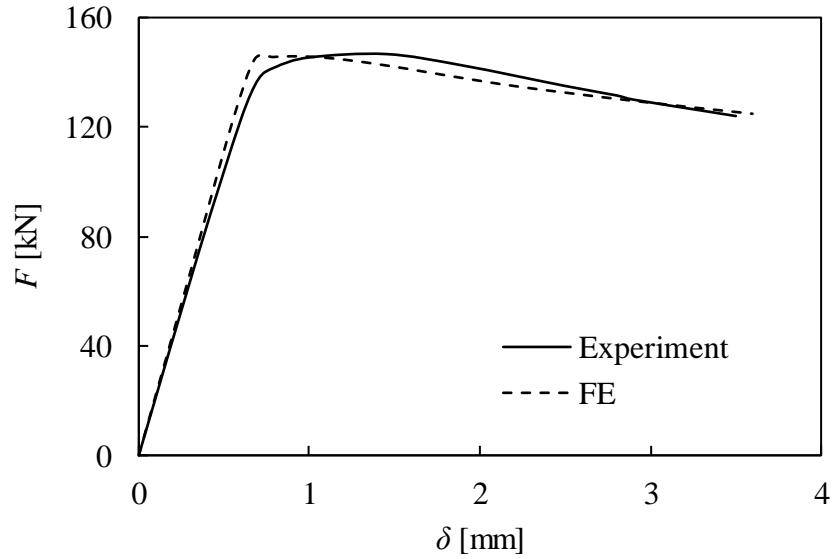


Figure 5.2: Comparison between typical FE and experimental load-deformation curves for 38.1×38.1×4.76-L115 specimen.

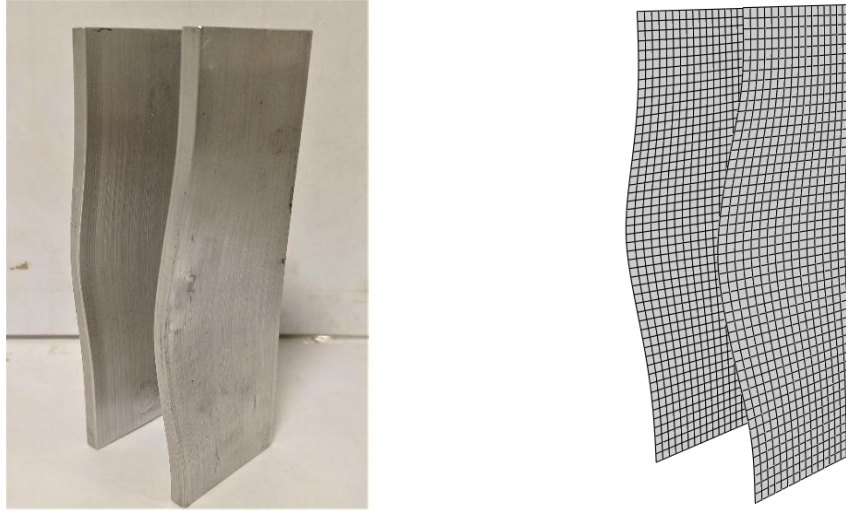


Figure 5.3: Comparison between typical experimental (left) and FE (right) failure modes for 50.8×50.8×6.35-L150 specimen.

Upon validation of the developed FE models, a series of parametric studies was performed. 5 different aspect ratios D/B were considered keeping the outer web depth D fixed to 150 mm, whilst the outer flange width B was ranging from 150 to 50 mm. The plate thickness varied from 2.5 to 22.0 mm to encompass a wide range of cross-sectional slenderness ratios β_f/ϵ . The length was set equal to 450 mm which is three times the maximum cross-sectional dimension. Table 5.2 lists the examined parameters considered for the C-section fix-ended stub columns. The material properties adopted in the parametric studies were based on the averaged stress-strain curves obtained from the tensile coupon tests of this study. The initial local geometric imperfections were accounted for with an amplitude of $t_f/15$. A total of 47 numerical analyses were carried out.

Table 5.2: List of key parameters considered in parametric studies for C-section fix-ended stub columns.

	Total FE analyses: 47
	1.0 (150 × 150)
	1.25 (150 × 120)
5 aspect ratios D/B ($D \times B$):	1.5 (150 × 100)
	2.0 (150 × 75)
	3.0 (150 × 50)
thicknesses ($t_f=t_w$) (mm)	2.50-22.00
resulting slenderness ratio β_f/ϵ	β_f/ϵ : 1.36-52.50

5.3. Pin-ended columns

5.3.1. Bare tubular cross-sections

FE models of BAT pin-ended column specimens were developed adopting the assumptions described in Subsection 3.3. An average element size of 5 mm was applied resulted from a mesh sensitivity study achieving accurate numerical results with a reasonable computational time. To simulate the pin-ended boundary conditions, a reference point was created on the centroid of the cross-section for each column end by considering the effective height of specimens measured in the tests. Top and bottom reference points were fixed against all translational and rotational degrees of freedom except the longitudinal translation at the loaded end and the rotational about the examined buckling axis. In line with past studies [73,141], the CFRP wraps were not explicitly modelled, but the prevention of a potential localised failure was considered through coupling constraints in the supports. The axial compressive loading was applied at the top reference point by specifying a displacement to replicate the loading condition employed in the tests. Figure 5.4 shows the modelled geometry of a typical BAT pin-ended column specimen along with the corresponding applied constraints and boundary conditions.

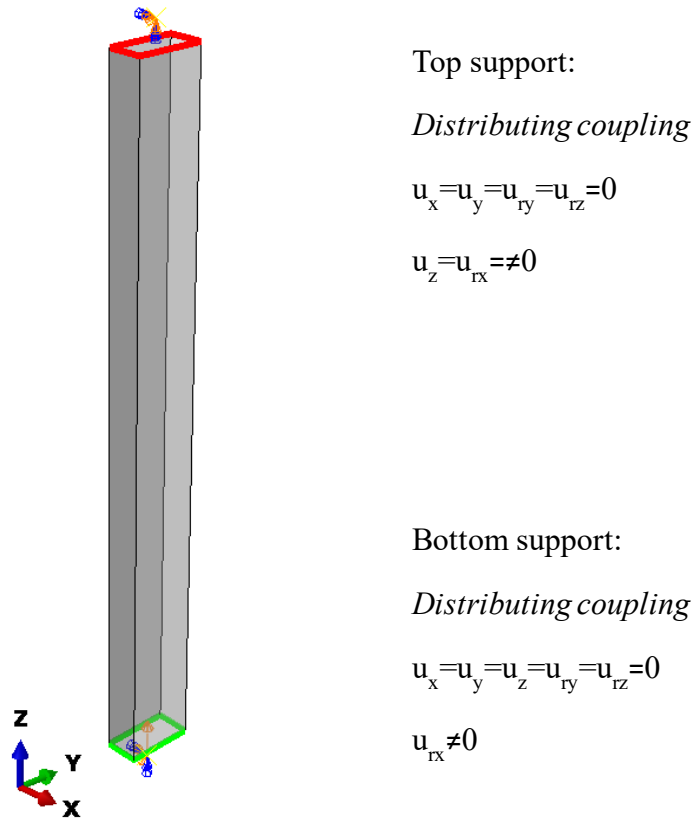


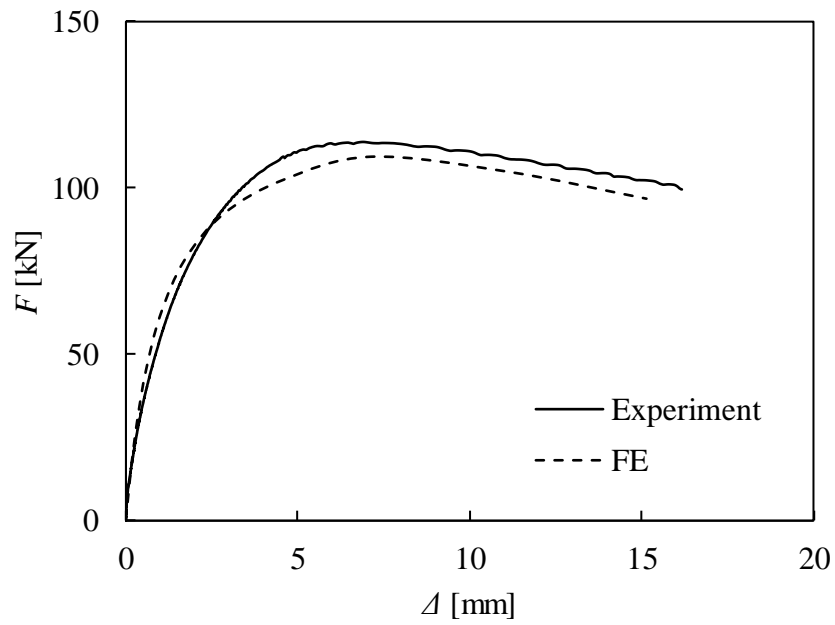
Figure 5.4: Modelled geometry of a typical BAT pin-ended column specimen and the corresponding applied constraints and boundary conditions.

The specimens investigated experimentally (see Subsection 4.3.1.) were utilised to validate the developed FE models based on the assumptions mentioned in Subsection 3.3. The accuracy of the models was evaluated by comparing the experimental and numerical results in terms of the ultimate capacities, load–mid-height lateral displacement and failure modes. An imperfection sensitivity study was conducted to determine suitable imperfection amplitudes to be considered in the subsequent parametric study. Four global imperfection amplitudes including the measured values and three fractions of the effective buckling length, i.e. $L_e/1000$, $L_e/1500$ and $L_e/2000$ were considered. In addition, local geometric imperfections with magnitude equal to $1/10$ of the cross-sectional thickness ($t/10$) were considered. This amplitude was based on the measured values ω_l and was found to provide accurate results. Table 5.3 presents the ratios of numerical to experimental values of ultimate capacities $F_{u,FE}/F_{u,Exp}$ for a range of global imperfections. Overall, a fairly good agreement between the test and numerical data has been obtained with mean values close to unity. It can be seen that the global amplitude $L_e/1000$ provided

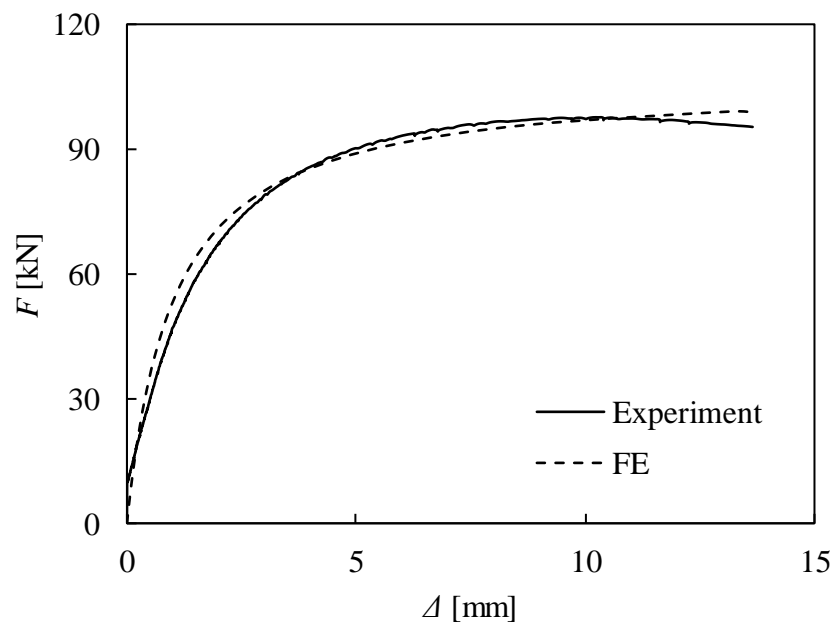
the most accurate predictions of ultimate capacities with mean value of $F_{u,FE}/F_{u,Exp}$ equal to 0.99. The comparison between experimental and numerical (for global imperfection amplitude $L_e/1000$) load–mid-height lateral displacement curves of typical specimens is depicted in Figure 5.5, showing a good comparison. Moreover, a typical successfully replicated failure mode by the FE model for 50.8×50.8×1.6 specimen is illustrated in Figure 5.6. Overall, it can be concluded that the developed FE models are capable of accurately predicting the structural response of BAT pin-ended columns.

Table 5.3: Comparison of test and FE results for varying imperfection amplitudes for BAT pin-ended columns.

Specimen	$F_{u,FE}/F_{u,Exp}$			
	Global Imperfection Amplitude			
	Measured	$L_e/1000$	$L_e/1500$	$L_e/2000$
50.8×50.8×1.6	1.02	0.95	0.98	1.00
50.8×50.8×3.3	0.94	0.96	1.00	1.02
50.8×50.8×4.8	0.90	0.95	0.98	0.99
76.2×76.2×3.3	0.94	0.95	0.97	0.98
76.2×76.2×4.8	1.00	0.99	1.02	1.03
76.2×76.2×6.4	1.01	0.97	0.98	1.01
76.2×38.1×3.3	1.04	1.04	1.05	1.06
76.2×50.8×3.3	0.91	1.10	1.13	1.16
101.6×50.8×3.3	1.04	1.01	1.02	1.02
Mean	0.97	0.99	1.01	1.03
COV	0.05	0.05	0.05	0.05



(a) 50.8x50.8x3.3



(b) 76.2x38.1x3.3

Figure 5.5: Experimental and numerical load–mid-height lateral deflection curves for BAT pin-ended columns.

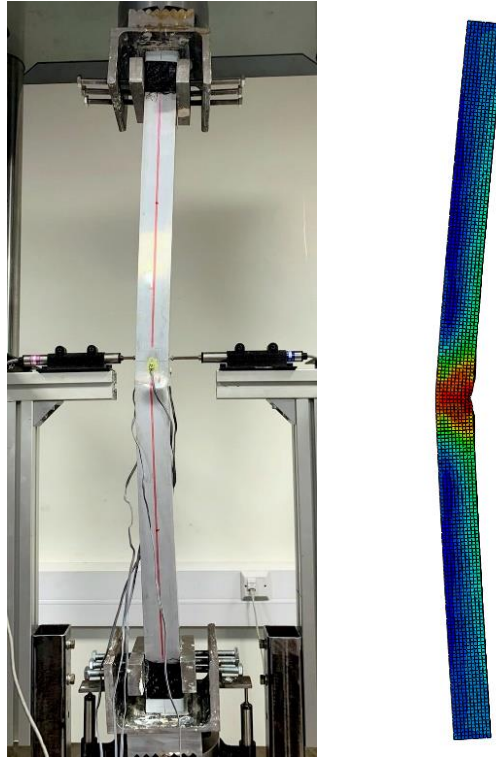


Figure 5.6: Experimental and numerical failure modes for 50.8×50.8×1.6 specimen.

Upon validation of the developed FE models, a series of parametric studies was performed to generate additional structural performance data over a wide range of cross-sections and member slendernesses. In total, 54 BAT pin-ended columns were modelled in this study. Square tubes with cross-sectional dimensions of 50×50 and wall thicknesses 1, 3 and 5 mm and rectangular tubes of 100×50 with 2, 6 and 10 mm thicknesses were considered. Both major and minor axis buckling was examined for the rectangular BAT columns. The specimen lengths were taken from 150 to 3000 mm to cover a wide range of member slendernesses $\bar{\lambda}$ from 0.14-1.78. Table 5.4 lists the examined parameters considered for the BAT pin-ended columns. The average measured stress-strain curves were defined for the aluminium alloy. The combination of initial local and global amplitudes of $t/10$ and $L_e/1000$ were adopted which were also employed successfully in similar studies [120,231].

Table 5.4: List of key parameters considered in parametric studies for BAT pin-ended columns.

Total FE analyses: 54	
2 aspect ratios D/B ($D \times B$):	1.0 (50×50)
	1.5 (100×50 – major axis buckling)
	1.5 (50×100 – minor axis buckling)
thicknesses (t) (mm)	1, 3, 5 (for 50×50)
	2, 6, 10 (for 100×50)
	2, 6, 10 (for 50×100)
column lengths L (mm)	150-3000
resulting member slendernesses $\bar{\lambda}$	$\bar{\lambda} : 0.14-1.78$

5.3.2. Concrete-filled tubular cross-sections

FE models of CFAT pin-ended column specimens were developed adopting the assumptions described in Subsection 3.3. Both core concrete and aluminium tube were simulated by C3D8R elements [142,229]. An average element size of 5 mm was applied resulted from a mesh sensitivity study achieving accurate numerical results with a reasonable computational time. To simulate the pin-ended boundary conditions, a reference point was created on the centroid of the cross-section for each column end by considering the effective height of specimens measured in the tests. Top and bottom reference points were fixed against all translational and rotational degrees of freedom except the longitudinal translation at the loaded end and the rotational about the examined buckling axis. In line with past studies [73,141], the CFRP wraps were not explicitly modelled, but the prevention of a potential localised failure was considered through coupling constraints in the supports. The axial compressive loading was applied at the top reference point by specifying a displacement to replicate the loading condition employed in the tests. Figure 5.7 shows the modelled geometry of a typical CFAT pin-ended column specimen along with the corresponding applied constraints and boundary conditions.

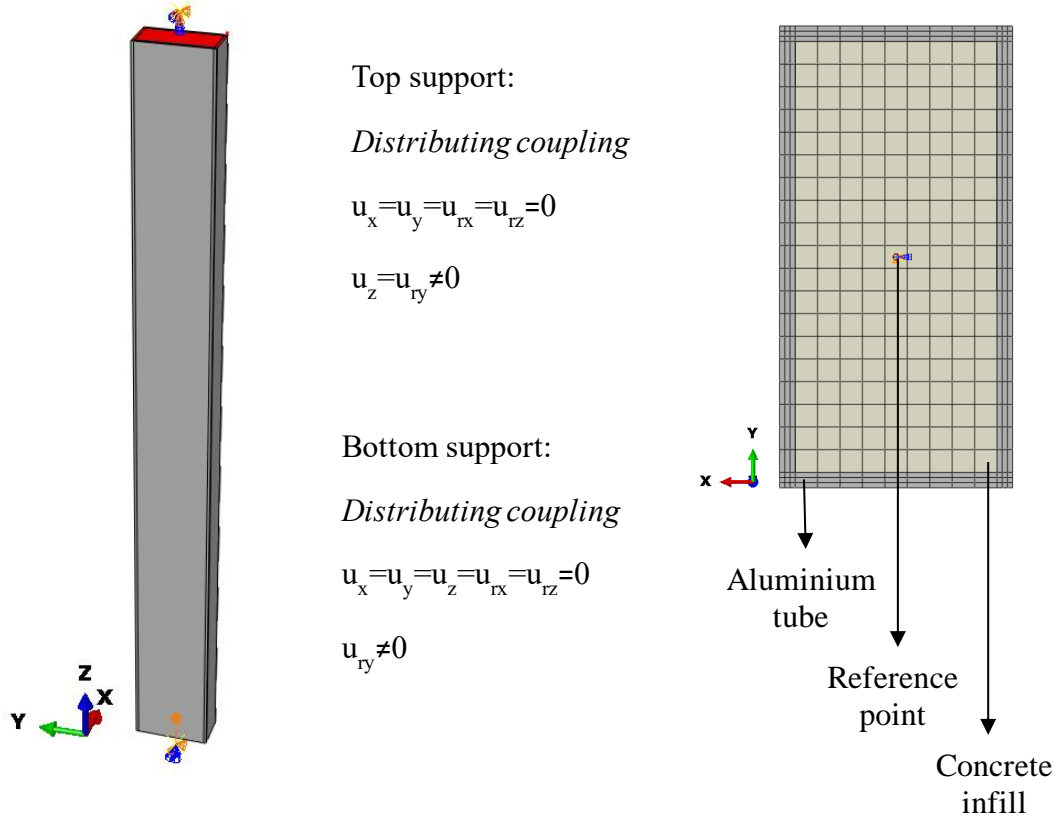


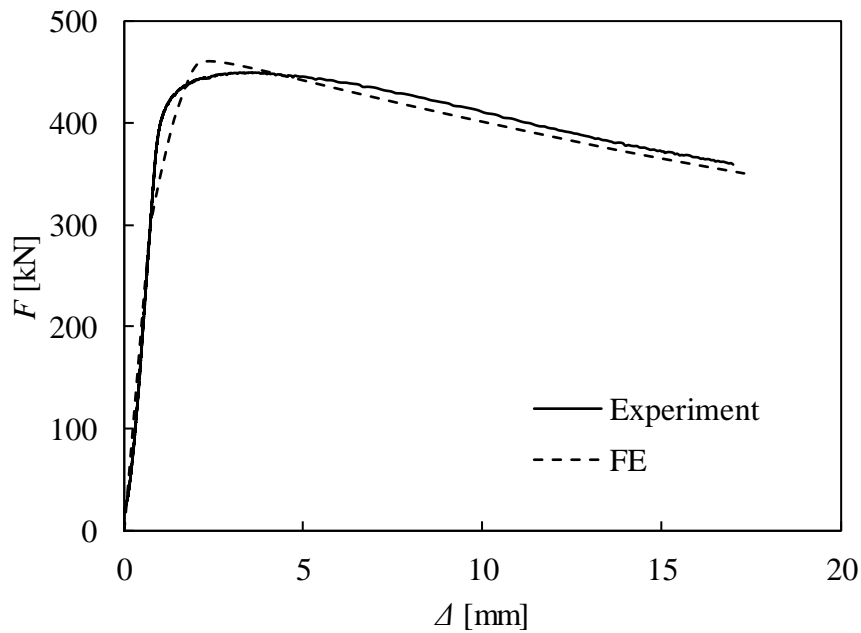
Figure 5.7: Modelled geometry of a typical CFAT pin-ended column specimen and the corresponding applied constraints and boundary conditions.

The specimens investigated experimentally (see Subsection 4.3.2.) were utilised to validate the developed FE models based on the assumptions mentioned in Subsection 3.3. The accuracy of the models was evaluated by comparing the experimental and numerical results in terms of the ultimate capacities, load–mid-height lateral displacement and failure modes. An imperfection sensitivity study was conducted to determine suitable imperfection amplitudes to be considered in the subsequent parametric study. Four global imperfection amplitudes ω_g including the measured values and three fractions of the critical buckling length, i.e., $L_e/1000$, $L_e/1500$ and $L_e/2000$ were considered. The effect of the initial local imperfections ω_l is negligible due to concrete infill and hence were not explicitly modelled [230,231]. Table 5.5 presents the ratios of numerical to experimental values of ultimate capacities $F_{u,FE}/F_{u,Exp}$ for a range of global imperfections. Overall, a fairly good agreement between the test and numerical data has been obtained with mean values close to unity. It can be seen that the global amplitude $L_e/1000$ provided the most accurate predictions of ultimate capacities with mean value of $F_{u,FE}/F_{u,Exp}$ equal to 0.98. The comparison between experimental and numerical (for global imperfection amplitude

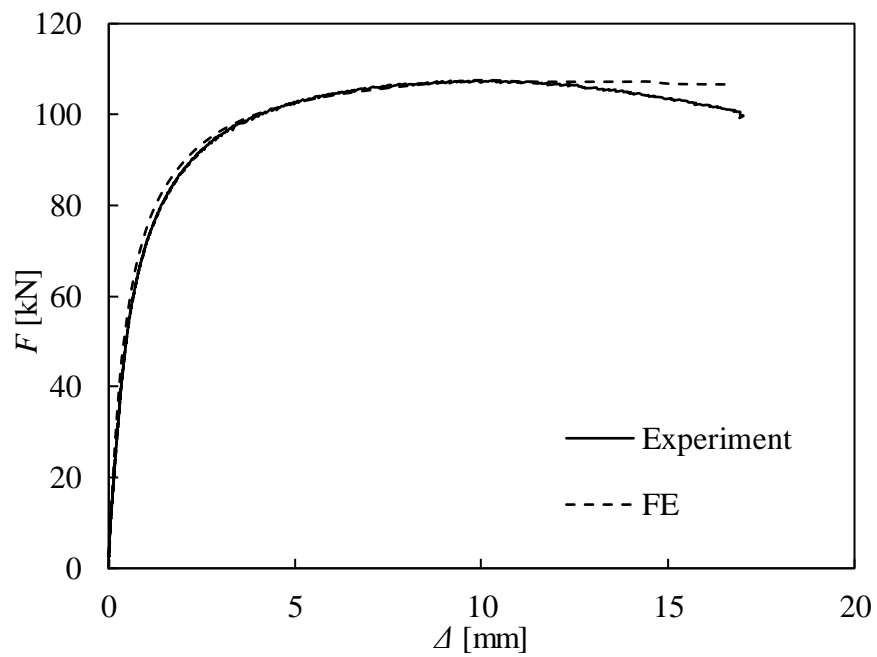
$L_e/1000$) load–mid-height lateral displacement curves of typical specimens is depicted in Figure 5.8, showing a good comparison. Moreover, a typical successfully replicated failure mode by the FE model for 76.2×76.2×4.8-C specimen is illustrated in Figure 5.9. Overall, it can be concluded that the developed FE models are capable of accurately predicting the structural response of CFAT pin-ended columns.

Table 5.5: Comparison of test and FE results for varying imperfection amplitudes for CFAT pin-ended columns..

Specimen	$F_{u,FE}/F_{u,Exp}$			
	Global Imperfection Amplitude			
	Measured	$L_e/1000$	$L_e/1500$	$L_e/2000$
50.8×50.8×1.6-C	0.87	0.83	0.85	0.87
50.8×50.8×3.3-C	1.02	1.02	1.05	1.06
50.8×50.8×4.8-C	0.87	0.90	0.92	0.94
76.2×76.2×3.3-C	1.19	1.08	1.12	1.43
76.2×76.2×4.8-C	1.07	1.04	1.07	1.09
76.2×76.2×6.4-C	1.20	1.06	1.14	1.47
76.2×38.1×3.3-C	1.12	1.00	1.03	1.11
76.2×50.8×3.3-C	1.02	0.93	0.94	0.97
101.6×50.8×3.3-C	1.25	1.05	1.12	1.14
Mean	1.05	0.98	1.02	1.12
COV	0.11	0.08	0.09	0.18



(a) 76.2×76.2×4.8-C



(b) 76.2×38.1×3.3-C

Figure 5.8: Experimental and numerical load–mid-height lateral deflection curves for CFAT pin-ended columns..



Figure 5.9: Experimental and numerical failure modes for 76.2×76.2×4.8-C specimen.

Upon validation of the developed FE models, a series of parametric studies was performed to generate additional structural performance data over a wide range of cross-sections and member slendernesses and to investigate the effect of the concrete infill. In total, 54 CFAT pin-ended columns were modelled in this study. Square tubes with cross-sectional dimensions of 50×50 and wall thicknesses 1, 3 and 5 mm and rectangular tubes of 100×50 with 2, 6 and 10 mm thicknesses were considered. Both major and minor axis buckling was examined for the rectangular BAT columns. The specimen lengths were taken from 500 to 2300 mm to cover a wide range of member slendernesses. Three different concrete cylinder strengths f_{ck} of 30, 50 and 70 MPa were also considered. Table 5.6 lists the examined parameters considered for the BAT pin-ended columns. The average measured stress-strain curves were defined for the aluminium alloy. The initial global amplitude of $L_e/1000$ was adopted which was also employed successfully in similar studies [120,231].

Table 5.6: List of key parameters considered in parametric studies for CFAT pin-ended columns.

	Total FE analyses: 54
2 aspect ratios D/B ($D \times B$):	1.0 (50 × 50)
	1.5 (100 × 50 – major axis buckling)
	1.5 (50 × 100 – minor axis buckling)
thicknesses (t) (mm)	1, 3, 5 (for 50 × 50)
	2, 6, 10 (for 100 × 50)
	2, 6, 10 (for 50 × 100)
column lengths L (mm)	500-2300
resulting member slendernesses $\bar{\lambda}$	$\bar{\lambda}$: 0.43-1.85
concrete cylinder strengths f_{ck} (MPa)	30, 50, 70

5.3.3. Channel cross-sections

FE models of C-section pin-ended column specimens were developed adopting the assumptions described in Subsection 3.3. An average element size of 3 mm was applied resulted from a mesh sensitivity study achieving accurate numerical results with a reasonable computational time. To simulate the pin-ended boundary conditions, a reference point was created on the centroid of the cross-section for each column end by considering the effective height of specimens measured in the tests. All degrees of

freedom were restrained at both reference points, apart from the rotational degree of freedom about the minor axis and the vertical translation at the loaded end. The stiffening effect provided by the underpinning bolts and the G-clamps was also taken into consideration assigning distributing coupling constraints at both end cross-sections to ensure that they remain undeformed during loading. Figure 5.10 displays the modelled geometry of a typical C-section pin-ended column specimen and the corresponding applied constraints and boundary conditions.

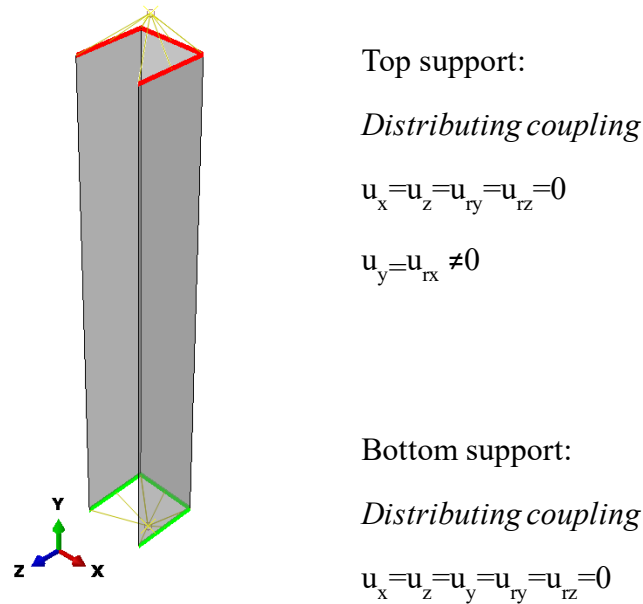


Figure 5.10: Modelled geometry of a typical C-section pin-ended column specimen and the corresponding applied constraints and boundary conditions.

The specimens investigated experimentally (see Subsection 4.3.3.) were utilised to validate the developed FE models based on the assumptions mentioned in Subsection 3.3. Aiming to assess the accuracy of the developed FE models and verify their suitability for the conduction of parametric studies, the numerical results were compared with those obtained from tests. Table 5.7 presents the ratios of the experimental $F_{u,Exp}$ over the FE $F_{u,FE}$ ultimate strengths for the considered imperfection amplitudes. It can be seen that the values of the initial imperfection amplitudes slightly influence the $F_{u,Exp}/F_{u,FE}$ ratio. The combination of the average measured local $t_f/15$ and global $L_e/1000$ imperfection amplitudes provided the best agreement between the experimental and FE response with mean value and corresponding COV of the $F_{u,Exp}/F_{u,FE}$ ratio of 1.00 and 0.03, respectively. A typical load-deformation curve obtained from test and FE analysis is

depicted in Figure 5.11. It can be seen that the compressive behaviour was accurately predicted throughout the loading history, including the initial stiffness, ultimate load, displacement corresponding to ultimate load and inelastic response exhibited during the tests. Moreover, a good agreement was achieved between the experimental and FE failure modes, as shown in Figure 5.12. It can be concluded that the developed FE models can accurately replicate the minor-axis buckling response of aluminium alloy C-sections.

Table 5.7: Comparison between the FE and experimental ultimate loads for C-section pin-ended columns for local imperfection amplitude $t_f/15$.

Specimen	$F_{u,Exp}/F_{u,FE}$		
	$L_e/1000$	$L_e/1500$	$L_e/2000$
50.8×50.8×6.35-L500	0.99	1.01	1.02
76.2×76.2×6.35-L500	1.03	1.04	1.04
76.2×76.2×6.35-L300	1.01	1.04	1.04
50.8×38.1×6.35-L500	0.96	0.97	0.99
50.8×38.1×3.18-L500	1.02	1.05	1.07
50.8×38.1×3.18-L300	1.03	1.05	1.06
50.8×25.4×3.18-L500	0.99	0.99	1.00
50.8×25.4×3.18-L300	0.96	1.00	1.04
mean	1.00	1.02	1.03
COV	0.03	0.03	0.03

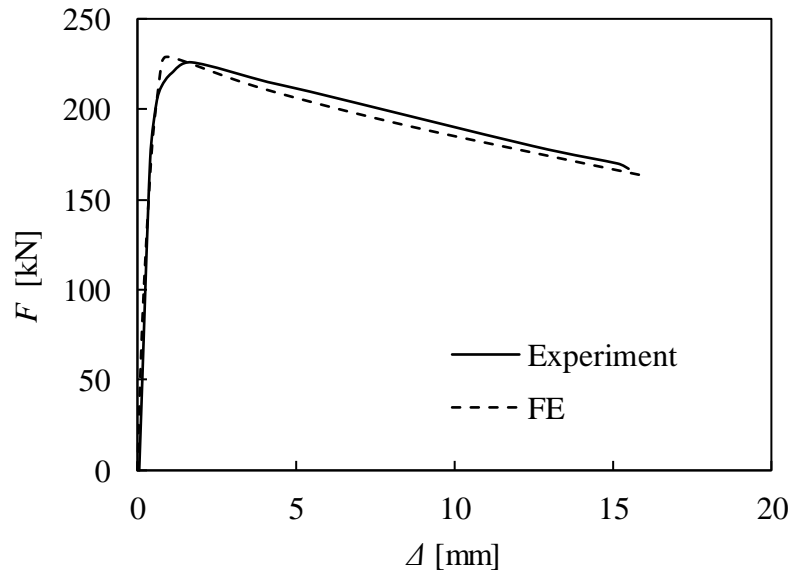


Figure 5.11: Comparison between typical FE and experimental load-deformation curves for 50.8×50.8×6.35-L500 specimen.

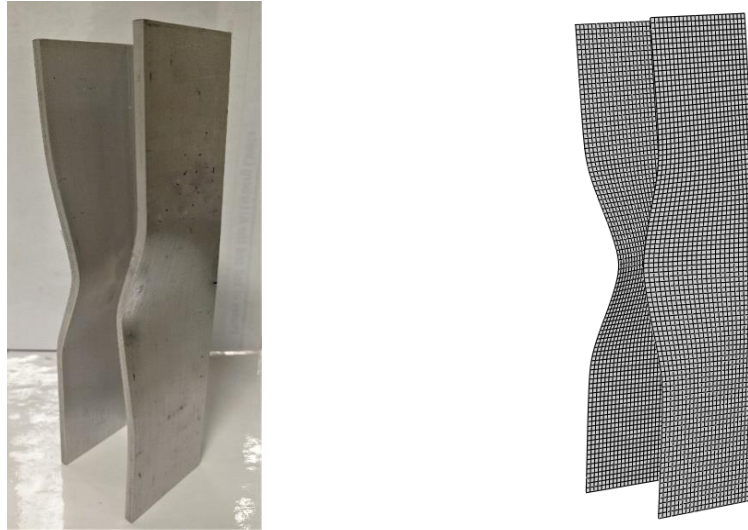


Figure 5.12: Comparison between typical experimental (left) and FE (right) failure modes for 76.2×76.2×6.35-L300 specimen.

Upon validation of the developed FE models, a series of parametric studies was performed. 3 different cross-sections were examined namely 100×100, 100×67 and 100×50 with corresponding aspect ratios D/B of 1.0, 1.5 and 2.0, respectively. Moreover, three plate thicknesses of 10, 13 and 16 mm. The members' length L was ranging from 600 to 1800 mm providing a broad range of member slendernesses $\bar{\lambda}$ from 0.36-2.04. Table 5.8 lists the examined parameters considered for the C-section pin-ended columns. The material properties adopted in the parametric studies were based on the averaged stress-strain curves obtained from the tensile coupon tests of this study. The initial local geometric imperfections were accounted for with an amplitude of $t_f/15$, whereas the global imperfection amplitude was taken as $L_e/1000$. A total of 45 numerical analyses were carried out.

Table 5.8: List of key parameters considered in parametric studies for C-section pin-ended columns.

Total FE analyses: 45	
3 aspect ratios D/B ($D \times B$):	1.0 (100 × 100)
	1.5 (100 × 67)
	2.0 (100 × 50)
thicknesses ($t_f=t_w$) (mm)	10, 13, 16
column lengths L (mm)	600-1800
resulting member slendernesses $\bar{\lambda}$	$\bar{\lambda}$: 0.36-2.04

5.4. Simply-supported beams

5.4.1. Bare rectangular tubular cross-sections

FE models of BAT simply-supported beam specimens were developed adopting the assumptions described in Subsection 3.3. A mesh convergence study was executed indicating that a uniform mesh with a size equal to the cross-sectional thickness provides reasonable computational time without compromising accuracy. Figure 5.13 displays the modelled geometry of a typical BAT beam specimen under four-point bending and the corresponding applied constraints and boundary conditions. Even though the tests displayed symmetry in geometry, loading and boundary conditions, the full cross-sectional geometric dimensions and length of the examined specimens were modelled. This was chosen so that to include possible antisymmetric local buckling modes which might have slightly lower corresponding eigenvalues than the corresponding symmetric ones [232]. To simulate the wooden blocks which were placed to prevent web crippling during testing, distributing coupling constraints were assigned at the supports and loading points (Figure 5.13). It is noteworthy that an additional sensitivity analysis demonstrated a minor effect of the local imperfection amplitude on the flexural response of the aluminium alloy continuous beams, in line with the past studies [98].

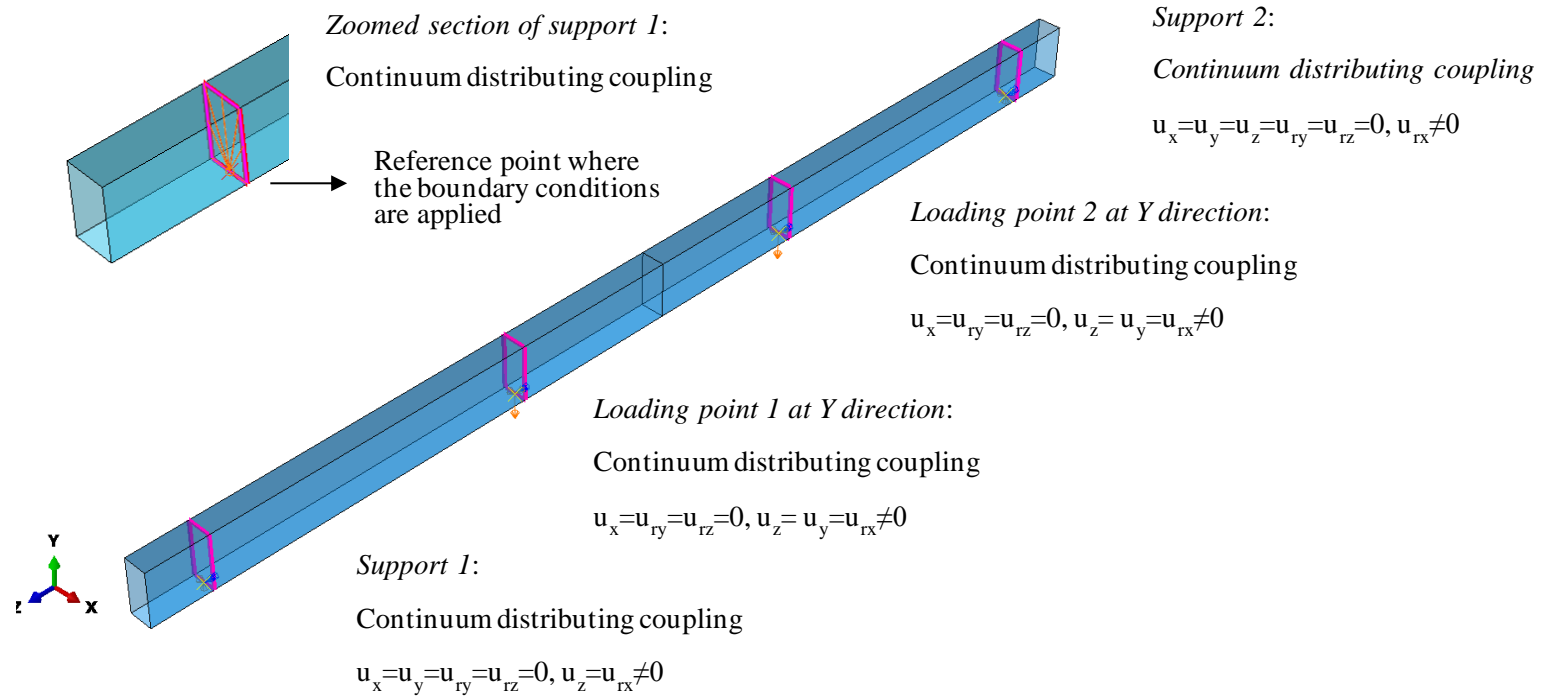
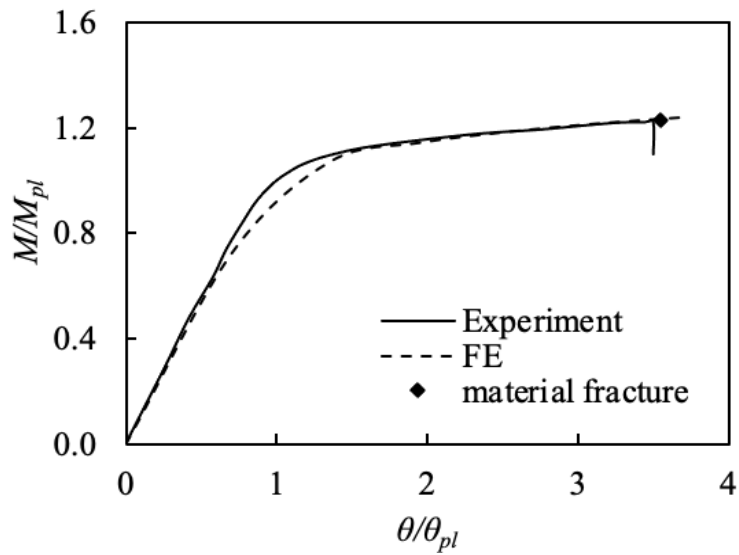


Figure 5.13: Modelled geometry of a typical C-section simply supported beam specimen and the corresponding applied boundary conditions.

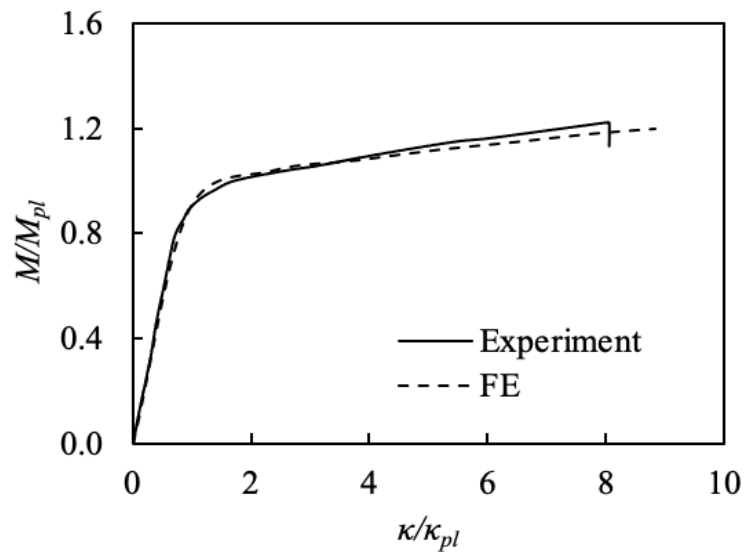
As can be observed there is a fairly good agreement between the test and FE results in terms of initial stiffness, ultimate load, post-ultimate behaviour and failure mechanism. It is worth mentioning that the 50.8×25.4×3.25 specimen under three-point bending failed by tensile fracture at the bottom flange. This failure pattern was considered within the simulations by monitoring the tensile strains and identifying the point where the developed strains reach the fracture strain ε_f measured from the tensile coupon tests. The numerically and experimentally obtained normalised moment-rotation curves for specimen 50.8×25.4×3.25 are depicted in Figure 5.14(a) and the rhombus signifies the point where the tensile fracture occurred. Overall, it can be considered that the FE models developed herein are capable of accurately replicating the flexural performance of aluminium alloy beams.

Table 5.9: Comparison of numerical and experimental ultimate loads for BAT simply-supported beams.

Specimen	$F_{u,FE}/F_{u,Exp}$
Three-point bending	
63.5× 38.1×3.25	1.02
50.8× 38.1×3.25	1.02
50.8× 25.4×3.25	1.00
38.1×25.4×3.25	1.00
38.1× 19.1×3.25	1.00
Four-point bending	
63.5× 38.1×3.25	1.01
50.8× 38.1×3.25	0.97
50.8× 25.4×3.25	1.00
38.1×25.4×3.25	1.00
38.1× 19.1×3.25	1.04
mean	1.01
COV	0.02

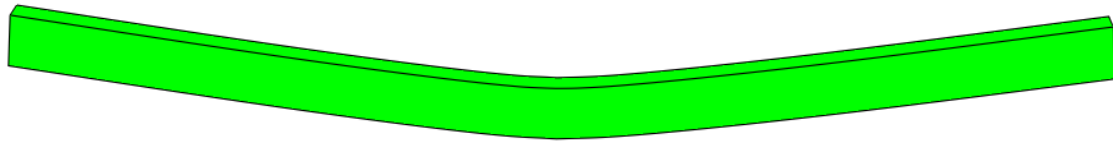
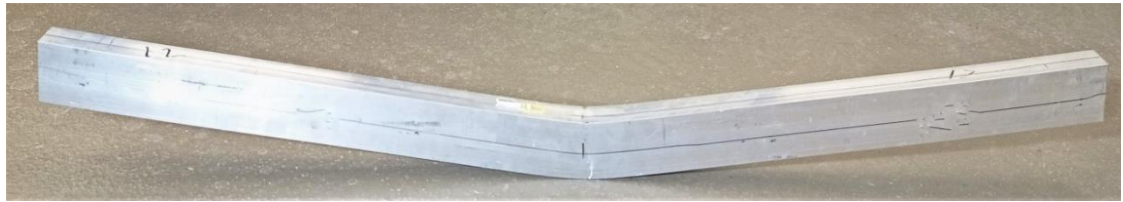


(a) Simply-supported beams
(50.8×25.4×3.25 under three-point bending)



(b) Simply-supported beams
(63.5×38.1×3.25 under four-point bending)

Figure 5.14: Comparison between typical numerical and experimental responses for BAT simply-supported beams.



(a) Simply-supported beams ($50.8 \times 25.4 \times 3.25$ under three-point bending)



(b) Simply-supported beams ($50.8 \times 25.4 \times 3.25$ under four-point bending)

Figure 5.15: Comparison between typical numerical and experimental failure modes for BAT simply-supported beams

5.4.2. Channel cross-sections

FE models of C-section simply-supported beam specimens were developed adopting the assumptions described in Subsection 3.3. A mesh convergence study was executed indicating that a uniform mesh with a size equal to $5 \text{ mm} \times 5 \text{ mm}$ provides reasonable computational time without compromising accuracy. Figure 5.16 displays the modelled geometry of a typical C-section beam specimen under four-point bending along with the corresponding applied constraints and boundary conditions. Despite the symmetry in loading, boundary conditions and geometry with respect to the plane of bending, the length and the cross-section of the examined beam specimens were modelled assigning their full geometrical dimensions to also consider possible antisymmetric local buckling modes [232]. To consider the stiffening effect provided by the underpinning bolts and

the G- clamps, distributing coupling constraints were assigned to ensure that the cross-sections at the respective locations remained undeformed during the analysis (Figure 5.16).

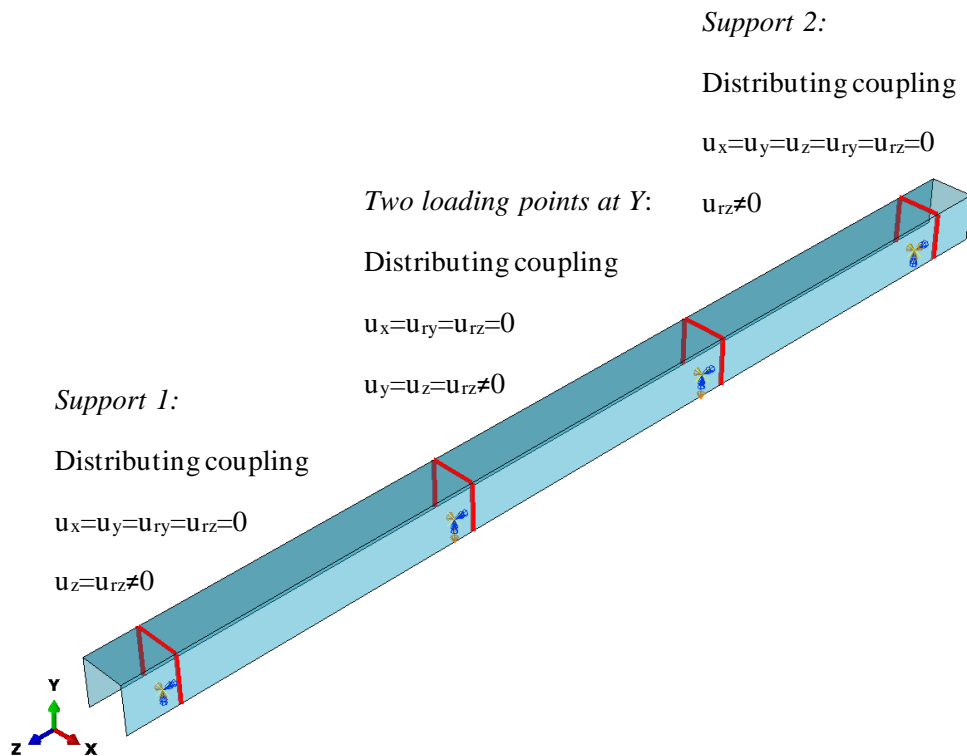


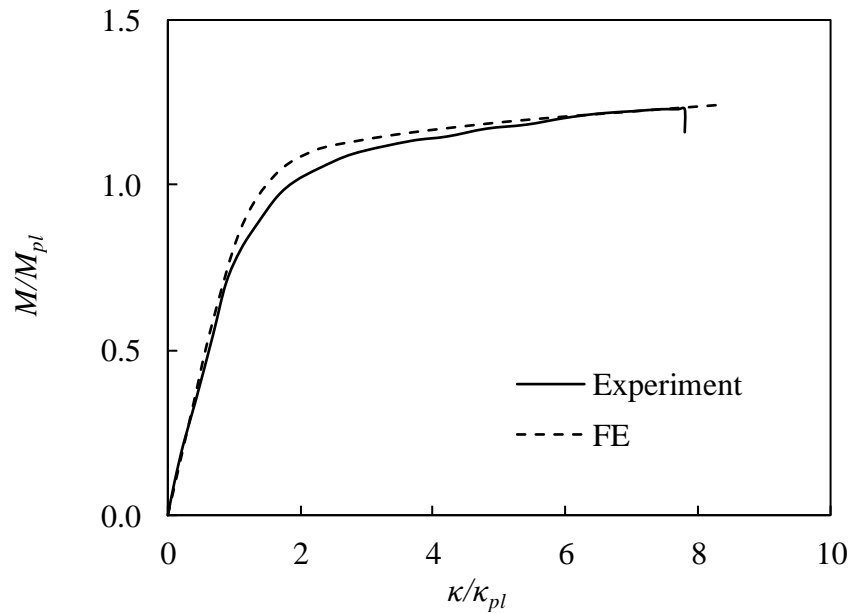
Figure 5.16: Modelled geometry of a typical C-section simply supported beam specimen and the corresponding applied boundary conditions.

The specimens investigated experimentally (see Subsection 4.4.4.) were utilised to validate the developed FE models based on the assumptions mentioned in Subsection 3.3. The accuracy level of the developed FE models was verified by comparing the numerical moment-curvature responses, ultimate bending moment capacities $M_{u,FE}$ and failure modes with the corresponding experimental ones. The $M_{u,Exp}/M_{u,FE}$ ratios are reported in Table 5.10, achieving a mean value and corresponding COV of 1.01 and 0.04, respectively, thereby suggesting accurate and consistent numerical predictions. Typical moment-curvature responses are depicted in Figure 5.17, showing that the developed FE models can capture well the experimental initial stiffness, ultimate bending moment capacity and inelastic response. Numerical failure modes also accurately capture the experimental ones, as shown in Figure 5.18. Thus, it can be concluded that the developed

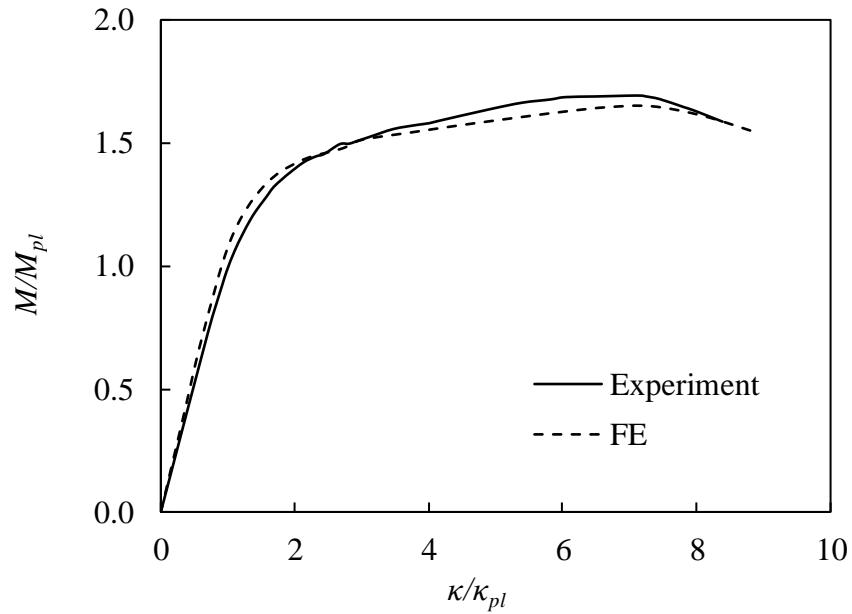
FE models can successfully predict the flexural performance of aluminium alloy C-sections.

Table 5.10: Comparison between the FE and experimental bending moment capacities for C-section simply-supported beams.

Specimen	$M_{u,Exp}/M_{u,FE}$
50.8×50.8×6.35-n	0.95
50.8×50.8×6.35-u	1.03
50.8×50.8×4.76-n	1.00
50.8×50.8×4.76-u	1.01
76.2×76.2×6.35-n	0.98
76.2×76.2×6.35-u	0.97
50.8×38.1×6.35-n	1.02
50.8×38.1×6.35-u	0.93
50.8×38.1×3.18-n	1.05
50.8×38.1×3.18-u	1.07
50.8×25.4×3.18-n	1.06
50.8×25.4×3.18-u	0.98
38.1×38.1×4.76-n	1.05
38.1×38.1×4.76-u	1.01
mean	1.01
COV	0.04

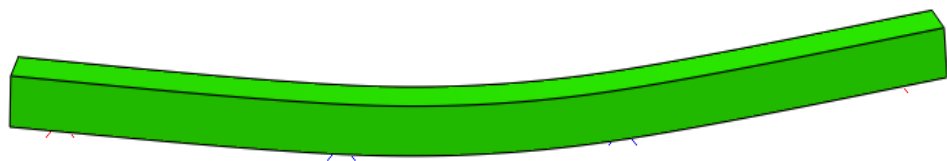


(a) 50.8×50.8×4.76-n

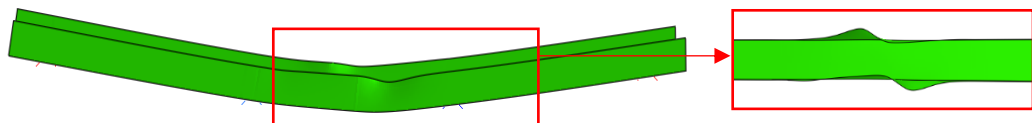
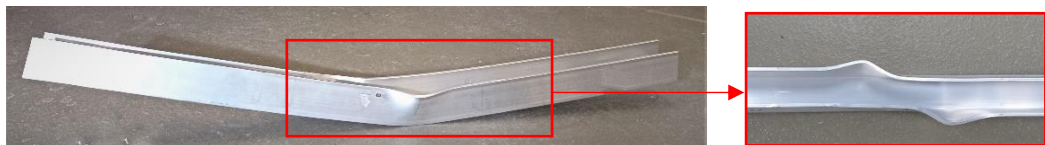


(b) 50.8×50.8×6.35-u

Figure 5.17: Comparison between typical FE and experimental normalised moment-curvature curves for C-section simply-supported beams.



(a) 50.8×50.8×4.76-n



(b) 50.8×50.8×6.35-u

Figure 5.18: Comparison between typical FE and experimental failure modes for C-section simply-supported beams.

Upon validation of the developed FE models, a series of parametric studies was performed to investigate the influence of key parameters on the flexural performance of C-sections. The examined parameters are summarised in Figure 5.11. Three different aspect ratios D/B were considered, namely 1.0, 1.5 and 2.0, keeping the outer web depth D fixed to 100 mm. A total of twelve cross-sectional thicknesses ($t_w=t_f$) were examined, extending the experimental data to a broad range of plate slendernesses. Particularly, the slenderness ratio β_w/ε ranges from 3.44 to 51.34, whilst the slenderness ratio β_f/ε ranges from 1.20 to 24.21. Moreover, the cross-sectional slenderness $\bar{\lambda}_{cs} = \sqrt{\sigma_{0.2}/\sigma_{cr}}$ ranges from 0.10 to 2.14. Aiming to extend the study to an additional structural aluminium alloy, two types of heat-treated aluminium alloys were investigated, namely 6082-T6 and 6063-T5, representing a typical high and normal strength heat-treated aluminium alloy, respectively. The average material properties obtained from the tensile coupon tests of this study were adopted for 6082-T6, whilst for 6063-T5 the material properties reported in [98] were adopted. The material properties of both examined aluminium alloys are summarised in Table 5.12. All specimens had a clear span $L=900$ mm and were subjected to four-point bending with two equal loads at third points considering both the “u” and “n” orientation. Initial local geometric imperfections were accounted for through the lowest buckling mode shape with an amplitude equal to the average measured local imperfection amplitude. A total of 140 numerical analyses were executed and the obtained results are discussed in the following subsections.

Table 5.11: List of key parameters considered in parametric studies for C-section simply-supported beams.

	Total FE analyses: 140
2 aluminium alloys	6082-T6 6063-T5
3 aspect ratios D/B ($D \times B$) (mm \times mm):	1.0 (100 \times 100) 1.5 (100 \times 66.7) 2.0 (100 \times 50)
12 plate thicknesses $t_w=t_f$ (mm)	2, 3, 4, 5, 6, 7, 8, 9, 10, 12, 14, 16 Resulting slenderness β_w/ε : 3.44-51.34 β_f/ε : 1.20-24.21 $\bar{\lambda}_{cs}$: 0.10-2.14

Table 5.12: Material properties for 6082-T6 and 6063-T5 [98] aluminium alloys considered in parametric studies.

	E (MPa)	$\sigma_{0.2}$ (MPa)	σ_u (MPa)	n	ε_u (mm/mm)	ε_f (mm/mm)
6082-T6	70885	286	317	32.7	0.09	0.16
6063-T5	69000	164	211	10.0	0.07	0.14

5.5. Continuous beams

FE models of BAT continuous beam specimens were developed adopting the assumptions described in Subsection 3.3. A mesh convergence study was executed indicating that a uniform mesh with a size equal to the cross-sectional thickness provides reasonable computational time without compromising accuracy. Figure 5.19 displays the modelled geometry of a typical BAT continuous beam specimen along with the corresponding applied constraints and boundary conditions. Even though the tests displayed symmetry in geometry, loading and boundary conditions, the full cross-sectional geometric dimensions and length of the examined specimens were modelled. This was chosen so that to include possible antisymmetric local buckling modes which might have slightly lower corresponding eigenvalues than the corresponding symmetric ones [232]. To simulate the wooden blocks which were placed to prevent web crippling during testing, distributing coupling constraints were assigned at the supports and loading points (Figure 5.19). It is noteworthy that an additional sensitivity analysis demonstrated a minor effect of the local imperfection amplitude on the flexural response of the aluminium alloy continuous beams, in line with the past studies [98].

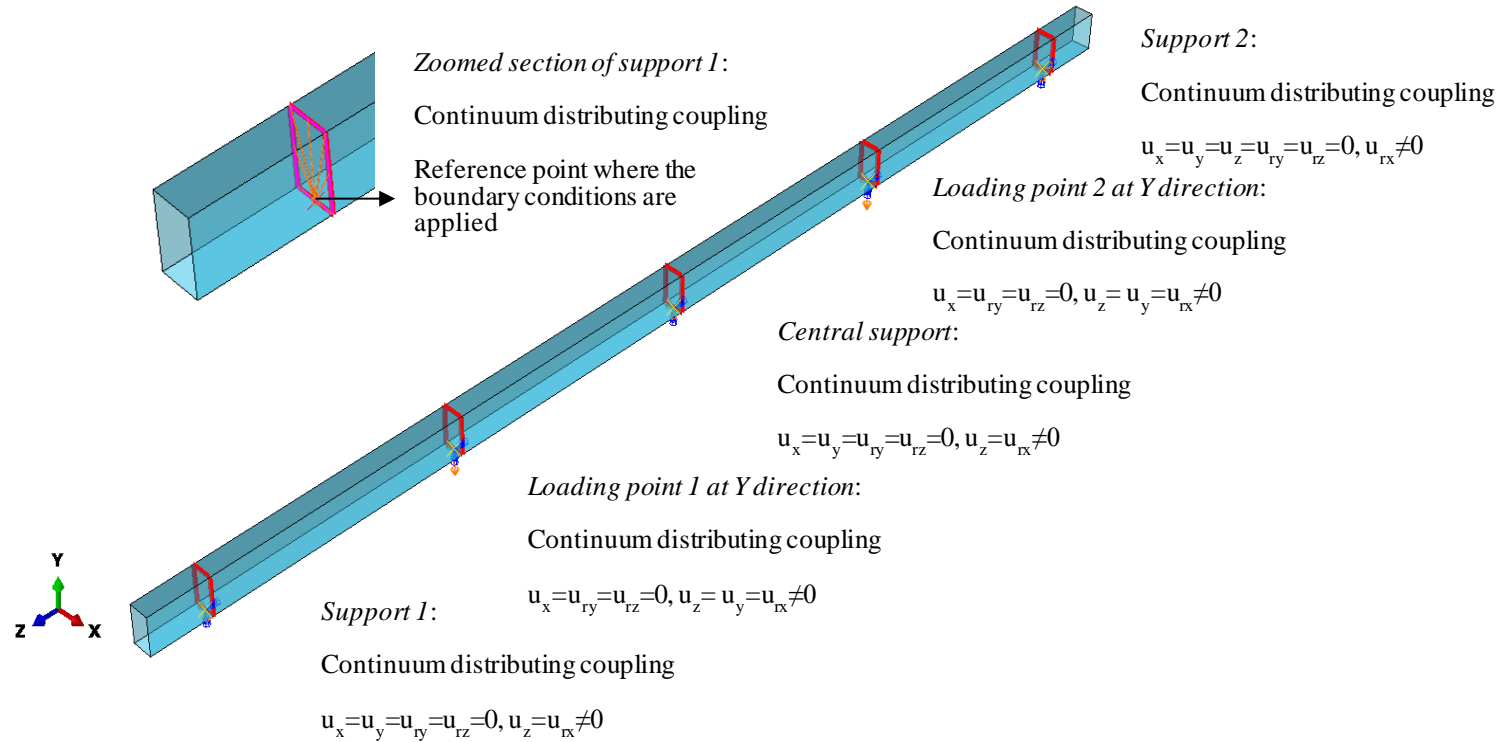


Figure 5.19: Modelled geometry of a typical BAT continuous beam specimen and the corresponding applied boundary conditions and constraints.

The specimens investigated experimentally (see Subsection 4.5.) were utilised to validate the developed FE models based on the assumptions mentioned in Subsection 3.3. The accuracy of the models was evaluated by comparing the experimental and numerical results in terms of the ultimate capacities, flexural response curves and failure modes. To this end, the numerical $F_{u,FE}$ over the experimental $F_{u,Exp}$ ultimate loads for each examined configuration are summarised in Table 5.13, showing a very good agreement. A typical response curve and failure mode obtained from the experiments and FE models are depicted in Figure 5.20 and Figure 5.21, respectively. As can be observed there is a fairly good agreement between the test and FE results in terms of initial stiffness, ultimate load, post-ultimate behaviour and failure mechanism (1st plastic hinge at the central support and 2nd and 3rd simultaneous hinges at loading points). Overall, it can be considered that the FE models developed herein are capable of accurately replicating the flexural performance of indeterminate aluminium alloy beams.

Table 5.13: Comparison of numerical and experimental ultimate loads for BAT continuous beams.

Specimen	$F_{u,FE}/F_{u,Exp}$
63.5× 38.1×3.25	1.03
50.8× 38.1×3.25	0.99
50.8× 25.4×3.25	1.04
38.1×25.4×3.25	1.02
38.1× 19.1×3.25	1.03
mean	1.02
COV	0.02

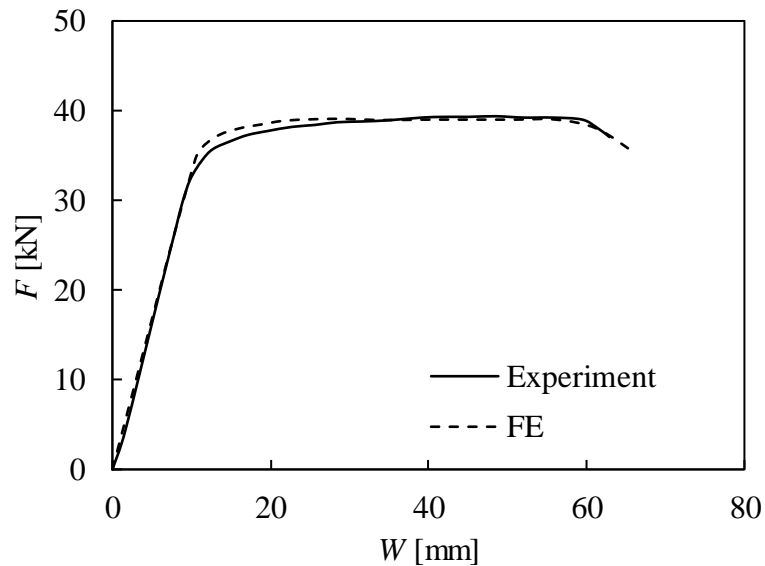


Figure 5.20: Comparison between typical numerical and experimental response of $50.8 \times 38.1 \times 3.25$ specimen.

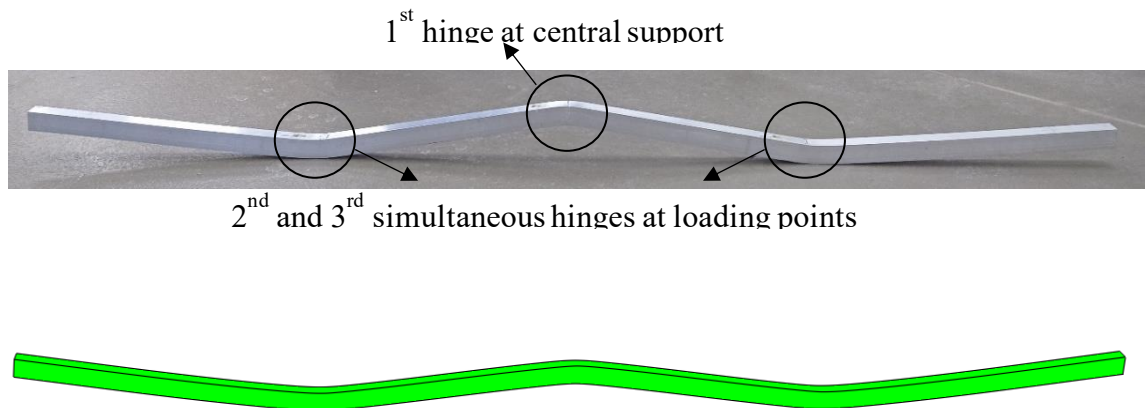


Figure 5.21: Comparison between typical numerical and experimental failure mode of $38.1 \times 25.4 \times 3.25$ specimen.

Following the successful validation of the flexural performance of aluminium alloy beams, a series of parametric studies was carried out to generate further data on aluminium alloy two-span continuous beams. The parameters under consideration are summarised in Table 5.14. Three different aspect ratios D/B were examined, namely 1.0, 1.5 and 2.0, keeping the outer web depth D fixed to 100 mm, whilst the outer flange width B was set equal to 100, 66.7 and 50 mm, respectively. A total of eight cross-sectional thicknesses were studied, extending the experimental results to a broad range of plate slendernesses. Particularly, the slenderness ratio β/ϵ of the flange (crucial constituent

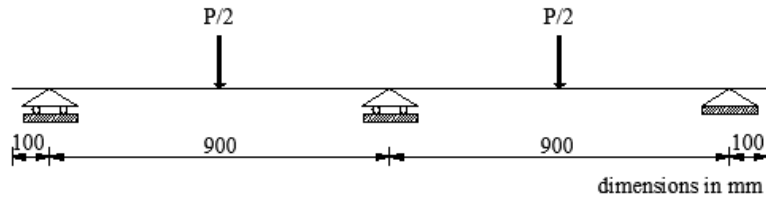
plate element) was ranging from 2.43 to 10.75. Moreover, three aluminium alloy types were considered, namely 6082-T6, 6061-T6 and 6063-T5. The former two alloys represent typical high strength heat-treated aluminium alloys, whilst the latter one represents a typical normal strength aluminium alloy. 6063-T5 aluminium alloy is often referred to as an architectural alloy and offers high corrosion resistance. 6061-T6 aluminium alloy is an American alloy offering medium to high strength and very good corrosion resistance. 6082-T6 is often referred to as a 'structural alloy' and is used predominantly in highly stressed applications such as roof trusses and bridges. For the 6082-T6 alloy, the average material properties obtained from the tensile coupon tests of this study were employed, whilst for the 6061-T6 and 6063-T5 alloys the material properties reported in [98] were adopted. Table 5.15 lists the material properties of the three aluminium alloys. The two-span continuous beam specimens had 2000 mm overall span length and 100 mm overhang at each end resulting in two equal spans of 900 mm each. Moreover, two loading configurations (LC1 and LC2) were, considered, as shown in Figure 5.22. Initial local geometric imperfections were accounted for through the lowest buckling mode shape with an amplitude equal to the average measured local imperfection amplitude. A total of 108 numerical analyses were executed and the obtained results were utilised in the following section to assess the possibility of applying plastic design to aluminium alloy indeterminate structures.

Table 5.14: List of examined parameters in parametric studies for BAT continuous beams.

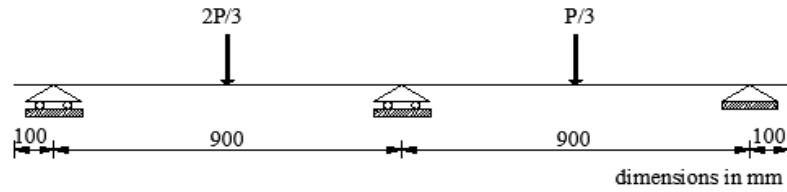
	Total FE analyses: 108
3 aluminium alloys	6082-T6
	6061-T6
	6063-T5
3 aspect ratios D/B ($D \times B$) (mm \times mm):	1.0 (100 \times 100)
	1.5 (100 \times 66.7)
	2.0 (100 \times 50)
8 plate thicknesses t (mm)	5.5, 6, 7, 8, 9, 10, 11, 12
	Resulting slenderness β/ϵ : 2.43-10.75

Table 5.15: Material properties for 6082-T6, 6061-T6 and 6063-T5 [98] aluminium alloys adopted in parametric studies.

	E (MPa)	$\sigma_{0.2}$ (MPa)	σ_u (MPa)	ε_u (mm/mm)	ε_f (mm/mm)	n	$\sigma_u/\sigma_{0.2}$
6082-T6	70302	282	316	0.09	0.14	27.50	1.12
6061-T6	66000	234	248	0.07	0.10	12.00	1.06
6063-T5	69000	164	211	0.07	0.14	10.00	1.29



(a) Load configuration 1 (LC1)



(b) Load configuration 2 (LC2)

Figure 5.22: Load configurations considered in parametric studies for BAT continuous beams.

5.6. Summary

This chapter presented the numerical investigation on the behaviour of aluminium alloy structural elements. To do so, FE models of the tested specimens were developed employing the commercial software package Abaqus [196] and were successfully calibrated based on the measured initial geometric imperfections and the material properties of the 6082-T6 aluminium alloy and the concrete infill reported at Chapter 4. The developed FE models were validated against the experimental data reported in Chapter 4. in terms of the initial stiffness, ultimate load, displacement corresponding to ultimate load and inelastic response exhibited during the tests achieving high accuracy and reliability. Upon validation, the FE models were used to conduct parametric studies, and hence to generate a large number of numerical data.

- 47 C-section fix-ended stub columns,
- 133 pin-ended columns (54 having BAT sections, 54 having CFAT sections and 45 having C-sections),
- 140 C-section simply-supported beams and
- 108 BAT continuous beams.

The numerical ultimate strengths in combination with those obtained experimentally were used to assess the accuracy and applicability of the current design rules and methods and suggest design recommendations.

CHAPTER 6

Analysis of the results and design recommendations

6.1. Introduction

The current chapter analyses the results obtained from the testing programme in conjunction with those generated from the parametric studies to examine the influence of the considered parameters on the behaviour of aluminium alloy structural elements. Moreover, the experimental and numerical ultimate strengths are utilised to assess the applicability and accuracy of the existing design specifications and methods and propose safe and economically efficient design recommendations. Note that all partial safety factors were set equal to unity for these assessments.

6.2. Fix-ended stub columns

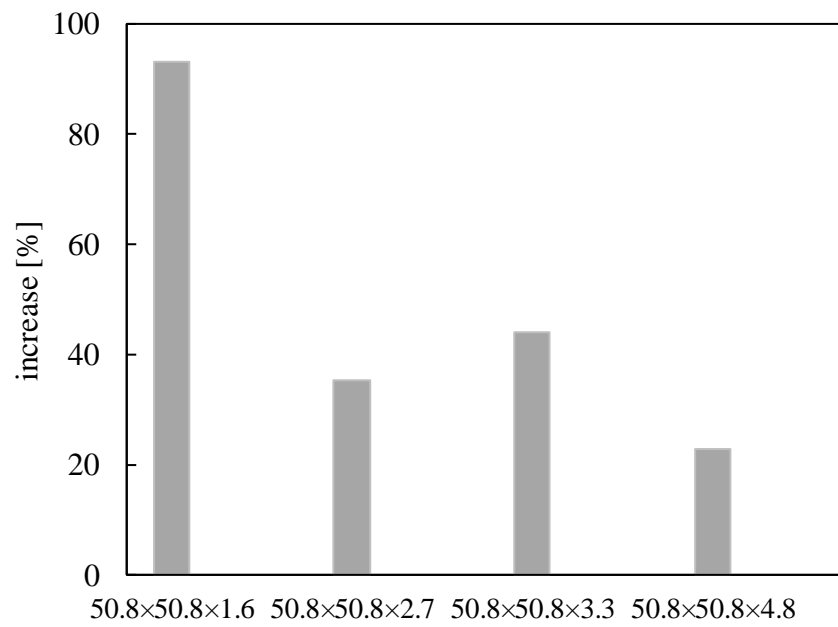
6.2.1. Concrete-filled tubular cross-sections

The effect of filling the aluminium tubes with concrete on their ultimate strength $F_{u,Exp}$ and deformation at failure $\delta_{u,Exp}$ is evaluated utilising the experimentally obtained results. Particularly, Table 6.1 presents the percentage increase $(F_{u,Exp,CFAT} - F_{u,Exp,BAT})/F_{u,Exp,BAT}$ in ultimate strength for each CFAT fix-ended stub column specimen (presented in Subsection 4.2.2.) with regards to the BAT fix-ended stub column specimens (presented

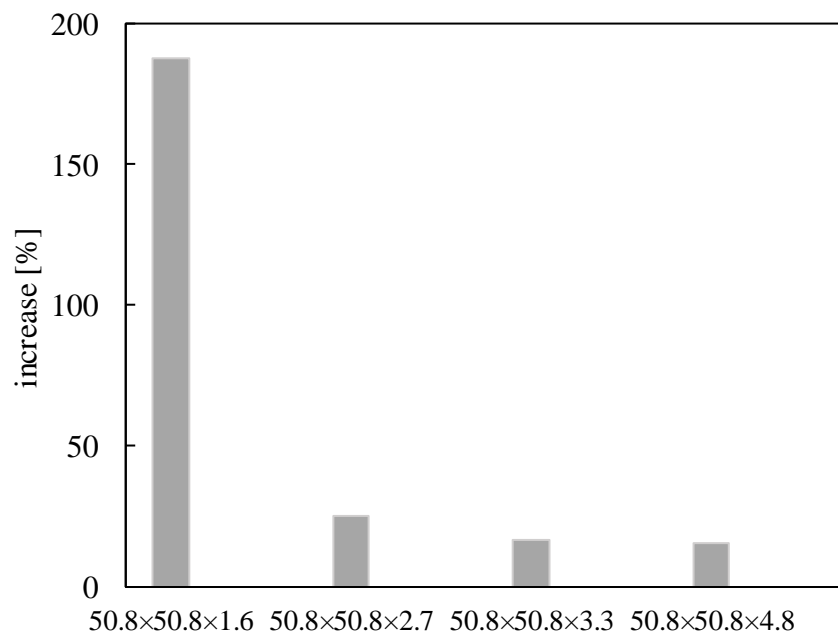
in Subsection 4.2.1.). In Figure 6.1, the average percentage increase values between the two replicate tests (a,b) are presented in chart form for each studied cross-section. The highest strength increase was observed for the section 50.8×50.8×1.6, where the infill significantly delayed the occurrence of local buckling resulting in quite higher ultimate strengths. Compared to the bare specimens, the addition of concrete infill increased the strength by 88.7% and 97.3% for the two studied sections 50.8×50.8×1.6, whilst the lowest increase has been observed for the 50.8×50.8×4.8 cross-section. This is related to the fact that this specimen (with 50.8×50.8×4.8 cross-section) comprises stocky aluminium plate elements, providing significant resistance to local buckling and thus the increased strength owing to the infill led to relatively small additional increase of the ultimate load. Moreover, for the two stockier specimens, i.e., 50.8×50.8×3.3 and 50.8×50.8×4.8, the strength increase had an average value of 49.9% and 23%, respectively. The percentage increase in displacement at failure $(\delta_{u,Exp,CFAT} - \delta_{u,Exp,BAT})/\delta_{u,Exp,BAT}$ for CFAT fix-ended stub column specimen is also presented in Table 6.1 and Figure 6.1. Overall, it is shown that with the addition of the infill, the displacement at which failure is noted, increases. This is more pronounced for the slenderest cross-section, reaching values almost 200% increase, for specimen 50.8×50.8×1.6-C-a. Overall, the experimental results demonstrate that filling the aluminium tubes with concrete has significantly improved response in terms of ultimate strength and deformation at failure.

Table 6.1: Effect of the concrete infill on the CFAT fix-ended stub column specimens compared with the BAT fix-ended stub column specimens.

Specimen	$(F_{u,Exp,CFAT} - F_{u,Exp,BAT})/F_{u,Exp,BAT}$	$(\delta_{u,Exp,CFAT} - \delta_{u,Exp,BAT})/\delta_{u,Exp,BAT}$
50.8×50.8×1.6-C-a	88.7%	198.5%
50.8×50.8×1.6-C-b	97.3%	176.8%
50.8×50.8×2.7-C-a	32.9%	35.6%
50.8×50.8×2.7-C-b	38.0%	14.9%
50.8×50.8×3.3-C-a	44.3%	20.7%
50.8×50.8×3.3-C-b	43.6%	12.4%
50.8×50.8×4.8-C-a	22.8%	18.1%
50.8×50.8×4.8-C-b	23.2%	13.5%



(a) ultimate strength



(b) displacement at failure

Figure 6.1: Effect of the concrete infill on the CFAT fix-ended stub column specimens compared with the BAT fix-ended stub column specimens, based on average values between the two replicates.

In absence of codified design rules for the prediction of the cross-sectional capacities of composite aluminium-concrete cross-sections, the present study will provide design recommendations on the basis of the design formulae for composite steel-concrete cross-sections available in EC4 [210]. Particularly, this study proposes the replacement of the material properties of steel by those of the examined aluminium alloy. The experimentally obtained ultimate strengths are utilised to assess the predicted cross-sectional capacity of the CFAT sections. Note that all partial safety factors are set equal to unity for these assessments. The following equation of [210] is used to calculate the cross-sectional capacity $F_{u,prop}$ of square and rectangular CFAT sections:

$$F_{u,prop} = A\sigma_{0.2} + 0.85A_c f_{ck} \quad (6.1)$$

where A_c and f_{ck} are the cross-sectional area and the characteristic compressive cylinder strength of the concrete infill. A is the cross-sectional area of the aluminium tube for Classes 1-3 cross-sections. For Class 4 cross-sections, the cross-sectional area A in Equation (6.1) is substituted by the effective cross-sectional area A_{eff} which is calculated by assuming a reduced thickness for the slender plate elements through a reduction factor ρ_c [5] as follows.

$$\rho_c = \frac{C_1}{(\beta_f/\varepsilon)} - \frac{C_2}{(\beta_f/\varepsilon)^2} \quad (6.2)$$

where the constants C_1 and C_2 were taken equal to 10 and 24, respectively.

It is noted that for aluminium structures, EN 1999-1-1 [5] adopts the cross-section classification for the treatment of local buckling in aluminium cross-sections under compression. Particularly, it defines slenderness limits for the constituent plate elements enabling to identify the extent to which the cross-sectional capacity is limited by the local buckling resistance. The limits are defined based on the material Class A or B (the herein examined 6082-T6 aluminium alloy is Class A) and on the cross-sectional slenderness ratio β/ε . Class 1 or ductile cross-sections are those which can develop their plastic resistance without the presence of local instabilities. Class 2 or compact cross-sections are those which can develop their plastic resistance with the presence of local instabilities in the plastic range. Class 3 or semi-compact cross-sections are those which can develop their elastic resistance, whilst local buckling prevents them from getting into the plastic

range. Class 4 or slender cross-sections are those which cannot reach yielding because of premature local buckling in the elastic range.

Implementing the formulae of Equations (6.1) and (6.2), the ultimate experimental over proposed strength ratio $F_{u,prop}/F_{u,Exp}$ for each CFAT tested cross-section are listed in Table 6.2. The cross-sectional class of the aluminium tubes are also presented in the same table. The obtained mean value of the $F_{u,prop}/F_{u,Exp}$ ratio is equal to 0.92, whilst all values of the strength ratios are lower than unity suggesting safe design strength predictions. Moreover, the resulting COV equal to 0.07 indicates relatively low scatter and satisfactory design consistency. Overall, it can be concluded that the combined formulae proposed herein for the strength prediction of CFAT cross-sections under uniform compression provide reasonably accurate results with good consistency.

Table 6.2: Proposed design strengths for CFAT cross-sections.

Specimen	Class (aluminium tube)	$F_{u,prop}/F_{u,Exp}$
50.8×50.8×1.6-C-a	4	0.99
50.8×50.8×1.6-C-b	4	0.94
50.8×50.8×2.7-C-a	3	0.99
50.8×50.8×2.7-C-b	3	0.98
50.8×50.8×3.3-C-a	2	0.88
50.8×50.8×3.3-C-b	2	0.87
50.8×50.8×4.8-C-a	1	0.84
50.8×50.8×4.8-C-b	1	0.83
mean		0.92
COV		0.07

6.2.2. Channel cross-sections

6.2.2.1. Assessment of Eurocode 9

EC9 [5] estimates the compressive resistance of a cross-section considering the material yield strength and the susceptibility of each constituent plate element to local buckling. According to Section 6.2.4 specified in EC9 [5], the resistance $F_{pred,cs,EC9}$ of C-sections subjected to uniform compression is estimated as follows.

$$F_{pred,cs,EC9} = F_{pl,Rk} = \begin{cases} A\sigma_{0.2} & \text{for Classes 1,2,3} \\ A_{eff}\sigma_{0.2} & \text{for Class 4} \end{cases} \quad (6.3)$$

where A_{eff} is the effective cross-sectional area calculated by assuming a reduced thickness for the slender plate elements as explained in Equation (6.2).

Table 6.3 lists the predicted-to-ultimate ratios $F_{pred,cs,EC9}/F_u$ together with the corresponding slenderness parameter β_f/ϵ of the flange. It can be seen that EC9 [5] provides safe design strength predictions but quite conservative with mean value of the $F_{pred,cs,EC9}/F_u$ ratio equal to 0.85 (much lower than unity). The same can also be concluded from Figure 6.2 which presents the $F_{pred,cs,EC9}/F_u$ ratios plotted against the β_f/ϵ values. This graph shows clearly that the level of conservatism of the current codified provisions increases for slender cross-sections, i.e., cross-sections with higher β_f/ϵ values. Additionally, the relatively low COV of 0.11 and the apparent scattering of the data points plotted in Figure 6.2 confirm the relatively low level of design consistency provided by the EC9 [5].

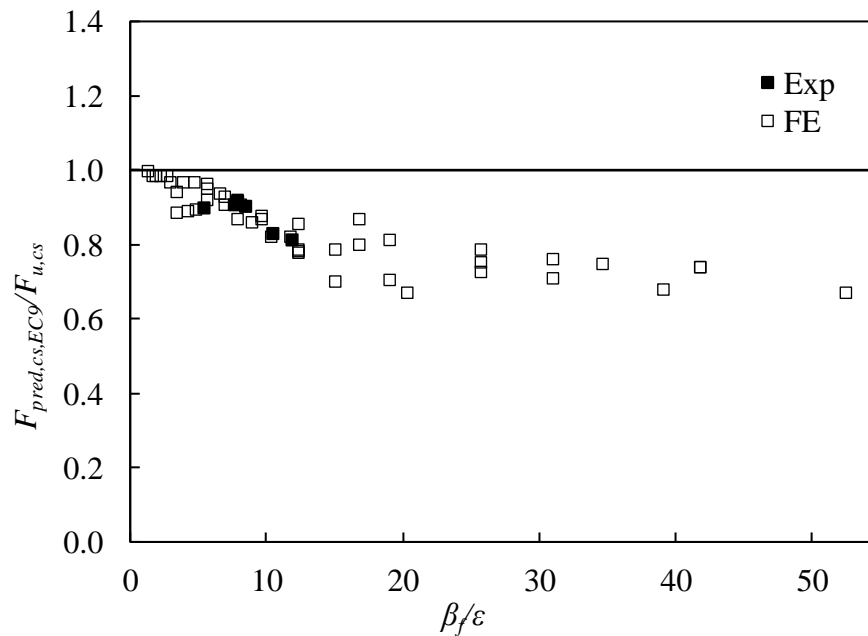


Figure 6.2: Comparison of experimental and FE results with EC9 [5] design strengths for fixed-ended stub columns.

Table 6.3: Predicted strength ratios for both experimental and numerical results for fix-ended stub columns.

Specimen	No	β_f/ε	$F_{pred,cs,EC9}/F_u$	λ_1	$F_{pred,cs,DSM}/F_u$
50.8×50.8×6.35-L150	1	7.49	0.90	0.35	1.00
50.8×50.8×4.76-L150	1	10.42	0.83	0.48	0.99
50.8×38.1×6.35-L150	1	5.46	0.89	0.32	0.89
50.8×38.1×3.18-L150	1	11.94	0.81	0.68	1.00
50.8×25.4×3.18-L150	1	7.62	0.90	0.58	0.95
38.1×38.1×4.76-L115	1	7.84	0.91	0.37	0.98
FE	47	1.36-52.50	0.85	0.19-2.49	0.96
		mean (all)	0.85		0.96
		COV (all)	0.11		0.04

6.2.2.2. Assessment of Direct Strength Method

The DSM is codified in Section E3.2.1 of [131] as an alternative and simplified design method for prediction of the cross-sectional compressive resistance of cold-formed carbon steel cross-sections. This method utilises the cross-sectional slenderness λ_1 and adopts a ‘strength curve’ allowing to directly determine the cross-sectional compressive resistance $F_{DSM,cs,pred}$ of a slender cross-section ($\lambda_1 > 0.776$). In case of a stocky cross-section ($\lambda_1 \leq 0.776$), the cross-sectional compressive resistance $F_{DSM,cs,pred}$ equals to the yield strength $A\sigma_{0.2}$ of the cross-section. The design formulae for both stocky and slender cross-sections are given by Equation (6.4).

$$F_{DSM,cs,pred} = \begin{cases} A\sigma_{0.2} & \text{for } \lambda_1 \leq 0.776 \\ \left[1 - 0.15 \left(\frac{F_{cr1}}{A\sigma_{0.2}} \right)^{0.4} \right] \left(\frac{F_{cr1}}{A\sigma_{0.2}} \right)^{0.4} A\sigma_{0.2} & \text{for } \lambda_1 > 0.776 \end{cases} \quad (6.4)$$

where $\lambda_1 = \sqrt{F_{ne}/F_{cr1}}$, $F_{ne} = A\sigma_{0.2}$ is the flexural buckling strength and $F_{cr1} = A\sigma_{cr}$ is the critical elastic local column buckling load where σ_{cr} is the elastic critical buckling stress of the cross-section. σ_{cr} accounts for the element interaction and can be obtained using either proposed analytical formulae [233] or numerical tools, such as CUFSM [234].

The predicted-to-ultimate $F_{pred,cs,DSM}/F_u$ ratios along with the corresponding cross-sectional slenderness λ_1 values are depicted in Table 6.3. The resulted mean value of the $F_{pred,cs,DSM}/F_u$ ratio is 0.96 and the corresponding COV is 0.04 denoting that the DSM

offers significantly more precise and consistent strength predictions compared to EC9 ($F_{pred,cs,EC9}/F_u=0.85$ and corresponding $COV=0.11$). Moreover, in Figure 6.3 the $F_{pred,cs,DSM}/F_u$ ratios are plotted against the cross-sectional slenderness λ_l values. Again, it can be concluded that the DSM provides higher design accuracy and consistency than EC9 [5] as the data points are closer to unity and less scattered.

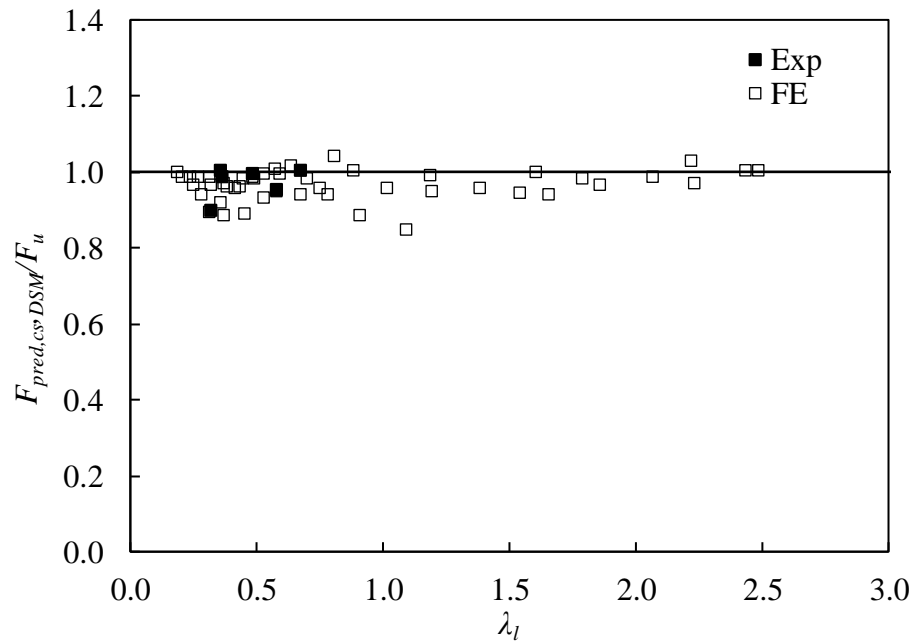


Figure 6.3: Comparison of experimental and FE results with DSM [235] design strengths for fix-ended stub columns.

6.3. Pin-ended columns

6.3.1. Bare tubular cross-sections

6.3.1.1. Assessment of Eurocode 9

EC9 [5] provides design rules for the strength of aluminium alloy columns under axial compression. The plastic cross-sectional resistance of square and rectangular bare columns is calculated by Equation (6.5).

$$F_{pl,Rk} = A\sigma_{0.2} \quad (6.5)$$

where A is the aluminium cross-sectional area for Classes 1-3 sections, whilst for Class 4 cross-sections the A in Equation (6.5) is substituted by the effective cross-sectional area A_{eff} as explained in Subsection 6.2.1.

The current EC9 [5] provisions for column strength adopt the buckling curve approach. The predicted buckling resistance N_{pred} is calculated by Equation (6.6).

$$F_{pred} = \chi F_{pl,Rk} \quad (6.6)$$

where the reduction coefficient χ is given by Equation (6.7).

$$\chi = \frac{1}{\phi + \left[\phi^2 - \bar{\lambda}^2 \right]^{0.5}} \leq 1.0 \quad (6.7)$$

The parameter ϕ and the member slenderness $\bar{\lambda}$ are calculated by Equations (6.8) and (6.9), respectively.

$$\phi = 0.5 \left[1 + 0.2(\bar{\lambda} - 0.1) + \bar{\lambda}^2 \right] \quad (6.8)$$

$$\bar{\lambda} = \sqrt{F_{pl,Rk} / F_{cr}} \quad (6.9)$$

where 0.2 is the recommended value for the imperfection factor α for Class A aluminium alloys, 0.1 is the recommended limit of the horizontal plateau $\bar{\lambda}_0$, and F_{cr} is the critical elastic buckling load, which is determined from Equation (6.10).

$$F_{cr} = \pi^2 (EI) / L_e^2 \quad (6.10)$$

where E is the modulus of elasticity of aluminium, I is the second moment of area of the aluminium tube and L_e is the effective buckling column length.

In order to assess the accuracy of EN 1999-1-1 [5] strength predictions, Figure 6.4 depicts the ultimate loads F_u obtained from the experiments and the FE study normalised by the plastic resistance $F_{pl,Rk}$ according to Equation (6.5) and plotted against the member slenderness $\bar{\lambda}$. The Eurocode (EC9) buckling design curve is also included in this figure. It can be seen that both the experimental and FE data are above the design curve, which signifies that the design predictions by the EN 1999-1-1 [5] are conservative.

Table 6.4 lists the F_{EC9}/F_u ratios, where F_{EC9} is the F_{pred} found from Equation (6.6) using EC9 buckling curve according to Equation (6.5). The ratios are reported together with the corresponding member slendernesses $\bar{\lambda}$ and the cross-sectional Class of the examined

columns. Based on both the FE and test data, the mean value of F_{EC9}/F_u ratio is 0.83 indicating that EN 1999-1-1 [5] underestimates the actual buckling strength of bare columns. Moreover, the high value of COV reported in Table 6.4 and the scattered predictions graphically shown in Figure 6.4 suggest relatively low level of design consistency of the EN 1999-1-1 [5] strength predictions.

Aiming to improve the accuracy of the current design rules for BAT slender columns, a revised buckling curve is recommended. On the basis of the obtained test and FE results, Equation (6.11) is proposed for the calculation of parameter ϕ for Class A aluminium alloys. This equation uses a revised imperfection factor α which is equal to 0.08, and a revised limit of the horizontal plateau $\bar{\lambda}_0$ which is equal to 0.2.

$$\phi = 0.5 \left[1 + 0.08(\bar{\lambda} - 0.2) + \bar{\lambda}^2 \right] \quad (6.11)$$

The proposed buckling curve is shown in Figure 6.4, whilst the corresponding $F_u/F_{prop,BAT}$ ratios are included in Table 6.4. $F_{prop,BAT}$ is the F_{pred} found from Equation (6.6), when applying Equations (6.5), (6.7) and (6.9)-(6.11) (i.e. replacing current Equation (6.8) with the proposed Equation (6.11)). As can be seen, the proposed curve improves the accuracy of the predicted strength values by 12%. The same observations can be drawn from Figure 6.5, where the ultimate loads N_u are plotted versus the strength predictions F_{pred} , showing that the proposed curve provides better strength predictions (i.e. closer to diagonal line) compared to those of EC9.

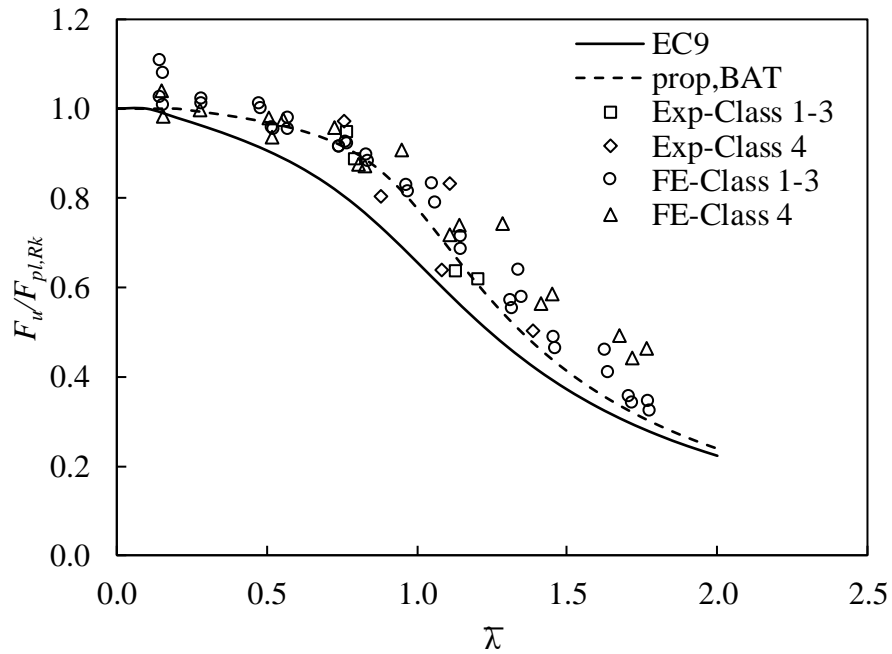


Figure 6.4: Comparison of experimental and numerical results with European and proposed design strengths for BAT columns.

Table 6.4: Predicted strength ratios for both experimental and numerical results for BAT columns.

Specimen	No	Class	$\bar{\lambda}$	F_{EC9}/F_u	$F_{prop,BAT}/F_u$
				Equations (6.5)-(6.10)	Equations (6.5)-(6.7) & Equations (6.9)-(6.11)
50.8×50.8×1.6	1	4	1.11	1.43	1.22
50.8×50.8×3.3	1	2	1.13	1.11	0.95
50.8×50.8×4.8	1	1	1.21	1.18	1.03
76.2×76.2×3.3	1	4	0.76	1.21	1.06
76.2×76.2×4.8	1	2	0.80	1.13	0.98
76.2×76.2×6.4	1	2	0.77	1.18	1.04
76.2×38.1×3.3	1	4	1.39	1.19	1.06
76.2×50.8×3.3	1	4	1.09	1.07	0.91
101.6×50.8×3.3	1	4	0.88	1.10	0.94
FE	36	1-3	0.14-1.78	1.13	1.06
	18	4	0.15-1.76	1.25	1.12
			mean (all)	0.85	0.97
			COV (all)	0.07	0.08

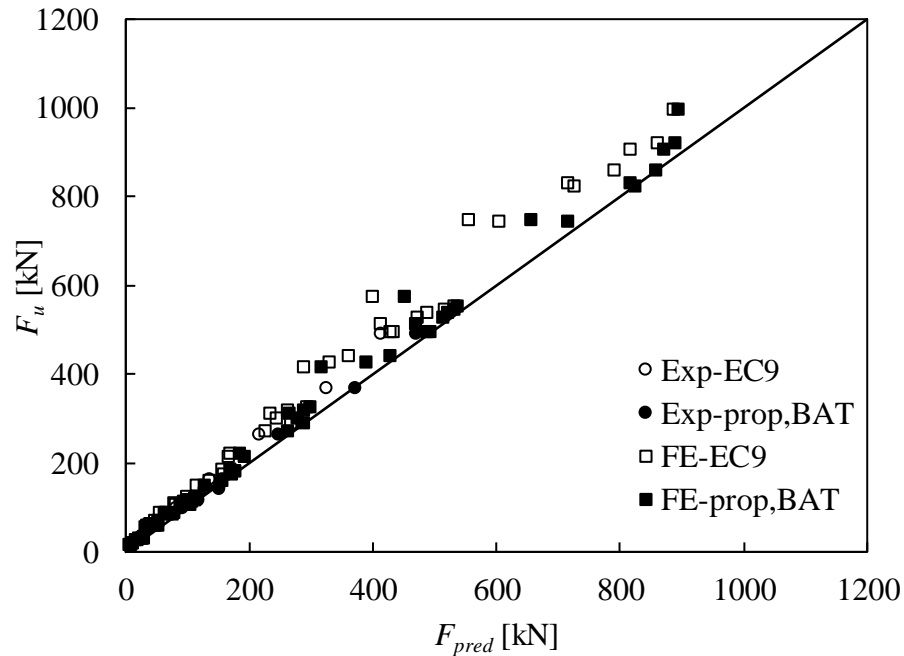


Figure 6.5: Comparison of experimental and numerical ultimate loads with design strengths based on European standards and proposed equations for BAT columns.

6.3.2. Concrete-filled tubular cross-sections

6.3.2.1. Effect of concrete infill, cross-sectional slenderness ratio β/ε and buckling axis

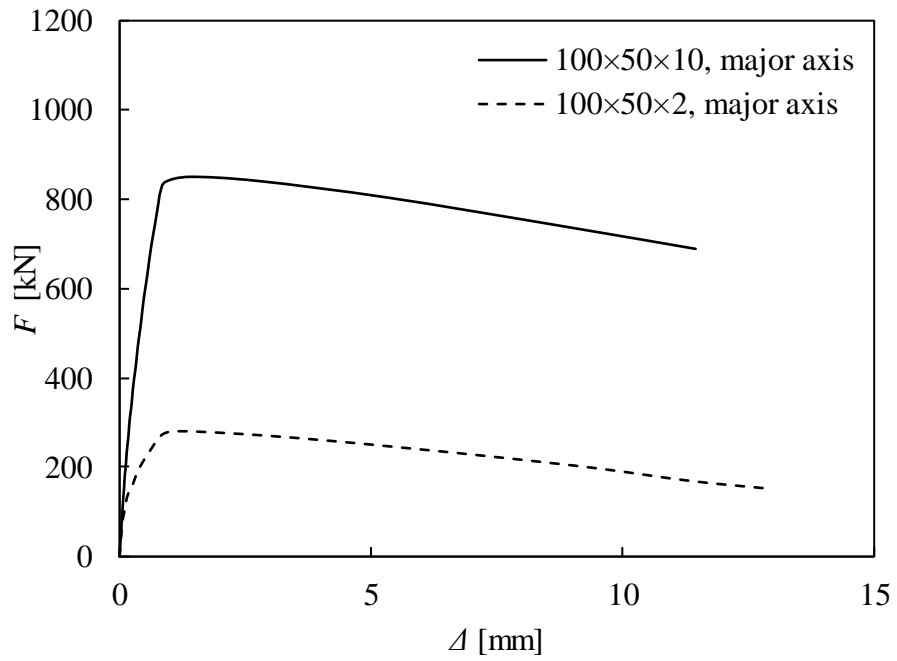
The effect of filling the aluminium tubes with concrete on their ultimate strength F_u and is evaluated utilising the experimentally and numerically obtained results. Table 6.5 presents the percentage increase $(F_{u,Exp,CFAT} - F_{u,Exp,BAT})/F_{u,Exp,BAT}$ in ultimate strength for each CFAT pin-ended stub column specimen (presented in Subsection 4.2.2. with regards to the BAT fix-ended stub column specimens (presented in Subsection 4.2.1. The cross-sectional slenderness ratio β/ε along with the member slenderness $\bar{\lambda}$ calculated according to EN 1999-1-1 [5] are also included in Table 6.5. From the reported cross-sectional and member slenderness values, it can be seen that for constant aluminium cross-section and for constant member length, the addition of concrete infill leads to a reduction in $\bar{\lambda}$ values. This, consequently, results in increased buckling capacity of CFAT columns. To evaluate the concrete's contribution, the percentage strength increase of the ultimate load $(F_{u,Exp,CFAT} - F_{u,Exp,BAT})/F_{u,Exp,BAT}$, owing to the presence of the concrete infill, is also listed in Table 6.5. It can be observed that the strength increase is generally higher for members

with higher β/ε , i.e. thinner plate elements. The highest increase, which was equal to 72%, has been observed for specimen 50.8×50.8×1.6 and can be related to the delay in the local buckling offered by the concrete infill. The specimen 76.2×76.2×6.4 experienced the least benefit due to the concrete infill. This is related to the fact that this specimen comprises stocky aluminium plate elements providing significant resistance to buckling and thus the increased stiffness owing to the concrete led to relatively small additional increase of the ultimate load.

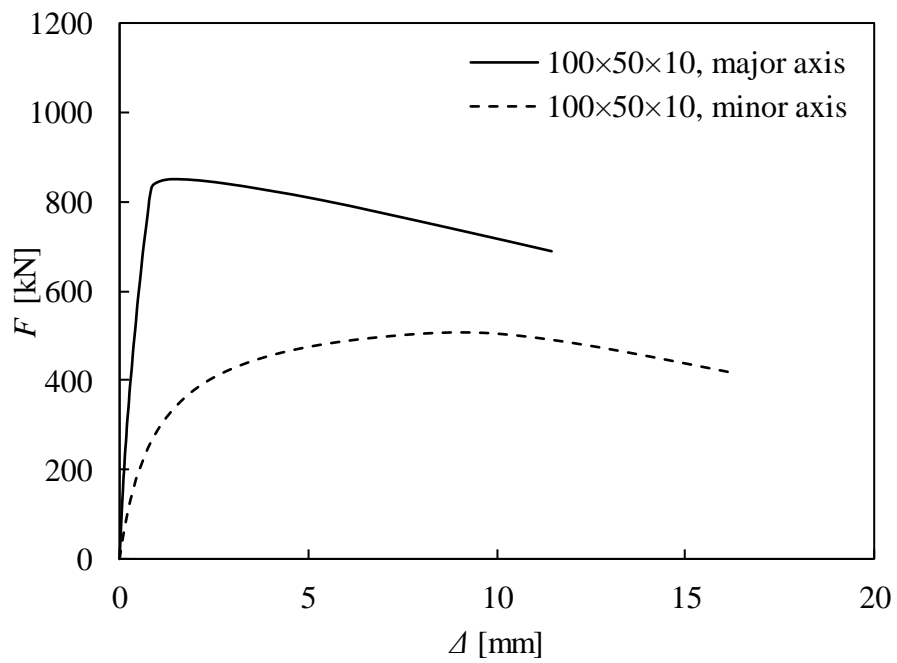
Table 6.5: Effect of the concrete infill on the CFAT pin-ended column specimens compared with the BAT pin-ended column specimens.

Specimen	β/ε	$\bar{\lambda}$	$(F_{u,Exp,CFAT} - F_{u,Exp,BAT})/F_{u,Exp,BAT}$
50.8×50.8×1.6	34.06	1.11	72%
50.8×50.8×1.6-C		0.98	
50.8×50.8×3.3	17.77	1.13	24%
50.8×50.8×3.3-C		1.09	
50.8×50.8×4.8	11.99	1.21	21%
50.8×50.8×4.8-C		1.18	
76.2×76.2×3.3	25.87	0.76	31%
76.2×76.2×3.3-C		0.70	
76.2×76.2×4.8	17.69	0.80	22%
76.2×76.2×4.8-C		0.76	
76.2×76.2×6.4	13.20	0.76	9%
76.2×76.2×6.4-C		0.75	
76.2×38.1×3.3	12.29	1.39	10%
76.2×38.1×3.3-C		1.38	
76.2×50.8×3.3	17.16	1.09	47%
76.2×50.8×3.3-C		1.05	
101.6×50.8×3.3	12.89	0.88	43%
101.6×50.8×3.3-C		0.87	

Figure 6.6 presents typical load versus mid-height lateral deflection curves obtained from the FE parametric study. In particular, Figure 6.6(a) displays the FE buckling behaviour of CFAT columns with constant member length and different cross-sectional thickness, showing higher load for lower cross-sectional slenderness. Figure 6.6(b) shows a comparison of a CFAT column with buckling about the major and minor axis, denoting improved strength in the former case.



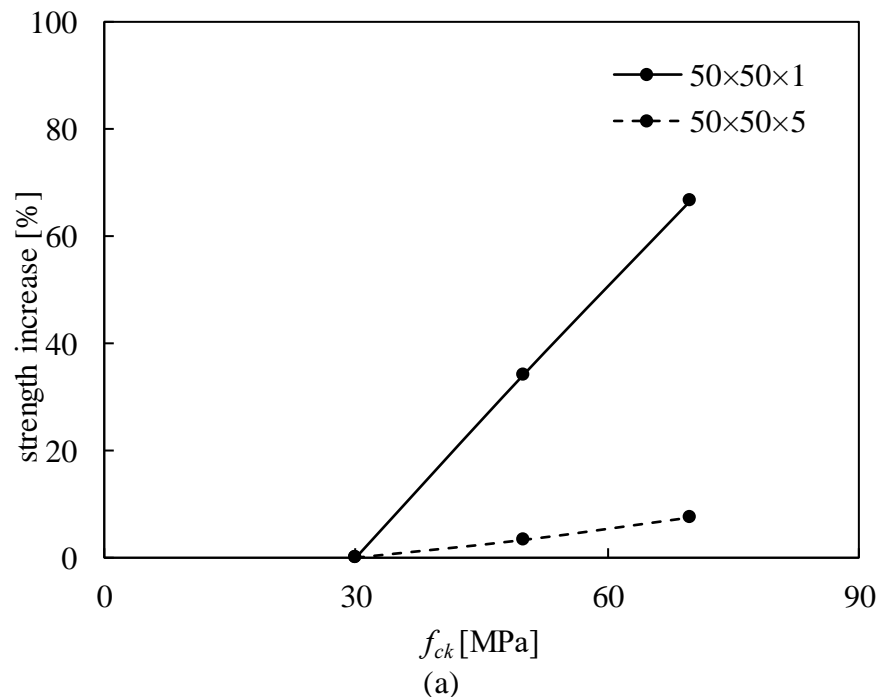
(a) $L_e = 1000$ mm



(b) $L_e = 1000$ mm

Figure 6.6: Typical load-mid-height lateral deflection curves for CFAT pin-ended columns from FE studies.

Aiming to evaluate the effect of the concrete grade on the ultimate strength of CFAT columns, the ultimate FE load values were used. Figure 6.7 presents the percentage strength increase owing to higher concrete grade $(F_{u,C50/70} - F_{u,C30})/F_{u,C30}$ with respect to the strength at C30 $F_{u,C30}$ for typical CFAT columns of constant length. It can be seen that the strength increase owing to higher concrete grade seems to be more pronounced in columns with thinner plate elements ($50 \times 50 \times 1$ vs $50 \times 50 \times 5$ and $100 \times 50 \times 2$ vs $100 \times 50 \times 10$). This has been observed for square tubes but also for the case of rectangular tubes under major and minor axis buckling. As will also be discussed in the following Subsection 6.3.2.2, the buckling strength is a function of the cross-sectional plastic resistances of the two materials, concrete and aluminium. Hence for increased concrete strength, the concrete's cross-sectional plastic resistance increases as well. The latter comprises a bigger percentage of the total cross-sectional plastic resistance for slender sections (in which the aluminium cross-sectional area is small) which in turn leads to a more significant increase to the ultimate load for higher concrete grades.



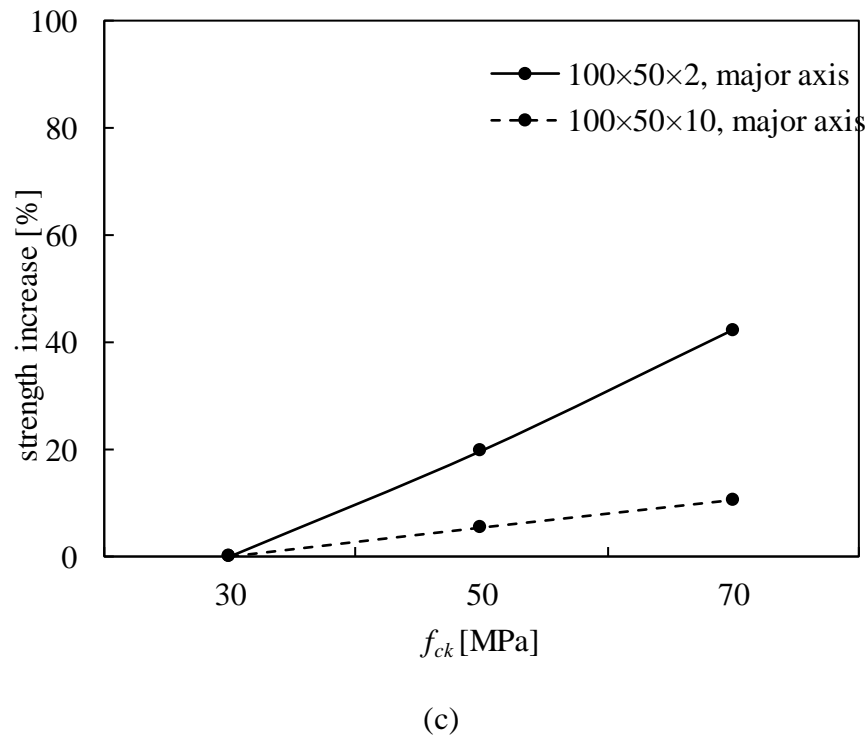
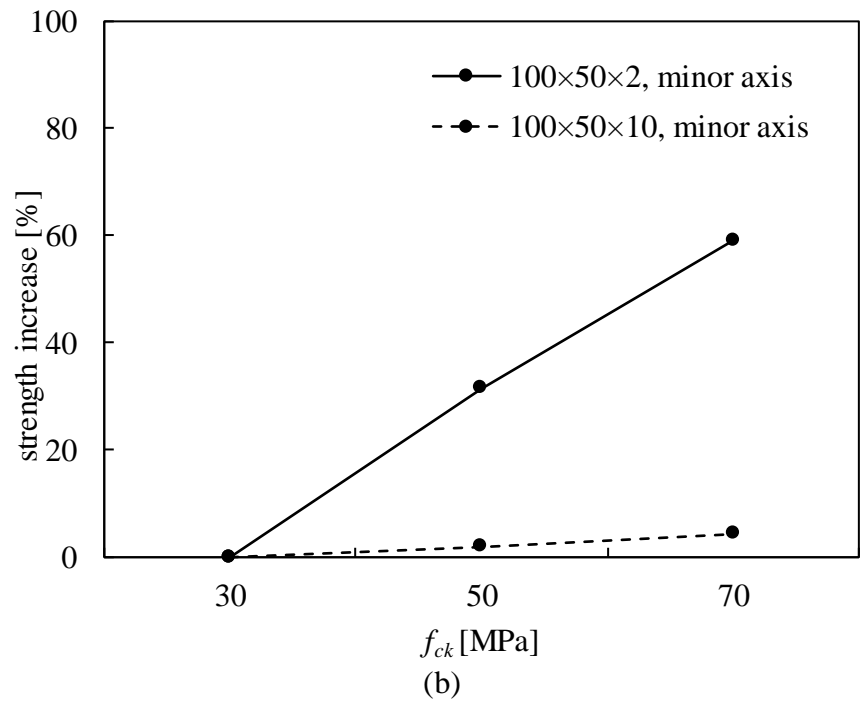


Figure 6.7: Effects of concrete compressive strengths f_{ck} on the ultimate strength of CFAT columns ($L_e=1000$ mm).

6.3.2.2. Design recommendations

In absence of design provisions for the aluminium-concrete composite columns, the present study adopts the design methodology for composite steel-concrete members

available in EN 1994-1-1 [210] for the prediction of the ultimate capacities of CFAT columns, replacing appropriately the material properties of steel by those of the aluminium alloy and proposes a buckling curve for CFAT columns on the basis of the experimental and numerical data.

According to [210], the plastic cross-sectional resistance $N_{pl,Rk}$ of square and rectangular concrete-filled columns can be calculated by Equation (6.12).

$$F_{pl,Rk} = A\sigma_{0.2} + 0.85A_c f_{ck} \quad (6.12)$$

The cross-section classification adopted by EN 1999-1-1 [5] is applied for the examined aluminium cross-sections. The member slenderness $\bar{\lambda}$ is calculated according to Equation (6.12), where the critical elastic buckling load is taken as follows.

$$F_{cr} = \pi^2 (EI + k_e E_c I_c) / L_e^2 \quad (6.13)$$

where E_c is the modulus of elasticity of concrete infill according to EN 1992-1-1 [197], I_c is the second moment of area of the concrete infill and k_e is the correction factor for the concrete which is taken equal to 0.6 [5].

Figure 6.8 shows the ultimate loads F_u obtained from the experiments and the FE study normalised by the plastic resistance $F_{pl,Rk}$ from Equation (6.12) and plotted against the member slenderness $\bar{\lambda}$ according to Equation (6.13), separately for cross-section classes. In the same graph, a proposed buckling design curve is also displayed following the EC9 methodology but with the imperfection factor and limit of the horizontal plateau calibrated on the basis of the obtained data according to Equation (6.14).

$$\phi = 0.5 \left[1 + 0.18(\bar{\lambda} - 0.2) + \bar{\lambda}^2 \right] \quad (6.14)$$

Based on Figure 6.8, it can also be observed that the Class 4 (slender) and Class 1-3 aluminium cross-sections follow a different trend, particularly for increasing member slenderness. This can also be considered together with the conclusion derived in Subsection 6.3.2.1, based on which the highest strength increase was noted for the most slender cross-section. In absence of sufficient experimental data for concrete-filled slender aluminium square and rectangular hollow sections at cross-sectional level, the present proposal was based on the currently adopted equations of EC9 for local buckling

(i.e., Equation (6.2)). However, future studies on this direction are recommended to gain a better understanding of the cross-sectional resistance of CFAT cross-sections.

Implementing EC9 Equation (6.2) for the effective cross-sectional area to account for local buckling in slender aluminium cross-sections, together with Equations (6.12) and (6.13) of EC4, Equations (6.7) and (6.9) of EC9 and the proposed Equation (6.14) in place of Equation (6.8), the proposed strength $F_{prop,CFAT}$ can be evaluated from Equation (6.6). The ultimate over proposed strength values $F_{prop,CFAT}/F_u$ are summarised in Table 6.5. The resulting overall mean value is 0.88, whilst the strength is more accurately predicted for stocky aluminium cross-sections ($F_{prop,CFAT}/F_u$ equal to 0.94 for Class 1-3). These values indicate that the combined design formulae proposed herein provide good predictions with reasonable consistency. The same can also be concluded from Figure 6.8 where the examined F_{pred} values deviate slightly from the diagonal line with relatively low scattering.

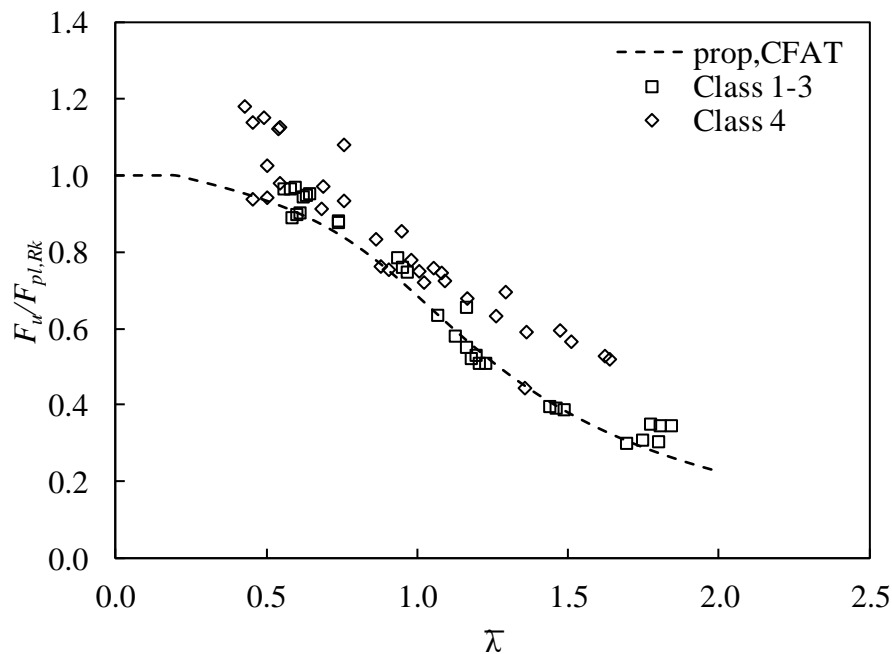


Figure 6.8: Comparison of experimental and numerical results with proposed design strengths for CFAT columns.

Table 6.6: Predicted strength ratios for both experimental and numerical results for CFAT columns.

Specimen	No	Class	$\bar{\lambda}$	$F_{prop,CFAT}/F_u$	
				Equations. (6.6),(6.7),(6.9) & Equations (6.12)-(6.14)	
				Class 1-3	Class 4
50.8×50.8×1.6-C	1	4	0.98	-	1.19
50.8×50.8×3.3-C	1	2	1.09	1.00	-
50.8×50.8×4.8-C	1	1	1.18	1.16	-
76.2×76.2×3.3-C	1	4	0.70	-	1.05
76.2×76.2×4.8-C	1	2	0.76	1.04	-
76.2×76.2×6.4-C	1	2	0.75	1.04	-
76.2×38.1×3.3-C	1	4	1.38	-	0.99
76.2×50.8×3.3-C	1	4	1.05	-	1.08
FE	31	1-3	0.57-1.85	1.08	-
	32	4	0.43-1.64	-	1.05
Mean				0.94	0.81
COV				0.09	0.14
mean (all)				0.88	
COV (all)				0.14	

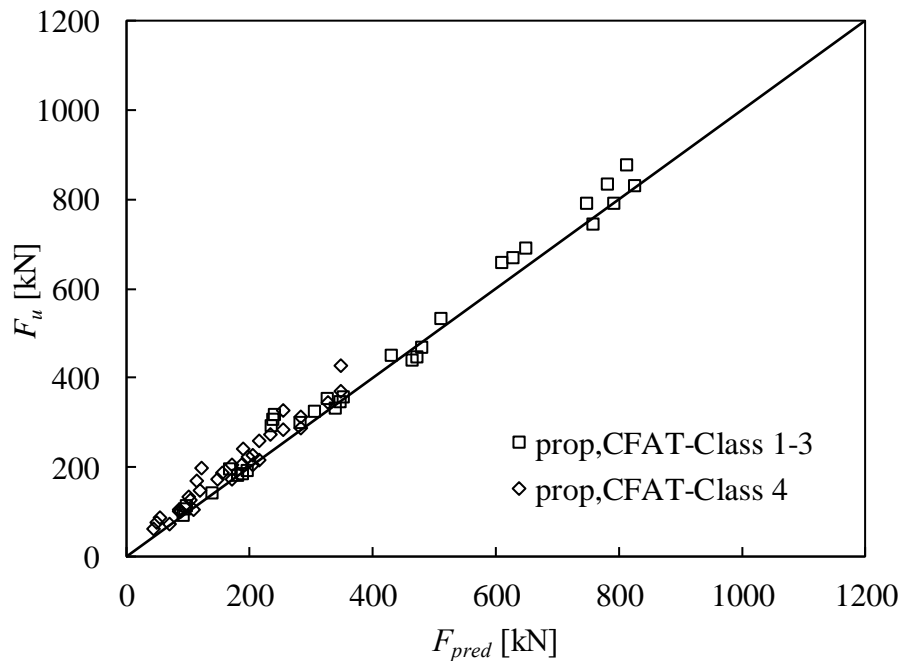


Figure 6.9: Comparison of experimental and numerical ultimate loads with proposed design strengths for CFAT columns.

6.3.3. Channel cross-sections

6.3.3.1. Assessment of Eurocode 9

According to Section 6.3.1 specified in EC9 [5], the design flexural buckling resistance $F_{pred,EC9}$ of C-section members subjected to uniform compression is estimated as follows.

$$F_{pred,EC9} = \chi F_{pl,Rk} \quad (6.15)$$

where the plastic cross-sectional resistance $F_{pl,Rk}$ and the reduction coefficient χ are given by Equations (6.5) and (6.7), respectively.

The applicability of the EC9 [5] design buckling curve is evaluated by comparing the obtained ultimate strengths F_u derived from pin-ended column tests and FE models with the respective codified predictions $F_{pred,EC9}$. To do so, the F_u were normalised by the corresponding plastic resistance $F_{pl,Rk}$ and were plotted against the member slenderness $\bar{\lambda}$ as shown in Figure 6.10. It can be seen that both the experimental and FE data points are above the design curve, suggesting that the design strength predictions are safe but conservative. The predicted-to-ultimate $F_{pred,EC9}/F_u$ ratios are also presented in Table 6.7 together with the corresponding member slenderness $\bar{\lambda}$ values. The resulted mean value of 0.87 of the $F_{pred,EC9}/F_u$ ratio denotes that EC9 [5] underestimates the actual flexural buckling resistance of 6082-T6 aluminium alloy columns. Moreover, the corresponding COV value of 0.08 together with the scattered data points displayed in Figure 6.10 suggest relatively low level of design consistency of EC9 [5] strength predictions.

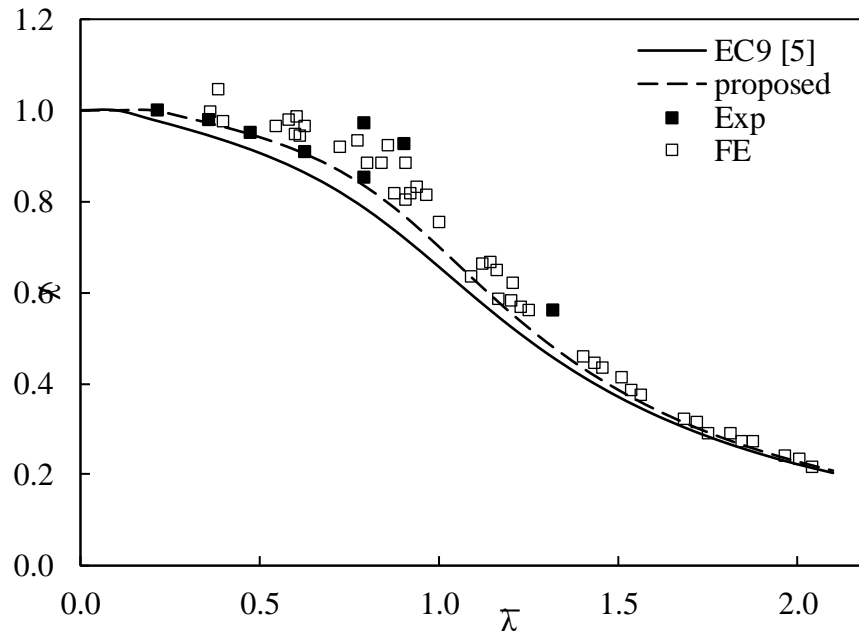


Figure 6.10: Comparison of experimental and FE results with EC9 [5] design strengths for pin-ended columns.

Aiming to improve the accuracy level of the current design rules provided by EC9 [5], the obtained experimental and FE results were utilised to propose a revised flexural buckling curve for Class A aluminium alloys. In particular, a revised imperfection factor α of 0.16 and a revised limit of the horizontal plateau $\bar{\lambda}_0$ of 0.2 are proposed based on a numerical optimisation procedure so that the best agreement between the EC9 strength predictions and the experimental and FE results to be obtained. The proposed flexural buckling curve is plotted in Figure 6.10, whilst the proposed predicted-to-ultimate ratios $F_{pred,EC9,prop}/F_u$ are included in Table 6.7. As can be seen, the achieved mean value of the $F_{pred,EC9,prop}/F_u$ ratio is 0.91 which is higher than that of the $F_{pred,EC9}/F_u$ ratio signifying that the proposed curve offers slightly more accurate strength predictions. The same can be drawn from Figure 6.10 where the data points are closer to the proposed buckling curve.

Table 6.7: Predicted strength ratios for both experimental and numerical results for pin-ended columns.

Specimen	No	$\bar{\lambda}$	$F_{pred,EC9}/F_u$	$F_{pred,EC9,prop}/F_u$	$\bar{\lambda}_c$	$F_{pred,DSM}/F_u$
50.8×50.8×6.35-L500	1	0.63	0.90	0.94	0.65	0.94
76.2×76.2×6.35-L500	1	0.36	0.76	0.78	0.40	0.96
76.2×76.2×6.35-L300	1	0.22	0.77	0.79	0.24	0.98
50.8×38.1×6.35-L500	1	0.90	0.78	0.83	0.90	0.79
50.8×38.1×3.18-L500	1	0.79	0.75	0.79	0.86	0.89
50.8×38.1×3.18-L300	1	0.48	0.78	0.81	0.51	0.95
50.8×25.4×3.18-L500	1	1.32	0.78	0.82	1.34	0.91
50.8×25.4×3.18-L300	1	0.79	0.77	0.82	0.80	0.81
FE	45	0.36-2.04	0.88	0.93	0.39-2.04	0.93
		mean (all)	0.87	0.91		0.93
		COV (all)	0.08	0.07		0.06

6.3.3.2. Assessment of Direct Strength Method

According to Section E.2 specified in DSM [235], the flexural buckling resistance $F_{pred,DSM}$ of C-section members under uniform compression is calculated as follows.

$$F_{pred,DSM} = F_{ne} = \begin{cases} (0.658^{\lambda_c^2}) A\sigma_{0.2} & \text{for } \lambda_c \leq 1.5 \\ \left(\frac{0.877}{\lambda_c^2}\right) A\sigma_{0.2} & \text{for } \lambda_c > 1.5 \end{cases} \quad (6.16)$$

where $\lambda_c = \sqrt{A\sigma_{0.2}/F_{cre}}$ is the column slenderness parameter and F_{cre} is the least of the applicable elastic flexural buckling stresses calculated in accordance with Sections E2.1 and E2.2 of [235]. Figure 6.11 displays the $F_{pred,DSM}/F_u$ ratios plotted against column slenderness parameter λ_c values suggesting that the DSM [235] provides accurate and relatively low scattered design strength predictions. Furthermore, Table 6.7 enumerates the predicted-to-ultimate $F_{pred,DSM}/F_u$ ratios along with the corresponding column slenderness parameter λ_c values. As can be seen the DSM [235] design rules exhibit the most accurate design strength predictions with mean value of the $F_{pred,DSM}/F_u$ ratio of 0.93. Higher design consistency is also provided since the corresponding COV is 0.06 which is the lowest values amongst those resulted from EC9 [5] and the revised EC9 design rules proposed herein.

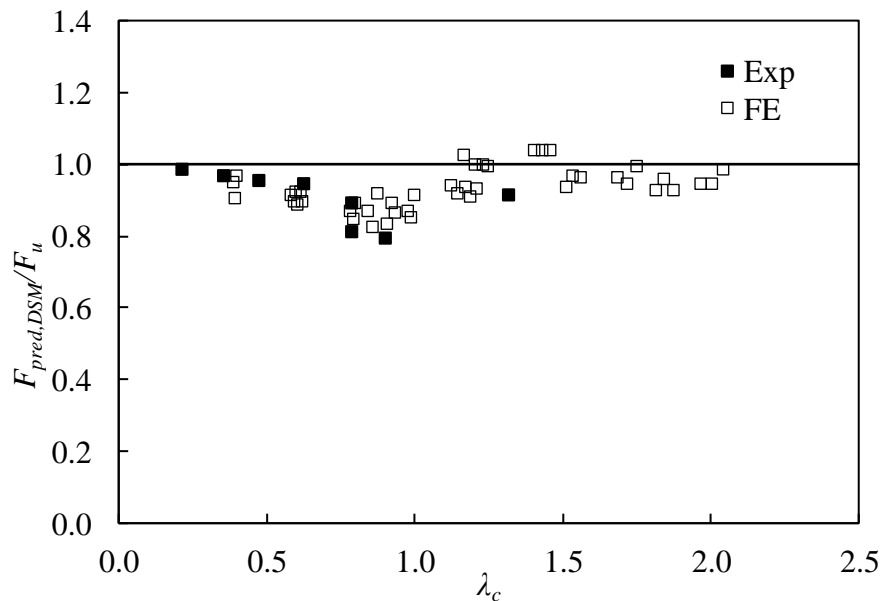


Figure 6.11: Comparison of experimental and FE results with DSM [235] design strengths for pin-ended columns.

6.4. Simply-supported beams

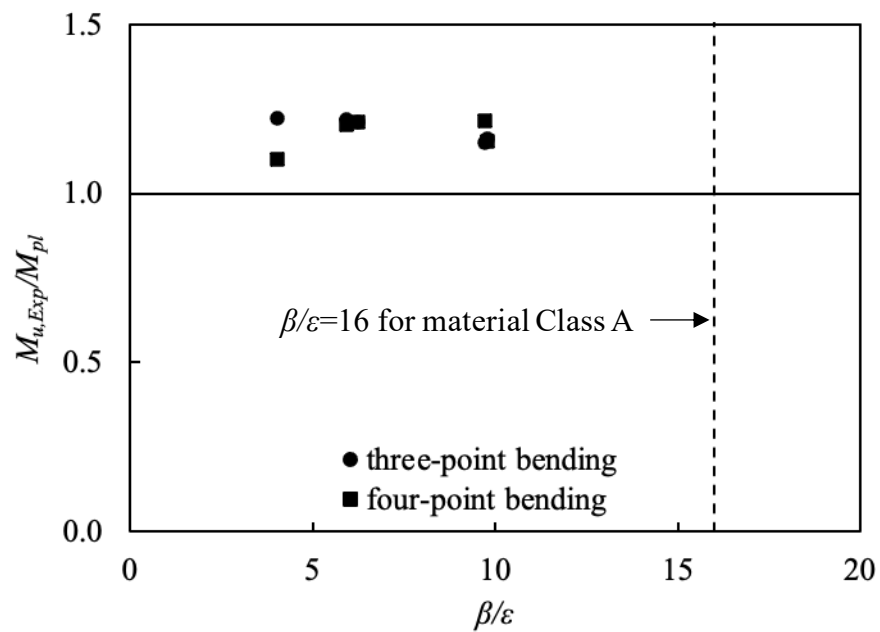
6.4.1. Bare rectangular tubular cross-sections

6.4.1.1. Assessment of Eurocode 9

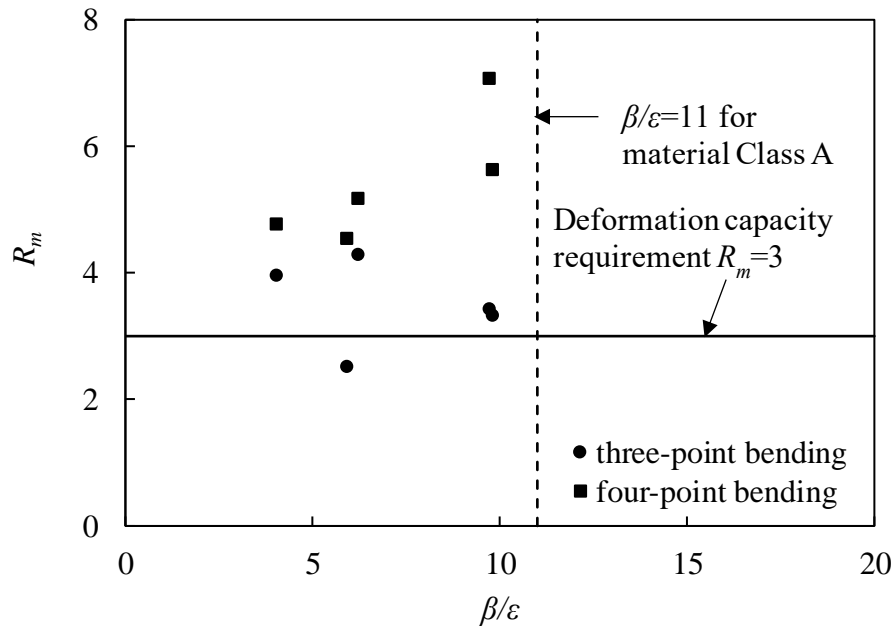
Section 6.2.5 of EC9 [5] provides design criteria for the cross-sectional moment resistance with design values dependent on the classification of the cross-section. As described in Subsection 6.2.1, EC9 [5] adopts a suitable cross-section classification framework to consider the local buckling effect on the cross-sectional structural response. For this reason, slenderness limits for the constituent plate elements are defined, enabling to identify the extent to which the cross-sectional resistance and rotational capacity is limited by the local buckling resistance. Class 1 or ductile cross-sections are capable of developing their collapse resistance without presence of local instabilities. Class 2 or compact cross-sections are capable of developing their plastic moment resistance, whilst their rotational capacity is limited by local instabilities. Class 3 or semi-compact cross-sections are able to reach their elastic moment resistance only since local buckling prevents them from getting into the plastic range. In Class 4 or slender cross-sections the ultimate behaviour is governed by significant local buckling phenomena and failure occurs before the attainment of the proof (yield) strength.

The experimental moment capacities obtained from the three- and four-point bending tests are utilised herein to assess the current EC9 [5] Class 1 and Class 2 slenderness limits for internal elements in compression. To this end, the experimental ultimate moments $M_{u,Exp}$ were normalised by the corresponding plastic moment resistances M_{pl} and were plotted against the slenderness ratio β/ϵ (Figure 6.12(a)); The same figure also displays the value of the current Class 2 slenderness limit $\beta/\epsilon=16$ for the examined 6082-T6 alloy, which is classified as Class A material. It can be seen that all data points are above the unity threshold line and on the left side from the current Class 2 slenderness limit value denoting design safety. For assessing the current Class 1 slenderness limit, the deformation capacity R was plotted against the slenderness ratio β/ϵ as shown in Figure Figure 6.12(b). The current slenderness limit for Class 1 cross-sections and material Class A is 11 and is also depicted in the same figure. Note that there is no specific deformation capacity requirement R for Class 1 cross-sections in EC9 [5] design

guidelines. However, Manganiello et al. [236] found that a minimum required value of $R=3$ adopted from carbon steel is suitable for the case of aluminium alloys. This value is considered in the present study and is included in Figure 6.12(b). As can be observed, all the examined cross-sections exhibited deformation capacity higher than the requirement except from 50.8×25.4×3.25 specimen which failed by material fracture under three-point bending. Overall, the results denote that the current Class 1 slenderness limit is acceptable.



(a) Class 2 slenderness limit



(b) Class 1 slenderness limit

Figure 6.12: Assessment of EC9 [5] slenderness limits for internal elements in compression.

According to Section 6.2.5 of EC9 [5], the cross-sectional moment resistance M_{EC9} for bending about one principal axis is defined as follows.

$$M_{EC9} = \alpha_0 W_{el} \sigma_{0.2}, \quad \alpha_0 = \begin{cases} W_{pl}/W_{el} & \text{for Class 1} \\ W_{pl}/W_{el} & \text{for Class 2} \\ 1.0 & \text{for Class 3} \\ W_{eff}/W_{el} & \text{for Class 4} \end{cases} \quad (6.17)$$

where a_0 is the shape factor, W_{pl} is the plastic section modulus of the gross cross-section, W_{el} is the elastic section modulus of the gross cross-section and W_{eff} is the effective elastic section modulus of the cross-section calculated using a reduced thickness for treatment of local buckling.

Despite the considerable effect of material nonlinearity, i.e., strain hardening, on the structural response of Class 1 cross-sections, there is no distinct difference in Equation (6.17) for the treatment of Class 1 and Class 2 cross-sections. Thus, EC9 [5] includes an alternative method in Annex F for a more accurate evaluation of the moment resistance of Class 1 cross-sections using a correction factor $\alpha_{M,j}$ to consider material strain hardening.

$$M_{EC9-F} = a_{M,1} W_{el} \sigma_{0.2} \quad (6.18)$$

$$a_{M,1} = \begin{cases} \alpha_5 = 5 - \frac{3.89 + 0.00190n}{a_0^{0.27+0.0014n}}, & 4\% \leq \varepsilon_u < 8\% \text{ (brittle alloys)} \\ \alpha_{10} = a_0^{[0.21 \log(1000n)]} 10^{[0.0796 - 0.0809 \log(n/10)]}, & \varepsilon_u \geq 8\% \text{ (ductile alloys)} \end{cases} \quad (6.19)$$

where α_5 and α_{10} are generalised shape factors depending on the ductility of the aluminium alloy as described in Annex G [5] and n is the strain hardening exponent.

Table 6.8 presents for each tested cross-section the ratios of the moment resistance according to Section 6.2.5 of EC9 [5] M_{EC9} and Annex F M_{EC9-F} over the experimentally obtained bending moment capacity $M_{u,Exp}$ under both test configurations. As can be seen, EC9 predictions appear to be safe as both mean values of the $M_{EC9}/M_{u,Exp}$ and $M_{EC9-F}/M_{u,Exp}$ ratios are lower than unity. Moreover, the resulting low COVs denote low scatter and thereby high design consistency. The moment resistances M_{EC9-F} were found to be more accurate, i.e., closer to unity, than the corresponding M_{EC9} ones, since Annex F accounts for material strain hardening within the calculations.

Table 6.8: Assessment of EC9 [5] and CSM design predictions for BAT simply-supported beams.

Specimen	β/ε	$M_{EC9}/M_{u,Exp}$	$M_{EC9-F}/M_{u,Exp}$	$\bar{\lambda}_{cs}$	$M_{CSM}/M_{u,Exp}$
three-point bending					
63.5×38.1×3.25	9.73	0.87	0.94	0.30	0.96
50.8×38.1×3.25	9.78	0.86	0.94	0.31	0.93
50.8×25.4×3.25	5.92	0.82	0.90	0.21	0.91
38.1×25.4×3.25	6.23	0.83	0.90	0.21	0.90
38.1×19.1×3.25	4.05	0.82	0.89	0.15	0.89
four-point bending					
63.5×38.1×3.25	9.73	0.82	0.89	0.30	0.91
50.8×38.1×3.25	9.78	0.87	0.95	0.31	0.94
50.8×25.4×3.25	5.92	0.83	0.91	0.21	0.92
38.1×25.4×3.25	6.23	0.83	0.90	0.21	0.90
38.1×19.1×3.25	4.05	0.91	0.99	0.15	0.99
mean		0.85	0.92		0.92
COV		0.03	0.03		0.03

6.4.1.2. Assessment of Continuous Strength Method for determinate structures

The CSM is a deformation-based design method rationally accounting for the influence of material strain hardening exhibited by stocky and slender cross-sections. CSM was originally devised for stainless steel and carbon steel stocky cross-sections [237-240]. In subsequent research studies [21,66], the design equations were modified to apply to aluminium alloys covering also the case of slender cross-sections. This method uses an experimentally derived base curve (Figure 6.13(a)) to define the maximum attainable strain ε_{CSM} of a cross-section depending on its cross-sectional slenderness $\bar{\lambda}_{cs}$. This base curve is described by the following equations.

$$\frac{\varepsilon_{CSM}}{\varepsilon_{0.2}} = \frac{0.25}{(\bar{\lambda}_{cs})^{3.6}} \leq \min\left(15, \frac{0.5\varepsilon_u}{\varepsilon_{0.2}}\right) \quad \text{for } \bar{\lambda}_{cs} \leq 0.68$$

$$\frac{\varepsilon_{CSM}}{\varepsilon_{0.2}} = \left(1 - \frac{0.222}{(\bar{\lambda}_{cs})^{1.05}}\right) \frac{1}{(\bar{\lambda}_{cs})^{1.05}} \quad \text{for } \bar{\lambda}_{cs} > 0.68 \quad (6.20)$$

where the strain at the ultimate tensile stress ε_u and the cross-sectional slenderness $\bar{\lambda}_{cs}$ are given by the Equations (6.21) and (6.22), respectively.

$$\varepsilon_u = 0.13\left(1 - \frac{\sigma_u}{\sigma_{0.2}}\right) + 0.059 \quad (6.21)$$

$$\bar{\lambda}_{cs} = \sqrt{\sigma_{0.2}/\sigma_{cr}} \quad (6.22)$$

where the elastic critical buckling stress σ_{cr} was calculated using the analytical equations derived from [233].

CSM assumes an elastic-linear hardening model to represent the aluminium alloy stress-strain response, shown in Figure 6.13(b). The strain hardening modulus E_{sh} can be calculated by the Equation (6.23).

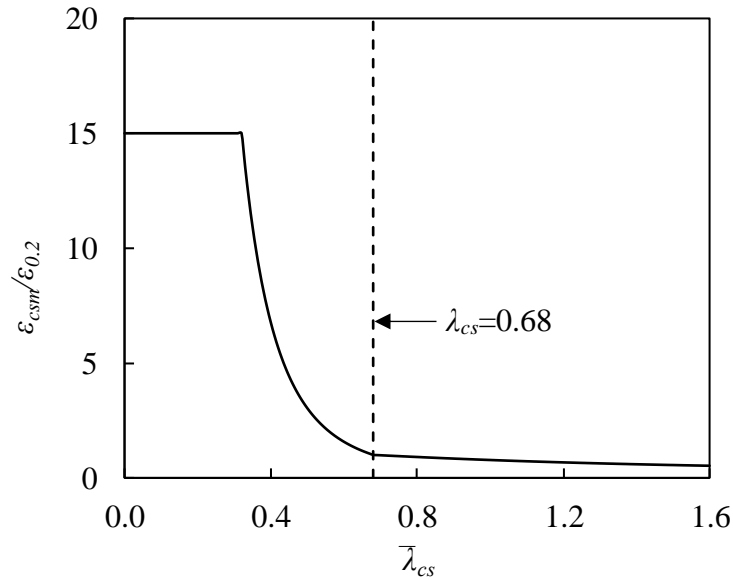
$$E_{sh} = \frac{\sigma_u - \sigma_{0.2}}{0.5\varepsilon_u - \varepsilon_{0.2}} \quad (6.23)$$

Based on the ε_{CSM} and the adopted elastic-linear hardening material behaviour, the cross-sectional bending moment capacity M_{CSM} can be determined as:

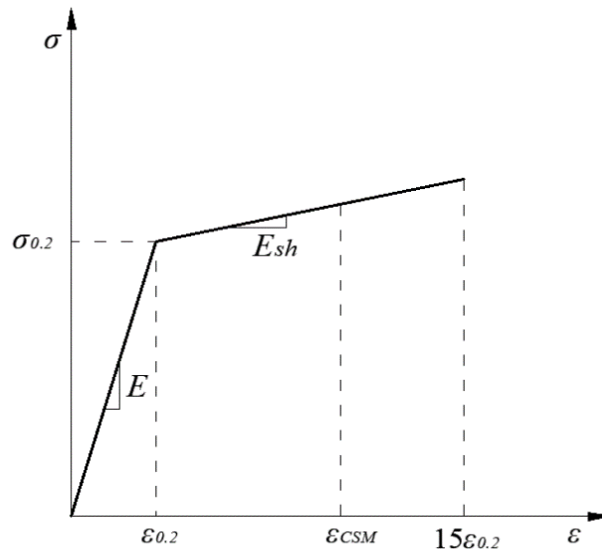
$$M_{CSM} = W_{pl} \sigma_{0.2} \left[1 + \frac{E_{sh}}{E} \frac{W_{el}}{W_{pl}} \left(\frac{\varepsilon_{CSM}}{\varepsilon_{0.2}} - 1 \right) - \left(1 - \frac{W_{el}}{W_{pl}} \right) / \left(\frac{\varepsilon_{CSM}}{\varepsilon_{0.2}} \right)^2 \right] \quad \text{for } \bar{\lambda}_{cs} \leq 0.68 \quad (6.24)$$

$$M_{CSM} = \frac{\varepsilon_{CSM}}{\varepsilon_{0.2}} W_{el} \sigma_{0.2} \quad \text{for } \bar{\lambda}_{cs} > 0.68$$

where W_{pl} is the plastic section modulus of the gross cross-section, W_{el} is the elastic section modulus of the gross cross-section and E is the modulus of elasticity.



(a) Strain ratio-cross-sectional slenderness curve



(b) Elastic-linear hardening material model

Figure 6.13: Base curve and material model adopted by CSM [66].

The ratio of the moment resistance M_{CSM} over the experimentally obtained bending moment capacity $M_{u,Exp}$ for each examined cross-section under both test configurations is listed in Table 6.8. It can be seen that the CSM which rationally accounts for the influence of material strain hardening exhibited by stocky cross-sections provides more accurate design predictions compared to Section 6.2.5 of EC9 [5]. However, the achieved accuracy level of the CSM and Annex F of EC9 [5] is the same since both design methods consider material strain hardening within the calculations.

6.4.2. Concrete-filled tubular cross-sections

6.4.2.1. Effect of depth-to-thickness ratio D/t of the aluminium tube

Figure 6.14 illustrates the effect of the depth-to-thickness ratio D/t of the aluminium tube on the flexural behaviour of CFAT simply-supported beams. From this figure, it can be seen that by decreasing the D/t from 31.80 to 10.57 (almost 3 times), the bending moment capacity increases from 1.45 to 5.01 (almost 3.5 times). Moreover, it can be drawn that the specimens with stockier cross-sections, i.e., lower values of D/t , exhibited higher ductility, since they failed at larger mid-span deflection values. Particularly, comparing the obtained ($M-W$) curves for 50.8×50.8×4.8-C and 50.8×50.8×1.6-C specimens, it can be seen that the former one failed at 29 mm vertical deflection which is almost double than that of the latter one. Finally, the slope of the initial elastic branch of the ($M-W$) curves for specimens with thicker cross-sections is larger denoting their improved flexural stiffness compared to their thinner counterparts.

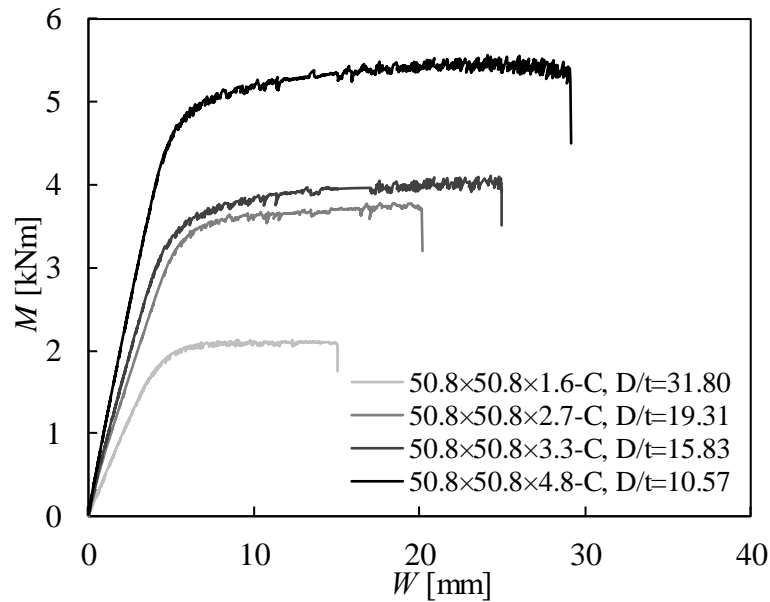


Figure 6.14: Effect of the depth-to-thickness ratio D/t of the aluminium tube on the flexural behaviour of CFAT simply-supported specimens.

6.4.2.2. Effect of concrete infill

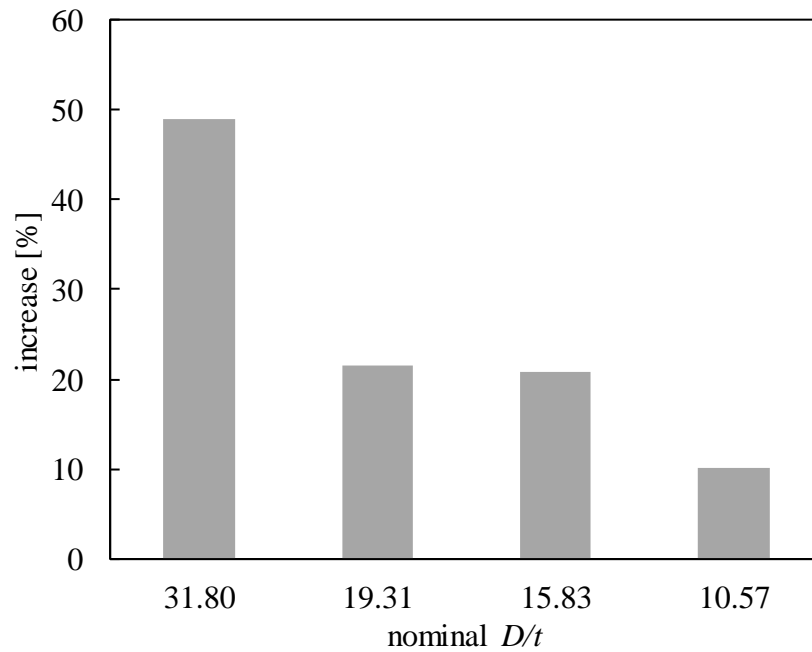
The experimentally obtained ultimate loads are utilised to evaluate the effect of filling the aluminium tubes with concrete on their ultimate strength and deformation, i.e., displacement and rotation at failure. As shown in Figure 6.15, the presence of the concrete infill considerably improved the initial stiffness of the members and prevented a potential failure due to local buckling occurrence. It can also be observed that in all cases, the specimens exhibited higher strength and deformation capacity compared to the BAT ones.

To further visualize the effect of infill, Table 6.9 presents the percentage increase $(M_{u,CFAT}-M_{u,BAT})/M_{u,BAT}$ in ultimate strength, the percentage increase $(\delta_{u,CFAT}-\delta_{u,BAT})/\delta_{u,BAT}$ in displacement at failure and the percentage increase $(\theta_{u,CFA}-\theta_{u,BAT})/\theta_{u,BAT}$ in rotation at failure for each CFAT specimen. Again, it can be seen that the presence of the concrete infill significantly improved the flexural performance of the BAT specimens in terms of ultimate strength and deformability. For example, in case of the slenderest section, i.e., $50.8 \times 50.8 \times 1.6$, the concrete infill increased the ultimate strength, displacement and rotation at failure by 49%, 226.80% and 227.18%, respectively. Additionally, Figure 6.15 presents the improved performance for the depth-to-thickness ratio D/t for each cross-

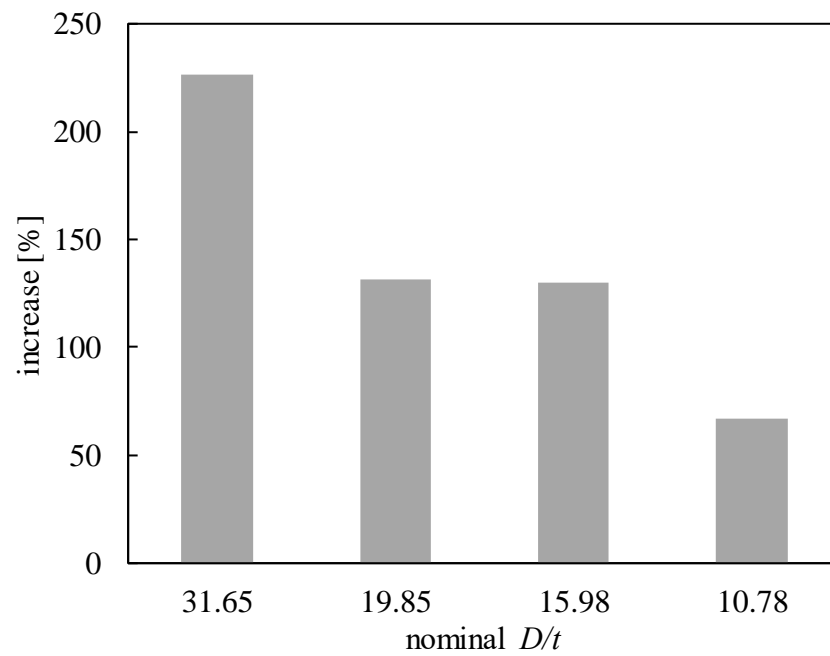
section. It can be observed that for higher D/t values, i.e., slenderer cross-sections, the percentage increase in the ultimate strength is more pronounced. Particularly, for $D/t = 31.80$, the ultimate strength increased by 49%, whilst for $D/t = 10.57$, the ultimate strength increased by 14.19%. This stems from the fact that the concrete infill in slenderer cross-sections significantly delayed the occurrence of local buckling resulting in quite higher ultimate strengths.

Table 6.9: Percentage increase in ultimate strength, displacement and rotation at failure due to infill.

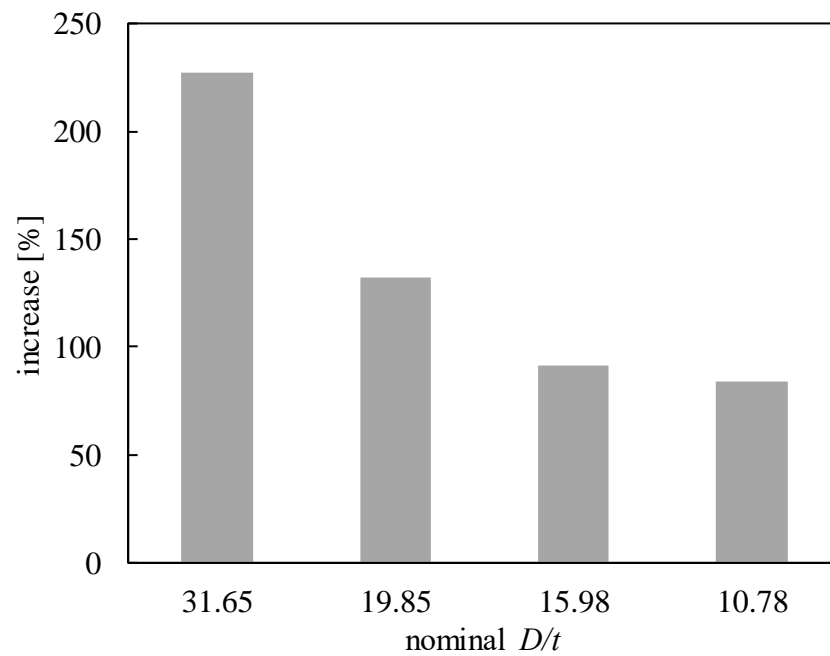
Specimen	$(M_{u,CFAT} - M_{u,BAT})/M_{u,BAT}$	$(\delta_{u,CFAT} - \delta_{u,BAT})/\delta_{u,BAT}$	$(\theta_{u,CFAT} - \theta_{u,BAT})/\theta_{u,BAT}$
50.8×50.8×1.6-C	48.9%	226.8%	227.2%
50.8×50.8×2.7-C	15.1%	131.4%	132.2%
50.8×50.8×3.3-C	20.8%	130.0%	91.3%
50.8×50.8×4.8-C	10.2%	67.2%	84.1%



(a) strength increase



(b) displacement at failure



(c) rotation at failure

Figure 6.15: Effect of the concrete infill on the CFAT simply-supported beam specimens compared with the BAT simply-supported beam specimens.

6.4.2.3. Design recommendations

In this section the experimental strengths are utilised to make design recommendations for the flexural strength prediction of CFAT members. Note that all partial safety factors are set equal to unity for these assessments. In absence of design criteria for the prediction of the flexural capacities of composite aluminium-concrete beams, the present study adopts the design criteria for composite steel-concrete beams available in EC4 [210]. Particularly, this study proposes the replacement of the material properties of steel by those of the examined aluminium alloy.

Based on the above recommendation, the flexural capacity of square and rectangular CFAT members can be obtained using the Equation (6.21) of EC4 [210].

$$M_{u,prop} = (W_{pl} - W_{pl,n})\sigma_{0.2} + 0.5(W_{plc} - W_{plc,n})f_{ck} \quad (6.25)$$

where W_{pl} and W_{plc} are the plastic section moduli of the aluminium tube and concrete, respectively, given by the Equations (6.26) and (6.27), respectively. $W_{pl,n}$ and $W_{plc,n}$ are the plastic section moduli of the aluminium tube and concrete from $2h_n$, respectively, given by the Equations (6.28) and (6.29), respectively. The term h_n , is the location of the neutral axis calculated by the Equation (6.30), where A_c and f_{ck} are the area and the compressive cylinder strength of the concrete, respectively. In Equations (6.26) and (6.27), r_{int} is the internal corner radius of the aluminium tube which is zero herein. Moreover, for the aluminium tubes, the cross-sectional classification framework provided by EC9 [5] should be applied to consider the local buckling effect on the cross-sectional response.

$$W_{pl} = \frac{BD^2}{4} - \frac{2}{3}(r_{int} + t)^3 - (r_{int} + t)^2(4 - \pi)\left(\frac{D}{2} - t - r_{int}\right) - W_{plc} \quad (6.26)$$

$$W_{plc} = \frac{(B - 2t)(D - 2t)^2}{4} - \frac{2}{3}r_{int}^3 - r_{int}^2(4 - \pi)\left(\frac{D}{2} - t - r_{int}\right) \quad (6.27)$$

$$W_{pl,n} = Bh_n^2 - W_{plc,n} \quad (6.28)$$

$$W_{plc,n} = (B - 2t)h_n^2 \quad (6.29)$$

$$h_n = \frac{A_c f_{ck}}{2Bf_{ck} + 4t(2\sigma_{0.2} - f_{ck})} \quad (6.30)$$

Table 6.10 presents the experimental over proposed $M_{u,prop}/M_{u,Exp}$ ultimate bending moment ratio for each CFAT tested cross-section. The slenderness ratio β/ε and the corresponding Class for each tested cross-section are also included in the same table. As can be seen, the proposed ultimate bending moments $M_{u,prop}$ appear to be safe as the corresponding mean values of the $M_{u,prop}/M_{u,Exp}$ ratio are lower than unity. Moreover, the resulting low COVs denote low scatter and thereby high design consistency. Overall, it can be concluded that the combined formulae [5,210] proposed herein for the design of flexural CFAT members provide good predictions with reasonable consistency. However, further studies are recommended to obtain a better understanding of the flexural behaviour of CFAT members.

Table 6.10: Proposed design strengths for GCFAT and CFAT beams.

Specimen	β/ε	Class	$M_{u,prop}/M_{u,Exp}$
50.8×50.8×1.6-C	12.82	4	0.77
50.8×50.8×2.7-C	8.04	3	0.87
50.8×50.8×3.3-C	6.08	2	0.85
50.8×50.8×4.8-C	3.79	1	0.86
mean			0.88
COV			0.05

6.4.3. Channel cross-sections

6.4.3.1. Influence of cross-sectional aspect ratio D/B , cross-sectional slenderness ratios β_w/ε and β_f/ε and aluminium alloy type

For all examined FE models, the exhibited moment-curvature response, the ultimate bending moment capacity and the failure mode were recorded. All C-sections under “u” bending orientation failed due to local buckling initiated in the compressed part of the flanges. For C-sections under “n” bending orientation, material yielding was the governing failure mode. To evaluate the generated results, the FE ultimate bending moments $M_{u,FE}$ were normalised by the corresponding plastic bending moment resistances M_{pl} and were plotted against the slenderness parameter β_w/ε and β_f/ε for the “n” and “u” bending orientation, respectively.

Figure 6.16 depicts the results for the “n” bending orientation separately for the three different aspect ratios under consideration. It is evident that the 6063-T5 C-sections exhibit higher normalised bending moment capacities throughout the considered β_w/ε

range, with the M_{pl} being exceeded by up to 30% compared to their 6082-T6 counterparts. This is related to the more favourable strain hardening properties of 6063-T5, i.e., lower strain hardening exponent n , which results in higher tangent stiffnesses in the inelastic range enabling for higher normalised bending moment capacities. Moreover, from Figure 6.16 it can be concluded that the aspect ratio does not significantly influence the bending moment capacity as the governing failure mode was material yielding.

Similarly, Figure 6.17 shows the results for the “u” bending orientation. It can be seen that the stocky 6063-T5 C-sections exhibit higher normalised bending moment capacities, with the M_{pl} being exceeded by up to 60% compared to their 6082-T6 counterparts. Again, this is related to the more favourable strain hardening properties of 6063-T5. For more slender C-sections, the influence of the aluminium alloy type on the normalised flexural behaviour is minimal, as failure is triggered by local buckling before the attainment of the yield strength. Moreover, the normalised bending moment capacity of slender sections significantly improves with decreasing aspect ratios. This is attributed to the beneficial influence of the plate element interaction on the local buckling response of the compression flange of sections with lower aspect ratios (i.e., shorter webs provide greater resistance to local buckling of the flanges).

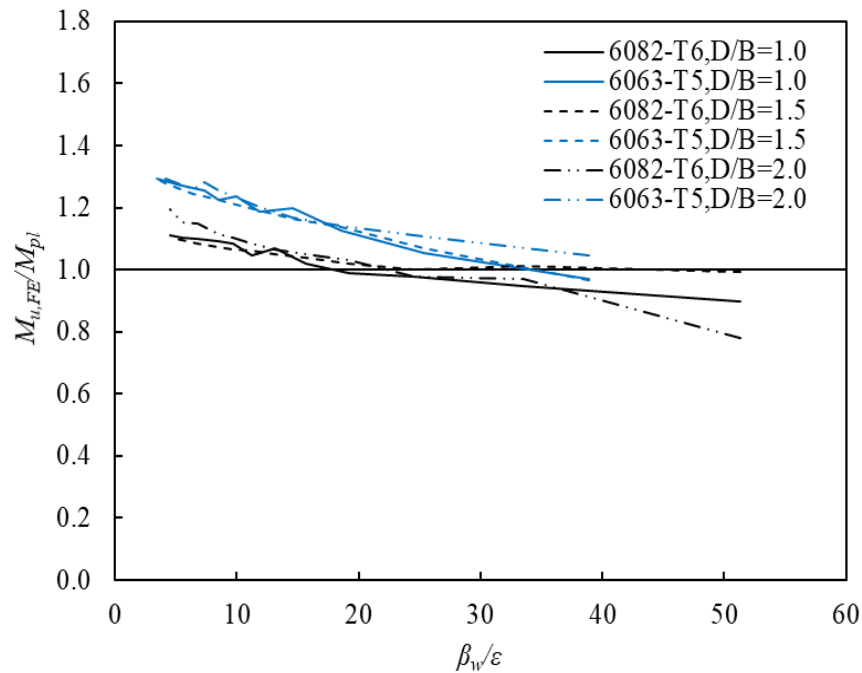


Figure 6.16: Normalised bending moment capacity $M_{u,FE}/M_{pl}$ of C-sections under “n” bending orientation.

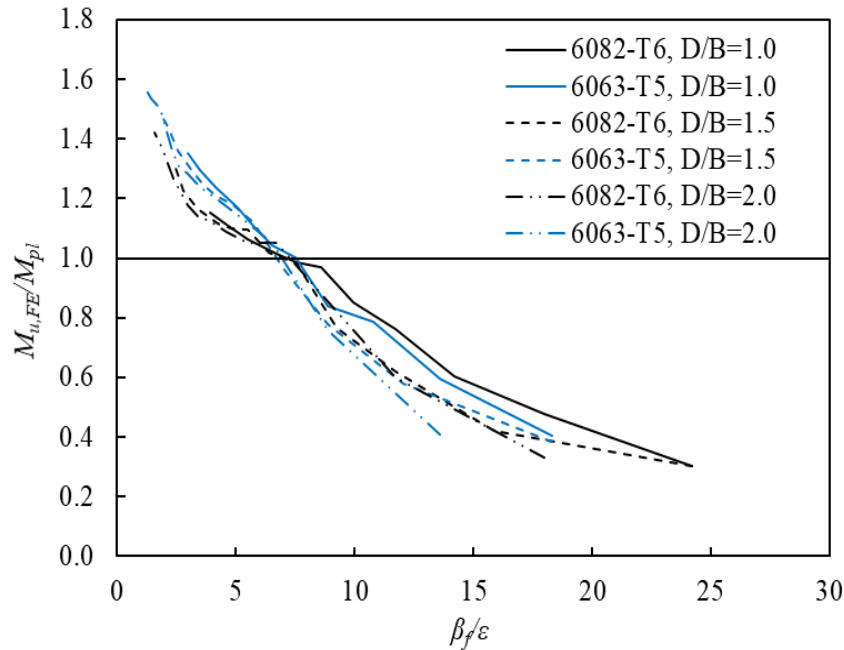


Figure 6.17: Normalised bending moment capacity $M_{u,FE}/M_{pl}$ of C-sections under “u” bending orientation.

6.4.3.2. Assessment of Eurocode 9 Class 2 and Class 3 slenderness limits for outstand elements under stress gradient

The values of experimental and FE bending moment resistance M_u of “u” bending orientation are utilised to assess the EC9 Class 2 and Class 3 slenderness limits for outstand elements under stress gradient. To do so, the M_u values were normalised by the corresponding M_{pl} and M_{el} and were plotted against the slenderness parameter β_f/ϵ of the flange in Figure 6.18 and Figure 6.19, respectively. Figure 6.18 will be used for the EC9 Class 2 slenderness limits evaluation, whereas Figure 6.19 will be used to assess the EC9 Class 3 ones. The Class 2 slenderness limit of $\beta_f/\epsilon=4.5$ for material Class A and Class B and the Class 3 slenderness limit of $\beta_f/\epsilon=6$ for material Class A and $\beta_f/\epsilon=5$ for material Class B are also included in these figures. For the limits to be accurate, the normalised moments should be above unity on the left side of the limit and below unity on the right side. As can be seen from both figures, the current slenderness limits are safe but conservative as cross-sections with values of β_f/ϵ ranging from the EC9 limits to 7 and to 12 could reach their plastic and elastic bending moment resistance, respectively. Therefore, both slenderness limit values could be relaxed leading to more accurate and thereby economical classification results.

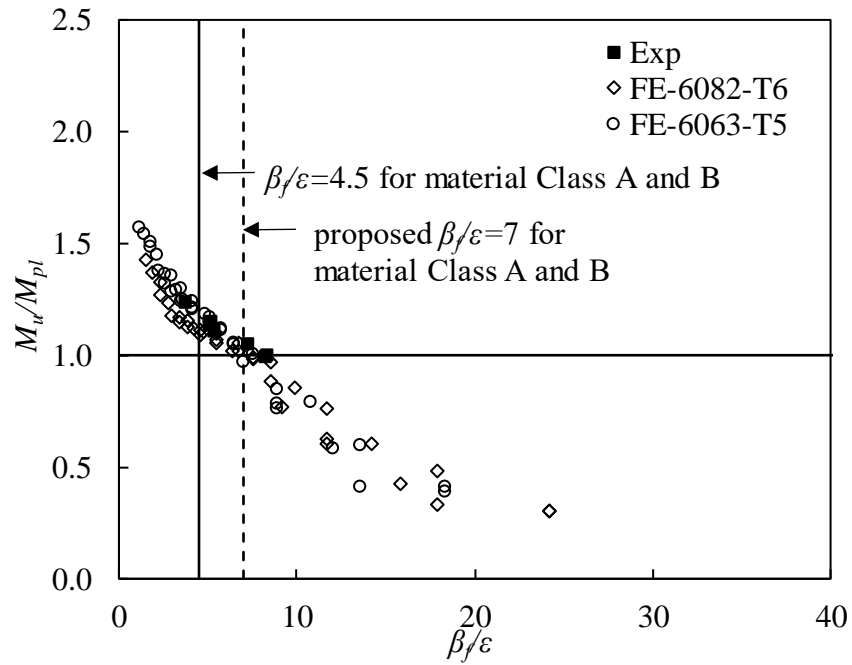


Figure 6.18: Assessment of Class 2 slenderness limits for outstand elements under stress gradient.

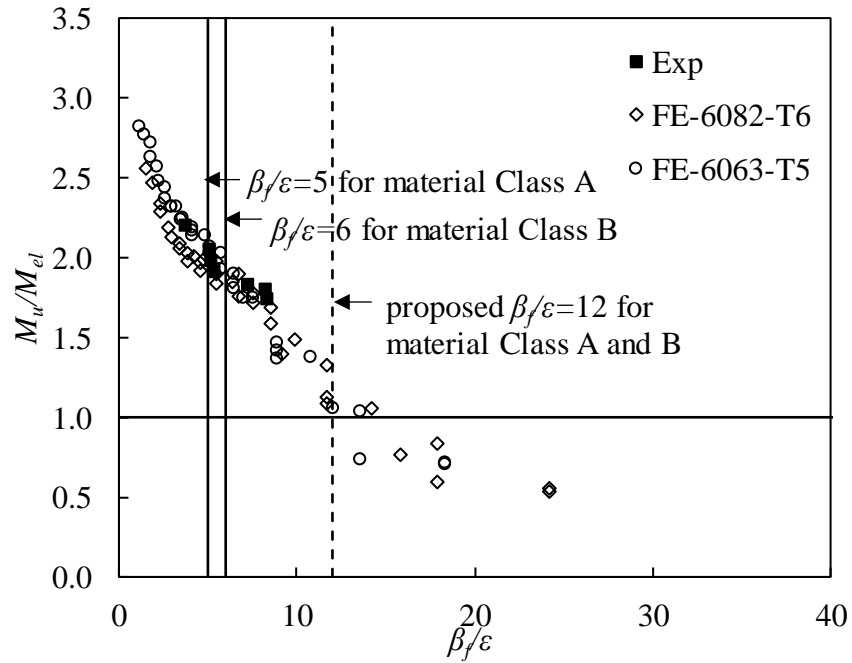


Figure 6.19: Assessment of Class 3 slenderness limits for outstand elements under stress gradient.

6.4.3.3. Assessment of Eurocode 9 Class 2 and Class 3 slenderness limits for internal elements in compression

The obtained data from “n” bending orientation are used to assess the applicability of the EC9 Class 2 and Class 3 slenderness limits for internal elements in compression. The experimental and FE M_u values are normalised by the corresponding M_{pl} and M_{el} and plotted against the slenderness parameter β_w/ε of the web in Figure 6.20 and Figure 6.21, respectively. As can be observed from Figure 6.20, the current Class 2 slenderness limits appear accurate, whilst Class 3 limits assessed in Figure 6.21 are safe but excessively conservative as all the data points are above and far from the unity threshold line.

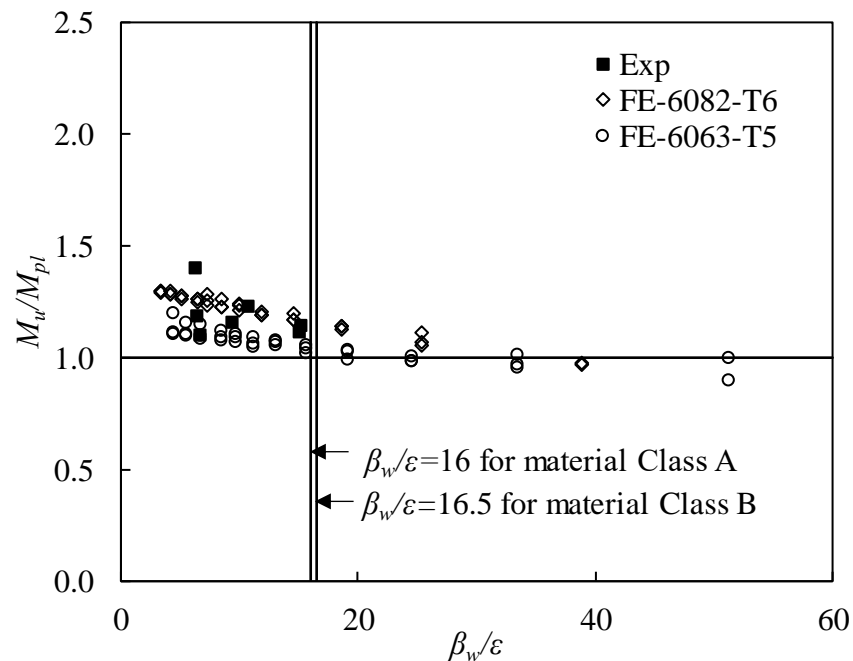


Figure 6.20: Assessment of Class 2 slenderness limits for internal elements in compression.

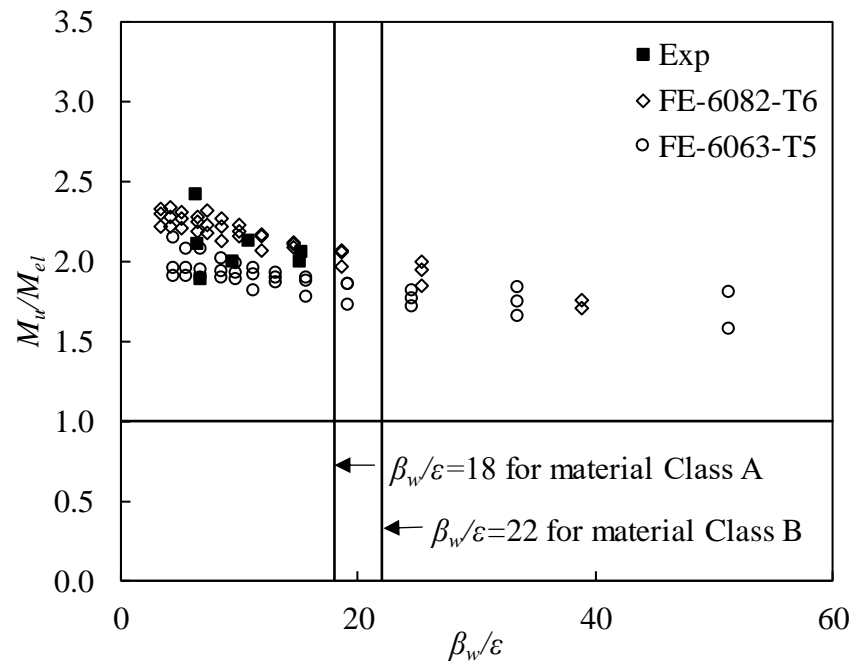
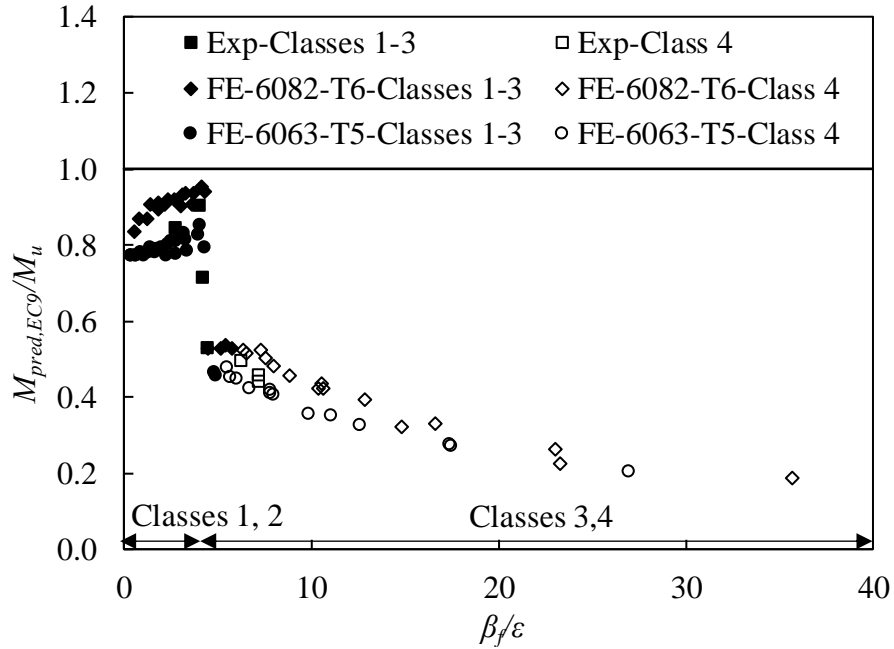


Figure 6.21: Assessment of Class 3 slenderness limits for internal elements in compression.

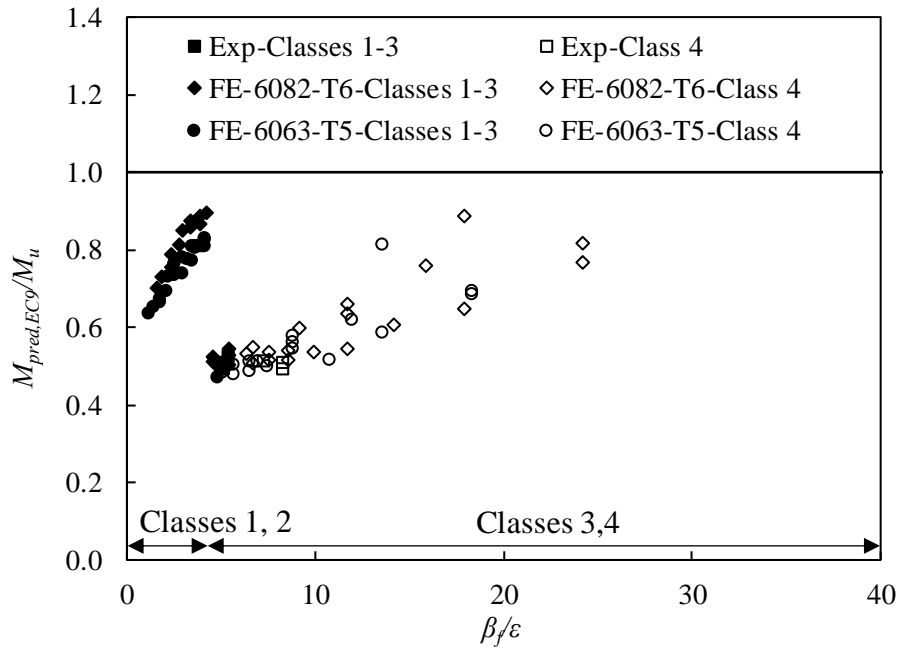
6.4.3.4. Assessment of Eurocode 9

Section 6.2.5 specified in EC9 [5], provides design equations to calculate the ultimate bending moment resistance $M_{pred,EC9}$ of C-sections subjected to minor-axis bending. Figure 6.22 presents the predicted-to-ultimate $M_{pred,EC9}/M_u$ moment ratios for both bending orientations plotted against the slenderness parameter β_w/ϵ of the flange. The $M_{pred,EC9}/M_u$ ratios are shown separately for the stocky (Classes 1-3) and slender (Class 4) cross-sections. Figure 6.22(a) shows that EC9 [5] provides safe and quite accurate design strength predictions for 6082-T6 stocky cross-sections, i.e., $M_{pred,EC9}/M_u$ values close to unity. For the 6063-T5 counterparts, the design strength predictions appear more conservative, since lower $M_{pred,EC9}/M_u$ values are provided, particularly for stockier sections. This is related to the fact that EC9 [5] does not consider the material strain hardening behaviour which is more pronounced for 6063-T5. Conversely, for both 6082-T6 and 6063-T5 slender cross-sections, EC9 [5] underestimates their bending moment capacity, i.e., $M_{pred,EC9}/M_u$ values are much lower than unity. This is related to the overly conservative Class 3 slenderness limit as shown in Figure 6.21 that leads to quite underestimated and uneconomical design strength predictions for slender cross-sections. For cross-sections examined with flange tips in compression, i.e., “u” bending orientation, EC9 [5] generally provides quite conservative design strength predictions for

both stocky and slender cross-sections as shown in Figure 6.22(b). However, for 6082-T6 stocky cross-sections, the predicted bending moment capacities are more accurate than the corresponding ones for 6063-T5 stocky cross-sections owing again to the lack of consideration of the material strain hardening properties.



(a) “n” bending orientation



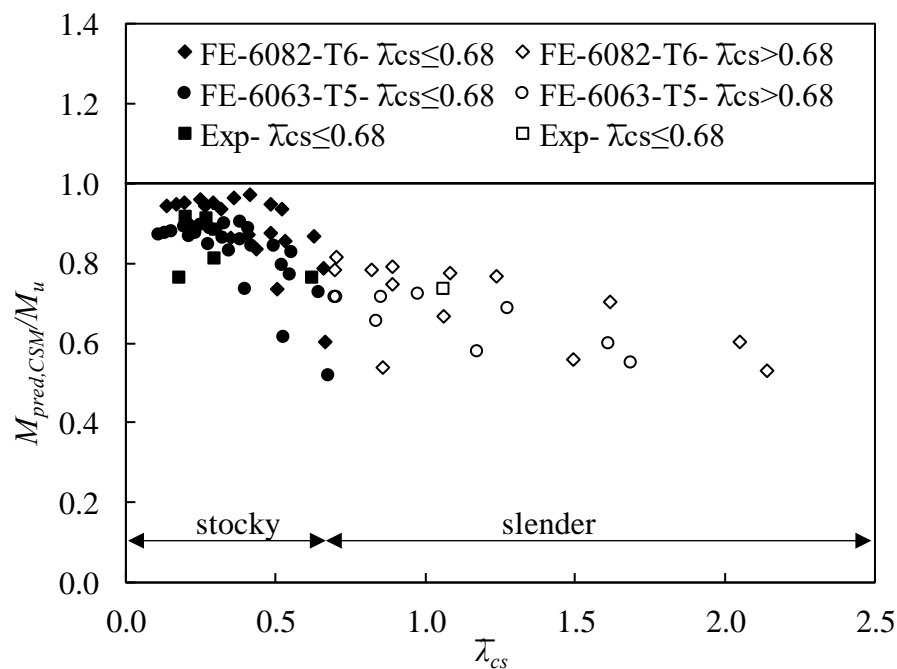
(b) “u” bending orientation

Figure 6.22: Assessment of EN 1999-1-1 [5] design strength predictions.

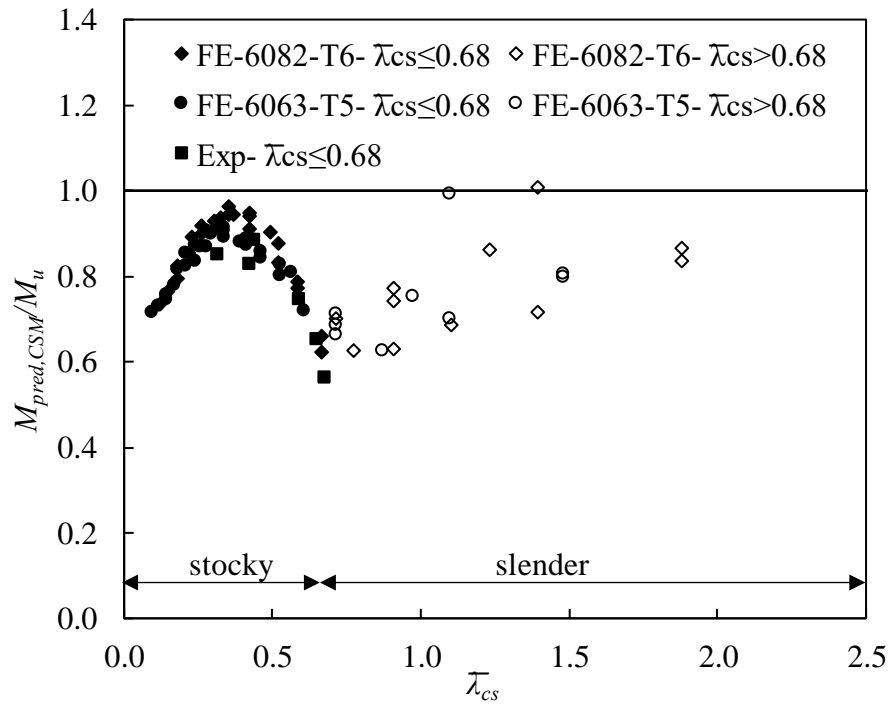
6.4.3.5. Assessment of Continuous Strength Method

The CSM is a deformation-based design approach that rationally accounts for the beneficial influence of material strain hardening which allows for stresses higher than the nominal yield strength [21,66,237-242]. The present study utilises the obtained experimental and FE results to assess the applicability of the design equations proposed by [241] for the cross-sectional ultimate moment capacity $M_{pred,CSM}$ of monosymmetric and asymmetric stainless steel cross-sections to aluminium alloy C-sections.

Figure 6.23 depicts the predicted-to-ultimate $M_{pred,CSM}/M_u$ moment ratios for both bending orientations plotted against the cross-sectional slenderness $\bar{\lambda}_{cs}$. The $M_{pred,CSM}/M_u$ ratios are shown separately for the stocky ($\bar{\lambda}_{cs} \leq 0.68$) and slender ($\bar{\lambda}_{cs} > 0.68$) cross-sections. As was expected, the CSM design strength predictions are quite improved compared to the corresponding EC9 ones for the stocky cross-sections under the “n” bending orientation, as they are able to take into account the strain hardening effect. Higher design accuracy is also observed for the cross-sections under the “u” bending orientation and particularly for the slender cross-sections.



(a) “n” bending orientation



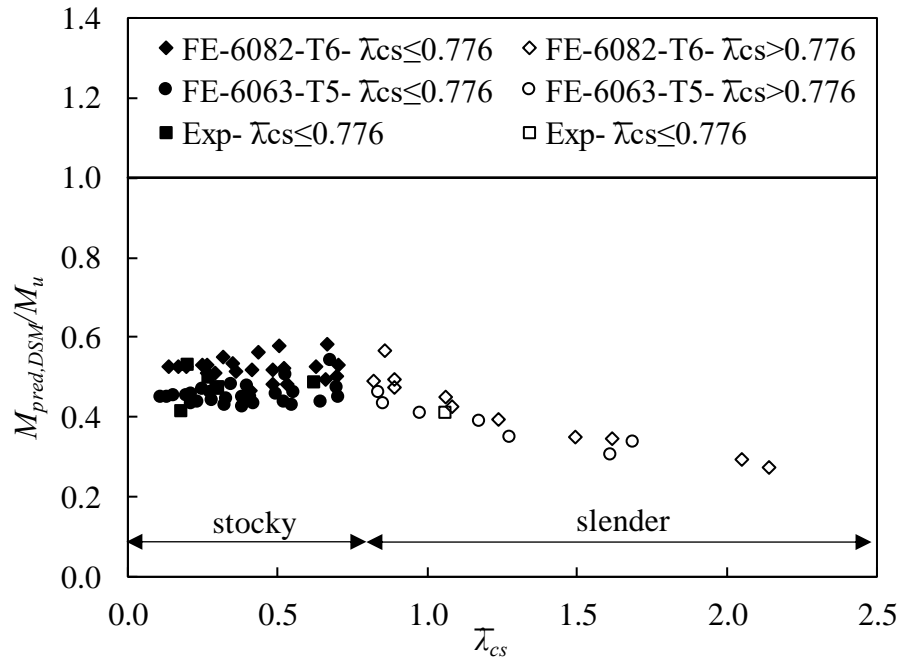
(b) “u” bending orientation

Figure 6.23: Assessment of CSM design strength predictions.

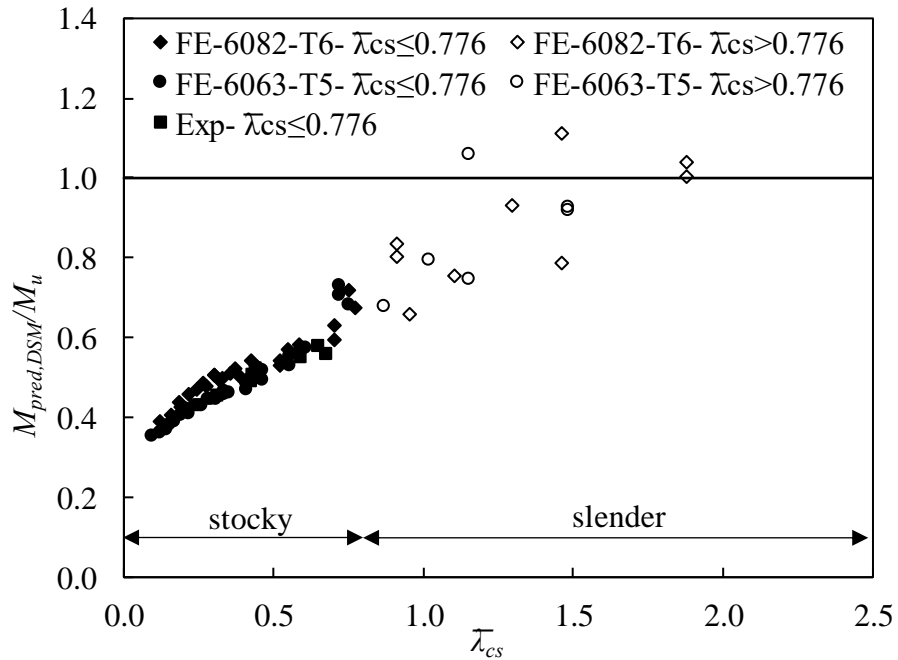
6.4.3.6. Assessment of Direct Strength Method

The DSM is codified in Section F3.2.1 of [131] as an alternative and simplified design method compared to the traditional effective width method [243,244]. The design formulae account for the beneficial exploitation of the plate element interaction and are used herein to estimate the cross-sectional flexural strength $M_{pred,DSM}$. Figure 6.24 presents the predicted-to-ultimate $M_{pred,DSM}/M_u$ moment ratios for both bending orientations plotted against the cross-sectional slenderness $\bar{\lambda}_{cs}$. The $M_{pred,DSM}/M_u$ ratios are shown separately for the stocky ($\bar{\lambda}_{cs} \leq 0.776$) and slender ($\bar{\lambda}_{cs} > 0.776$) cross-sections. Figure 6.24(a) suggests that the DSM is overly conservative, consistently underestimating the flexural strength of both stocky and slender cross-sections with web in compression, i.e., “n” bending orientation. On the other hand, the DSM design strength predictions for cross-sections with flange tips in compression, i.e., “u” bending orientation, appear to be more accurate for increasing $\bar{\lambda}_{cs}$, although more scattered (Figure 6.24(b)). Moreover, this method assumes that the cross-section exhibits linear

stress distribution throughout at failure, which is incorrect as discussed in the following section.



(a) "n" bending orientation

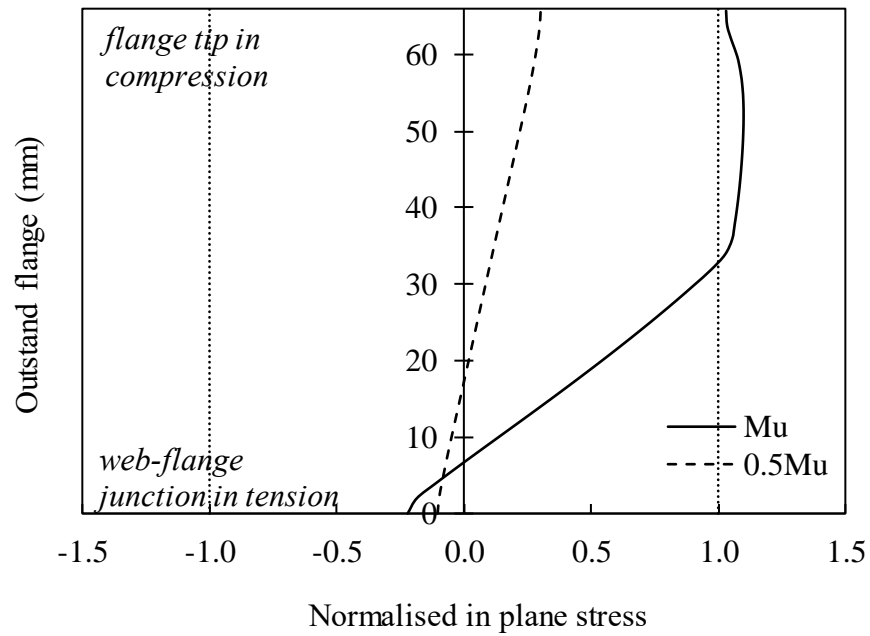


(b) "u" bending orientation

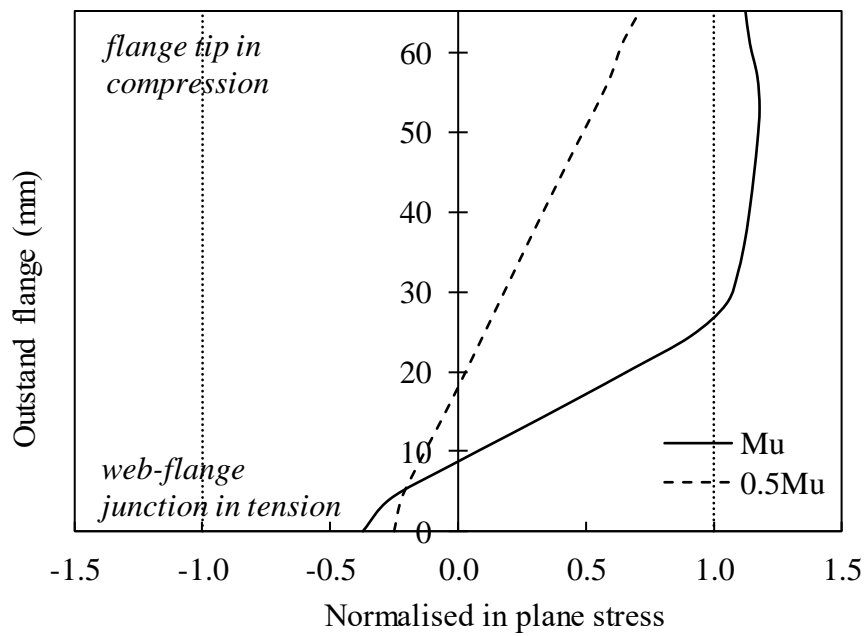
Figure 6.24: Assessment of DSM design strength predictions.

6.4.3.7. Assessment of Plastic effective width method – General

Past studies [245-247] on steel slender I-sections subjected to minor axis bending, i.e., having the flange outstands under stress gradient, demonstrated that slender cross-sections often exhibit inelastic response. Moreover, it was found [248] that the strain at the ultimate state can be many times higher than the yield strain. Therefore, the adopted principle of linear elastic stress distribution with the maximum stress at yield capacity is fundamentally incorrect and leads to overly conservative design strength predictions [249]. Bambach et al. [249-251] considered these observations to derive a general method, known as plastic effective width method, for strength prediction of slender cross-sections with flange outstands under any stress gradient. The present study investigates whether these observations are also applicable in case of aluminium alloy slender C-sections. On this direction, the stress distribution profiles of the flanges, as obtained from the parametric studies where the full profile could be captured, are evaluated. Figure 6.25 and Figure 6.26 display the in-plane longitudinal stress distribution over the flange at the mid-span of the beam for the slenderest examined cross-sections under “u” and “n” bending orientation, respectively. Particularly, these figures provide the stress distribution in the elastic range when the bending moment of the section is $0.5M_u$ and at failure when M_u is reached. Note that the in-plane stresses are normalised by the corresponding yield stress. Both figures denote that the relative slender C-sections exhibit inelastic reserve capacity which allows for loading higher than the yield strength without failing within the elastic range. This observation is in line with findings for steel C-sections in [245].

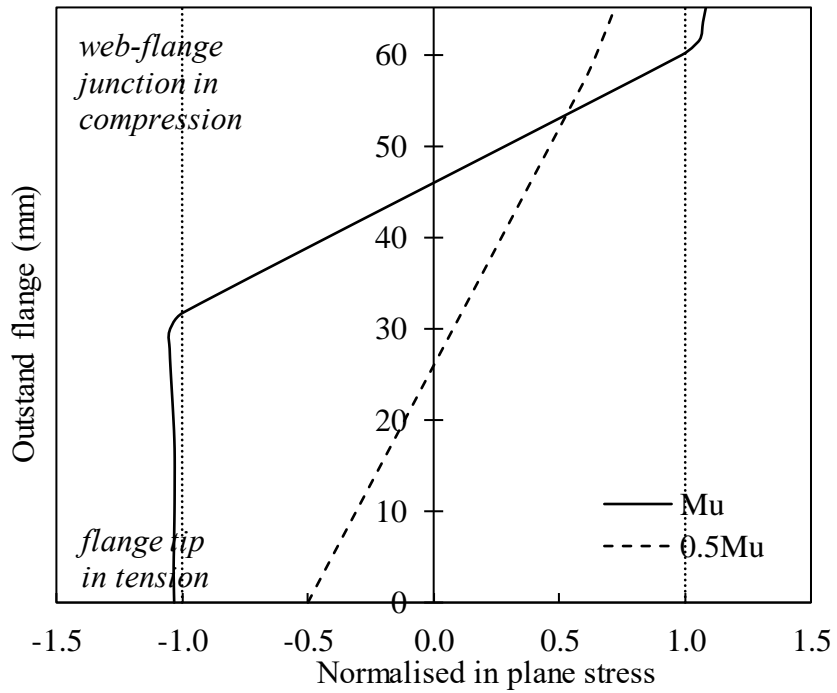


(a) 6082-T6 ($100 \times 66.7 \times 2$ - $D/B=1.5$ - $\beta_f/\epsilon=24.21$ - $\bar{\lambda}_{cs}=1.88$)

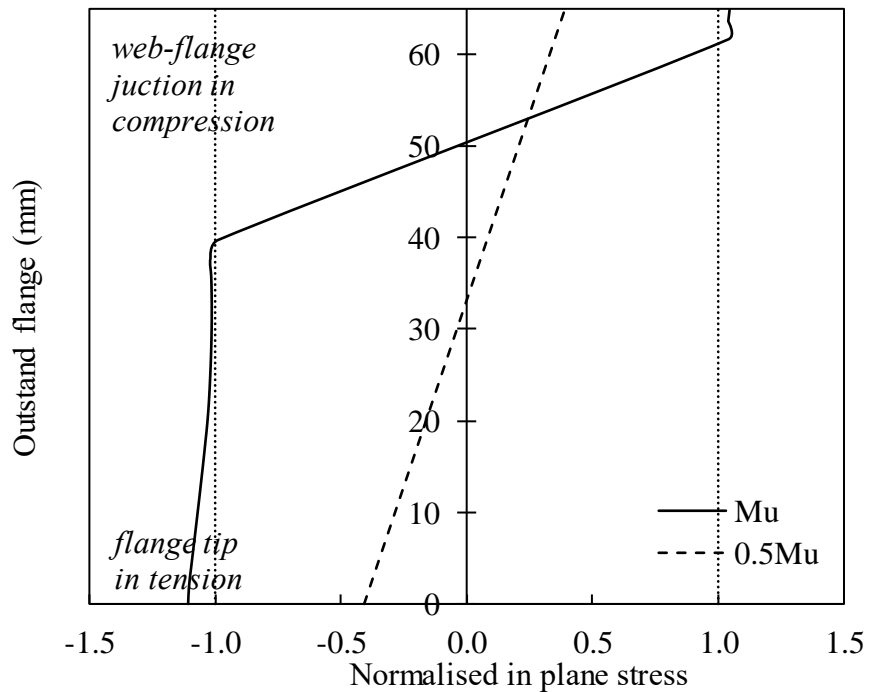


(b) 6063-T5 ($100 \times 66.7 \times 2$ - $D/B=1.5$ - $\beta_f/\epsilon=18.33$ - $\bar{\lambda}_{cs}=1.48$)

Figure 6.25: Longitudinal stress distribution over the flange at mid-span of the slenderest 6082-T6 and 6063-T5 C-sections under “u” bending configuration.



(a) 6082-T6 ($100 \times 66.7 \times 2$ - $D/B=1.5$ - $\beta_f/\epsilon=23.33$ - $\bar{\lambda}_{cs}=2.14$)



(b) 6063-T5 ($100 \times 66.7 \times 2$ - $D/B=1.5$ - $\beta_f/\epsilon=17.55$ - $\bar{\lambda}_{cs}=1.69$)

Figure 6.26: Longitudinal stress distribution over the flange at mid-span of the slenderest 6082-T6 and 6063-T5 C-sections under “n” bending configuration.

6.4.3.8. Assessment of Plastic effective width method – “u” bending orientation

The plastic effective width method suggests that a slender C-section in minor axis bending and under the “u” bending orientation can be designed using a maximum compression strain of C_y times the yield strain ε_y , where C_y is given by Equation (6.31). Equation (6.32) expresses the effective width b_e of the cross-section which resists loading upon local buckling occurrence and is defined at distance e_{cc2} from the flange tip (Equation (6.33)). Following, the distance x_p from the neutral axis of the effective cross-section to the extreme tensile fibre is calculated by Equation (6.34). Upon calculation of the parameters defined in Equations (6.35-6.42) and assuming an elastic-perfectly plastic stress distribution, the design flexural strength $M_{pred,pl-eff-w}$ can be calculated summing the moments derived from the force resultants of the stress blocks of the effective cross-section. The detailed procedure is given in [250], whilst the involved symbols are explained schematically in Figure 6.27.

$$C_y = 3.67 - 1.98 \frac{b_f}{t_f} \sqrt{\frac{\sigma_{0.2}}{E}}, 1 \leq C_y \leq 3 \quad (6.31)$$

$$b_e = 0.4(1 + \psi) \bar{\lambda}_{cs}^{-0.75} B \leq b_c \quad (6.32)$$

$$e_{cc2} = 0.55(1 + \psi)B - b_e \quad (6.33)$$

$$x_p = \frac{2b_e t_f (B - b_e/2 - e_{cc2}) + 2b_t t_f b_t/2 + (D - 2t_f)t_w t_w/2}{2b_e t_f + 2b_t t_f + (D - 2t_f)t_w} \quad (6.34)$$

$$b_t = \frac{B^2 t_f + (D - 2t_f)t_w^2/2}{2B t_f + (D - 2t_f)t_w} \quad (6.35)$$

$$K = \frac{C_y \varepsilon_{0.2}}{B - x_p - e_{cc2}} \quad (6.36)$$

$$b_g = \frac{\varepsilon_{0.2}}{K} \quad (6.37)$$

$$b_c = B - x_p \quad (6.38)$$

$$b_p = x_p - 0.5t_w - b_g \quad (6.39)$$

$$\sigma_w = (x_p - 0.5t_w)KE \quad (6.40)$$

$$c = b_t - b_g - b_p \quad (6.41)$$

$$\sigma_c = (cK)E \quad (6.42)$$

Equations (6.43(a)) and (6.44(b)) are proposed considering the cases of the web being either in elastic or plastic stress state, respectively. If $b_g \geq x_p - 0.5t_w$ the web is under elastic stress state and the design flexural strength $M_{pred,pl-eff-w}$ is given by Equation (6.43(a)):

$$M_{pred,pl-eff-w} = 2\sigma_{0.2}t_f b_e \left(B - e_{cc2} - b_e/2 - x_p \right) + \frac{2}{3}\sigma_c t_f c^2 + \frac{2}{3}\sigma_w t_f x_p^2 + \sigma_w t_w (D - 2t_f)(x_p - 0.5t_w) \quad (6.43(a))$$

If $b_g < x_p - 0.5t_w$ the web is under plastic stress state and the design flexural strength, $M_{pred,pl-eff-w}$, is given by Equation (6.43(b)):

$$M_{pred,pl-eff-w} = 2\sigma_{0.2}t_f b_e \left(B - e_{cc2} - b_e/2 - x_p \right) + \frac{2}{3}\sigma_c t_f c^2 + \frac{2}{3}\sigma_{0.2}t_f b_g^2 + 2\sigma_{0.2}t_f b_p (b_g + b_p/2) + \sigma_{0.2}t_w (D - 2t_f)(x_p - 0.5t_w) \quad (6.43(b))$$

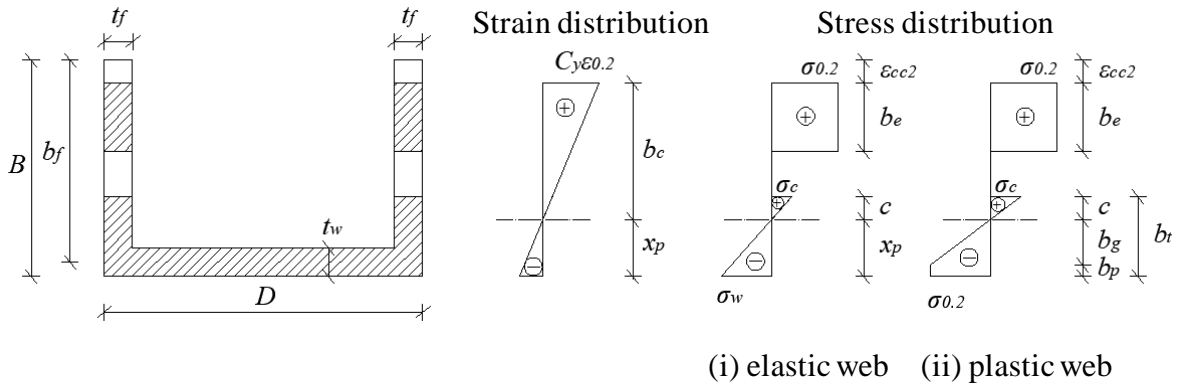


Figure 6.27: Plastic Effective Width Method - Strain and stress distribution profiles of the outstand flanges of a C-section under “u” bending orientation.

To evaluate the applicability of the plastic effective width method on C-sections with tip flanges in compression, the predicted-to-ultimate $M_{pred,pl-eff-w} / M_u$ moment ratios are plotted against the slenderness parameter β_f/ϵ of the flange in Figure 6.28. It can be concluded that the design method proposed by [250] provides more accurate strength predictions throughout the considered slenderness range compared to the design codes and methods assessed in Subsections 6.4.3.4-6.4.3.6, but in many cases conservative.

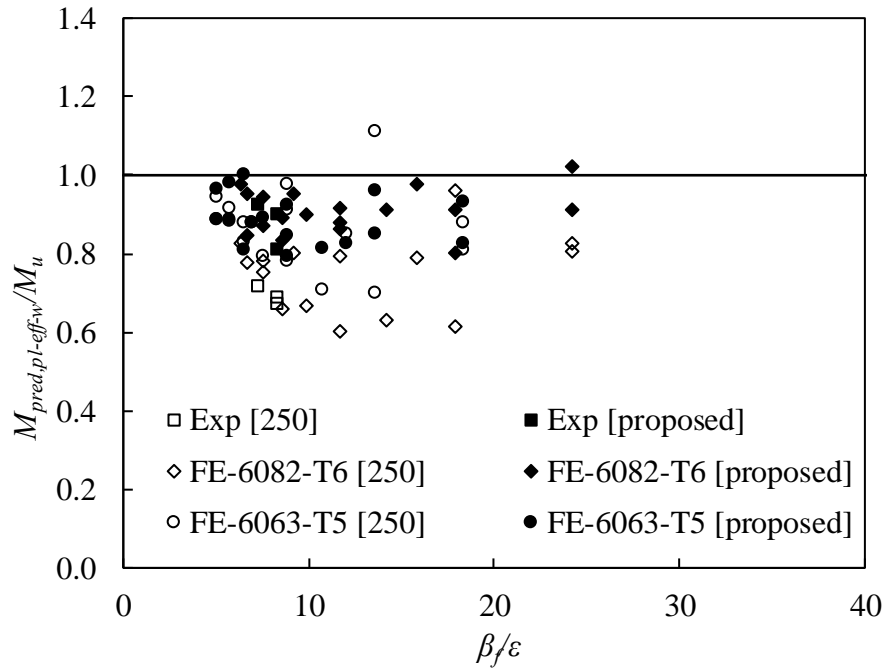


Figure 6.28: Assessment of Plastic Effective Width Method design strength predictions for Class 4 C-sections under “u” bending orientation.

To improve the accuracy and consistency of the plastic effective width method for C-sections, two design equations are proposed to replace Equations (6.31) and (6.32) considering the obtained experimental and FE results. The new design proposed equation for the strain coefficient C_y was found using the stress and strain distribution profiles of the C-sections obtained from the parametric studies. As shown in Figure 6.27, C_y is the ratio of the strain at the ultimate state at distance e_{cc2} from the flange tip over the yield strain $\varepsilon_{0.2}$. Therefore, the strain coefficient $C_{y,FE}$ was calculated for all the examined C-sections using the corresponding FE in-plane longitudinal strain at the reference location e_{cc2} . According to Figure 6.29, the calculated $C_{y,FE}$ values were found to have an exponential relationship with respect to $\frac{b_f}{t_f} \sqrt{\frac{\sigma_{0.2}}{E}}$ which is already used for the calculation of the strain coefficient C_y in Equation (6.42). For this reason, regression analysis was conducted for the data of Figure 6.29 to obtain Equation (6.44) for the calculation of C_y . Aiming to improve the design accuracy and consistency, Equation (6.32) for the effective width b_e was recalibrated to Equation (6.45) on the basis of the $M_{pred,ple-eff-w}/M_u$ values obtained from the experimental and FE results of this work.

$$C_y = 1.95 \left(\frac{b_f}{t_f} \sqrt{\frac{\sigma_{0.2}}{E}} \right)^{-0.65}, \quad 1 \leq C_y \leq 3 \quad (6.44)$$

$$b_e = 2.5 \left(\frac{b_f}{t_f} \right)^{-0.8} B \leq b_c \quad (6.45)$$

The $M_{pred, pl-eff-w}/M_u$ ratios according to the proposed design equations are also plotted in Figure 6.28. It can be observed that the use of the plastic effective width method in conjunction with the proposed design equations has significantly improved its accuracy and provides a higher degree of consistency for the bending moment capacities of C-sections with tip flanges in compression.

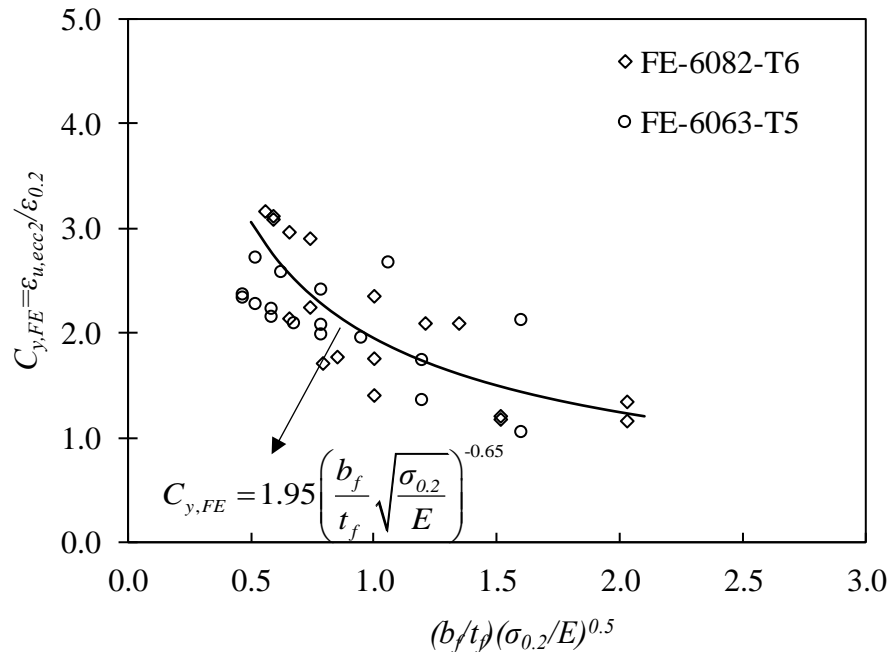
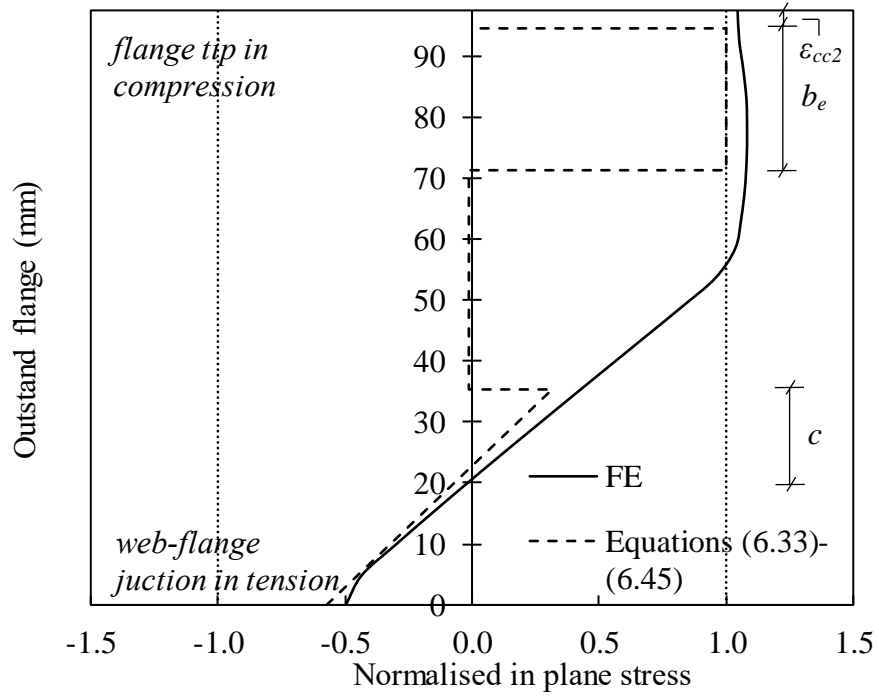
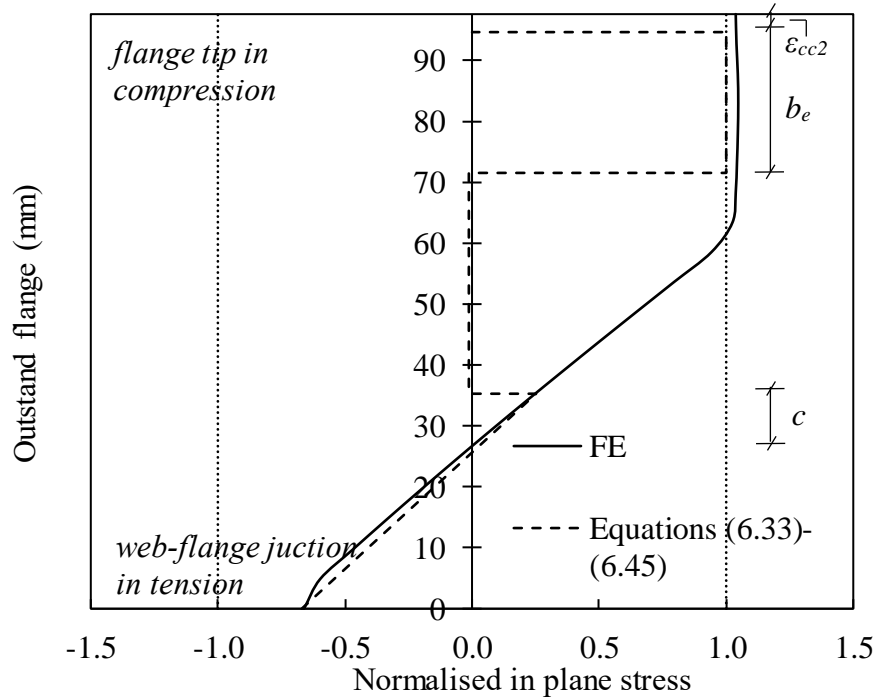


Figure 6.29: Strain coefficient $C_{y,FE}$ derived from FE results.

To further assess the proposed design formulae for the plastic effective width method for C-sections with tip flanges in compression (“u” bending orientation), the stress distribution profiles exported from the FE analyses were compared with the corresponding ones resulted from theoretical calculations. Typical examples of this comparison for both examined aluminium alloys are depicted in Figure 6.30 showing a quite good agreement between the numerically and theoretically predicted (using Equations (6.33)-(6.45) stress distribution profiles.



(a) 6082-T6 ($100 \times 100 \times 5$ - $D/B=1.0$ - $\beta_f/\epsilon=14.23$ - $\bar{\lambda}_{cs}=1.11$)



(b) 6063-T5 ($100 \times 66.7 \times 2$ - $D/B=1.5$ - $\beta_f/\epsilon=10.77$ - $\bar{\lambda}_{cs}=0.87$)

Figure 6.30: Comparison between FE and calculated stress distribution for typical 6082-T6 and 6063-T5 C-sections under "u" bending orientation.

6.4.3.9. Assessment of Plastic effective width method – “n” bending orientation

In case of a slender C-section in minor axis bending and under “n” orientation, the maximum compression strain during design can be taken 3 times the yield strain ε_y ($C_y = 3$) [250]. For this bending configuration, it was found that for all practical B/t ratios, the compressive strains at the web-flange junction and the tensile strains at the flange tip do not result in lateral displacements in the compressed zone [251]. Thereby, there are no ineffective parts of the cross-section and thus it is assumed that under this strain gradient, the cross-section is fully effective [251]. Similarly to the design procedure of C-sections under the “u” bending orientation and in line with Figure 6.31, Equations (6.46)-(6.50) are used to calculate the basic parameters. The design flexural strength $M_{pred,pl-eff-w}$ is determined employing Equation (6.51).

$$K = \frac{C_y \varepsilon_{0.2}}{x_p} \quad (6.46)$$

$$b_g = \frac{\varepsilon_{0.2}}{K} \quad (6.47)$$

$$b_{pc} = x_p - b_g \quad (6.48)$$

$$b_t = B - x_p \quad (6.49)$$

$$b_{pt} = b_t - b_g \quad (6.50)$$

$$M_{pred,pl-eff-w} = \frac{4}{3} \sigma_{0.2} t_f b_g^2 + 2 \sigma_{0.2} t_f b_{pt} (b_g + 0.5 b_{pt}) + 2 \sigma_{0.2} t_f b_{pc} (b_g + 0.5 b_{pc}) + \sigma_{0.2} t_w (D - 2 t_f) (x_p - 0.5 t_w) \quad (6.51)$$

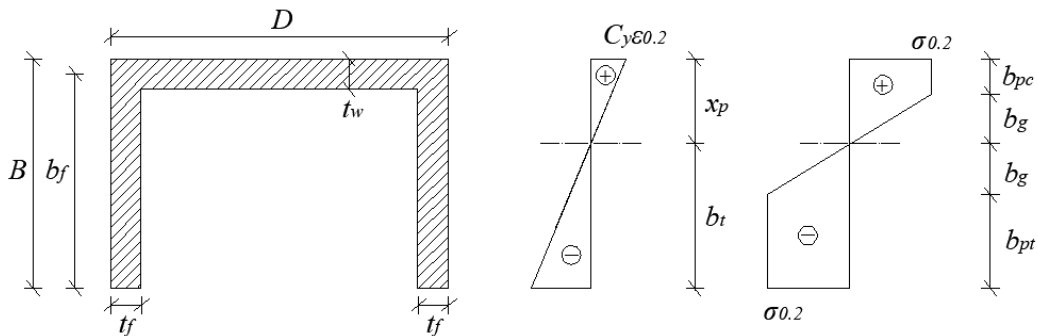


Figure 6.31: Plastic Effective Width Method-Strain and stress distribution profiles of the outstand flanges of a C-section under “n” bending orientation.

The applicability of the plastic effective width method on C-sections under “n” bending orientation is assessed in Figure 6.32, where the predicted-to-ultimate $M_{pred,pl-eff-w}/M_u$ moment ratios are plotted against the slenderness parameter β_f/ϵ of the flange. This figure indicates that the design method proposed by [250] generally provides accurate strength predictions for Class 4 6082-T6 and 6063-T5 C-sections under “n” bending orientation.

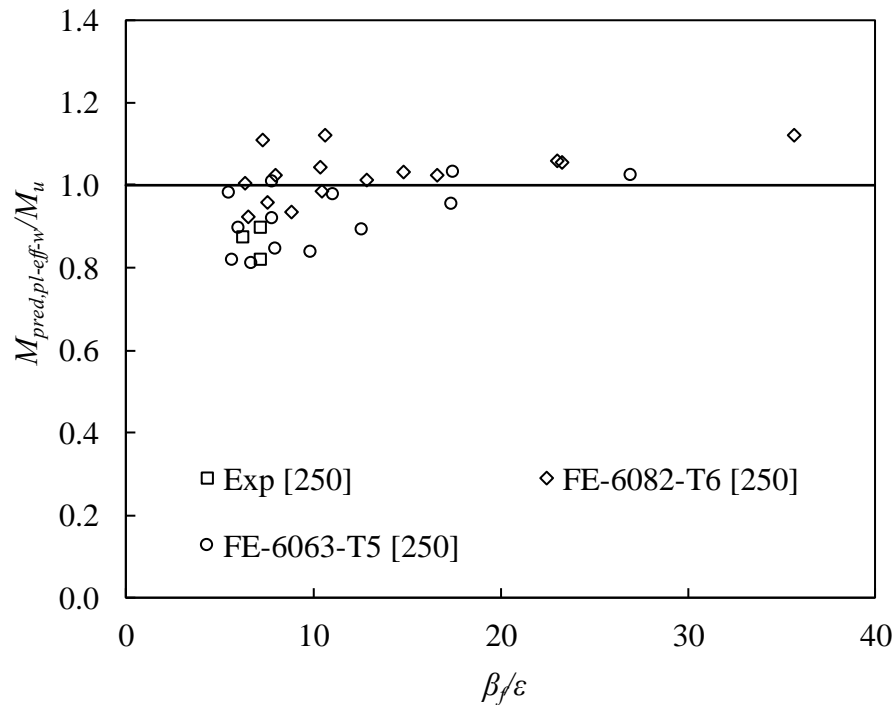
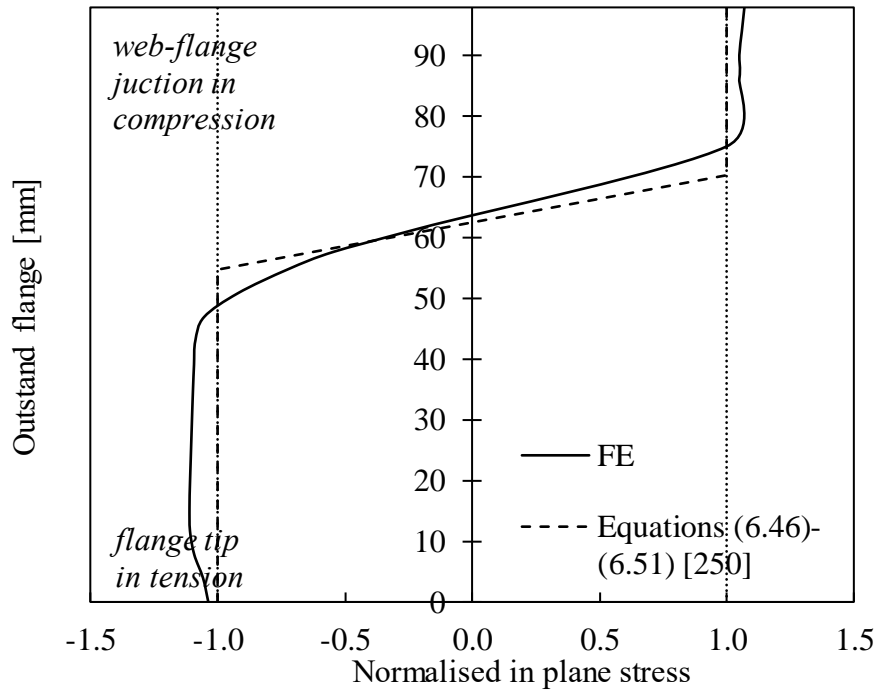
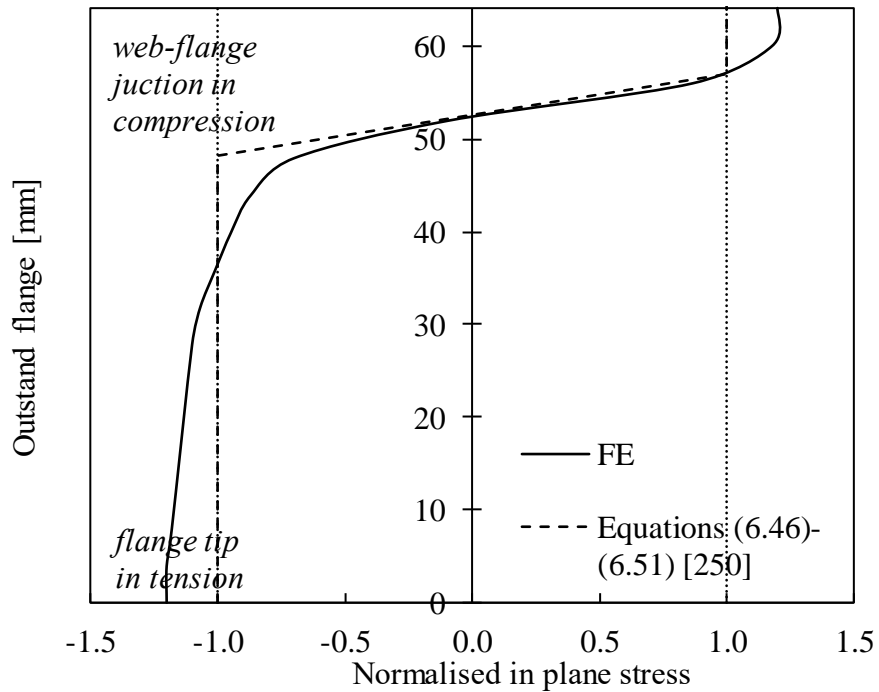


Figure 6.32: Assessment of Plastic Effective Width Method design strength predictions for Class 4 C-sections under “n” bending orientation.

To further assess the design formulae of the plastic effective width method proposed by [250] for C-sections with web in compression (“n” bending orientation), the stress distribution profiles exported from the FE analyses were compared with the corresponding ones resulted from theoretical calculations. Typical examples of this comparison for both examined aluminium alloys are depicted in Figure 6.33 showing a quite good agreement between the numerically and theoretically predicted [250] stress distribution profiles.



(a) 6082-T6 ($100 \times 100 \times 4$ - $D/B=1.0$ - $\beta_f/\varepsilon=16.63$ - $\tau_{cs}=1.40$)



(b) 6063-T5 ($100 \times 66.7 \times 4$ - $D/B=1.5$ - $\beta_f/\varepsilon=7.89$ - $\tau_{cs}=0.72$)

Figure 6.33: Comparison between FE and calculated stress distribution for typical 6082-T6 and 6063-T5 C-sections under "n" bending orientation.

6.4.3.10. Comparison of design codes and methods

This section quantifies the design accuracy and consistency provided by the codes and methods previously discussed in Subsections 6.4.3.4-6.4.3.9. For this purpose, the M_{pred}/M_u ratios are summarised in Tables 6.11 and 6.12 for the “n” and “u” bending orientation, respectively. The results are also presented separately for stocky and slender cross-sections, where applicable.

Regarding “n” bending orientation, EC9 is conservative for stocky C-sections exhibiting average M_{pred}/M_u ratio of 0.79, whilst for slender C-sections the level of conservatism significantly increases to average M_{pred}/M_u ratio of 0.40. The lack of accuracy is more pronounced for the DSM which consistently underestimates the ultimate bending moment capacities by 53%. Conversely, ultimate bending moment capacities derived from CSM appear to be quite improved for stocky C-sections with average M_{pred}/M_u ratio of 0.85. However, the average M_{pred}/M_u ratio decreases to 0.67 for slender C-sections, showing a significant underestimation of the ultimate bending moment capacities. The plastic effective width method was found to provide accurate and relatively consistent design strength predictions for slender C-sections resulting in average to a M_{pred}/M_u ratio of 0.98 and a corresponding COV value of 0.09.

Direct comparisons based on the results listed in Table 6.12 denote that EC9 underestimates by 36% the ultimate bending moment capacities of C-sections under “u” bending orientation. Furthermore, CSM was found to provide the most accurate design strength predictions for stocky C-sections exhibiting an average M_{pred}/M_u ratio of 0.83. On the other hand, the obtained results denote that DSM largely underestimate the ultimate bending moment capacities for stocky C-sections, although it offers quite accurate design strength predictions for slender C-sections. Improved accuracy and consistency are achieved by the plastic effective width method which results in average to a M_{pred}/M_u ratio of 0.81 and a corresponding COV of 0.13. It was also shown that the proposed design equations are capable of more accurately capturing the plastic stress distribution of the buckled flanges of slender sections increasing the average M_{pred}/M_u ratio to 0.90. Higher design consistency is also achieved since the corresponding COV is further improved to 0.07 which is the lowest value amongst those ones resulted from the codes and the other methods.

Table 6.11: Assessment of design strength predictions for C-sections under “n” bending orientation.

	M_{pred}/M_u											
	6082-T6 (Exp)			6082-T6 (FE)			6063-T5 (FE)			All		
	No Exp	mean	COV	No FE	mean	COV	No FE	mean	COV	No (Exp + FE)	mean	COV
Stocky cross-sections												
EC9 (Classes 1-3)	4	0.75	0.19	20	0.82	0.18	22	0.77	0.13	46	0.79	0.17
CSM ($\bar{\lambda}_{cs} \leq 0.68$)	6	0.84	0.08	21	0.89	0.10	21	0.83	0.11	48	0.85	0.11
DSM ($\bar{\lambda}_{cs} \leq 0.776$)	6	0.48	0.07	23	0.52	0.06	27	0.46	0.05	56	0.49	0.08
Slender cross-sections												
EC9 (Class 4)	3	0.46	0.05	15	0.40	0.27	13	0.37	0.21	31	0.40	0.24
CSM ($\bar{\lambda}_{cs} > 0.68$)	1	0.74	0.00	14	0.68	0.15	14	0.64	0.13	29	0.67	0.14
DSM ($\bar{\lambda}_{cs} > 0.776$)	1	0.41	0.00	12	0.42	0.20	8	0.40	0.15	21	0.41	0.18
Plastic effective width [250] (Class 4)	3	0.86	0.04	15	1.03	0.06	13	0.93	0.09	31	0.98	0.09
All cross-sections												
EC9 (All)	7	0.63	0.28	35	0.64	0.39	35	0.62	0.34	77	0.63	0.36
CSM (All)	7	0.83	0.09	35	0.81	0.17	35	0.78	0.15	77	0.80	0.16
DSM (All)	7	0.47	0.09	35	0.49	0.15	35	0.44	0.10	77	0.47	0.13

Table 6.12: Assessment of design strength predictions for C-sections under “u” bending orientation.

	M_{pred}/M_u											
	6082-T6 (Exp)			6082-T6 (FE)			6063-T5 (FE)			All		
	No Exp	mean	COV	No FE	mean	COV	No FE	mean	COV	No (Exp + FE)	mean	COV
Stocky cross-sections												
EC9 (Classes 1-3)	4	0.58	0.23	17	0.71	0.21	18	0.73	0.12	39	0.71	0.19
CSM ($\lambda_{cs} \leq 0.68$)	7	0.77	0.15	22	0.86	0.11	26	0.83	0.07	55	0.83	0.10
DSM ($\lambda_{cs} \leq 0.776$)	7	0.52	0.08	26	0.52	0.14	29	0.48	0.20	62	0.50	0.17
Slender cross-sections												
EC9 (Class 4)	3	0.50	0.02	18	0.62	0.18	17	0.56	0.16	38	0.59	0.18
CSM ($\lambda_{cs} > 0.68$)	-	-	-	13	0.77	0.14	9	0.75	0.14	22	0.76	0.14
DSM ($\lambda_{cs} > 0.776$)	-	-	-	9	0.89	0.16	6	0.87	0.15	15	0.88	0.16
Plastic effective width [250] (Class 4)	3	0.69	0.03	18	0.78	0.12	17	0.88	0.10	38	0.81	0.13
Proposed design method (Class 4)	3	0.88	0.06	18	0.91	0.06	17	0.89	0.07	38	0.90	0.07
All cross-sections												
EC9 (All)	7	0.55	0.20	35	0.67	0.21	35	0.65	0.19	77	0.64	0.19
CSM (All)	7	0.77	0.15	35	0.83	0.13	35	0.81	0.10	77	0.81	0.12
DSM (All)	7	0.52	0.08	35	0.61	0.31	35	0.55	0.33	77	0.58	0.31

6.5. Continuous beams

6.5.1. Assessment of plastic design concept

According to conventional elastic design, the design collapse load is determined when the first plastic hinge forms in the most heavily stressed cross-section of the structure. Conversely, plastic design exploits the ability of indeterminate structures for bending moment redistribution until a sufficient number of plastic hinges forms and imminent collapse occurs. Plastic design utilises the structure's reserve strength beyond the elastic state and thus allowing the structural members to sustain further loading upon their plastic moment capacity is reached. In elastic design, each structural member must have a design bending moment capacity M_d greater than that obtained from an elastic analysis M^* . Under the design loading, if $M_d=M^*$ for one structural member, the first plastic hinge forms at the design load level along the curve as depicted in Figure 6.34. Thus, the cross-section employed in practice is chosen to have $M_d>M^*$, so that the first plastic hinge of the structure occurs at a load level above the design loading. Conversely, plastic design requires that the last plastic hinge occurs at or above the design load level. Figure 6.34 indicates that for the same design loading, the plastic design concept requires a "lighter" structure consisting of components with smaller cross-sections. Thereby, significant material savings can be achieved resulting in a more economically efficient design.

The plastic design may be applied provided that the rotational capacity at the location of the plastic hinges is sufficient to maintain their plastic moment capacity and ability to undergo large inelastic rotations without exhibiting local buckling. Thus, the ductility features of the construction material are one of the key-properties to ensure satisfactory performance and attainment of the plastic collapse load.

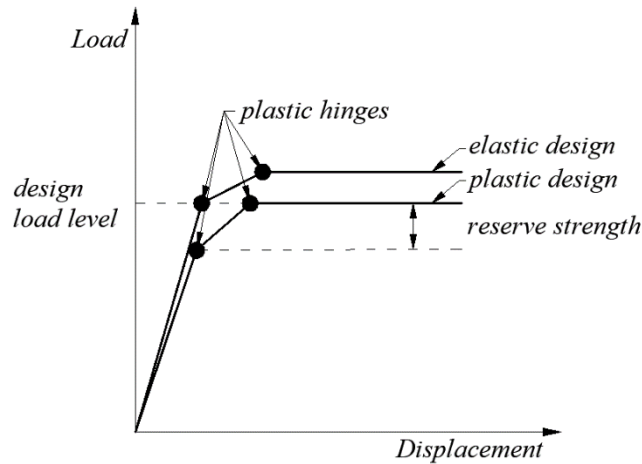


Figure 6.34: Comparison between elastic and plastic design concept.

6.5.2. Assessment of traditional plastic design method

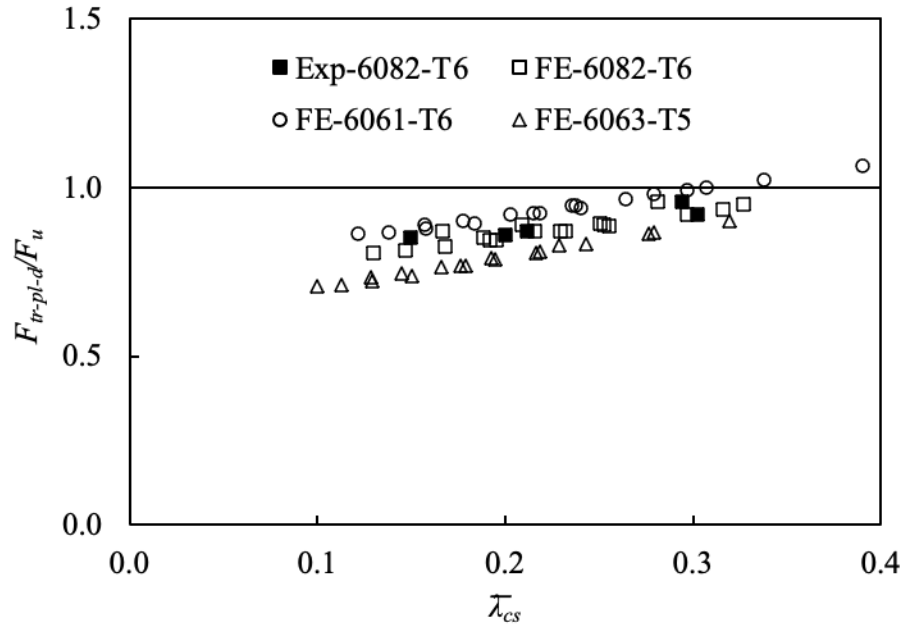
The traditional plastic design method is conventionally employed to indeterminate structures comprising Class 1 cross-sections. This method accounts for moment redistribution and thus the design collapse load corresponds to the load level which causes a collapse mechanism based on the formation of consecutive plastic hinges. Each plastic hinge forms when the most heavily stressed cross-section reaches its plastic moment capacity $M_{tr-pl-d}$ which is given by the following Equation.

$$M_{tr-pl-d} = W_{pl} \sigma_{0.2} \quad (6.52)$$

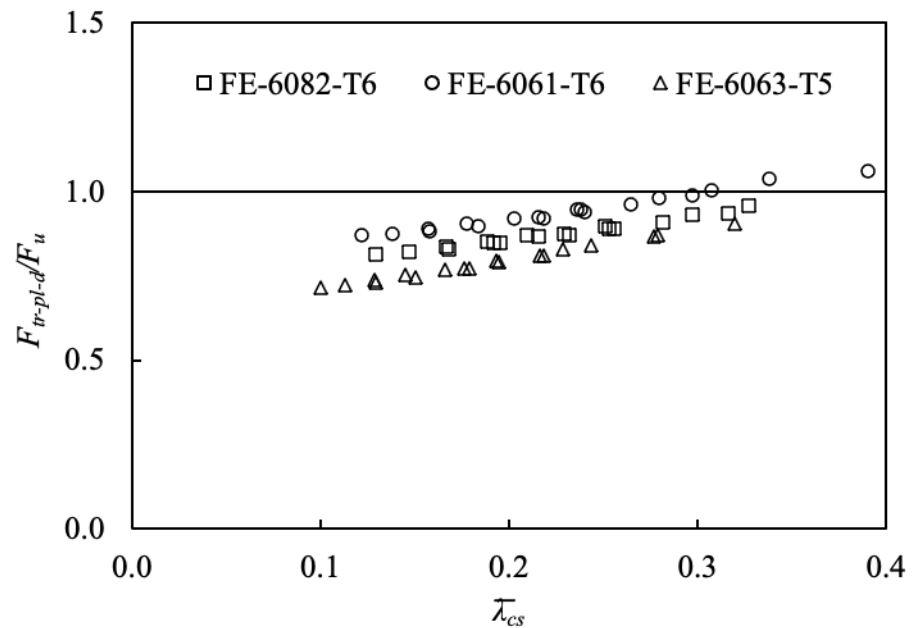
For simplicity, traditional plastic design idealises the material behaviour adopting an elastic-perfectly plastic stress-strain relationship and thus the additional strength resulting from strain hardening is ignored. Thereby, as far as traditional plastic design method is concerned, the theoretical collapse load ($F_{tr-pl-d}$) is expected to be slightly underestimated.

Figure 6.35 displays the ratio of the theoretical over the experimentally and numerically obtained strengths $F_{tr-pl-d}/F_u$ for both load configurations LC1 and LC2. From this figure, it can be concluded that the traditional plastic design method provides safe but slightly conservative ultimate strengths, i.e., data points below the unity threshold line, particularly for stockier sections. Moreover, it can be observed that the ultimate strengths corresponding to 6082-T6 and 6063-T5 cross-sections appear to be more conservative compared to their 6061-T6 counterparts. This is related to the fact that the traditional

plastic design method adopts an elastic-perfectly plastic stress-strain relationship ignoring the material strain hardening behaviour, which is more pronounced in 6082-T6 and 6063-T5 aluminium alloys as shown in Table 5.15.



(a) LC1

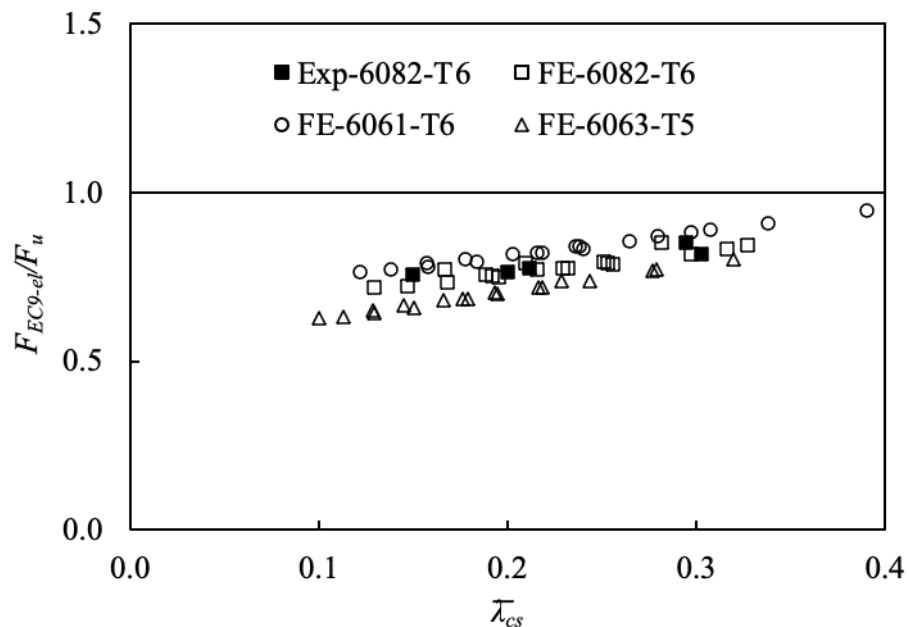


(b) LC2

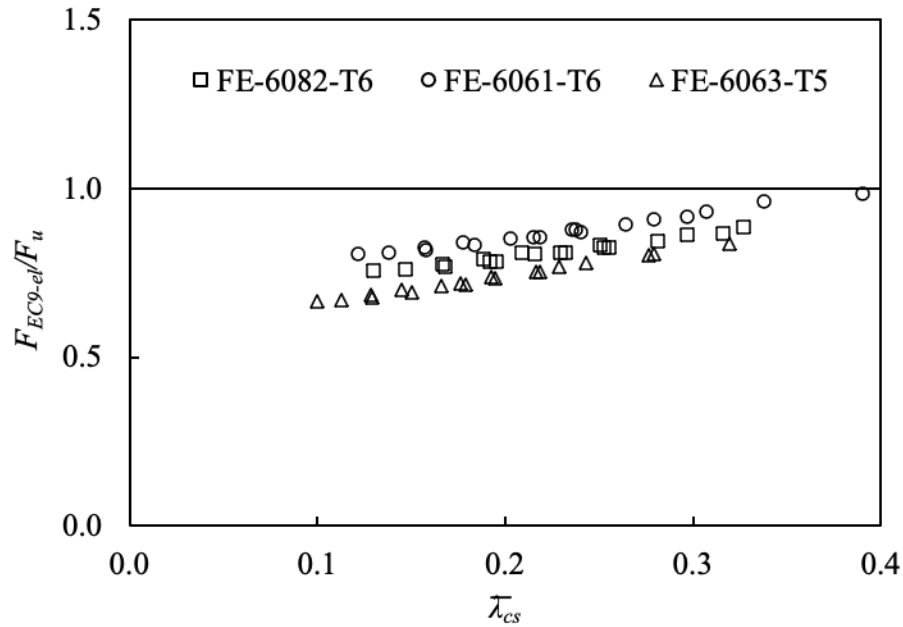
Figure 6.35: Assessment of traditional plastic design method.

6.5.3. Assessment of Eurocode 9

EC9 [5] in the main part adopts the elastic global analysis for the design of indeterminate aluminium alloy structures neglecting the ability for moment redistribution at system level due to statical indeterminacy. Thus, the theoretical collapse load is defined when the most heavily stressed cross-section of the structure reaches its bending moment capacity given by Equation (6.17). However, in ductile indeterminate structures, redistribution of bending moments will occur regardless of whether this was considered or not during the design process. Hence, the structure will fail at a higher loading level than that predicted by the design. Thereby, the global elastic design concept is expected to provide overly conservative design predictions, particularly for aluminium alloy indeterminate structures with stocky cross-sections, i.e., Class 1. To assess this, Figure 6.36 presents the ratio of the theoretical over the experimentally and numerically obtained strengths F_{EC9-el}/F_u for both load configurations LC1 and LC2. As can be seen, all data points are below and far from the unity threshold line, denoting that the global elastic analysis leads to considerably underestimated strength predictions.



(a) LC1



(b) LC2

Figure 6.36: Assessment of EC9 [5] using global elastic analysis.

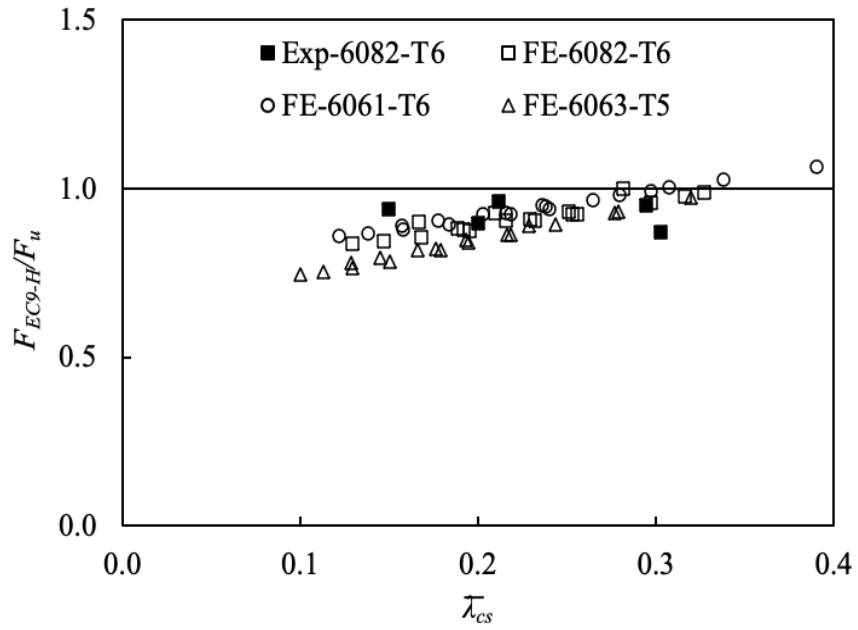
However, EC9 [5] is the first international design code which allows plastic design including the plastic hinge method in Annex H. This method applies mainly to Class 1 cross-sections but may be used in Class 2 and Class 3 cross-sections by considering the local buckling effect while determining the ultimate strength. In any case, it should be assured that the structural ductility of the employed aluminium alloy is sufficient for the development of a fully plastic mechanism. The bending moment capacity M_{EC9-H} according to Annex H of EC9 [5] can be calculated using the Equation (6.53). The key diversion between the plastic hinge method and the traditional plastic design method is that the former considers the beneficial effect of material strain hardening through a correction factor η providing more accurate design provisions.

$$M_{EC9-H} = \alpha_{\zeta} \eta W_{el} \sigma_{0.2} \quad (6.53)$$

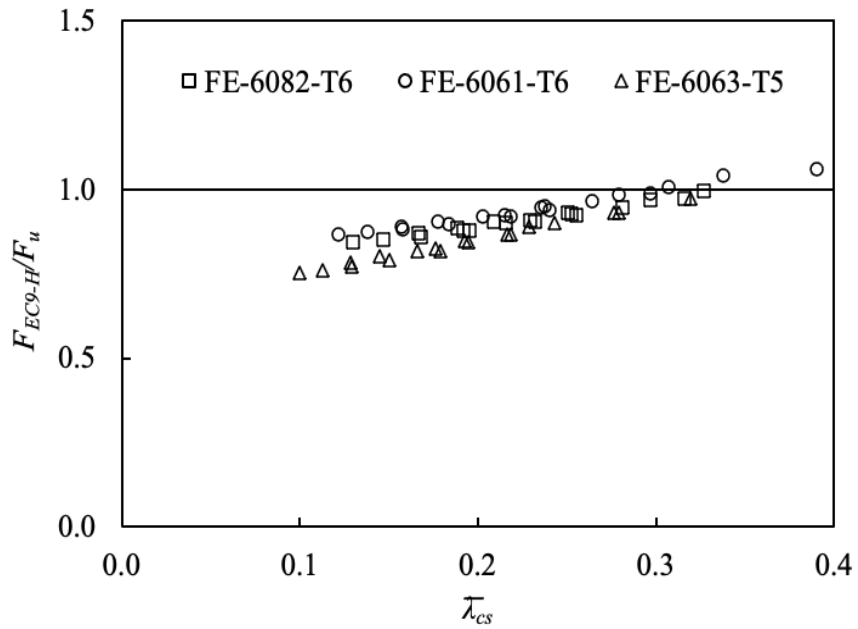
where α_{ζ} is the shape factor depending on the ductility of the aluminium alloy as described in Annex G [5].

Figure 6.37 presents the ratio of the theoretical over the experimentally and numerically obtained strengths F_{EC9-H}/F_u for both load configurations LC1 and LC2. Upon comparing Figure 6.36 and Figure 6.37, it can be observed that the ratio values in the latter case are

closer to unity threshold line denoting that the plastic hinge method results in more accurate and thereby more economically efficient strength predictions. Moreover, the plastic hinge method through the consideration of material strain hardening provides higher level of accuracy than the traditional plastic design method, which approximates the stress-strain response adopting an elastic-perfectly plastic material model (Figure 6.35).



(a) LC1



(b) LC2

Figure 6.37: Assessment of European design provisions using plastic hinge method from Annex-H [5].

6.5.4. Assessment of Continuous Strength Method for indeterminate structures

The CSM for aluminium alloy determinate structures was extended to cover indeterminate structures [66] adopting merits from the traditional plastic design method allowing for moment redistribution at system level (global plastic analysis). The novelty of this method is that it adopts an elastic-linear hardening material behaviour rather than an elastic-perfectly plastic material behaviour as traditional plastic design method does. Therefore, it accounts for material strain hardening at cross-sectional level resulting in a more accurate estimation of the bending moment capacity. According to CSM, the required rotation at each plastic hinge is different and thus the bending moment capacity differs in each cross-section. As has been mentioned, the CSM is a deformation-based design method evaluating the bending moment capacity based on a strain ratio proportional to the plastic hinge rotational demand. For a given structural configuration, the CSM design collapse load can be determined employing the following summarised steps:

1. Similarly to traditional plastic design method, the location of the i plastic hinges of the considered collapse mechanism and the rotation θ_i for each plastic hinge should be determined.
2. The cross-sectional slenderness $\bar{\lambda}_{cs}$ at each plastic hinge location is calculated using the Equation (6.22).
3. Based on the CSM base curve, the maximum attainable strain ε_{CSM} at each cross-section is defined employing Equation (6.20).
4. The rotational plastic hinge demand α_i for each plastic hinge is computed according to Equation (6.54):

$$\alpha_i = \frac{\theta_i D_i}{(\varepsilon_{CSM} / \varepsilon_{0.2})_i} \quad (6.54)$$

where D_i is the cross-sectional depth.

The critical (first) plastic hinge is defined as the one which undergoes the highest plastic hinge rotational demand $\alpha_{\max} = \max \{ \alpha_i \}$ and it is assigned the maximum strain ratio $(\varepsilon_{CSM} / \varepsilon_{0.2})_{\max}$.

5. The strain ratio at each subsequent plastic hinge $(\varepsilon_{CSM}/\varepsilon_{0.2})_{hinge,i}$ is reduced and is calculated in proportion to the rotational hinge demand α_i .

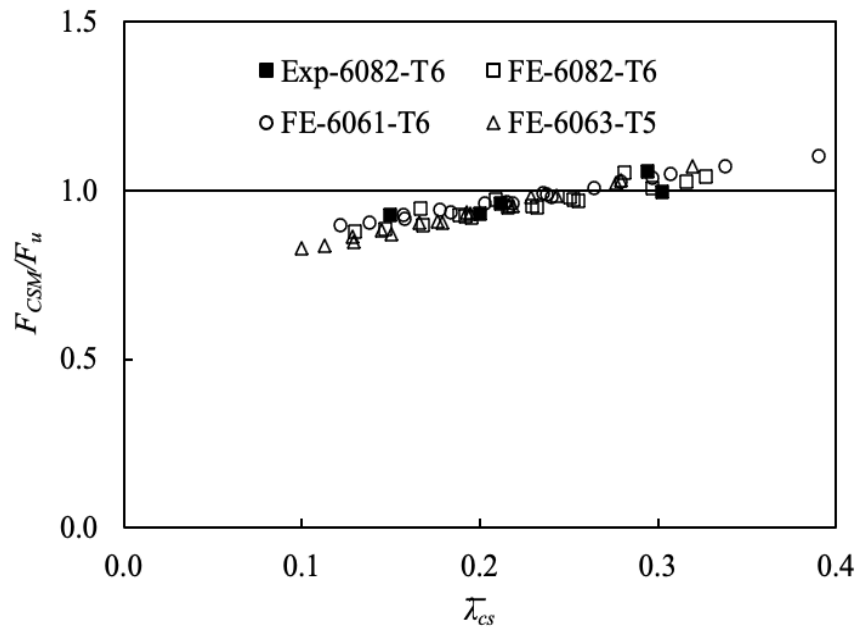
$$\left(\frac{\varepsilon_{CSM}}{\varepsilon_{0.2}} \right)_{hinge,i} = \frac{\alpha_i}{\alpha_{max}} \left(\frac{\varepsilon_{CSM}}{\varepsilon_{0.2}} \right)_{max} \leq \left(\frac{\varepsilon_{CSM}}{\varepsilon_{0.2}} \right)_i \quad (6.55)$$

6. The cross-sectional bending moment capacity M_i at each plastic hinge, is evaluated based on the corresponding strain ratio $(\varepsilon_{CSM}/\varepsilon_y)_{hinge,i}$ using the Equation (6.55).
7. The theoretical CSM collapse load of the considered structural configuration is determined by equating the external work done by the applied loads F_j through virtual displacements δ_j and the internal work resulting from the rotations θ_i at the plastic hinges.

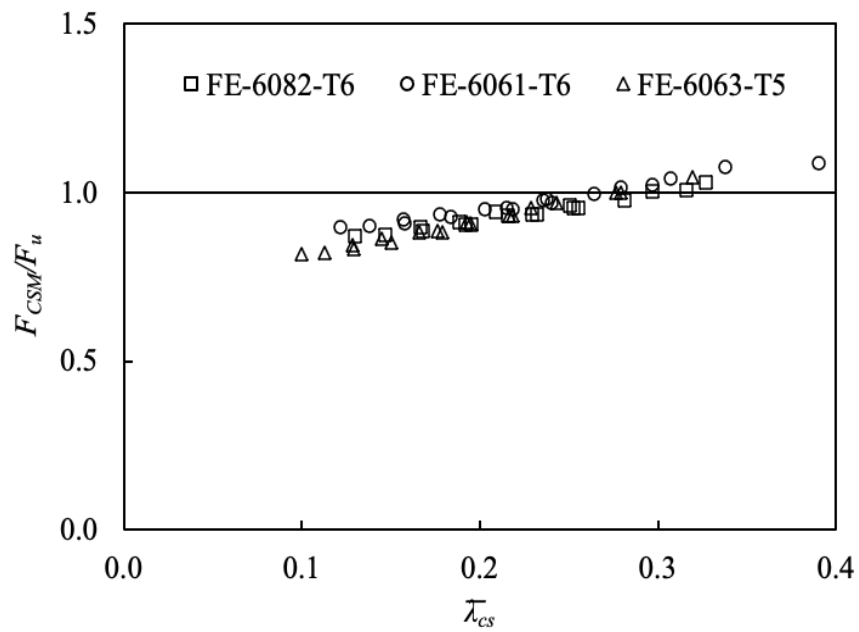
$$\sum_j F_j \delta_j = \sum_i M_i \theta_i \quad (6.56)$$

Note that global plastic analysis in CSM should be considered only for a minimum $(\varepsilon_{CSM}/\varepsilon_{0.2})_{max}$ value of 3.6 for SHS/RHS cross-sections, otherwise elastic global analysis should be employed [66].

This method is due to lead to improved design predictions owing to the allowance for moment redistribution at system level and the systematic exploitation of material strain hardening at cross-sectional level. To assess this, Figure 6.38 presents the ratio of the theoretical over the experimentally and numerically obtained strengths F_{CSM}/F_u for both load configurations LC1 and LC2. As can be seen, the CSM design equations provide accurate strength predictions as all data points are close to the unity threshold line.



(a) LC1



(b) LC2

Figure 6.38: Assessment of CSM.

6.5.5. Comparison of design codes and methods

Aiming to evaluate the potential of applying plastic design on aluminium alloy indeterminate structures, this section quantifies the design accuracy and consistency provided by the design methods discussed in the previous sections. For this purpose, the ratios of the theoretical over the experimentally and numerically obtained strengths are summarised in Table 6.13. The results are also presented separately for the different examined load configurations and aluminium alloys. It can be seen that the application of global elastic analysis, which neglects the ability for moment redistribution at system level provides the most conservative strength predictions, achieving a mean value of the F_{EC9-e}/F_u ratio equal to 0.79. However, the ultimate loads obtained from the traditional plastic design method, the plastic hinge method of Annex H of EC9 [5] and the CSM provide improved predictions. These methods employ the plastic design concept which utilises the structure's reserve strength beyond the elastic state allowing for higher collapse load than that corresponding to the first yield of the structure. Comparisons amongst these three methods denoted that the traditional plastic design offers the most conservative ultimate loads with a mean value of the $F_{tr-pl-d}/F_u$ ratio equal to 0.87. Better accuracy and particularly 14% and 20% is achieved by the plastic hinge method and CSM, which predicted strength ratio with mean values of 0.90 and 0.95, respectively. The improved accuracy owes to the fact that both plastic hinge method and CSM account for the effect of material strain hardening, whilst the traditional plastic design method adopts the approximation of the elastic-perfectly plastic stress-strain relationship. It is noteworthy that the CSM offers slightly more consistent ultimate loads compared to plastic hinge method, achieving the lowest value of COV amongst those resulted from the other design methods. Overall, it can be concluded that plastic design concept and particularly the plastic hinge method included in Annex H of EC9 [5] and CSM can be employed in case of aluminium alloy indeterminate structures providing accurate design strength predictions.

Table 6.13: Assessment of design methods for aluminium alloy continuous beams.

Load configuration	Aluminium alloy	No Exp	No FE	No Exp+FE	$F_{tr-pl-d}/F_u$	F_{EC9-el}/F_u	F_{EC9-H}/F_u	F_{CSM}/F_u
LC1	6082-T6	5	18	23	0.88	0.78	0.92	0.96
	6061-T6	-	18	18	0.94	0.83	0.94	0.98
	6063-T5	-	18	18	0.79	0.70	0.84	0.93
LC2	6082-T6	-	18	18	0.87	0.81	0.91	0.94
	6061-T6	-	18	18	0.94	0.87	0.94	0.97
	6063-T5	-	18	18	0.79	0.73	0.84	0.91
mean	All	5	108	113	0.87	0.79	0.90	0.95
COV					0.09	0.09	0.08	0.07

CHAPTER 7

Conclusions and future research

7.1. Fix-ended stub columns

7.1.1. Concrete-filled tubular cross-sections

The current study (see Subsection 4.2.2.) investigates experimentally the potential of combining 6082-T6 aluminium alloy with concrete to develop a composite structural cross-section. For this purpose, a total of 16 stub columns, including 8 BAT (see Subsection 4.2.1.) and 8 CFAT specimens (see Subsection 4.2.2.) were subjected to uniform compression. Based on the experimental results, the following conclusions are drawn:

- (1) The governing failure mode of the stub column specimens was local buckling. For some composite specimens, splitting of the aluminium tube along the corner was also observed upon occurrence of inelastic local buckling.
- (2) The experimental findings denoted that the concrete infill enhanced notably the cross-sectional performance of the aluminium tubes, as its presence braced the aluminium tubes to resist the developed deformations, thus allowing for higher strength and displacement compared to BAT specimens.
- (3) Compared to BAT specimens, the average strength increase and the average increase of the displacement at failure was in the range of 23%-93.1% and 15.8-

187.6%, respectively, for CFAT specimens. The percentage strength increase is more pronounced for the slenderest aluminium cross-sections. This is attributed to the delay to local buckling offered by the infill in sections with more slender aluminium tubes.

- (4) In absence of codified criteria for composite aluminium-concrete cross-sections, the present study proposes adopting the European design formulae for composite steel-concrete cross-sections replacing the material properties of steel by those of aluminium alloy. The proposed design methodology was found to be suitable for the composite cross-sections, providing reasonably accurate and consistent strength predictions (mean value of the experimental over the proposed strengths $F_{u,prop}/F_{u,Exp}$ equal to 0.92 and the corresponding COV equal to 0.07).

7.1.2. Channel cross-sections

The current study investigates experimentally (see Subsection 4.2.3.) and numerically (see Subsection 5.2.1.) the cross-sectional response of 6082-T6 aluminium alloy channels. For this purpose, a total of 6 fix-ended stub columns were subjected to uniform compression, whilst 47 additional performance data were generated through FE modelling. Based on the experimental and numerical results, the following conclusions are drawn:

- (1) Comparisons between the European provisions and the experimental and FE ultimate strengths showed that EC9 [5] provides safe design strength predictions but quite conservative (mean value of the predicted over the experimental/FE strengths $F_{pred,cs,EC9}/F_u$ equal to 0.85) and particularly the level of conservatism increases for slender cross-sections, i.e., cross-sections with higher β_f/ε values. Additionally, the relatively low COV of 0.11 denotes the relatively low level of design consistency provided by the EC9 [5].
- (2) Relative comparisons denoted that the DSM is suitable for the design of aluminium alloy C-sections subjected to concentric compression providing the most accurate and consistent design strength predictions (mean value of the predicted over the experimental/FE strengths $F_{pred,cs,EC9}/F_u=0.96$ and corresponding COV=0.04).

7.2. Pin-ended columns

7.2.1. Bare tubular cross-sections

The current study investigates experimentally (see Subsection 4.3.1.) and numerically (see Subsection 5.3.1.) the buckling behaviour of 6082-T6 aluminium alloy BAT pin-ended columns. For this purpose, a total of 8 columns were tested having pin-ended boundary conditions allowing rotation about the minor axis, whilst 54 additional performance data were generated through FE modelling. Based on the experimental and numerical results, the following conclusions are drawn:

- (1) The predominant failure mode obtained from tests was flexural buckling.
- (2) The comparison between the European provisions and the experimental and FE results for BAT pin-ended columns showed that the current codified equations underestimate the actual strength of BAT pin-ended columns.
- (3) A revised buckling curve was proposed for BAT pin-ended columns which was able to improve the strength prediction of square and rectangular Class A aluminium tubes by 12% compared to that of EC9 [5].

7.2.2. Concrete-filled tubular cross-sections

The current study investigates experimentally (see Subsection 4.3.2.) and numerically (see Subsection 5.3.2.) the buckling behaviour of CFAT pin-ended columns. For this purpose, a total of 8 columns were tested having pin-ended boundary conditions allowing rotation about the minor axis, whilst 54 additional performance data were generated through FE modelling. Based on the experimental and numerical results, the following conclusions are drawn:

- (1) Based on the experimental programme, the predominant failure mode was flexural buckling.
- (2) It was shown that the concrete infill effectively delays buckling. Consequently, the CFAT columns exhibited higher strength and stiffness compared to the BAT columns examined in Subsection 4.3.1.
- (3) Based on the experimental programme, the strength increase for constant member length owing to the concrete infill was more significant in case of slender cross-

sections. The highest increase, which was equal to 72%, has been observed for the most slender cross-section and can be attributed to the delay in the local buckling offered by the concrete infill.

- (4) Based on the FE study, the strength increase for constant member length owing to higher concrete grade appeared more pronounced for slender cross-sections. Future research to verify this conclusion in a wide variety of cross-sections and aluminium alloys is recommended.
- (5) In absence of design provisions for aluminium-concrete composite columns, the present study proposed adopting the European design formulae for composite steel-concrete members with the material properties of steel replaced by those of aluminium alloy. A new buckling design curve was proposed on the basis of the experimental and numerical data and used in conjunction with the European standards. The proposal was found to be suitable for the design of CFAT columns providing reasonably accurate and consistent strength predictions.
- (6) A different trend has been observed on the performance of CFAT columns comprising Class 4 aluminium sections. Further research is recommended to evaluate the cross-sectional performance of concrete-filled Class 4 aluminium square and rectangular tubes.

7.2.3. Channel cross-sections

The current study investigates experimentally (see Subsection 4.3.3.) and numerically (see Subsection 5.3.3.) the minor-axis buckling behaviour of 6082-T6 aluminium alloy channels. For this purpose, a total of 8 pin-ended columns were subjected to uniform compression, whilst 45 additional performance data were generated through FE modelling. Based on the experimental and numerical results, the following conclusions are drawn:

- (1) Comparisons between the European provisions and the experimental and FE ultimate strengths denoted that EC9 [5] underestimates the actual flexural buckling resistance of 6082-T6 aluminium alloy columns (mean value of the predicted over the experimental/FE strengths $F_{pred,cs,EC9}/F_u$ ratio equal to 0.87), whilst the relatively low COV of 0.08 suggests the relatively low level of design consistency provided by the EC9 [5].

- (2) A new flexural buckling curve is proposed based on both the experimental and numerical results improving further the design accuracy of EC9 [5].
- (3) Relative comparisons denoted that the DSM is suitable for the design of aluminium alloy C-section columns under concentric compression providing the most accurate and consistent design strength predictions (mean value of the predicted over the experimental/FE strengths $F_{pred,DSM}/F_u=0.93$ and corresponding COV=0.06).

7.3. Simply-supported beams

7.3.1. Bare rectangular tubular cross-sections

The current study investigates experimentally (see Subsection 4.4.1.) the flexural behaviour of BAT simply-supported beams. For this purpose, five stocky RHS cross-sections made from 6082-T6 heat-treated aluminium alloy were tested employing three- and four-point bending configurations. Based on the experimental results, the following conclusions are drawn:

- (1) Relative assessment denoted that the current EC9 [5] Class 1 and Class 2 slenderness limits for internal elements in compression are acceptable.
- (2) The experimentally obtained bending moment capacities $M_{u,Exp}$ were compared with those predicted according to Section 6.2.5 of EC9 [5] M_{EC9} and the alternative method included in Annex F of EC9 [5] M_{EC9-F} showing that in both cases, EC9 predictions appear to be safe and consistent (mean value of the predicted over the experimental strengths $M_{EC9}/M_{u,Exp}=0.85$ and corresponding COV=0.03, and $M_{EC9-F}/M_{u,Exp}=0.92$ and corresponding COV=0.03).
- (3) Relative comparisons denoted that the CSM which rationally accounts for the influence of material strain hardening exhibited by stocky cross-sections provides more accurate design predictions compared to Section 6.2.5 of EC9 [5]. However, the achieved accuracy level of the CSM and Annex F of EC9 [5] is the same since both design methods consider material strain hardening within the calculations.

7.3.2. Concrete-filled tubular cross-sections

The current study investigates experimentally (see Subsection 4.3.3.) the potential of combining 6082-T6 aluminium alloy with concrete to develop a composite structural cross-section. For this purpose, a total of 8 beams, including 4 BAT (see Subsection 4.2.2.) and 4 CFAT specimens (see Subsection 4.3.3.) were subjected to three-point bending. Based on the experimental results presented in subsections 4.2.2. and 4.3.3., the following conclusions are drawn:

- (1) The BAT specimens failed due to material yielding accompanied by inelastic local buckling on the upper flange, whilst the specimen with the slenderest cross-section failed due to local buckling on the upper flange. All CFAT specimens exhibited significant inelastic in-plane deformations and failed by tensile fracture at the lower flange of the aluminium tube.
- (2) The experimental results demonstrated that by decreasing the depth-to-thickness D/t ratio of the BAT/CFAT sections, the bending moment capacity and the exhibited ductility increases.
- (3) The presence of the infill in CFAT specimens braced the aluminium tubes to resist the developed deformations and thus allowed for higher strength and stiffness compared to BAT specimens.
- (4) The percentage increase in the ultimate strength is more pronounced for higher D/t values. The highest increase, which was equal to 48.93% has been observed for the slenderest cross-section and can be attributed to the delay in the local buckling owing to the concrete infill.
- (5) In absence of codified provisions for aluminium-concrete composite beams, the present study proposes adopting the European design formulae for composite steel-concrete members replacing the material properties of steel by those of aluminium alloy.
- (6) The proposed design methodology was found to be suitable for the design of CFAT beams providing reasonably accurate and consistent strength predictions.

7.3.3. Channel cross-sections

The current study investigates experimentally (see Subsection 4.4.4.) and numerically (see Subsection 5.4.2.) the flexural response of 6082-T6 aluminium alloy channels. For this purpose, a total of 14 beams were subjected to four-point bending under “n” and “u” bending orientations, whilst 140 additional performance data were generated through FE modelling. Based on the experimental and numerical results, the following conclusions are drawn:

- (1) It was shown that that all beam specimens under “u” bending orientation failed due to local buckling initiated in the compressed part of the flanges. For beam specimens under “n” bending orientation, material yielding was the governing failure mode.
- (2) Assessment of EC9 Class 2 and Class 3 slenderness limits for outstand elements under stress gradient denoted that both values could be relaxed. The same conclusion was drawn for Class 3 slenderness limit for internal elements in compression which was found excessively conservative.
- (3) Regarding C-sections under “n” bending orientation, both EC9 [5] and DSM provide conservative design strength predictions, whilst CSM appears to offer quite improved results for stocky cross-sections. Regarding C-sections under “u” bending orientation, EC9 [5] underestimates (36%) the actual bending moment capacities, whilst CSM and DSM provide the most accurate design strength predictions for stocky and slender cross-sections, respectively.
- (4) The applicability of the plastic effective width method to slender aluminium alloy C-sections was evaluated leading to quite accurate design strength predictions, while improved design formulae, resulting to predicted over ultimate strength ratio of 90%, were proposed.
- (5) Overall, it is recommended that the modified plastic effective width method can be employed for the design of slender aluminium alloy C-sections subjected to minor axis bending.

7.4. Continuous beams

The current study investigates experimentally (see Subsection 4.5.) and numerically (see Subsection 5.5.) the structural performance and design of aluminium alloy indeterminate structures examining the potential of applying the plastic design concept on 6082-T6 aluminium alloy. Five stocky RHS cross-sections made from 6082-T6 heat-treated aluminium alloy were tested as two-span continuous beams to explore the possibility for moment redistribution, whilst 108 additional performance data were generated through FE modelling. Based on the experimental and numerical results, the following conclusions are drawn:

- (1) Relative comparisons denoted that the plastic design concept and specifically the plastic hinge method and CSM are suitable for the design of aluminium alloy indeterminate structures. These two design methods address sufficiently the issue of strain hardening at cross-sectional level and moment redistribution at system level resulting in accurate strength predictions. Particularly, the plastic hinge method included in Annex H of EC9 [5] and CSM provided predicted strength ratio with mean values of 0.90 and 0.95, respectively, which are 14% and 20% more accurate of the corresponding one resulted from global elastic analysis.
- (2) This study fundamentally extends the pool of performance data for aluminium alloy indeterminate structures by reporting for the first time research results for the relatively new 6082-T6 aluminium alloy along with a detailed numerical study for the already investigated 6061-T6 and 6063-T5 aluminium alloys. Overall, it is concluded that utilising the structure's reserve strength beyond the elastic state allows for higher collapse loads and thereby the full utilisation of the potential of aluminium alloys as a structural material.

7.5. Research impact

The potential impact and benefits from this research work to industry are summarised as follows:

- (1) This study fundamentally extends the pool of performance data for aluminium alloy structures by reporting research results on the compressive and flexural behaviour of the relatively new 6082-T6 aluminium alloy which has been already employed in various structural applications around the world.
- (2) This study concludes that the current design guidelines and particularly EC9 provide conservative strength predictions which are opposed to an efficient design philosophy from an economical point of view. This is related to the fact that the design formulae are based on limited amount of experimental and numerical studies. Therefore, enhancing the experimental and numerical data allows for a deeper comprehension of structural aluminium alloys' response and design, thereby increasing structural engineers' confidence towards a more frequent employment of this material in modern structures.
- (3) The assessment results of the EC9 design criteria along with the suggested modifications foster a future refinement of the code towards a safer and more economically efficient design framework. Economically attractive design solutions will make aluminium alloys a competitive construction material, capable of efficiently responding to the challenges encountered in real-life structures.
- (4) Moreover, it was shown that in case of composite steel-concrete members, the concerns regarding the high self-weight and the corrosion of the steel tubes can be overcome replacing the steel with aluminium alloys. The use of aluminium alloys can reduce the self-weight of the composite members and extend their applicability in structures located in humid environments. The compressive and flexural performance was evaluated herein showing promising results.
- (5) Finally, this study examined thoroughly the potential of employing plastic design on aluminium alloy indeterminate structures. Even though aluminium alloys may have less ductility compared to steel, it was found that they have sufficient

rotational capacity allowing for application of the plastic design concept which results in more economical cross-sections.

7.6. Suggestions for future work

Aiming to increase structural engineers' confidence towards a more frequent employment of aluminium alloys as primary structural material, design methods that are both simple to use and efficient, yet safe, are needed. To this end, additional research work is recommended herein and is summarised in Table 7.1.

The present thesis proposed revised buckling curves for bare square/rectangular tubular (see Subsection 6.3.1.) and channel (see Subsection 6.3.3.) pin-ended columns improving the strength prediction of Class A aluminium columns compared to that of EC9. However, further research is needed to assess the proposed buckling curves for additional cross-sectional shapes and aluminium alloys categorised as Class A, thus facilitating their inclusion in future versions of the design specifications.

In absence of design provisions for aluminium-concrete composite structural beams and columns, the present thesis proposed adopting the European design formulae for composite steel-concrete members with the material properties of steel replaced by those of aluminium alloy. Moreover, a new buckling design curve was proposed on the basis of the experimental and numerical data and used in conjunction with the European standards. Further studies are deemed necessary to verify the applicability of the suggested design methodology and optimise the relevant design equations.

As mentioned in Subsection 6.3.2. different trend has been observed on the performance of concrete-filled tubular columns comprising Class 4 aluminium sections. Therefore, further research is recommended to evaluate the cross-sectional performance of concrete-filled Class 4 aluminium square and rectangular tubes.

As concluded in Subsection 7.3.1. the design criteria derived from CSM and Annex F of EC9 [5] provide enhanced flexural strength prediction for bare square/rectangular tubular cross-sections through consideration of material strain hardening within the calculations. The applicability of the aforementioned design criteria could also be extended to elliptical

or oval hollow cross-sections which have been recently introduced as tubular construction products.

Furthermore, as concluded in Subsection 7.3.3. the modified plastic effective width method can be employed for the design of slender aluminium alloy C-sections subjected to minor axis bending. However, more experimental and numerical studies covering different aluminium alloy types are needed to assess further the accuracy and consistency level of the modified design equations.

The present thesis thoroughly examined the inelastic response of aluminium alloy indeterminate structures and particularly two-span continuous beams. As concluded in Subsection 7.4. even though aluminium alloys may have less ductility compared to steel, they still have sufficient rotational capacity allowing for moment redistribution and thereby the application of plastic design concept. Employing the plastic design concept and utilising the structure's reserve strength beyond the elastic state allows for higher collapse loads and thereby the full utilisation of the potential of aluminium alloys as a structural material. To validate further this conclusion, a series of experimental and numerical work on the inelastic response of aluminium alloy frames would be required.

Similar to the research on bare tubular and channel section structural elements, experimental and numerical studies could also be conducted on castellated and cellular beams and columns. These structural elements have already been successfully employed in steel frames providing significant material savings and savings in the cladding costs, whilst their lighter appearance also entails certain aesthetic advantages.

The reduced material ductility of aluminium alloys is expected to affect the deformation capacity of aluminium alloy structures. The execution of experimental and numerical investigations on different types of aluminium alloy connections together with the study of the robustness of aluminium alloy structures is hence recommended.

A life cycle analysis could be performed to quantify the sustainability gains related to the use of aluminium alloys as primary structural material. Comparisons with other conventional structural material such as steel, reinforced concrete and timber are suggested in order to visualise the potential environmental benefits through the employment of aluminium alloys in structural engineering. The latter could add

significant value to the research on the structural performance of aluminium alloy members.

Finally, it is suggested, the results obtained in this study to be shared with the Joint Research Centre so that to be considered in the second generation of Eurocodes.

Table 7.1: Summary of recommended future work.

	Future work	Scope
1.	Additional tests/numerical studies on aluminium alloy cross-sections employing different cross-sectional shapes and Class A aluminium alloys.	Verify the revised buckling curves proposed in Subsections 6.3.1 and 6.3.3 for pin-ended columns.
2.	Additional tests/numerical studies on aluminium-concrete composite structural beams and columns.	Verify the applicability of the suggested design methodology and optimise the relevant design equations.
3.	Additional tests/numerical studies on aluminium-concrete composite structural columns comprising Class 4 aluminium square and rectangular tubular sections.	Investigate further the cross-sectional performance of concrete-filled Class 4 aluminium square and rectangular tubes.
4.	Tests/numerical studies on aluminium alloy elliptical or oval hollow cross-sections.	Evaluate the applicability of the design criteria included in the CSM and Annex F of EC9.
5.	Additional tests/numerical studies on aluminium alloy channel sections made from different aluminium alloy types.	Assess further the accuracy and consistency level of the modified plastic effective width method proposed in Subsection 7.3.3.
6.	Tests/numerical studies on aluminium alloy frames.	Explore further the possibility of plastic design on aluminium alloy indeterminate structures.
7.	Tests/numerical studies on castellated and cellular beams and columns.	Investigate the structural performance and assess the applicability of the current design rules.
8.	Tests/numerical studies on different types of aluminium alloy connections. Examine the robustness of aluminium alloy structures.	Examine the influence of reduced material ductility on the structural performance.
9.	Perform Life Cycle Analysis for aluminium alloys and other conventional structural materials.	Quantify the environmental impacts of aluminium alloy structures and compare with their counterparts made from other conventional structural materials.

References

1. All about Aluminium. Aluminium in construction. [cited 2022 May 1].
2. The Aluminium Association. Aluminium Alloys 101. [cited 2022 May 1].
3. Aluminium-The Green Metal. Hazlemere. [cited 2022 May 1].
4. GB 50429-2007. Code for design of aluminium structures. Ministry of Construction of the People's Republic of China.
5. European Committee for Standardization (EC9). Eurocode 9: Design of aluminium structures. Part 1-1: General structural rules - General structural rules and rules for buildings. BS EN 1999-1-1:2007, CEN:2007. BSI; 2007.
6. Australian/New Zealand Standard (AS/NZS) Aluminium structures part 1: Limit state design. AS/NZS 1664.1:1997. Standards Australia, Sydney, Australia. 1997.
7. The Aluminum Association (AA), Aluminum design manual. Washington, DC, 2020. 2020.
8. St Mary Axe, London, UK. [cited 2022 May 31].
9. The Sage Gateshead, Gateshead Quays, UK. [cited 2022 May 31].
10. Ferrari World, Abu Dhabi, UAE. [cited 2022 May 31].
11. Gaylord Texan Resort & Convention Center, Grapevine, Texas, USA. [cited 2022 May 31].
12. The Crystal, London, UK. [cited 2022 May 31].
13. The Iceberg Skating Palace, Sochi, Russia. [cited 2022 May 31].
14. The Co-operative Group, Manchester, UK. [cited 2022 May 31].
15. Kaufman JG. Introduction to Aluminium Alloys and Tempers. ASM International. Materials Park, OH: ASM International; 2000. 14–28 p.
16. Davis JR. Alloying: Understanding the Basics. Materials Park, OH: ASM

- International; 2001. 351–416 p.
17. Mazzolani FM. Aluminium Structural Design. Vienna: Springer Verlag GmbH; 2003. 394 p.
 18. Ramberg W, Osgood WR. Description of stress-strain curves by three parameters. Vol. Technical. Washington, D.C.: National Advisory Committee for Aeronautics; 1943.
 19. Foster ASJ, Gardner L, Wang Y. Practical strain-hardening material properties for use in deformation-based structural steel design. *Thin-Walled Struct.* 2015;92:115–29.
 20. Alsanat H, Gunalan S, Guan H, Keerthan P, Bull J. Experimental study of aluminium lipped channel sections subjected to web crippling under two flange load cases. *Thin-Walled Struct.* 2019;141:460–76.
 21. Su M-N, Young B, Gardner L. Testing and Design of Aluminum Alloy Cross Sections in Compression. *J Struct Eng.* 2014;140(9).
 22. Moen LA, Hopperstad OS, Langseth M. Rotational Capacity Of Aluminum Beams Under Moment Gradient. I: Experiments. *J Struct Eng.* 1999;125(8):910–20.
 23. Baehre R. Trycktastravorav elastoplastikt material-nagrafrageställningar (Comparison between structural behaviour of elastoplastic material). Tekn Arne Johnson Ingenjorsbyrå. 1966;
 24. De Matteis G, Brando G, Mazzolani FM. Pure aluminium: An innovative material for structural applications in seismic engineering. *Constr Build Mater.* 2012;26(1):677–86.
 25. Guo X, Shen Z, Li Y. Stress-strain relationship and physical-mechanical properties of domestic structural aluminum alloy. *J Build Struct.* 2007;06:110–7.
 26. Steinhardt PJ, Nelson DR, Ronchetti M. Bond-orientational order in liquids and glasses. *Phys Rev B.* 1983;28:784–805.
 27. Wang Y, Fan F, Qian H, Zhai X. Experimental study on constitutive model of

- high-strength aluminum alloy 6082–T6. *J Build Struct.* 2013;34(6):113–20.
28. Hopperstad OS, Langseth M, Remseth S. Cyclic stress-strain behaviour of alloy AA6060 , Part I: Uniaxial experiments and modelling. *Int J Plast.* 1995;11(6):725–39.
 29. Chaboche JL. Constitutive equations for cyclic plasticity. *Int J Plast.* 1989;5:247–302.
 30. Hopperstad OS, Langseth M, Remseth S. Cyclic stress-strain behaviour of alloy AA6060 T4 , Part II: Biaxial experiments and modelling. *Int J Plast.* 1995;11(6):741–62.
 31. Dusicka P, Tinker J. Global Restraint in Ultra-Lightweight Buckling-Restrained Braces. *J Compos Constr.* 2013;17(1):139–50.
 32. Guo X, Wang L, Shen Z, Zou J, Liu L. Constitutive model of structural aluminum alloy under cyclic loading. *Constr Build Mater.* 2018;180:643–54.
 33. Lai YFW, Nethercot DA. Strength of aluminium members containing local transverse welds. *Eng Struct.* 1992;14(4):241–54.
 34. Mazzolani FM. Aluminum alloy structures. 2nd ed. London: E& FN Spon; 1995.
 35. Zhu J-H, Young B. Effects of transverse welds on aluminum alloy columns. *Thin-Walled Struct.* 2007;45(3):321–9.
 36. Kaufman JG. Properties of Aluminum Alloys: Tensile, Creep, and Fatigue Data at High and Low Temperatures [Internet]. ASM International; 1999. (The aluminum association).
 37. Langhelle NK. Experimental validation and calibration of nonlinear finite element models for use in design of aluminium structures exposed to fire. Norwegian University of Science and Technology, Trondheim; 1999.
 38. Hepples W, Wale D. High temperature tensile properties of 6082-T651. 1992.
 39. Faggiano B, De Matteis G, Landolfo R, Mazzolani FM. Behaviour of aluminium alloy structures under fire. Vol. 10, *Journal of Civil Engineering and Management.*

- Vilnius Gedminas Technical University; 2004. p. 183–90.
40. Maljaars J, Soetens F, Katgerman L. Constitutive model for Aluminum alloys exposed to fire conditions. *Metall Mater Trans A Phys Metall Mater Sci* 39A(april 2008), 778-789. 2008;
 41. Dorn J.E. Some Fundamental Experiments on High Temperature Creep. *J Mech Phys Solids*. 1954;3:85–116.
 42. Harmathy TZ. A Comprehensive Creep Model. *J Fluids Eng*. 1967;89(3):496–502.
 43. Kandare E, Feih S, Lattimer BY, Mouritz AP. Larson – Miller Failure Modeling of Aluminum in Fire. *Metall Mater Trans A*. 2010;41(12):3091–9.
 44. Larson FR, Miller J. A Time-Temperature Relationship for Rupture and Creep Stresses. *Trans ASME*. 1952;74(5):765–75.
 45. Kandare E, Feih S, Kootsookos A, Mathys Z, Lattimer BY, Mouritz AP. Creep-based life prediction modelling of aluminium in fire. *Mater Sci Eng A*. 2010;527(4–5):1185–93.
 46. Feih S, Kandare E, Lattimer BY, Mouritz AP. Structural analysis of compression deformation and failure of aluminum in fire. *J Struct Eng*. 2011;137(7):728–38.
 47. Chen Z, Lu J, Liu H, Liao X. Experimental investigation on the post-fire mechanical properties of structural aluminum alloys 6061-T6 and 7075-T73. *Thin-Walled Struct*. 2016;106:187–200.
 48. Su M-N, Young B. Material properties of normal and high strength aluminium alloys at elevated temperatures. *Thin-Walled Struct*. 2019;137:463–71.
 49. British Standards Institution. Eurocode 9 : Design of aluminium structures. Part 1 - 2: Structural fire design. BS EN 1999-1-2:2007, CEN:2007. BSI; 2010. 58 p.
 50. Mazzolani FM, Faella C, Piluso V, Rizzano G. Assessment of stub columns tests for aluminium alloys. In: 2nd International Conference on Coupled Instabilities in Metal Structures, CIMS '96. London: Imperial College Press; 1996. p. 539–46.

51. Langseth M, Hopperstad OS. Local buckling of square thin-walled aluminium extrusions. *Thin-Walled Struct.* 1997;27:117–26.
52. Hopperstad OS, Langseth M, Tryland T. Ultimate strength of aluminium alloy outstands in compression: experiments and simplified analysis. *Thin-Walled Struct.* 1999;34:279–94.
53. Mazzolani FM, Piluso V, Rizzano G. Experimental analysis of aluminium alloy channels subjected to local buckling under uniform compression. In: *Italian Conference on Steel Construction*. Acai Servizi, Milano, Italy; 2001.
54. Faella C, Mazzolani FM, Piluso V, Rizzano G. Local Buckling of Aluminum Members: Testing and Classification. *J Struct Eng.* 2000;126(3):353–60.
55. Zhu J-H, Wang P, Liu T. Numerical simulation and design of aluminum compression members with plain and lipped channel sections. *J Build Struct.* 2010;31:163–8.
56. Mazzolani FM, Piluso V, Rizzano G. Local Buckling of Aluminum Alloy Angles under Uniform Compression. *J Struct Eng.* 2011;137(2):173–84.
57. Liu M, Zhang L, Wang P, Chang Y. Buckling behaviors of irregular section aluminum alloy columns under axial compression. *Eng Struct.* 2015;95:127–37.
58. Liu M, Zhang L, Wang P, Chang Y. Experimental investigation on local buckling behaviors of stiffened closed-section thin-walled aluminum alloy columns under compression. *Thin-Walled Struct.* 2015;94:188–98.
59. Yuan HX, Wang YQ, Chang T, Du XX, Bu YD, Shi YJ. Local buckling and postbuckling strength of extruded aluminium alloy stub columns with slender I-sections. *Thin-Walled Struct.* 2015;90:140–9.
60. Wang Y, Fan F, Lin S. Experimental investigation on the stability of aluminium alloy 6082 circular tubes in axial compression. *Thin-Walled Struct.* 2015;89:54–66.
61. Feng R, Young B. Experimental Investigation of Aluminum Alloy Stub Columns

- with Circular Openings. *J Struct Eng.* 2015;141(11):1–10.
62. Feng R, Zhu W, Wan H, Chen A, Chen Y. Tests of perforated aluminium alloy SHSs and RHSs under axial compression. *Thin-Walled Struct.* 2018;130:194–212.
 63. Feng R, Mou X, Chen A, Ma Y. Tests of aluminium alloy CHS columns with circular openings. *Thin-Walled Struct.* 2016;109:113–31.
 64. Gardner L, Ashraf M. Structural design for non-linear metallic materials. *Eng Struct.* 2006;28(6):926–34.
 65. Ashraf M, Young B. Design formulations for non-welded and welded aluminium columns using Continuous Strength Method. *Eng Struct.* 2011;33(12):3197–207.
 66. Su M-N, Young B, Gardner L. The continuous strength method for the design of aluminium alloy structural elements. *Eng Struct.* 2016;122:338–48.
 67. Su M-N, Young B, Gardner L. Classification of aluminium alloy cross-sections. *Eng Struct.* 2017;141:29–40.
 68. Manevich AIĀ. Effect of strain hardening on the buckling of structural members and design codes recommendations. *Thin-Walled Struct.* 2007;45:810–5.
 69. Adeoti GO, Fan YJW, Zhai XM. Stability of 6082-T6 aluminum alloy columns with H-section and rectangular hollow sections. *Thin-Walled Struct.* 2015;89:1–16.
 70. Wang YQ, Wang ZX, Hu XG, Han JK, Xing HJ. Experimental study and parametric analysis on the stability behavior of 7A04 high-strength aluminum alloy angle columns under axial compression. *Thin-Walled Struct.* 2016;108:305–20.
 71. Wang YQ, Yuan HX, Chang T, Du XX, Yu M. Compressive buckling strength of extruded aluminium alloy I-section columns with fixed-pinned end conditions. *Thin-Walled Struct.* 2017;119:396–403.
 72. Moen CD, Schafer BW. Direct strength method for design of cold-formed steel columns with holes. *J Struct Eng.* 2011;137(5):559–70.

-
73. Feng R, Liu J. Numerical investigation and design of perforated aluminium alloy SHS and RHS columns. *Eng Struct.* 2019;199.
 74. Chang Y, Liu M, Wang P. Interacted buckling failure of thin-walled irregular-shaped aluminum alloy column under axial compression. *Thin-Walled Struct.* 2016;107:627–47.
 75. Wang ZX, Wang YQ, Sojeong J, Ouyang YW. Experimental investigation and parametric analysis on overall buckling behavior of large-section aluminum alloy columns under axial compression. *Thin-Walled Struct.* 2018;122:585–96.
 76. Zhu J-H, Li Z-Q, Su M-N, Young B. Behaviour of aluminium alloy plain and lipped channel columns. *Thin-Walled Struct.* 2019;135:306–16.
 77. Zhu J-H, Young B. Tests and Design of Aluminum Alloy Compression Members. *J Struct Eng.* 2006;132(7):1096–107.
 78. Zhu JH, Young B. Aluminum alloy tubular columns-Part I: Finite element modeling and test verification. *Thin-Walled Struct.* 2006;44(9):961–8.
 79. Zhu J-H, Young B. Aluminum alloy tubular columns-Part II: Parametric study and design using direct strength method. *Thin-Walled Struct.* 2006;44(9):969–85.
 80. Zhu JH, Young B. Experimental investigation of aluminum alloy circular hollow section columns. *Eng Struct.* 2006;28:207–15.
 81. Zhu J-H, Young B. Numerical investigation and design of aluminum alloy circular hollow section columns. *Thin-Walled Struct.* 2008;46:1437–49.
 82. Zhu J-H, Li Z-Q, Su M-N, Young B. Numerical study and design of aluminium alloy channel section columns with welds. *Thin-Walled Struct.* 2019;139:139–50.
 83. Langhelle NK, Amdahl Jø. Experimental And Numerical Analysis of Aluminium Columns Subjected to Fire [Internet]. The Eleventh International Offshore and Polar Engineering Conference. Stavanger, Norway: International Society of Offshore and Polar Engineers; 2001. p. 8.

84. Suzuki J-I, Ohmiya Y, Wakamatsu T, Harada K. Evaluation of Fire Resistance of Aluminum Alloy Members. *Fire Sci Technol*. 2005;24(4):237–55.
85. Maljaars J, Soetens F, Snijder HH. Local buckling of aluminium structures exposed to fire. Part 1: Tests. *Thin-Walled Struct*. 2009;47(11):1404–17.
86. Maljaars J, Soetens F, Snijder HH. Local buckling of aluminium structures exposed to fire Part 2: Finite element models. *Thin-Walled Struct*. 2009;47(11):1418–28.
87. Maljaars J, Twilt L, Soetens F. Flexural buckling of fire exposed aluminium columns. *Fire Saf J*. 2009;44(5):711–7.
88. Maljaars J, Soetens F, Snijder H. H. Local Buckling of Fire-Exposed Aluminum Members: New Design Model. *J Struct Eng*. 2010;136(1):66–75.
89. Liu M, Chang Y, Wang P, Zhang L. Buckling behaviors of thin-walled aluminum alloy column with irregular-shaped cross section under axial compression in a fire. *Thin-Walled Struct*. 2016;98:230–43.
90. Jiang S, Xiong Z, Guo X, He Z. Buckling behaviour of aluminium alloy columns under fire conditions. *Thin Walled Struct*. 2018;124(1239):523–37.
91. Panlilo F. The theory of limit design applied to magnesium alloy and aluminium alloy structures. *R Aerinautical Soc*. 1947;534–71.
92. Mazzolani FM, Capelli M, Spasiano G. Plastic analysis of aluminium alloy members in bending. *Aluminium*. 1985;61(10):734–41.
93. Welo T. Inelastic deformation capacity of flexurally-loaded aluminium alloy structures. Norwegian University of Science and Technolog; 1990.
94. Opheim BS. Bending of thin-walled aluminium extrusions. Norwegian University of Science and Technology; 1996.
95. Moen LA, De Matteis G, Hopperstad OS, Langseth M, Landolfo R. Rotational Capacity Of Aluminum Beams Under Moment Gradient. II: Numerical Simulations. *J Struct Eng*. 1999;125(8):921–9.

-
96. De Matteis G, Moen LA, Langseth M, Landolfo R, Hopperstad OS, Mazzolani FM. Cross-sectional classification for aluminum beams-parametric study. *J Struct Eng.* 2001;127(3):271–9.
 97. Su M-N, Young B, Gardner L. Deformation-based design of aluminium alloy beams. *Eng Struct.* 2014;80:339–49.
 98. Su M-N, Young B, Gardner L. Continuous beams of aluminum alloy tubular cross sections. I: Tests and FE model validation. *J Struct Eng.* 2015;141(9).
 99. Su M-N, Young B, Gardner L. Continuous beams of aluminum alloy tubular cross sections. II: Parametric study and design. *J Struct Eng.* 2015;141(9).
 100. Su M-N, Young B, Gardner L. Flexural response of aluminium alloy SHS and RHS with internal stiffeners. *Eng Struct.* 2016;121:170–80.
 101. Zhu J-H, Young B. Design of Aluminum Alloy Flexural Members Using Direct Strength Method. *J Struct Eng.* 2009;135(5):558–66.
 102. Kim Y, Peköz T. Ultimate flexural strength of aluminum sections. *Thin-Walled Struct.* 2010;48:857–65.
 103. Kim Y, Peköz T. Numerical Slenderness Approach for design of complex aluminum extrusions subjected to flexural loading. *Thin-Walled Struct.* 2018;127:62–75.
 104. Castaldo P, Nistri E, Piluso V. Ultimate behaviour of RHS temper T6 aluminium alloy beams subjected to non-uniform bending: Parametric analysis. *Thin-Walled Struct.* 2017;115:129–41.
 105. Piluso V, Pisapia A, Nistri E, Montuori R. Ultimate resistance and rotation capacity of low yielding high hardening aluminium alloy beams under non-uniform bending. *Thin-Walled Struct.* 2019;135:123–36.
 106. Feng R, Shen C, Lin J. Finite element analysis and design of aluminium alloy CHSs with circular through-holes in bending. *Thin-Walled Struct.* 2019;144.
 107. Feng, R. and Shen C. Bending tests on perforated CHSs in aluminum alloy. *Eng*

- Struct. 2019;
108. Montuori R, Nastro E, Piluso V, Pisapia A. Ultimate behaviour of high-yielding low-hardening aluminium alloy I-beams. *Thin-Walled Struct.* 2020;146:106463.
 109. Cheng M, Shi Y, Wang Y. Analysis of lateral stability of I-section aluminum beams. *Sci China Ser E Technol Sci.* 2006;49(6):742–51.
 110. GB 50017-2003. Code of Design of Steel Structures. Beijing: China Planning Press. Beijing: China Planning Press; 2003.
 111. Wang YQ, Yuan HX, Shi YJ, Cheng M. Lateral torsional buckling resistance of aluminium I-beams. *Thin-Walled Struct.* 2012;50(1):24–36.
 112. Wang YQ, Wang ZX, Yin FX, Yang L, Shi YJ, Yin J. Experimental study and finite element analysis on the local buckling behavior of aluminium alloy beams under concentrated loads. *Thin-Walled Struct.* 2016;105:44–56.
 113. Matusiak M. Strength and ductility of welded structures in aluminium alloys. Norwegian University of Science and Technology; 1999.
 114. Wang T, Hopperstad OS, Lademo OG, Larsen PK. Finite element modelling of welded aluminium members subjected to four-point bending. *Thin-Walled Struct.* 2007;45(3):307–20.
 115. Meulen ORRV Der, Soetens F, Maljaars J. Experimental Analysis of Stability of Aluminium Beams in Case of Fire. *J Struct Fire Eng.* 2014;5(2):161–74.
 116. Clark JW. Eccentrically loaded aluminum columns. *Trans ASCE.* 1955;120(116):1116–32.
 117. Klöppel K, Bärsch W. Versuche zum kapitel ”stabilitätsfälle” der neufassung von din 4113. *Aluminium.* 1973;49(10).
 118. Gilson S, Cescotto S. Experimental research on the buckling of aluminium alloy columns with unsymmetrical cross-section. *Lab Mécanique des Mater Théorie des Struct* Liege, Liege, Belgium. 1982;
 118. Zhu J-H, Young B. Experimental Investigation of Aluminum Alloy Thin-Walled

- Tubular Members in Combined Compression and Bending. *J Struct Eng.* 2006;132(12):1955–66.
119. Zhu JH, Young B. Aluminum alloy circular hollow section beam-columns. *Thin-Walled Struct.* 2006;44(2):131–40.
120. Zhao Y, Zhai X, Sun L. Test and design method for the buckling behaviors of 6082-T6 aluminum alloy columns with box-type and L-type sections under eccentric compression. *Thin-Walled Struct.* 2016;100:62–80.
121. Zhao Y, Zhai X, Wang J. Buckling behaviors and ultimate strength of 6082-T6 aluminum alloy columns with square and circular hollow sections under eccentric compression – Part I: Experiments and finite element modelling. *Thin-Walled Struct.* 2019;143.
122. Zhao Y, Zhai X, Wang J. Buckling behaviors and ultimate strength of 6082-T6 aluminum alloy columns with square and circular hollow sections under eccentric compression – Part II: Parametric study, design provisions and reliability analysis. *Thin-Walled Struct.* 2019;143.
123. Zhu S, Guo X, Liu X, Jiang S. Bearing capacity of aluminum alloy members under eccentric compression at elevated temperatures. *Thin-Walled Struct.* 2018;127:574–87.
124. Huynh LAT, Pham CH, Rasmussen KJR. Mechanical properties and residual stresses in cold-rolled aluminium channel sections. *Eng Struct.* 2019;199:109562.
125. Moen CD, Igusa T, Schafer BW. Prediction of residual stresses and strains in cold-formed steel members. *Thin-Walled Struct.* 2008;46(4):1274–89.
126. Gardner L, Cruise R. Modeling of residual stresses in structural stainless steel sections. *J Struct Eng.* 2009;135(1):42–53.
127. AISI. Standard Test Method for Determining the Web Crippling Strength of Cold-Formed Steel Beams (AISI S909). Washington, D.C.; 2008.
128. Tryland T, Langseth M, Hopperstad OS. Nonperfect aluminium beams subjected

- to concentrated loading. *J Struct Eng.* 1990;125:900–9.
129. Zhou F, Young B. Aluminum tubular sections subjected to web crippling-Part I: Tests and finite element analysis. *Thin-Walled Struct.* 2008;46(4):339–51.
 130. Zhou F, Young B. Aluminium tubular sections subjected to web crippling—Part II: Proposed design equations. *Thin-Walled Struct.* 2008;46(4):352–61.
 131. NAS. North American Specification for the Design of Cold-Formed Steel Structural Members. American Iron and Steel Institute, Washington, DC. 2001.
 132. Zhou F, Young B, Zhao X. Tests and Design of Aluminum Tubular Sections Subjected to Concentrated Tests and Design of Aluminum Tubular Sections Subjected. *J Struct Eng ASCE.* 2009;135(7):806–17.
 133. Zhou F, Young B. Web crippling of aluminium tubes with perforated webs. *Eng Struct.* 2010;32(5):1397–410.
 134. Chen Y, Chen X, Wang C. Aluminum tubular sections subjected to web crippling. *Thin-Walled Struct.* 2015;90:49–60.
 135. Su M-N, Young B. Design of aluminium alloy stocky hollow sections subjected to concentrated transverse loads. *Thin-Walled Struct.* 2018;124:546–57.
 136. Alsanat H, Gunalan S, Keerthan P, Guan H. Web crippling behaviour and design of aluminium lipped channel sections under two flange loading conditions. *Thin-Walled Struct.* 2019;144.
 137. Zhou F, Young B. Web crippling of aluminium alloy channel sections with flanges restrained. *Thin-Walled Struct.* 2020;148:106576.
 138. European Committee for Standardization (EC3) (2005) Eurocode 3: Design of Steel Structures, Part 1-3: General Rules-Supplementary Rules for Cold-Formed Members and Sheeting, BS EN 1993-1-3:2005, CEN:2005. BSI.
 139. American Institute of Steel Construction, AISC Committee (2010) Specification for Structural Steel Buildings, Chicago, Illinois, 2010.
 140. Zhou F, Young B. Tests of concrete-filled aluminum stub columns. *Thin-Walled*

- Struct. 2008;46(6):573–83.
141. Zhou F, Young B. Concrete-filled aluminum circular hollow section column tests. *Thin-Walled Struct.* 2009;47(11):1272–80.
 142. Zhou F, Young B. Numerical analysis and design of concrete-filled aluminum circular hollow section columns. *Thin-Walled Struct.* 2012;50(1):45–55.
 143. Zhou F, Young B. Concrete- filled double-skin aluminum circular hollow section stub columns. *Thin-Walled Struct.* 2018;133:141–52.
 144. Wang F-C, Zhao H-Y, Han L-H. Analytical behavior of concrete- filled aluminum tubular stub columns under axial compression. *Thin-Walled Struct.* 2019;140:21–30.
 145. GB 50936-2014. Technical code for concrete filled steel tubular structures. 2014.
 146. Feng R, Chen Y, Gong W. Flexural behaviour of concrete-filled aluminium alloy thin-walled SHS and RHS tubes. *Eng Struct.* 2017;137:33–49.
 147. Chen Y, Feng R, Gong W. Flexural behavior of concrete-filled aluminum alloy circular hollow section tubes. *Constr Build Mater.* 2018;165:173–86.
 148. Chen Y, Feng R, Xu J. Flexural behaviour of CFRP strengthened concrete-filled aluminium alloy CHS tubes. *Constr Build Mater.* 2017;142:295–319.
 149. Architectural Institute of Japan (AIJ), Recommendations for Design and Construction of Concrete Filled Steel Tubular Structures, Architectural Institute of Japan, Tokyo, Japan, 1997. 1997.
 150. Wu C, Zhao XL, Duan WH. Design rules for web crippling of CFRP strengthened aluminium rectangular hollow sections. *Thin-Walled Struct.* 2011;49:1195–207.
 151. Islam SMZ, Young B. FRP strengthened aluminium tubular sections subjected to web crippling. *Thin-Walled Struct.* 2011;49:1392–403.
 152. Islam SMZ, Young B. Web crippling of aluminium tubular structural members strengthened by CFRP. *Thin-Walled Struct.* 2012;59:58–69.

153. Islam SMZ, Young B. Design of CFRP-strengthened aluminium alloy tubular sections subjected to web crippling. *Thin-Walled Struct.* 2018;124:605–21.
154. Praveen P, Yarlagadda PKDV. Meeting challenges in welding of aluminum alloys through pulse gas metal arc welding. *J Mater Process Technol.* 2005;164–165:1106–12.
155. Soetens F. Welded connections in aluminium alloy structures. *Heron.* 1987;32(1).
156. European Recommendations for aluminium alloy structures (ECCS). First Edit. 1978.
157. TGB-Aluminium, Technical Principles for the design of building structures, Aluminium structures, Netherlands Standard NEN 3854. 1983.
158. CP 118, The structural use of aluminium, British Standard Code of Practice (replaced by BS 8118). 1969.
159. Chan T, Porter Goff R. Welded aluminium alloy connections: test results and BS8118. *Thin-Walled Struct.* 2000;36(4):265–87.
160. De Matteis G, Corte GD, Mandara A, Mazzolani FM. Experimental behaviour of aluminium t-stub connections. In: *Connections in Steel Structures V.* Amsterdam; 2004.
161. De Matteis G, Naqash MT, Brando G. Effective length of aluminium T-stub connections by parametric analysis. *Eng Struct.* 2012;41:548–61.
162. Kim TS. Block Shear strength of single shear four-bolted connections with aluminium alloys – experiment and design strength comparison. *Appl Mech Mater.* 2012;217–219:386–9.
163. Cho YH, Kim TS. Estimation of ultimate strength in single shear bolted connections with aluminum alloys (6061-T6). *Thin-Walled Struct.* 2016;101:43–57.
164. Wang ZX, Wang YQ, Zhang GX, Shi YJ. Tests and parametric analysis of aluminum alloy bolted joints of different material types. *Constr Build Mater.*

- 2018;185:589–99.
165. De Matteis G, Mandara A, Mazzolani FM. T-stub aluminium joints : influence of behavioural parameters. *Comput Struct*. 2000;78(1–3):311–27.
 166. Brando G, Sarracco G, De Matteis G. Strength of an Aluminum Column Web in Tension. *J Struct Eng*. 2014;141(7).
 167. Adeoti GO, Feng F, Huihuan MA, Shen S. Investigation of aluminium bolted joint (HBJ) system behavior. *Thin-Walled Struct*. 2019;144:106100.
 168. Guo X, Xiong Z, Luo Y, Qiu L, Liu J. Experimental investigation on the semi-rigid behaviour of aluminium alloy gusset joints. *Thin-Walled Struct*. 2015;87:30–40.
 169. Guo X, Xiong Z, Luo Y, Xu H, Liang S. Block tearing and local buckling of aluminum alloy gusset joint plates. *J Struct Eng*. 2016;20(2):820–31.
 170. Guo X, Xiong Z, Luo Y, Qiu L, Huang W. Application of the Component Method to Aluminum Alloy Gusset Joints. *Adv Struct Eng*. 2015;18(11):1931–46.
 171. European Committee for Standardization (EC3) (2005) Eurocode 3: Design of Steel Structures, Part 1-8: Design of Joints. BS EN 1993-1-8:2005, CEN:2005. BSI. 2005.
 172. Guo X, Zhu S, Liu X, Wang K. Study on out-of-plane fl exural behavior of aluminum alloy gusset joints at elevated temperatures. *Thin-Walled Struct*. 2018;123:452–66.
 173. Guo X, Zhu S, Liu X, Liu L. Experimental study on hysteretic behavior of aluminum alloy gusset joints. *Thin-Walled Struct*. 2018;131:883–901.
 174. Shi M, Xiang P, Wu M. Experimental investigation on bending and shear performance of two-way aluminum alloy gusset joints. *Thin-Walled Struct*. 2018;122:124–36.
 175. Liu H, Ying J, Meng Y, Chen Z. Flexural behavior of double- and single-layer aluminum alloy gusset-type joints. *Thin-Walled Struct*. 2019;144.

-
176. Kesawan S, Mahendran M, Baleshan B. Section moment capacity tests of complex-shaped aluminium mullions. *Thin-Walled Struct.* 2018;131:855–68.
 177. Kesawan S, Mahendran M. Member moment capacity of complex-shaped aluminium mullions under wind suction loading. *Thin-Walled Struct.* 2019;144:106258.
 178. Scheperboer IC, Efthymiou E, Maljaars J. Local buckling of aluminium and steel plates with multiple holes. *Thin-Walled Struct.* 2016;99:132–41.
 179. Tsavdaridis KD, Efthymiou E, Adugu A, Hughes JA, Grekavicius L. Application of structural topology optimisation in aluminium cross-sectional design. *Thin-Walled Struct.* 2019;139:372–88.
 180. Ampatzis AT, Psomiadis VG, Efthymiou E. Plastic collapse of hardening spatial aluminium frames: A novel shakedown-based approach. *Eng Struct.* 2017;151:724–44.
 181. He L, Liu C, Wu Z, Yuan J. Stability analysis of an aluminum alloy assembly column in a modular support structure. *Thin-Walled Struct.* 2019;135:548–59.
 182. Formisano A, Lombardi L, Mazzolani FM. Perforated metal shear panels as bracing devices of seismic-resistant structures. *J Constr Steel Res.* 2016;126:37–49.
 183. De Matteis G, Brando G, Mazzolani FM. Hysteretic behaviour of bracing-type pure aluminium shear panels by experimental tests. *Earthq Eng Struct Dyn.* 2011;40(10):1143–62.
 184. De Matteis G, Mazzolani FM, Panico S. Pure aluminium shear panels as dissipative devices in moment-resisting steel frames. *Earthq Eng Struct Dyn.* 2007;36(7):841–59.
 185. Kissell JR, Ferry RL. *Aluminium Structures: A Guide to Their Specification and Design.* 2nd ed. New York: John Wiley & Sons, Inc; 2002. 465 p.
 186. Hill HN, Clark JW, Brungraber RJ. *Design of welded aluminum structures.* J

- Struct Div, ASCE. 1960;86(6):101–124.
187. Ellobody E, Feng R, Young B. *Finite Element Analysis and Design of Metal Structures*. Elsevier Inc; 2014. 205 p.
188. Ziemian R. *Guide to stability design criteria for metal structures*. 6th ed. John Wiley & Sons, Inc; 2010.
189. Buchanan C, Real E, Gardner L. Testing, simulation and design of cold-formed stainless steel CHS columns. *Thin-Walled Struct*. 2018;130:297–312.
190. Theofanous M, Chan TM, Gardner L. Structural response of stainless steel oval hollow section compression members. *Eng Struct*. 2009;31(4):922–34.
191. Hrennikoff A. Solution of Problems of Elasticity by the Framework Method. *J Appl Mech*. 2021;8(4):A169–75.
192. McHenry D. A lattice analogy for the solution of stress problems. *J Inst Civ Eng*. 1943;21(2):59–82.
193. Clough R, Martin H, Topp U. Stiffness and deflection analysis of complex structures. *J Aeronaut Sci*. 1956;23(9):805–24.
194. Clough R. The finite element method in plane stress analysis. In: *American Society of Civil Engineers, 2nd Conference on Electronic computation*. Pittsburg; 1960. p. 345–78.
195. Belytschko T. Efficient large-scale nonlinear transient analysis by finite elements. *Int J Numer Methods Eng*. 1981;10(3):579–96.
196. Hibbit, Karlsson, Sorensen. *ABAQUS: Theory Manual*. Providence, RI (USA): Dassault Systemes Corporation; 2018.
197. European Committee for Standardisation (EC2). *Eurocode 2: Design of Concrete Structures. Part 1-1: General rules and rules for buildings*. BS EN 1992-1-1: CEN:2004. BSI; 2004.
198. Tao Z, Wang Z Bin, Yu Q. Finite element modelling of concrete-filled steel stub columns under axial compression. *J Constr Steel Res*. 2013;89:121–31.

-
199. Yu T, Teng JG, Wong YL, Dong SL. Finite element modeling of confined concrete-I: Drucker-Prager type plasticity model. *Eng Struct.* 2010;32(3):665–79.
 200. De Nicolo B, Pani L, Pozzo E. Strain of concrete at peak compressive stress for a wide range of compressive strengths. *Mater Struct.* 1994;27(4):206–10.
 201. Samani AK, Attard MM. A stress-strain model for uniaxial and confined concrete under compression. *Eng Struct.* 2012;41:335–49.
 202. Hordijk DA. Local approach to fatigue of concrete. Delft University of Technology; 1991.
 203. FIP. CEB-FIP Model Code 1990. London: Thomas Telford Ltd.; 1993.
 204. Bažant ZP, Becq-Giraudon E. Statistical prediction of fracture parameters of concrete and implications for choice of testing standard. *Cem Concr Res.* 2002;32(4):529–56.
 205. Wang F, Young B, Gardner L. Compressive testing and numerical modelling of concrete-filled double skin CHS with austenitic stainless steel outer tubes. *Thin Walled Struct.* 2019;141:345–59.
 206. Rasmussen KJR, Hancock GJ. Design of thin-walled plain channel section columns against flexural buckling. *Thin-Walled Struct.* 1994;20(1–4):219–40.
 207. Jandera M, Gardner L, Machacek J. Residual stresses in cold-rolled stainless steel hollow sections. 2008;64:1255–63.
 208. Dai X, Lam D. Numerical modelling of the axial compressive behaviour of short concrete-filled elliptical steel columns. *J Constr Steel Res.* 2010;66(7):931–42.
 209. K-J B, Wilson E. Solution methods for eigenvalue problems in structural mechanics. *Int J Numer Methods Eng.* 1973;6(2):213–26.
 210. European Committee for Standardisation (EC4). Eurocode 4: Design of Composite Steel and Concrete Structures. Part 1-1: General Rules and Rules for Buildings. BS EN 1994-1-1: 2004. CEN:2004. BSI; 2004.
 211. Su M, Young B, Asce M, Gardner L. Testing and Design of Aluminum Alloy

- Cross Sections in Compression. 2014;140(9):1–11.
212. Han L. Tests on stub columns of concrete-filled RHS sections. 2002;58:353–72.
213. Liu D, Gho WM, Yuan J. Ultimate capacity of high-strength rectangular concrete-filled steel hollow section stub columns. *J Constr Steel Res.* 2003;59(12):1499–515.
214. Guo L, Zhang S, Kim WJ, Ranzi G. Behavior of square hollow steel tubes and steel tubes filled with concrete. *Thin-Walled Struct.* 2007;45(12):961–73.
215. Zhang L, Wang F, Liang Y, Zhao O. Press-braked S690 high strength steel equal-leg angle and plain channel section stub columns: Testing, numerical simulation and design. *Eng Struct.* 2019;201:109764.
216. Chen M, Young B. Experimental and numerical investigation on cold-formed steel semi-oval hollow section compression members. *J Constr Steel Res.* 2018;151:174–84.
217. Wang F, Liang Y, Zhao O. Experimental and numerical studies of pin-ended press-braked S960 ultra-high strength steel channel section columns. *Eng Struct.* 2020;215:110629.
218. Zhang L, Tan KH, Zhao O. Press-braked stainless steel channel section columns failing by flexural buckling: Testing, numerical simulation and design. *Thin-Walled Struct.* 2020;157:107066.
219. Rasmussen KJR, Hancock GJ. Tests of High Strength Steel Columns. *J Constr Steel Res.* 1995;34:27–52.
220. Theofanous M, Saliba N, Zhao O, Gardner L. Bending strength of hot-rolled elliptical hollow sections. *J Struct Eng.* 2016;125(9):97–109.
221. Wang J, Afshan S, Gkantou M, Theofanous M, Baniotopoulos C, Gardner L. Flexural behaviour of hot-finished high strength steel square and rectangular hollow sections. *J Constr Steel Res.* 2016;121:97–109.
222. Ricles JM, Sause R, Green PS, Kuhlmann U. Definition of Flange Slenderness

- Limits on the Basis of Rotation Capacity Values. 1989;0296(97):323–35.
223. Ricles JM, Sause R, Green PS. High-strength steel: implications of material and geometric characteristics on inelastic flexural behavior. 1998;0296(97):323–35.
224. Lay MG, Galambos TV. Inelastic steel beams under uniform moment. *J Struct Div.* 1965;91(6):67–93.
225. Lay MG, Galambos TV. Inelastic beams under moment gradient. *J Struct Div.* 1967;93(1):381–99.
226. Chan TM, Gardner L. Bending strength of hot-rolled elliptical hollow sections. *J Constr Steel Res.* 2008;64(9):971–86.
227. Theofanous M, Liew A, Gardner L. Experimental study of stainless steel angles and channels in bending. *Structures.* 2015;4:80–90.
228. Zhang L, Wang F, Liang Y, Zhao O. Experimental and numerical studies of press-braked S690 high strength steel channel section beams. *Thin-Walled Struct.* 2020;148:106499.
229. Zhou F, Young B. Compressive strengths of concrete-filled double-skin (circular hollow section outer and square hollow section inner) aluminium tubular sections. *Adv Struct Eng.* 2019; 1–17.
230. Gardner L, Talja A, Baddoo NR. Structural design of high-strength austenitic stainless steel. *Thin-Walled Struct.* 2006;44:517–28.
231. Tao Z, Uy B, Liao F, Han L. Nonlinear analysis of concrete-filled square stainless steel stub columns under axial compression. *J Constr Steel Res.* 2011;67(11):1719–32.
232. Theofanous M, Saliba N, Zhao O, Gardner L. Ultimate response of stainless steel continuous beams. *Thin-Walled Struct.* 2014;83:115–27.
233. Seif M, Schafer BW. Local buckling of structural steel shapes. *J Constr Steel Res.* 2010;66(10):1232–47.
234. Li Z, Schafer BW. Buckling analysis of cold-formed steel members with general

- boundary conditions using CUFSM: conventional and constrained finite strip methods. In: 20th International Specialty Conference on Cold-Formed Steel Structures. St. Louis, Missouri, U.S.A.; 2010.
235. NAS. North American Specification for the Design of Cold-Formed Steel Structural Members. American Iron and Steel Institute, Washington, DC, 2012 (AISI S100-12).
236. Manganiello M, De Matteis G, Landolfo R. Inelastic flexural strength of aluminium alloys structures. *Eng Struct.* 2006;28(4):593–608.
237. Gardner L, Wang F, Liew A. Influence of strain hardening on the behavior and design of steel structures. *Int J Struct Stab Dyn.* 2011;11(5):855–75.
238. Gardner L. The continuous strength method. *Struct Build.* 2008;161(SB3):127–33.
239. Gardner L, Theofanous M. Discrete and continuous treatment of local buckling in stainless steel elements. *J Constr Steel Res.* 2008;64:1207–16.
240. Afshan S, Gardner L. The continuous strength method for structural stainless steel design. *Thin Walled Struct.* 2013;68:42–9.
241. Zhao O, Gardner L. The continuous strength method for the design of mono-symmetric and asymmetric stainless steel cross-sections in bending. *J Constr Steel Res.* 2018;150:141–52.
242. Zhao O, Afshan S, Gardner L. Structural response and continuous strength method design of slender stainless steel cross-sections. *Eng Struct.* 2017;140:14–25.
243. Schafer BW, Peköz T. Direct strength prediction of cold-formed steel members using numerical elastic buckling solutions. *Int Spec Conf Cold-Formed Steel Struct Recent Res Dev Cold-Formed Steel Des Constr.* 1998;69–76.
244. Schafer BW. Review: The Direct Strength Method of cold-formed steel member design. *J Constr Steel Res.* 2008;64(7–8):766–78.
245. Gkantou M, Bock M, Theofanous M. Design of stainless steel cross-sections with

- outstand elements under stress gradients. *J Constr Steel Res.* 2021;179:106491.
246. GC C. Thin walled I-sections in compression and bending. [Sydney]: Sydney University; 1997.
247. Rusch A, Lindner J. Remarks to the Direct Strength Method. 2001;39:807–20.
248. Bambach MR, Rasmussen KJR. Tests of Unstiffened Plate Elements Under Combined Compression and Bending. 2004;130:1602–10.
249. Bambach MR, Rasmussen KJR. Design Provisions for Sections Containing Unstiffened Elements with Stress Gradient. 2004;130:1620–8.
250. Bambach MR, Rasmussen KJR, Ungureanu V. Inelastic behaviour and design of slender I-sections in minor axis bending. *J Constr Steel Res.* 2007;63(1):1–12.
251. Bambach MR, Rasmussen KJR. Effective Widths of Unstiffened Elements with Stress Gradient. 2006;130(10):1611–9.